Innovative Subsurface Learning and Hawaiian Exploration using Advanced Tomography (ISLAND HEAT) Phase 1 Final Report

Ian Warren,[1*] Michael J. Friedel,[2] Erin Wallin,[2] Nicole Lautze,[2] Z. Jason Hou,[3] D.W. Vasco,[4] Stanislav Glubokovskikh,[4] Roland Gritto,[5] Steve Jarpe,[6] Stephen J. Martel,[2] Piyoosh Jaysaval,[3] Huiying Ren,[3] Alain Bonneville,[3] Hannah Pauling,[1] Amanda Kolker,[1] and Greg Rhodes[1*]

1 National Renewable Energy Laboratory

** former employees*

2 University of Hawai'i-Manoa

3 Pacific Northwest National Laboratory

4 Lawrence Berkeley National Laboratory

5 Array Information Technology

6 Jarpe Data Solutions

NREL is a national laboratory of the U.S. Department of Energy
Office of Energy Efficiency & Renewable Energy
Operated by the Alliance for Sustainable Energy, LLC

This report is available at no cost from the National Renewable Energy Laboratory (NREL) at www.nrel.gov/publications.

Contract No. DE-AC36-08GO28308

Technical Report
NREL/TP-5700-87316
September 2023

Innovative Subsurface Learning and Hawaiian Exploration using Advanced Tomography (ISLAND HEAT) Phase 1 Final Report

Ian Warren,[1*] Michael J. Friedel,[2] Erin Wallin,[2] Nicole Lautze,[2] Z. Jason Hou,[3] D.W. Vasco,[4] Stanislav Glubokovskikh,[4] Roland Gritto,[5] Steve Jarpe,[6] Stephen J. Martel,[2] Piyoosh Jaysaval,[3] Huiying Ren,[3] Alain Bonneville,[3] Hannah Pauling,[1] Amanda Kolker,[1] and Greg Rhodes[1*]

1 National Renewable Energy Laboratory

** former employees*

2 University of Hawai'i-Manoa

3 Pacific Northwest National Laboratory

4 Lawrence Berkeley National Laboratory

5 Array Information Technology

6 Jarpe Data Solutions

Suggested Citation

Warren, Ian, Michael J. Friedel, Erin Wallin, Nicole Lautze, Z. Jason Hou, D.W. Vasco, Stanislav Glubokovskikh, Roland Gritto, Steve Jarpe, Stephen J. Martel, Piyoosh Jaysaval, Huiying Ren, Alain Bonneville, Hannah Pauling, Amanda Kolker, and Greg Rhodes. 2023. *Innovative Subsurface Learning and Hawaiian Exploration using Advanced Tomography (ISLAND HEAT) Phase 1 Final Report*. Golden, CO: National Renewable Energy Laboratory. NREL/TP-5700-87316. https://www.nrel.gov/docs/fy23osti/87316.pdf.

NREL is a national laboratory of the U.S. Department of Energy
Office of Energy Efficiency & Renewable Energy
Operated by the Alliance for Sustainable Energy, LLC

This report is available at no cost from the National Renewable Energy Laboratory (NREL) at www.nrel.gov/publications.

Contract No. DE-AC36-08GO28308

Technical Report
NREL/TP-5700-87316
September 2023

National Renewable Energy Laboratory
15013 Denver West Parkway
Golden, CO 80401
303-275-3000 • www.nrel.gov

NOTICE

This work was authored in part by the National Renewable Energy Laboratory, operated by Alliance for Sustainable Energy, LLC, for the U.S. Department of Energy (DOE) under Contract No. DE-AC36-08GO28308. Funding provided by the U.S. Department of Energy Office of Energy Efficiency and Renewable Energy Geothermal Technologies Office. The views expressed herein do not necessarily represent the views of the DOE or the U.S. Government.

Cover Photos by Dennis Schroeder: (clockwise, left to right) NREL 51934, NREL 45897, NREL 42160, NREL 45891, NREL 48097, NREL 46526.

Preface

Hawai‘i is an ideal candidate for expansion of geothermal power production due to high power prices and strong demand for reliable and flexible baseload power generation. Additionally, the existence of a proven geothermal resource increases the likelihood of further geothermal potential. However, while it is estimated that there is more than 1,000 MW of geothermal potential on the Hawaiian Islands, there are few surface manifestations such as hot springs, fumaroles, or hydrothermal alteration deposits. Realistic conceptual models, an integrated exploration approach, and advanced geophysical imaging techniques are required to define the fingerprint of prospective resources and target heat and permeability prior to drilling expensive, high risk, exploratory wells. Unfortunately, geophysical surveys over large areas can be expensive, and the nonunique solutions of their inversions lead to greater uncertainty when interpreted independently and without a complete understanding of magmatic hydrothermal signatures.

To avoid collecting expensive detailed geophysical surveys over expansive prospective regions, this project leverages and enhances the existing play fairway analysis (PFA) results and validates a conceptual model-driven, optimized, least-cost exploration and geophysical suite at a proven geothermal field with known permeability: Puna Geothermal Venture, located in the Lower East Rift Zone. The abundance of pre-, syn-, and, with this study, post-eruptive geophysical characterization of the geothermal regime at and around the broader Puna system offers a rare control opportunity to elucidate geophysical expressions within a dynamic magmatic setting. Application of the methodology at a second prospective site identified by the PFA, Mauna Kea, serves as confirmation of the integrated approach. In this study, conceptual models and their associated geologic characteristics and geophysical signatures of ocean-island hydrothermal systems are developed and informed by the existing field. Surface and subsurface geologic and geophysical data are commonly correlated and jointly inverted using machine learning and sensitivity analysis of the multiple inputs.

Acknowledgment

This work was supported by funding from the U.S. Department of Energy Geothermal Technologies Office.

List of Acronyms

AMT	audiomagnetotelluric
CBA	complete Bouguer anomalies
BEM	boundary element
BMU	best-matching unit
DEM	digital elevation model
DEzs	Differential Evolution MCMC with snooker update and sampling from past states
DOE	U.S. Department of Energy
ERZ	East Rift Zone
GPS	Global Positioning System
GSU	geothermal stratigraphic units
GTO	Geothermal Technologies Office
HVO	Hawaiian Volcano Observatory
InSAR	Interferometric Synthetic Aperture Radar
IRIS	Incorporated Research Institutions for Seismology
ISLAND HEAT	Innovative Subsurface Learning and Hawaiian Exploration using Advanced Tomography
LiDAR	light detection and ranging
LERZ	Lower East Rift Zone
MCMC	Markov Chain Monte Carlo
MML	multimodal machine learning
MSOM	Modified Self-Organizing Map
MT	magnetotelluric
NREL	National Renewable Energy Laboratory
PFA	play fairway analysis
PGV	Puna Geothermal Venture
PNNL	Pacific Northwest National Laboratory
PTA	Pōhakuloa Training Area
REMAS	Rapid Earthquake Monitoring & Analysis System
rms	root mean-squared
RTP	reduction to pole
SOH	State Observation Hole
TC	terrain correction
TDR	tilt derivative
TE	transverse electric
TM	transverse magnetic
UH	University of Hawai‘i
USGS	United States Geological Survey

Executive Summary

Hawai‘i is an ideal candidate for expansion of geothermal power production due to strong demand for reliable and flexible baseload power generation. However, nearly all of the estimated 1,000+ MW on the Hawaiian Islands exhibit no apparent surface hot springs, fumaroles, or alteration. Because of that, an integrated exploration approach is needed that combines realistic conceptual models, advanced geophysical imaging techniques, and existing play fairway analysis (PFA) results. This integrated approach can define the fingerprint of prospective resources as well as target heat and permeability to reduce the risks of drilling exploratory wells.

The Innovative Subsurface Learning and Hawaiian Exploration using Advanced Tomography (ISLAND HEAT) project—detailed in this report—aims to leverage and enhance existing Hawai‘i geothermal PFA results and validate a conceptual model-driven, optimized, least-cost exploration and geophysical suite at a proven geothermal field with known permeability, the Puna Geothermal Venture, located in the Lower East Rift Zone. The abundance of geophysical scrutinization before, during, and after the 2018 Kilauea eruption at and around the broader Puna system offers a rare opportunity to elucidate geophysical expressions within a dynamic magmatic rift setting. Development of the methodology continues with its application at a second prospective site identified by the PFA, Mauna Kea, which serves as confirmation of the integrated approach.

In Phase 1, the development of conceptual models and their associated predicted geologic characteristics and geophysical signatures of ocean-island hydrothermal systems are informed by diverse data sets. The project has focused on compiling and updating data from the Hawai’i PFA project, specifically at Kilauea’s Lower East Rift Zone and at the Mauna Kea Saddle Region. Data include tabulated well/drill data, magnetotelluric (MT) data, aeromagnetic data, gravity data, and digitized self-potential data and derivatives of these. Gravity and MT data have been inverted for density and resistivity, respectively. This modeling includes analysis and preparation of the data sets for joint inversions in Phase 2. New, stochastic code has been developed and tested for 1-, 2-, and 3D forward and inverse modeling of MT and gravity data. Seismic data from before, during, and after the 2018 Kilauea eruption have been processed to yield compressional velocity (Vp), shear wave velocity (Vs), and the ratio of Vp/Vs after relocation and refinement of data from available earthquake catalogues. Global Positioning System (GPS) and Interferometric Synthetic Aperture Radar (InSAR) data have been used to understand deformation associated with the 2018 Kilauea eruption and to model fracture formation and its relationship to permeability at Puna Geothermal Venture. These data together are being used to inform multimodal machine learning algorithms in order to identify and predict the numerical and categorical features associated with hidden geothermal systems.

Table of Contents

List of Figures

List of Tables

1 Introduction

Multiple favorable geothermal prospects have been identified through play fairway analysis (PFA) in the state of Hawai‘i (Lautze et al. 2017). The University of Hawai‘i (UH), the National Renewable Energy Laboratory (NREL), and additional team members partnered to perform further study on two of these areas: the Lower East Rift Zone (LERZ) of Kilauea, where a known geothermal resource exists, and the Mauna Kea Saddle Region, where PFA identified a high probability of a geothermal resource.

The objective of the Innovative Subsurface Learning and Hawaiian Exploration using Advanced Tomography (ISLAND HEAT) project is to support the advancement of science related to developing geothermal energy by reducing the risks, costs, and uncertainty of geothermal exploration and improving the success rate of well drilling through optimization of an innovative, multi-attribute synthesis calibrated using proven heat and permeability data. Our work effort was two-fold: (1) to compile and integrate existing data; and (2) to complete iterative and machine learning-assisted common correlation and inversion of existing data sets to improve subsurface confidence and understanding of the unique integrated geophysical signature of a productive geothermal system.

This report details ISLAND HEAT Phase 1 activities including compilation, processing, integration, and interpretation of existing data.

Section 2 highlights activities including compilation of existing data from a variety of sources and revised stress analysis and geologic analyses for the two main sites of interest. We then present results from application of multimodal machine learning (MML) for 3D characterization of hidden groundwater and geothermal resources.

Section 3 summarizes the gravity, magnetotelluric (MT), and audiomagnetotelluric (AMT) data availability and data quality. It also details the development of new forward and inverse models for multigeophysics measurements, including gravity and AMT/MT data, and inversion outputs as spatial models of density and electrical resistivity to the machine learning and data synthesis teams for physics-based interpretation and conceptual model development.

Section 4 details analysis of statistical parameters of seismicity, which can help to illustrate links to potential geothermal resources on the island. In this task, we updated the double-difference relocated catalog for seismicity on the island of Hawai‘i, created by Matoza et al. (2013). This included recent seismicity of the last decade, harnessing the improvements in station coverage during that period and leveraging the tremendous amount of seismic monitoring of the Hawaiian Volcano Observatory (HVO) network. Subsequently, the updated and refined catalog was analyzed to identify seismicity and statistical properties.

Section 5 details the use of Interferometric Synthetic Aperture Radar (InSAR) to improve upon previous Global Positioning System (GPS)-based estimates of tectonic strain rate, which is often taken as an indication of the presence of permeability. GPS, InSAR, and light detection and ranging (LiDAR) data were combined to create detailed fault models for the areas of interest, develop slip models of the two-dimensional fault surfaces, and ultimately inform the conceptual model and integrated 3D geologic model.

Section 6 outlines the path forward towards developing and refining existing conceptual models for LERZ and at Mauna Kea. Revised conceptual models will help guide final survey designs for new geophysical data collections to augment existing data and decrease uncertainty in existing conceptual models.

Finally, in Section 7 a data collection plan for Phase 2 is proposed to fill in gaps in existing MT and gravity data and bring in new information in the form of seismic velocities and self-potential. Combined with existing data, the proposed collection will enhance our understanding of Hawai‘i’s subsurface and help refine the characteristics and occurrence of producible geothermal resources.

2 Hawai‘i Play Fairway Analysis, Data Compilation, and Multimodal Machine Learning

Early ISLAND HEAT project activities included compilation of existing data, knowledge, and expertise for the two sites of interest, LERZ and Mauna Kea, on the Big Island of Hawai‘i. In this task, the team compiled and provided publicly available relevant pre-, syn-, and post-eruptive geological, geophysical, geochemical, remote sensing, and drilling data held by institutions and subject matter experts such as the University of Hawai‘i (UH) at Mānoa and HVO.

We performed traditional inversion methods and modeling of the geophysical data sets prior to applying machine learning on inverted datasets for 3D characterization of hidden groundwater and geothermal resources.

Section 2.1 describes data compilation and analysis, as well as inversion and modeling results. Section 2.2 addresses structural control on permeability. Section 2.3 then presents results from MML.

2.1 Data Compilation and Inversion of Existing Data Sets

2.1.1 Compilation of LERZ and Mauna Kea Saddle Region Data

Multiple data sets related to the two focus areas (LERZ and Mauna Kea Saddle Region) are shown in Figure 1 and Table 1, which respectively show and list the geophysical data sets provided to the project and the locations of wells, MT, and gravity stations. In addition to providing gravity, aeromagnetic, and MT data to the project (Table 1), UH tabulated well log information that had previously been available only as .pdf reports. The information in older well logs tends to be sparse, with most sources describing just the lithology, although some do present groundwater temperature and chemistry data and/or rock properties such as the depth at which distinctive lava flows are encountered or the depth of a dike intrusion. Such information is worthwhile for MML as the MML model can benefit from even sparse information. The newly tabulated data for State Observation Holes (SOH) 1, 2 and 4, wells that were drilled into Kilauea’s LERZ in 1991–1992, have been included along with logging results from two recently drilled deep wells in the Saddle Region: PTA2 and KMA1. We also digitized and uploaded the results from the 1979 LERZ self-potential survey collected by Microgeophysics Corporation for Atlantic Richfield Company.

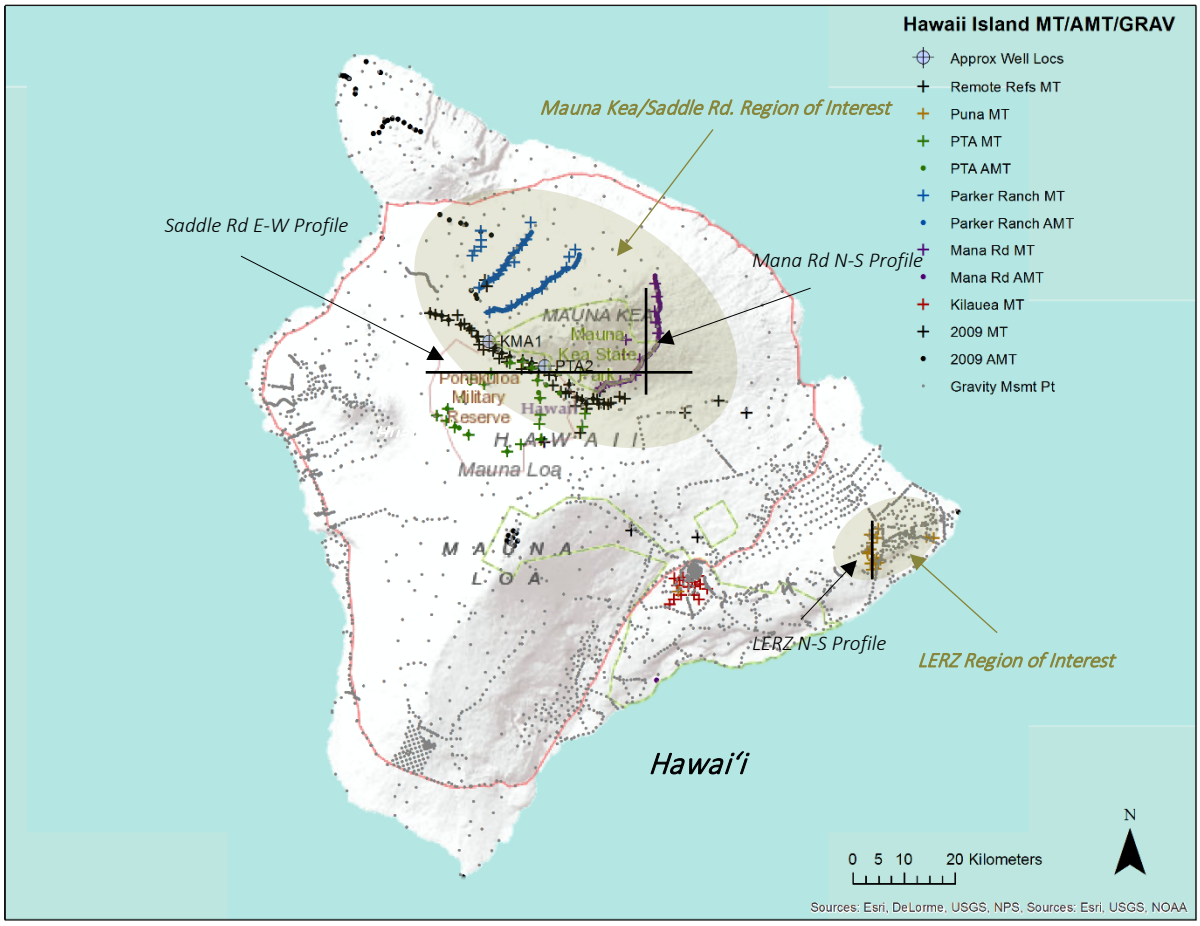

Figure 1. Map of Hawai'i showing well locations for PTA2, KMA1; MT profiles for Saddle Road, Mana Road, and LERZ; and locations of MT, AMT and gravity measurements.

Table 1. Existing Geophysical Data for Hawai‘i Island

Data Set ID	Number of Stations	Notes
Kīlauea MT	18	1D Models and Data Files uploaded to ISLAND HEAT database[d,e,f]
PTA[a] MT[b]	23	1D Models uploaded to ISLAND HEAT database
PTA AMT[c]	20	Data Files uploaded to ISLAND HEAT database
2009 MT	52	1D and 2D Profile Models and Data Files uploaded to ISLAND HEAT database
2009 AMT	64	Data Files uploaded to ISLAND HEAT database
Puna MT	16	1D Models and Data Files uploaded to ISLAND HEAT database
Parker Ranch AMT	72	Data Files uploaded to ISLAND HEAT database
Parker Ranch MT	27	1D Models uploaded to ISLAND HEAT database
Mana Rd MT	12	1D and 2D Profile Models uploaded to ISLAND HEAT database
Mana Rd AMT	56	Data Files uploaded to ISLAND HEAT database
Gravity	3411	Data Files uploaded to ISLAND HEAT database
Aeromagnetic	Island Wide	Data Files uploaded to ISLAND HEAT database
PTA2	WELL	Data uploaded to ISLAND HEAT database
SOH1	WELL	Data extracted from pdf report, tabulated, and uploaded to ISLAND HEAT database
SOH2	WELL	Data extracted from pdf report, tabulated, and uploaded to ISLAND HEAT database
SOH4	WELL	Data extracted from pdf report, tabulated, and uploaded to ISLAND HEAT database
1979 SP Survey	850	Data Digitized and uploaded to ISLAND HEAT database

[a] PTA (Pōhakuloa Training Area)
[b] MT (magnetotelluric,station spacing 1-4 km, frequencies = 10-4 to 500 Hz)
[c] AMT (audio-magnetotelluric, station spacings ~500 m, collected with Stratagem EH4, frequencies = 15.8 to 104 Hz)
[d] Data Files are in *.edi format
[e] Coordinates (World Geodetic System 1984) of all data locations have been uploaded to ISLAND HEAT database on the Data Foundry on OpenEI
[f] ISLAND HEAT database is on Data Foundry on OpenEI

2.1.2 Reprocess and Invert Geophysical Data Sets Prior to Applying Machine Learning

This report is the first to present several MT data sets collected by UH in Kilauea's LERZ and surrounding Mauna Kea. Pierce and Thomas (2009) describe AMT and MT data collected along the Humu‘ula section of Saddle Road between Mauna Kea and Mauna Loa in 2004 and 2008 respectively. Additional AMT and MT data were acquired by UH researchers between 2012 and 2015. Survey areas during those years included the Kilauea summit (2012–2013), Kilauea's LERZ (2013), Pōhakuloa Training Area (PTA) in the Saddle Region (2013), and Parker Ranch and Mana Road around the west and east flanks of Mauna Kea (2014–2015). Thomas, Lienert, and Wallin (2015) presented initial 2D resistivity profiles from the PTA MT survey at the Fall 2015 meeting of the American Geophysical Union.

In the following, we describe the results from the application of traditional inversion methods and modeling of the geophysical data sets listed in Table 1. By doing so, we compare a variety of data and their models and analyze how the relationships between their properties vary. Many of the available data or models have not been collocated previously with any other data or modeled properties. As will be discussed below, MML is well suited to use sparse and noncollocated data for feature selection, prediction, and clustering. The following sections describe products of the processing and modeling of these various geophysical data sets, as well as of stress analyses, and how they feed into MML where collocation is not required.

2.1.2.1 Reprocessing and Interpretation of Island-Wide Aeromagnetics and Gravity

2.1.2.1.1 Aeromagnetics

Aeromagnetic data were collected over Hawai‘i Island during two surveys in 1978 by the U.S. Geological Survey (Godson et al. 1981). We have gridded them first as total magnetic field intensity values, following the total magnetic field intensity calculation by reduction to pole (RTP; Finn, personal communication, 2021) so that anomalies caused by an arbitrary source were not influenced by magnetic inclination (i.e., anomalies were shifted above causative bodies to what they would be if the magnetic field were vertical and magnetization occurred only by induction). The grid spacing of 400 m accommodates the two flight-line spacings (.8 and 1.6 km) of the 1978 survey (Hildenbrand, Rosenbaum, and Kauahikaua 1993). Total magnetic field intensity and reduction to pole grids have been uploaded to Data Foundry for use in MML. The total magnetic field intensity is shown in map view in Figure 2, with the reduction to pole map in Figure 3. The RTP map reveals shallow magnetic intrusions along Kilauea’s East Rift Zone (ERZ) flanked by a deeper magnetic low, which agrees with the findings reported by Hildenbrand, Rosenbaum, and Kauahikaua (1993), and the magnetic susceptibility cross section across the middle East Rift Zone of Kilauea modelled by Carol Finn (personal communication) displayed in Figure 4.

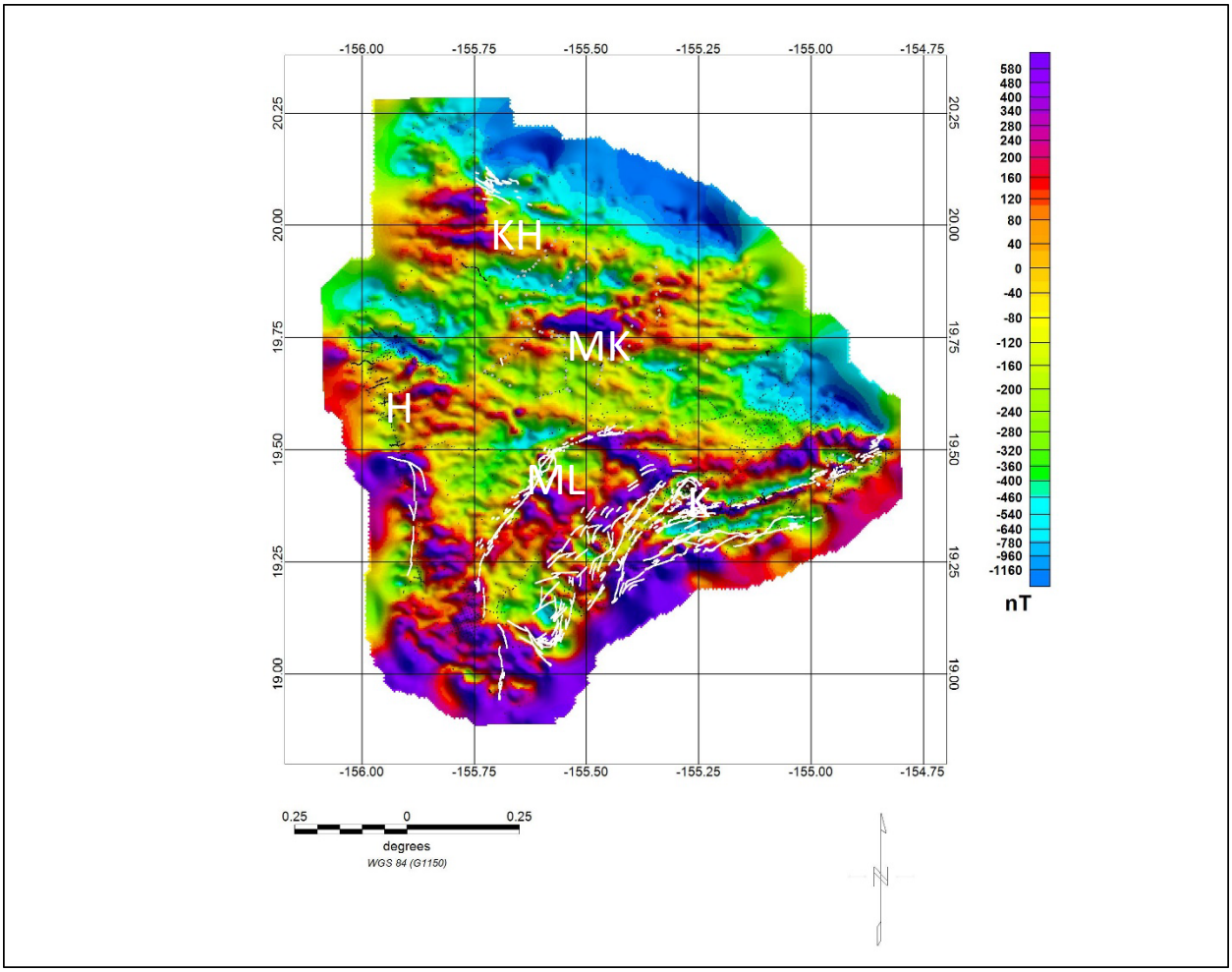

Figure 2. Map of total magnetic field intensity on the Hawai‘i Island. White lines indicate mapped faults. Red and purple colors show regions with high magnetic susceptibility.

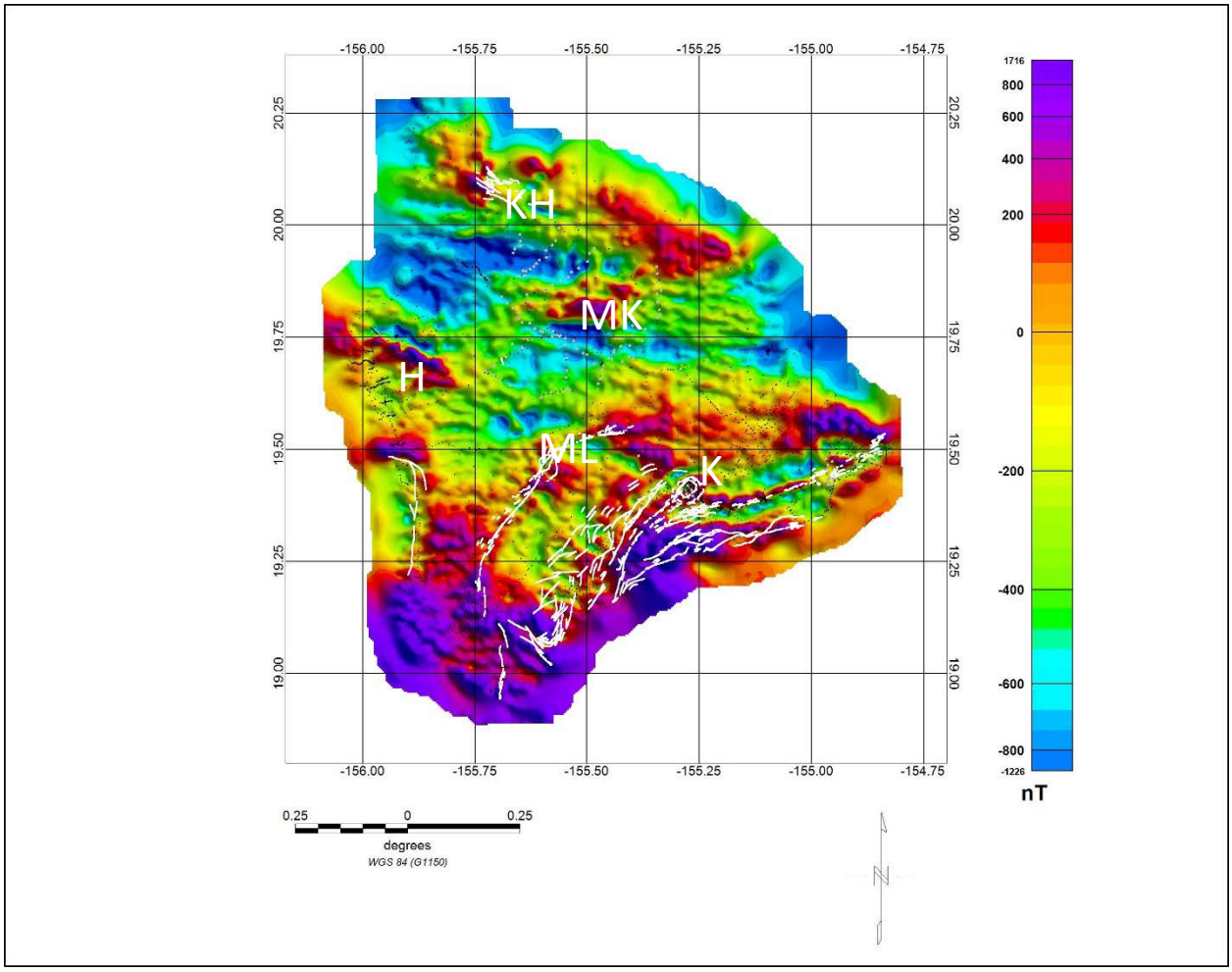

Figure 3. Map of reduction to pole anomalies on Hawai‘i Island. White lines indicate mapped faults. Red and purple colors show regions with high magnetic susceptibility.

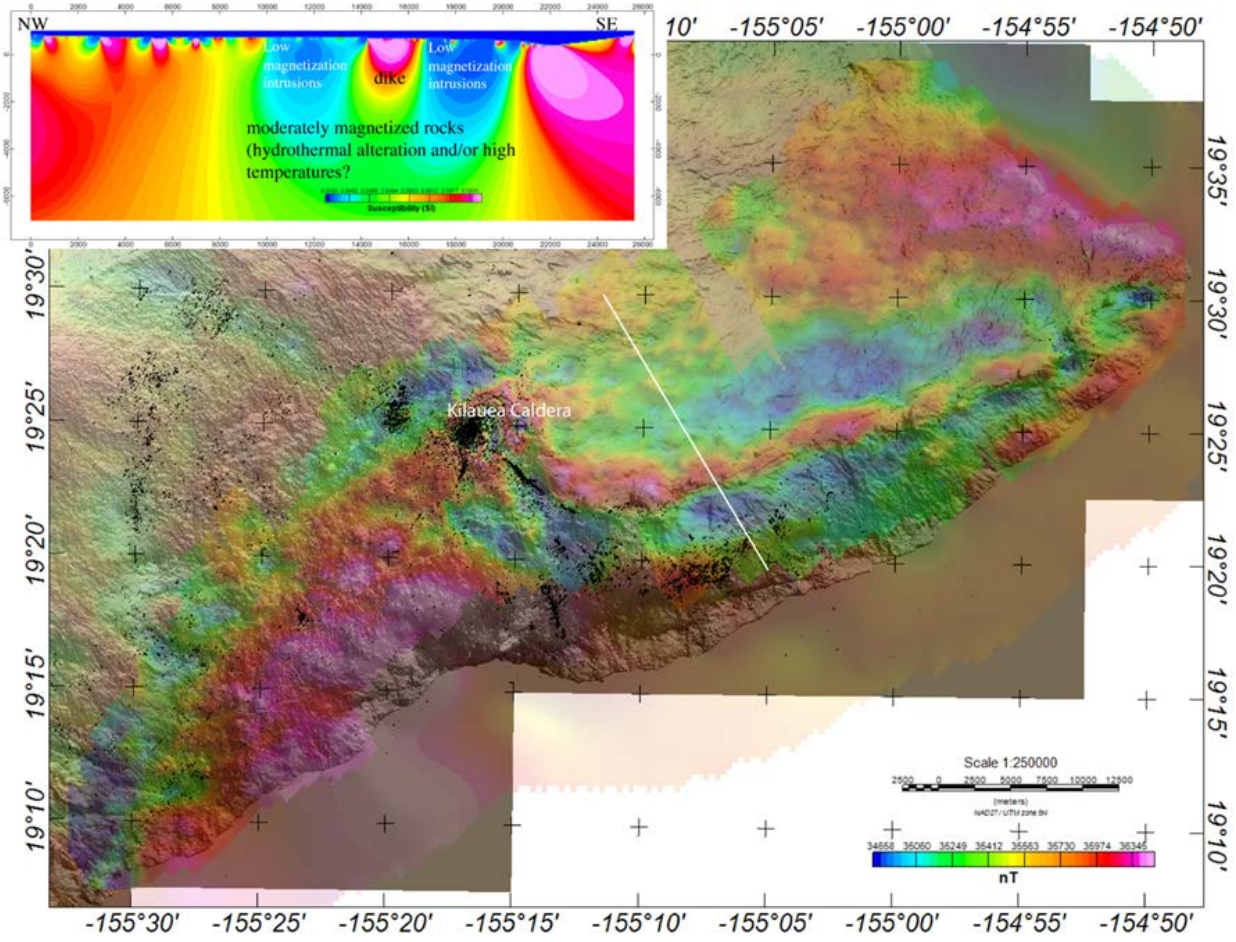

Figure 4. Magnetic profile modeled by Finn (personal communication, 2022).

2.1.2.1.2 Gravity

We began with observed and theoretical gravity data at 3,000 sites across Hawai‘i Island downloaded from sciencebase.gov (Kauahikaua 2017). We then added an additional 111 gravity measurements collected by UH between 2014 and 2015. The *.csv* files that we uploaded onto the ISLAND HEAT database contain new calculations of complete Bouguer anomalies (CBA) at 3411 locations. All data collection coordinates are in WGS 1984. The gravity measurement locations are shown in Figure 1.

Terrain correction (TC) is the last step of the gravity data reduction to obtain CBAs, where:

$$\text{CBA} = g_{obs} - g_N + g_{fa} - g_{sb} + g_{TC},$$

The terms g_{obs} and g_N are the observed and theoretical gravity at a measurement point, and g_{fa} and g_{sb} are the free air and Bouguer slab corrections respectively. The first four terms of the right-hand side of the expression comprise the simple Bouguer anomaly, and the final term is the terrain correction (Blakely 1995). The terrain corrections were initially calculated using GSOLVE (McCubbine et al. 2018) starting with $\rho_{land} = 2.67$ Mg/m^3, $\rho_{water\ surface} = 1.03$ Mg/m^3, and $\rho_{bathymetry} = \rho_{land} - \rho_{water\ surface} = 1.64$ Mg/m^3, using the following resolution digital elevation model

(DEM) grids. They include land and bathymetry elevations (Peterson, personal communication, 2021):

- 10 m DEM grid for terrain correction calculations between 2 and 2,610 m from each data point, which was the finest DEM grid available that covered all data points
- 250 m grid for terrain correction calculations between 2,610 m and 21.9 km from data point
- 2,000 m grid for terrain correction calculations between 21.9 and 167 km from each data point.

For modeling, we wanted a reduction density (ρ_{red}) that produces a CBA that is not over- or undercorrected and therefore not correlated with topography and one that identifies the shallow (<3 km) intrusions of interest to the geothermal resource. Once the terrain corrections and CBA were calculated for the initial ρ_{land} =2.67 Mg/m^3 data set, the individual terrain corrections were back calculated so that total TCs could be quickly calculated for different reduction densities (ρ_{red}) including 2.25 Mg/m^{3}and 2.45 Mg/m^3. We then gridded and mapped the CBA for three ρ_{red} values and extracted multiple profiles to check for under- or overcorrection of the data set. Figure 5 shows the CBAs for the three densities plotted with topography. These data came from the gravity and topography data from the Southwest Rift Zone of Kilauea (marked on map). An ideal reduction density will produce a CBA that only identifies a density anomaly and does not correlate with topography. In Figure 5, the gravity profiles for the three densities are not strikingly unique from one another; however, a density of ρ_{red} = 2.67 Mg/m^3 was selected based on similar densities utilized by other authors (Flinders et al. 2013; Kauahikaua 2000; Finn, personal communication, 2022). In Phase 2, we can recalculate CBAs for higher reduction densities to determine if 2.67 Mg/m^3 is ideal or if a higher reduction density provides a better comparison with topography profiles.

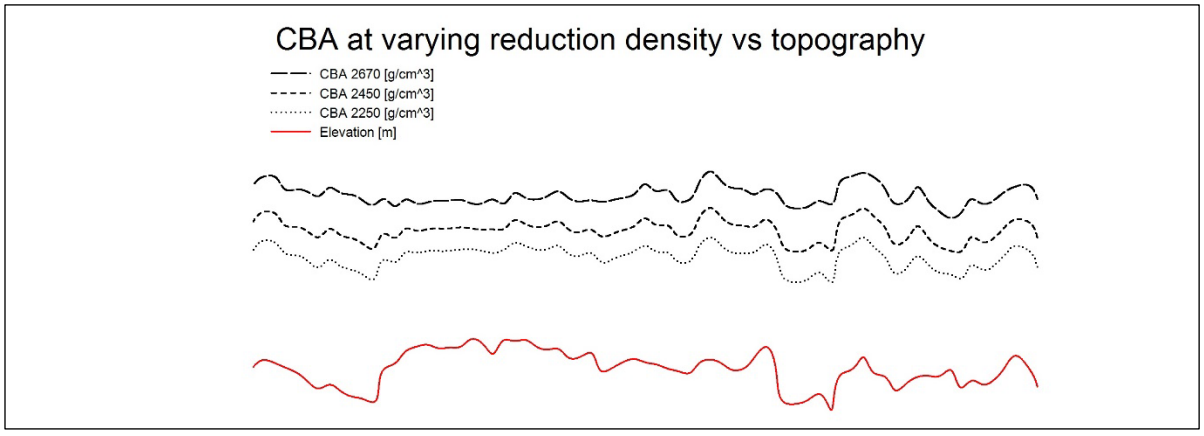

Figure 5. Comparison of CBAs for three reduction densities and topography. Multiple profiles appear to show no large differences using the three reduction density values.

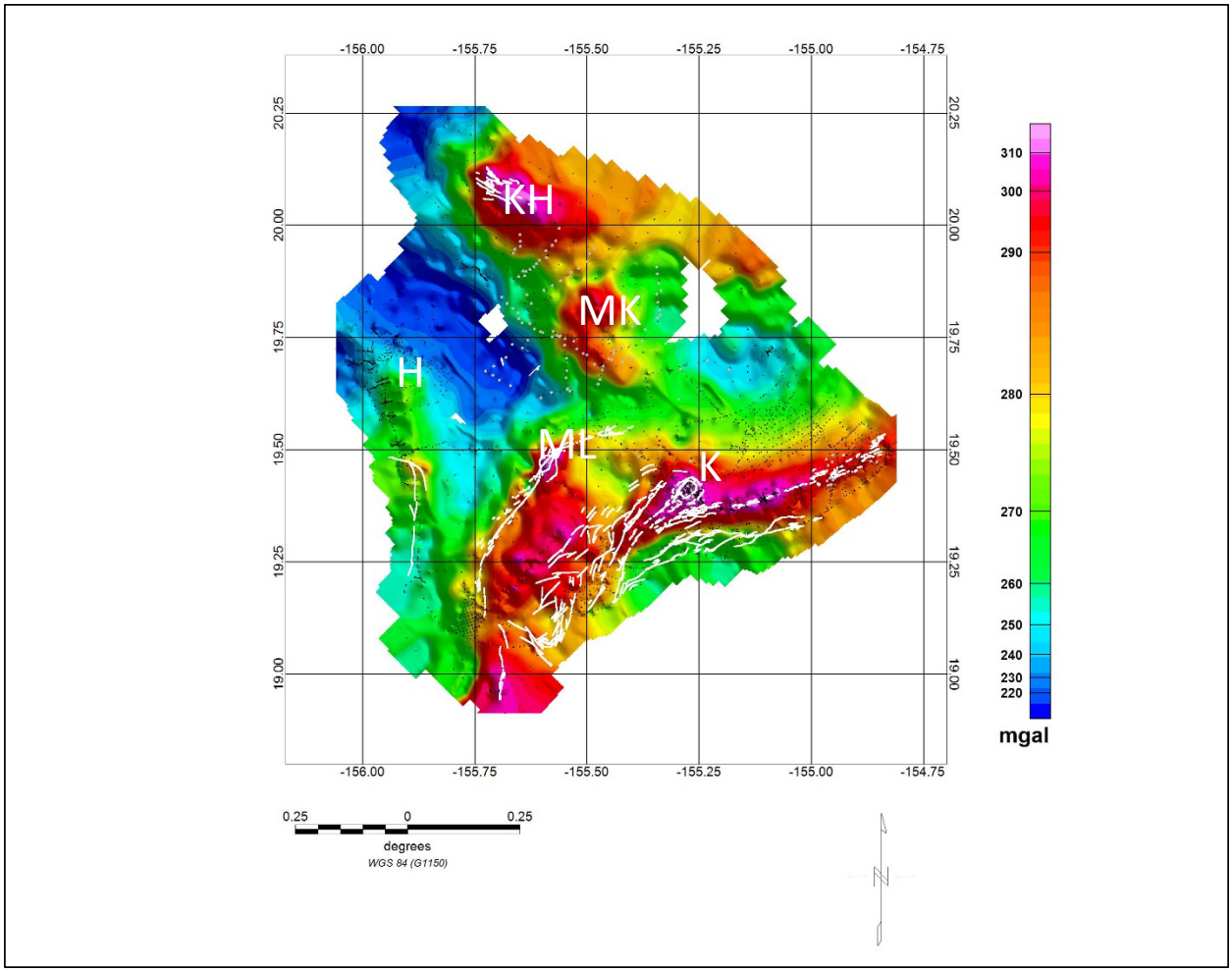

Figure 6. CBA for reduction density, ρ_{red} = 2.67Mg/m3

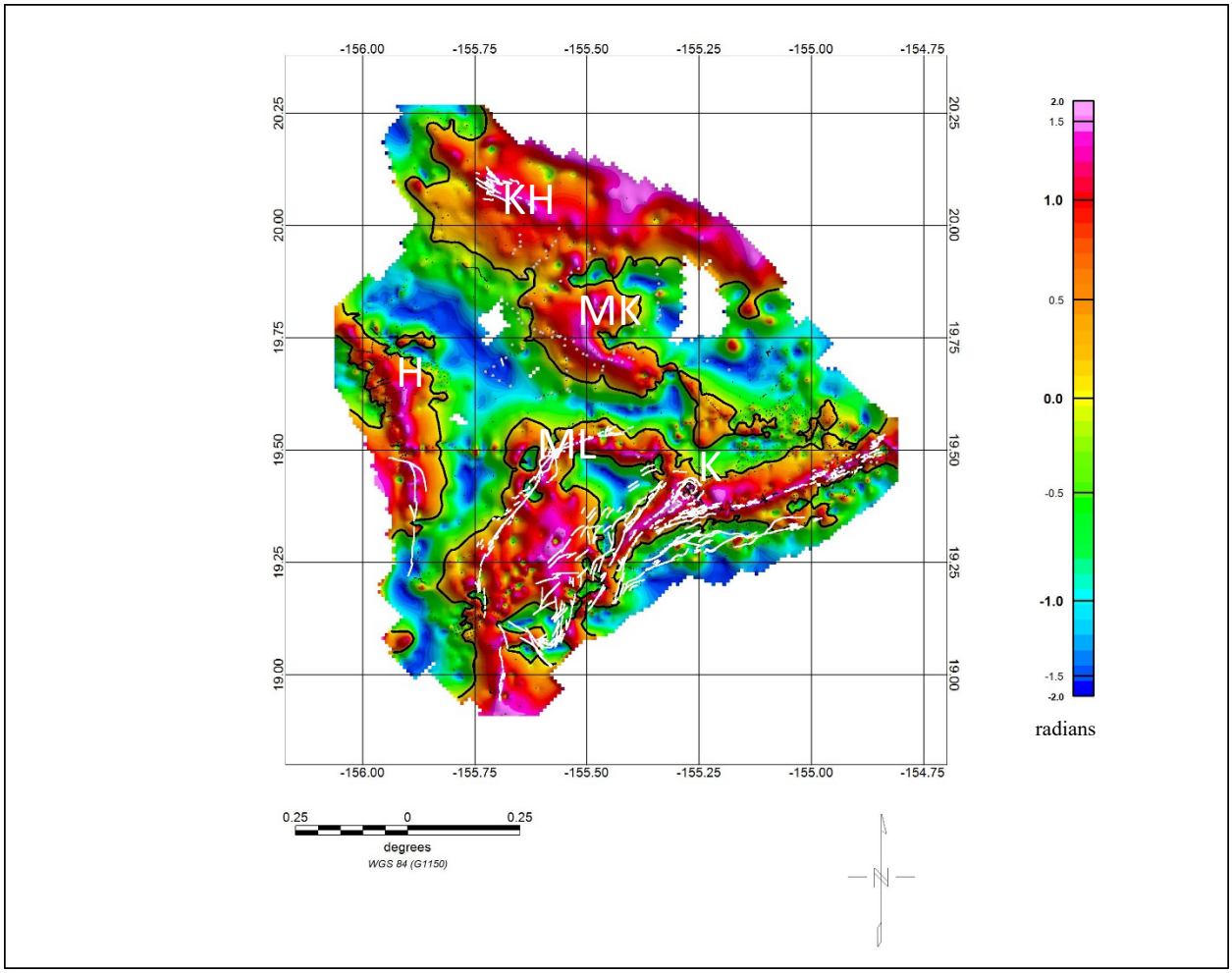

Figure 7. Tilt derivative map of Big Island gravity data

2.1.2.2 Interpretation of Aeromagnetic and Gravity Data

For ISLAND HEAT Phase 1, in addition to the three-dimensional gravity modeling performed by Pacific Northwest National Laboratory (PNNL) (Bonneville, personal communication), we used gradients to help interpret the horizontal location of anomalous bodies in the island-wide gravity and aeromagnetic data. We followed the methodology described by Hinze et al. (2013) and Rosid and Aprilia (2020) and compared to results from work done by Hildenbrand et al. (1993) and Kauahikaua (2000). Following RTP, the aeromag data were filtered to obtain first order vertical derivatives and tilt derivatives (TDR). The tilt derivative is defined as the arctangent of the first vertical derivative divided by the total horizontal gradient,

$$\emptyset = tan^{-1} \frac{\frac{\partial D}{\partial z}}{\sqrt{\frac{\partial D^2}{\partial x} + \frac{\partial D^2}{\partial y}}},$$

where D (in this case) is the magnetic field after reduction to pole. The same processing sequence was also applied to the island-wide gravity data. For both cases, the zero contour of the tilt derivative approximately delineated the edge of a source (black contour line in Figure 8). In the Hawaiian volcanic setting, variations in composition, grain size, and concentration of

titanomagnetite largely account for aeromagnetic anomalies, while alteration of older buried material tends to decrease magnetization (Hildenbrand et al. 1993). The two-dimensional model across the ERZ (Figure 4) demonstrates the variability of magnetization. We interpreted Figure 8a as showing a dike intrusion flanked by less magnetic or deeper intrusions. This corresponds to findings at SOH-4 where susceptibilities increase at a depth of about 1 km and then decrease near 2.5 km, likely due to the high temperatures of shallow magma (Hildenbrand et al. 1993). The sensitivity of magnetic data to shallow structures and the sensitivity of gravity data to deeper structure are evident in Figure 8a and b. The dense cores and rift zones of Mauna Loa, Mauna Kea, Kohala, Hualālai, and Kilauea are clearly seen in the TDR of the gravity data (Figure 8b – right panel), but they are much less evident in the magnetic TDR map (Figure 8a – left panel). Essentially, no anomaly appears in the aeromagnetic TDR associated with Mauna Kea. The transition from highly magnetized tholeiitic to less magnetized alkalic basalt occurred during the evolution of shield volcanoes. This transition allowed us to see details in the tholeiitic basalts at Kilauea and Mauna Loa that we could not detect in the alkalic basalts at Mauna Kea or Hualālai. Further, the mapped fault systems, such as the Hilina fault system, were better resolved in the TDR aeromagnetic map (Figure 8a) than in the gravity map (Figure 8b), indicating that these fault systems might not extend to great depth.

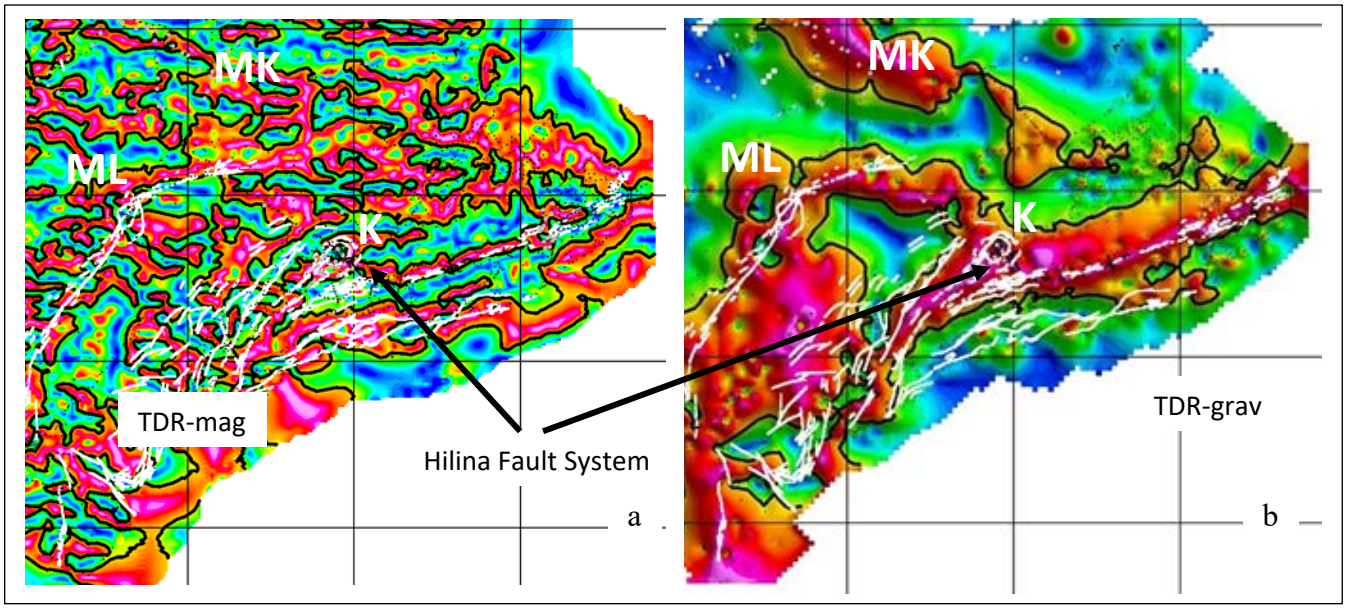

Figure 8. Tilt derivative maps of aeromagnetic (left panel) and gravity (right panel) data for Hawai'i Island. Magnetic data are more sensitive to shallow structures while gravity method indicates deeper structures.

2.1.2.2.3 Magnetotellurics

The MT method exploits natural electromagnetic wavefields generated by global lightning and ionospheric electrical current sources to resolve Earth resistivity (in inverse, Earth's conductivity). The broadband frequency of the sources (0.002 to >1,000 s period, or 500 to <0.001 Hertz) allows for resolution from shallow depths ~100 m (high-frequency or short-period data) to as far as the upper mantle (low-frequency or long-period data). Resistivity is sensitive to small amounts of fluids (including melts) and has yielded insight into shield volcanic systems, revealing likely fluid

source zones, conduits, and controlling structures. To meet the proposed objectives, UH has reprocessed and analyzed the Hawai'i Island MT and AMT data sets. As shown in Figure 1, the Hawai'i Island data set includes surveys from Kilauea's summit and LERZ, the Saddle Road, Mana Road, Pōhakuloa Training Area, Parker Ranch, and Kohala. We initially discuss resistivity modeling and then present results of MT models for Kilauea's LERZ and the Mauna Kea Saddle Region.

2.1.2.2.4 Resistivity Modeling

To model resistivity in one and two dimensions, we employed a combination of open-source software including MTPy (Kirkby et al. 2019; Krieger and Peacock 2014) and Occam1D (Key 2009; Constable et al. 1987) and commercial packages already available at UH including WinGLink and Matlab. We also prepared a set of .edi files for three-dimensional modeling and joint inversion of the Mauna Kea area planned for Phase 2.

The MT data file format is *.edi*, which contains the real and imaginary impedances and frequency so that the apparent resistivity and phase can be easily calculated. MT data are presented as apparent resistivity and phase sounding curves (Figure 9). These curves exhibit noise evidenced by large error bars across the MT "deadband" (periods of 2 to 10 seconds; Figure 9) where signals tend to be weak. We reprocessed the time series data for the LERZ and PTA using another open-source software, *emtf* (Egbert 1997), to produce less noisy resistivity and phase curves; however, this resulted in little improvement over the data processing that was completed between 2013 and 2015 using the aforementioned software packages. Thus, in order to address the noise, we removed outliers and data with large errors from the apparent resistivity and phase data sets. The resulting *.edi* files still contain all the information of the original data, including noise, but the data to be used in the inversion have been edited. For modeling, we fit a smooth curve to the remaining data points, which enabled resistivity and phase values at a consistent set of frequencies across the multiple MT sites. Curve smoothing can, however, distort our data and yield artifacts in inversion results. To mitigate against such artifacts, we downweighted some smoothed data in our MML procedure.

2.1.2.2.4.1 Lower East Rift Zone

The following section describes collocated models of seismic (V_P/V_S), density, and resistivity profiles across the LERZ. The relationships between these properties will vary due to data noise, or the highly variable subsurface structures including intrusions, heterogeneous permeability, porosity, fluid properties, etc.

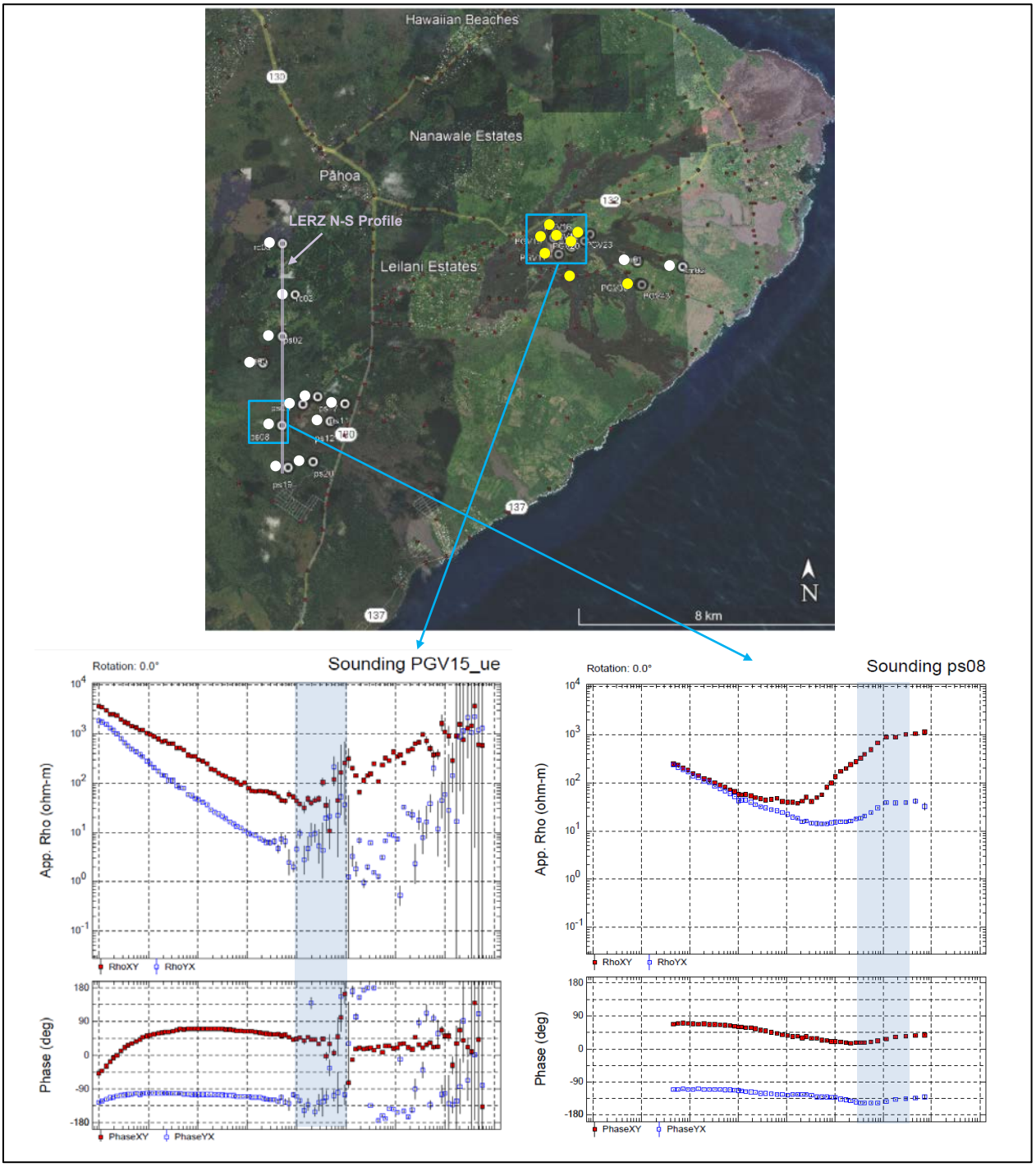

Figure 9. Map of MT soundings and gravity measurement points (top). UH MT locations are shown as white circles; Ormat MT soundings are indicated by yellow circles. The location of a 2D profile running north to south across LERZ is indicated by the grey line. The panels at the bottom are examples of the LERZ MT soundings. Ormat's sounding from PGV (lower left) exhibits noise across the deadband, for the period between 2 and 20 seconds shown by the blue band. UH sounding ps08 (lower right) is much less noisy. The overall data quality across the LERZ is variable. Ormat soundings all showed loss of signal at deadband frequencies.

In addition to the MT data collected by UH in 2013, we were given access to the *.edi* files for the PGV property collected by Ormat geophysicists, and initially wanted to include these in a 2D profile model across the LERZ. The Ormat resistivity curves (Figure 9 – right upper panel) exhibit weak signals across the MT deadband (shaded area indicating the period between 2 and 20 seconds) compared to the ps08 sounding (Figure 9 – right lower panel). The cause of this is speculative; it could reflect shallow conductors that diffuse signals and limit signal penetration depth. In the conditions at the LERZ, with conductive subsurface features including both brackish and saline waters as well as high temperatures, the resolution of MT data is a concern. A rule of thumb is that MT data can resolve a layer whose thickness is greater than 10% of the signal penetration depth. This is a broad generalization and is not applicable below conductors, where thin resistive layers are difficult to resolve. However, the UH MT LERZ data, including data at those frequencies making up the Ormat MT deadband, do not have the same noisy signal. UH data were collected over a long time-window (minimum of 48 hours to several days) at each site, which may have helped to improve signal. Moreover, the UH data may have been acquired during periods of higher solar flare activity, thus resulting in higher induced signal.

Further evidence indicates that extended data acquisition time improved LERZ MT results. Using velocity modeling, we see an increase in resistivity close to where we expect the Mohorovicic discontinuity, or "Moho." This indicates that shallow conductors did not completely degrade MT signals (Figure 10). Estimating the depth of the Moho with resistivity and velocity models is important as a constraint in the MML problem. Figure 10 compares the 1D resistivity of LERZ MT sites ps08 and ps19 to profiles at the same location extracted from the velocity model. Near a depth of 10 km, there is an increasing resistivity (consistent with the lower crust) with a maximum near 20 km, below which is an order-of-magnitude drop. The velocity models enable the identification of the Moho, where V_P/V_S decreases. We expect the seismic Moho and electric Moho to be offset in depth. This is because velocity and resistivity will vary depending on fluid and gas saturation. As the fluid and gas saturation increase, the V_P/V_S ratio usually increases, whereas the resistivity decreases. A decrease in V_P/V_S and an increase in resistivity occur at depths greater than 10 km, but the limitations of both MT and velocity models to resolve features at those depths must be taken into consideration.

Apparent resistivity, phase, and 1D Occam model plots for all MT data points were uploaded to the ISLAND HEAT database on the Data Foundry on OpenEI. We have also uploaded *.edi* format data files to the database for the MT stations at Kilauea's summit and LERZ, Saddle Road, and all AMT stations.

We inverted the MT data in two dimensions where MT station coverage and data quality allowed for it. Station coverage was sparse in Puna, but we inverted a north-south trending 2D profile (shown in Figure 11). The model indicates a strong 4 Ωm conductor from 250 m to 1,250 m below sea level flanked by resistive structures (Figure 13). The upper panel of Figure 11 is resistivity (higher resistivity is shown in blues and purples; reds are conductive). Both density and V_P/V_S models were provided by Denlinger and Flinders (personal communication, 2021). The middle panel of Figure 11 is density extracted along the LERZ N-S profile, and the lower panel is V_P/V_S. Depth (m) is marked on the left axis of each plot. The view of the profile is from the east. The relationships between V_P/V_S, density, and resistivity are apparent. Typically, high V_P/V_S correlates positively with high electrical conductivity. There is a slightly elevated density associated with the resistive and low V_P/V_S sections of the profile (southern half). The scale and resolution of the three models (resistivity, density, V_P/V_S) presented in Figure 11 are different. We do not expect that the

subsurface structures of Hawai‘i Island are one- or two-dimensional, and we will show an example of how out-of-plane conductors and resistors impact 2D modeling in our discussion of the Mauna Kea resistivity (below).

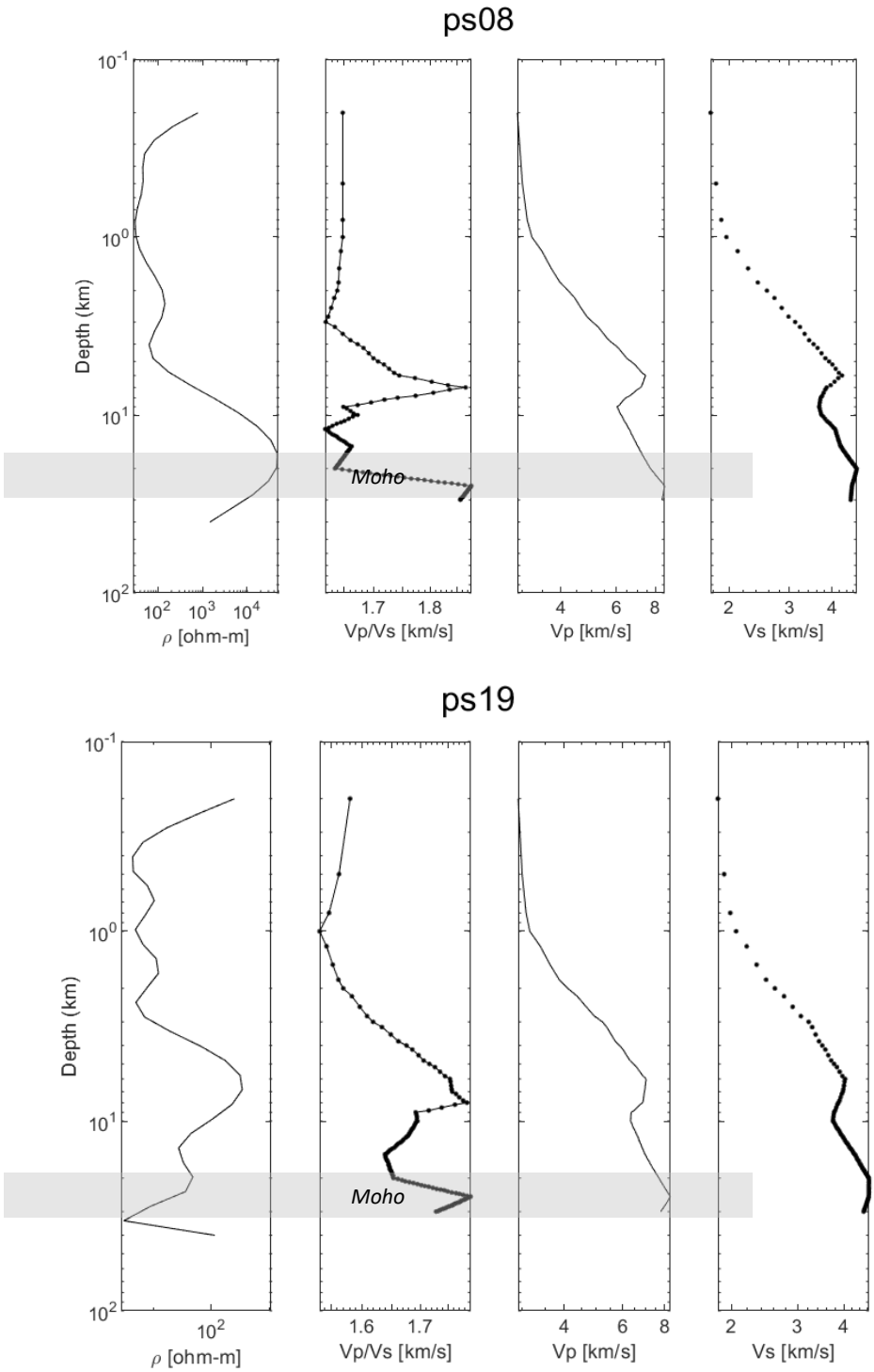

Figure 10. One-dimensional resistivity model and V_P/V_S at LERZ station ps08 and ps19. Decrease in V_P/V_S and increase in resistivity delineate Moho.

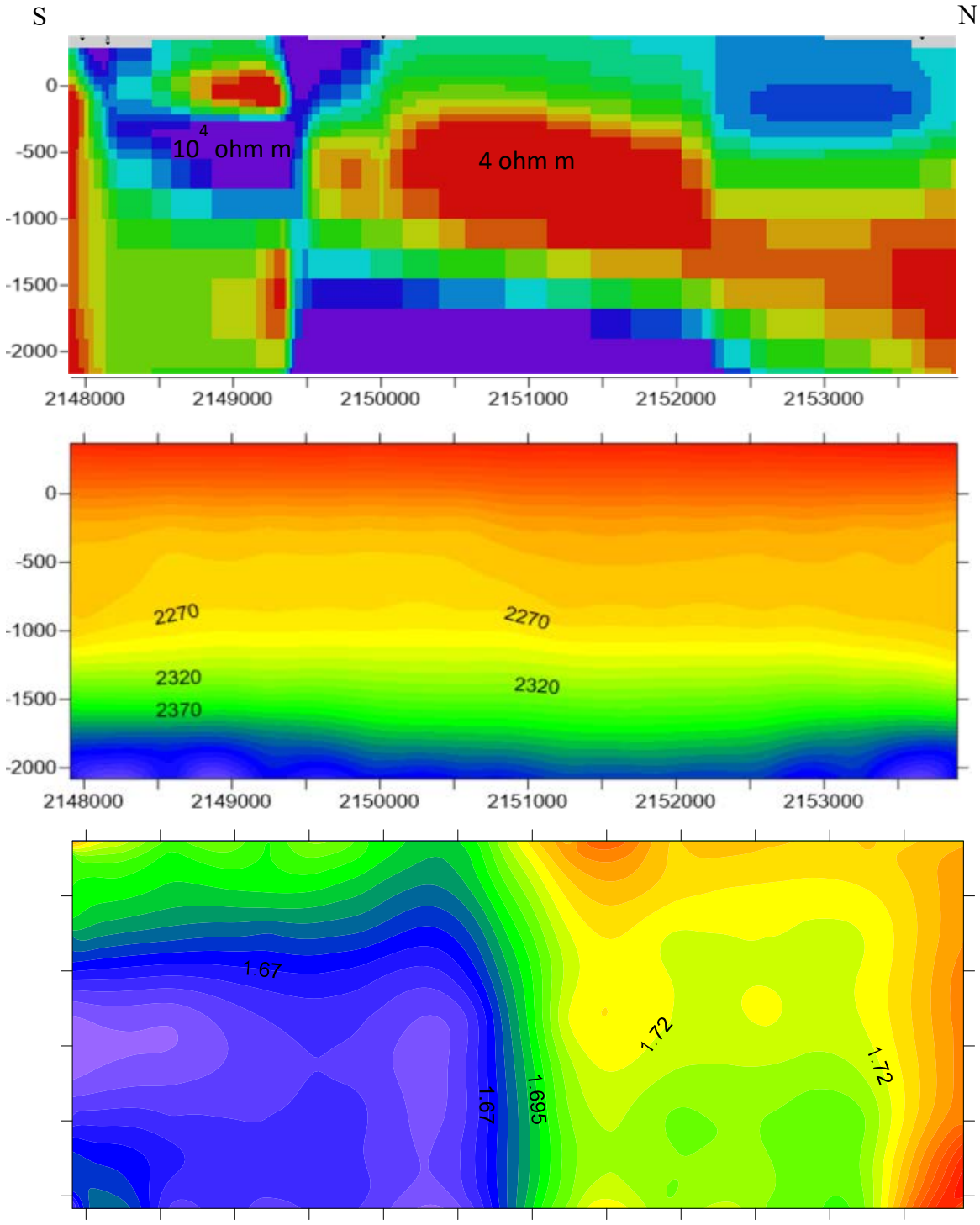

Figure 11. Collocated resistivity (transverse magnetic-transverse electric [TMTE] mode), density, and velocity (V_P/V_S) models along NS profile across LERZ. Upper panel is resistivity (higher resistivity in blues and purples; reds are conductive). Middle panel is density, and lower panel is V_P/V_S. Depth (m) is marked on the left axis of each plot. The view of the profile is from the east.

2.1.2.2.4.2 Mauna Kea Saddle Region

Figure 1 shows the location of profiles of MT data that we reprocessed and inverted in two dimensions for Mana Road and Saddle Road. For the MT profiles across the Saddle and around Mauna Kea, we expected that structures (e.g., dikes, rift zones, and fault) generally strike approximately north-south between the summits of Mauna Kea and Mauna Loa and perpendicular to the volcano flanks for the profiles around Mauna Kea. Therefore, we prioritized inverting the B polarization, where the E field was discontinuous at structures perpendicular to the profile. With an x direction of geographic north (000°) and a y direction of geographic east (090°) for the east-west profiles, the B polarization (transverse magnetic [TM] mode) will be the electric field in the y direction and the magnetic field in the x direction, also called the EyHx mode. For the north-south profiles, the B polarization would be the ExHy mode. The TM mode or B polarization was more influenced by deeper structure and not as prone to shallow horizontal features as the transverse electric (TE) mode and as such results in a smoother model. The TM mode profile for Saddle Road is shown in Figure 12a. Following the TM mode inversion, we inverted the same data simultaneously for TM and TE modes using the same 100-ohm m half-space starting model. Comparing the two resistivity profiles, we found that the TMTE mode (Figure 12b) is sensitive to the out-of-plane and shallow structures that distort the signal. Note that the data for the stations has been projected onto an east-west profile, with the western stations actually located north of the profile, and the eastern stations located south of the profile.

Numerous sources of noise that impact MT data exist in the Saddle Road area. These include vehicular traffic, high-voltage power lines (mostly parallel to the Saddle Road), and percussion noise from military range activity at PTA (motion affects magnetic coils in the MT instruments). In addition, the signal in the deadband is weak, perhaps worsened, during short acquisition periods. As a result, data quality varies among the different MT sites. Therefore, we used smoothed sounding curves in our inversion. Smoothing was necessary owing to noisy data, even though that introduces the potential for large errors between the observed data and the fitting curves. Static shifts were present at a few locations. These were shifted so that high frequency ExHy (E polarizations) were brought to the same resistivity values exhibited by the B polarization (EyHx).

The Rodi-Mackie (2001) 2D inversion (WinGLink) was set to allow for a high number of iterations so that the inversion could converge. Additional inversion settings included second derivative minimization and equal grid Laplacian minimizing the total model. The smoothing parameter Beta equaled 1.0, so that horizontal smoothing increased at the same rate as vertical smoothing. The error floor was set to 5% for resistivity and phase. For the TM mode, the chi-square statistic was reduced to less than 2,000, with model roughness near 500 and a root mean-squared (rms) misfit of 1.3 in 722 iterations. Inverting the TE mode from a 100 ohm m halfspace produced a higher chi-square value (13,000), with model roughness near 900, and an rms misfit of 3.45 at iteration 287, when the rms misfit could no longer be reduced. The TMTE simultaneous inversion converged at 308 iterations with model roughness less than 1,000. Figure 12c shows a trade-off curve between rms misfit and model roughness. The profiles presented are at convergence, but the trade-off curve indicates we might have a more robust model if we reduce the number of iterations to around 150 where rms and model roughness are minimized.

The TM mode inversion results of the Saddle Road data (Figure 12a) indicate resistivity changes that correspond to some of the features discovered while drilling and core logging: the bottom of a resistor corresponding to the observed water table starting near 550 m continuing to total depth, a

conductor at 900 m depth where temperature increases, and zones of secondary alteration are observed in the core as progressively consolidated flow contacts and oxidation of magnetite to hematite.

A resistivity cross section for MT data collected on Mana Road is shown in Figure 13. Herbert Pierce (personal communication, 2021) created this model for a report to Hawai‘i’s Department of Business Economic and Development and Tourism. The conductor just right of center results from two MT stations, 12 and 13, and it is apparent from the resistivity and phase curves above the profile that MT site 13 is noisy compared to site 1 nearer the south end of the profile. As we move into Phase 2, this is a place to collect additional data to verify the existence of the conductor, as there is no associated gravity high (map in Figure 6 and Figure 7).

While 2D resistivity profiles are interesting and informative, the TE mode is particularly sensitive to out-of-plane resistors and conductors; these can substantially impact 2D inversion results, yielding artifacts that appear as vertical features that propagate from the surface to depth (Figure 12b). We look forward to completing the 3D inversion in Phase 2 of this project to better understand heat sources and associated structure under the Saddle Region.

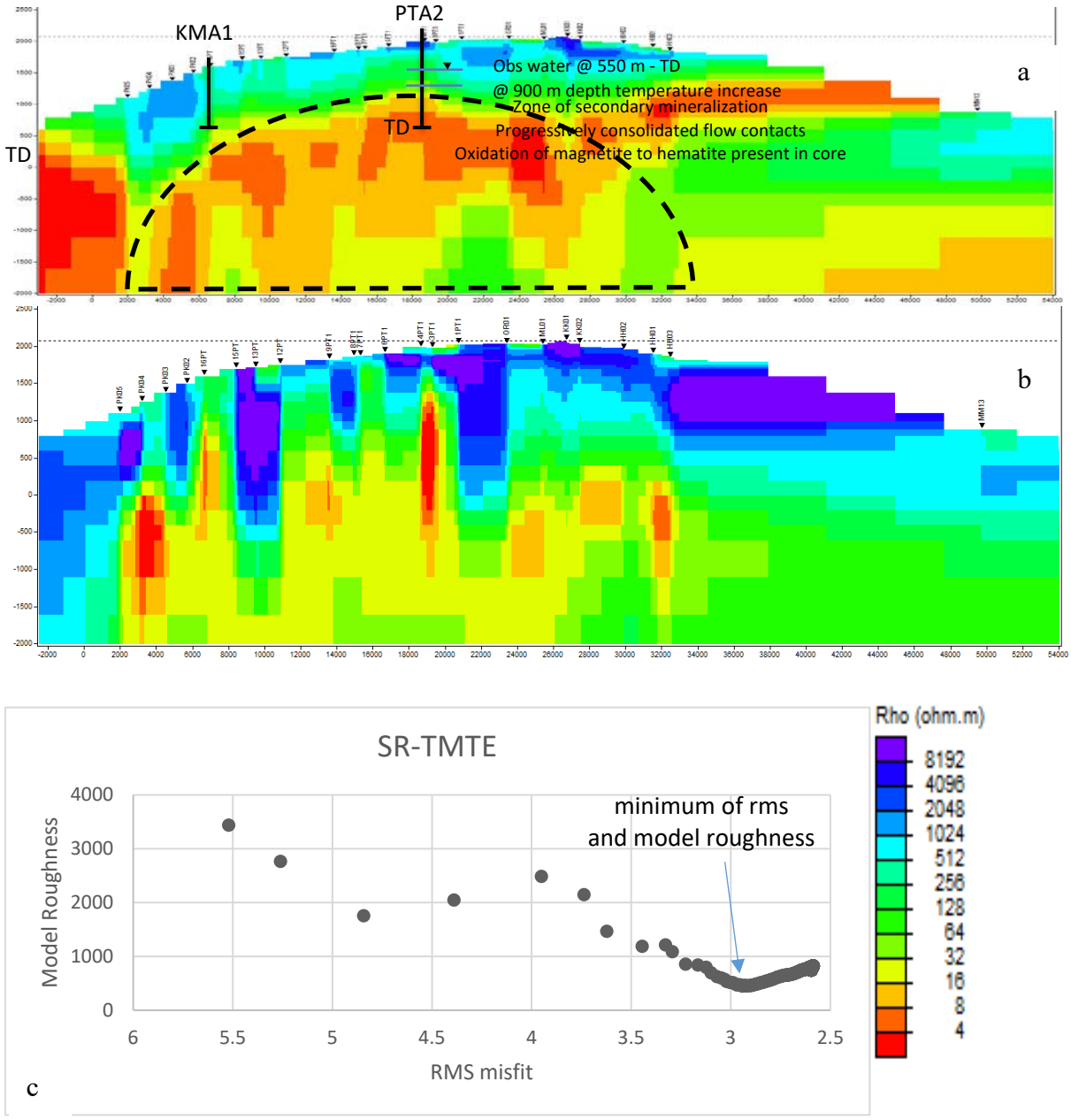

Figure 12. TM inversion. (a) At 722 iterations. (b) At 308 iterations. (c) Model roughness versus RMS misfit for the Saddle Road TMTE 2D resistivity model.

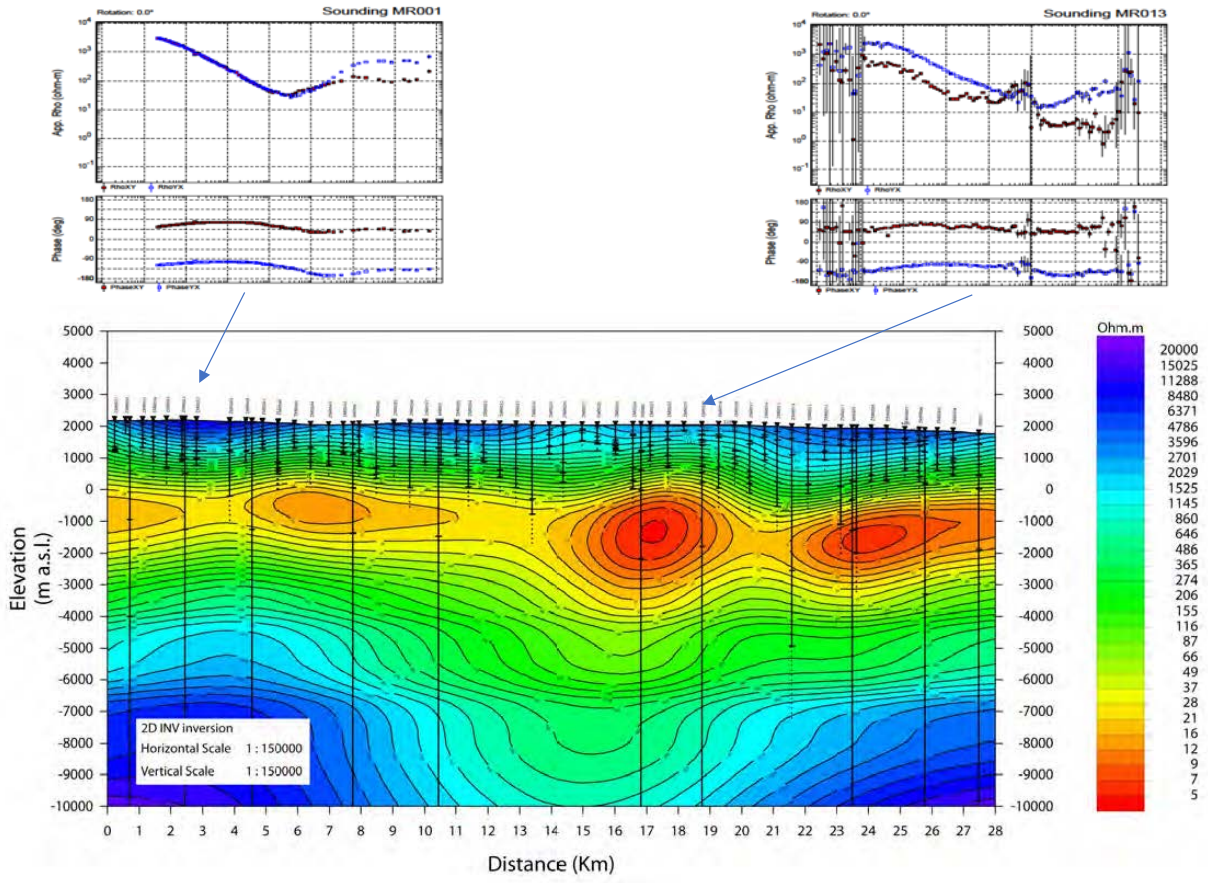

Figure 13. Electrical resistivity from Mana Road MT and AMT data shows a high conductivity from -1,000 m to 0 m above sea level. This is approximately the same depth range where 100°C water was encountered at PTA immediately south of the southern extent of the Mana Road.

2.1.3 Proposed Research and Next Steps

Compiling and modeling the existing data has helped identify data gaps that can be addressed in Phase 2. At the time of writing, the United States Geological Survey (USGS) plans to collect airborne electromagnetic and MT data within the boundaries of Hawai‘i Volcanoes National Park. However, these data probably will not become publicly available for several years.

2.1.3.1 Additional Data Collection

The Mauna Kea MT data are sparse. We plan to fill in the data set with additional MT stations to help constrain the 3D inversion. While the 3D inversion code HexMT can invert sparse data, it is particularly important to collect data near the summit of Mauna Kea.

We will recollect MT data near sites MR012 and MR013 on Mana Road to confirm the presence of the conductor that shows in the 2D Mana Road resistivity profile. We will also collect gravity data at any additional MT sites and in the vicinity of the conductor on Mana Road to verify that there is no density high associated with the possible high conductivity zone.

To obtain additional information, we will study the feasibility of, and if deemed possible, deploy passive seismic nodes around the Mauna Kea Saddle Region. This would result in a data set that includes resistivity, density, and velocity.

2.1.3.2 Inversion and Modeling

The inversion and modeling will include the following:

- 3D inversion of data comprising the Mauna Kea region including MT soundings from Saddle Road, PTA, Parker Ranch, and Mauna Road MT data
- 3D joint inversion of Mauna Kea Saddle Region and LERZ data sets that include gravity, resistivity, and seismicity.

2.2 Structural Control of Permeability at Kilauea Volcano, Hawai‘i

Basaltic rocks host important regional aquifers in Hawai‘i, as well as in Washington, Oregon, and Idaho; and they host aquifers of local extent in other states as well (Whitehead 1994; Miller et al. 1997). Understanding how fluids flow in basalts is important for developing and properly managing groundwater and geothermal resources, and for managing groundwater contamination. This report focuses on the potential for geothermal resources in Hawai‘i, but our research efforts should also illuminate how to better develop and manage basaltic aquifers in general.

This report specifically evaluates the roles of heat, groundwater, and permeability in assessing the geothermal potential in Hawai‘i. We use various geochemical and geophysical methods to directly or indirectly infer where sufficient heat and groundwater might exist to form a geothermal resource. Existing direct data on the permeability in the subsurface, however, is sparse. This section of the report describes how we utilize information from structural geology and the theory of the mechanics of solids to help evaluate permeability.

Fluid flow in basalt is well-known to be complicated, as the permeability of basalt is typically highly heterogeneous and anisotropic (Freeze and Cherry 1979). Much of the literature (e.g., Cheng et al. 2022) that addresses the permeability of basalt focuses on contributions stemming from how basalt flows when it is a liquid or is deposited in the form of volcanic ejecta. Geologic structures that develop once the basalt solidifies also contribute substantially to the permeability, but they have received less attention. Foremost among these structures are faults and fractures.

Here, we focus on specific sites on Hawai‘i Island (Figure 14): features at Kilauea caldera and on rift zones of Kilauea. Kilauea is targeted for two reasons: (1) it is a site of demonstrated geothermal potential (the PGV) that could be developed further; and (2) the exposures of geologic structures on Kilauea are outstanding. A general understanding of the structural impact on permeability gained at Kilauea can be transferred to Lāna‘i, other parts of the Island of Hawai‘i, as well as other islands in the state.

This section, specifically focused on structure, is organized into five parts. Section 2.2.1 reviews factors affecting the hydrology of fracture volcanic rock. Section 2.2.2 describes the structure around Kilauea caldera and along rift zones of Kilauea, and presents evidence of the impact of geologic structures on the permeability. Section 2.2.3 reviews how the stress field tends to affect the permeability in fractured rock masses. Section 2.2.4 explores the stress field within the ERZ of Kilauea volcano. Section 2.2.5 discusses how the stress field might be evaluated better with

additional theoretical research and how the results can be incorporated into the UH machine learning procedure.

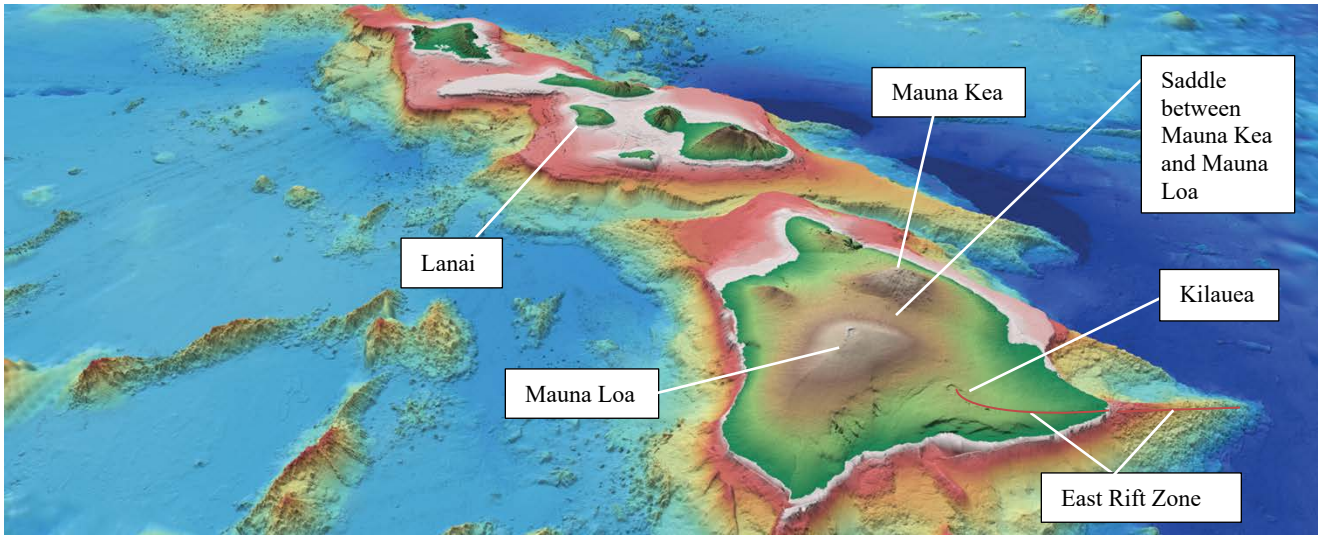

Figure 14. Relief map of the Hawaiian Islands.

Source: https://www.usgs.gov/media/images/3-d-hawaii-volcanoes-national-park-map

2.2.1 Review of Factors Affecting the Hydrology of Fractured Volcanic Rock

2.2.1.1 General Hydrologic Characteristics of Fractured Rock Systems

The hydrologic behavior of fractured rocks can differ decidedly from the hydrologic behavior of porous rocks. Flow paths in fractured rock systems can be discontinuous, reflecting the discontinuous nature of the fracture systems themselves. The flow rates in fractures can be much higher than the flow rates through unfractured porous media (see, e.g., Jaeger, Cook, and Zimmerman 2007). The flow rate in fractures tends to be proportional to the cube of the fracture aperture (Snow 1965), which in turn is sensitive to the stresses acting on the facture (Witherspoon et al. 1980; Jaeger, Cook, and Zimmerman 2007). The permeability of fractured media thus is sensitive to the stresses in a rock mass, especially the stress perpendicular to the dominant fractures. The permeability of a fractured rock mass also depends on how connected the fractures are (Jaeger, Cook, and Zimmerman 2007).

2.2.1.2 Volcanic Factors That Affect Permeability

Although this section of the report focuses on structural controls on permeability, we acknowledge that volcanic processes also affect permeability. Some volcanic processes increase permeability, others decrease permeability, and others can preserve permeability. Volcanic features also contribute to the anisotropy of the permeability in basalts.

2.2.1.3 Dikes

Dikes are nearly vertical, tabular geologic structures that can feed lava flows. Basaltic dikes on Hawai‘i commonly lack the vesicles (gas bubbles) that form in lava flows and hence are relatively dense. For this reason, dikes are associated with gravitational highs. Dikes form nearly vertical aquicludes or aquitards in many places in Hawai‘i. They are not perfect aquicludes because they commonly contain cooling fractures that are perpendicular to the dikes and that extend across the

dikes. The spacing of these cooling fractures tends to be similar to the dike thickness. Basaltic dikes in Hawai‘i generally are less than 2 meters thick. Individual dikes can have vertical and horizontal extents of several kilometers. Dikes are abundant beneath calderas and along rift zones. The dikes in a rift zone strike parallel to the rift zone as a whole.

2.2.1.4 Tops and Bottoms of Lava Flows

The tops and bottoms of many lava flows are rubbly. Thus, even though the permeability of the core of a lava flow will tend to be low, the permeability of flow tops and bottoms will tend to be relatively high. Flow tops and bottoms will be nearly horizontal and elongated along the direction of lava flow, so they contribute to the anisotropy of permeability in basalt.

2.2.1.5 Lava Tubes

Lava tubes are common on Kilauea. They can have radii as great as a few meters and can be many kilometers long. Lava tubes thus greatly increase the permeability of basalts. Lava tubes will be nearly horizontal and aligned along the direction of lava flow, so they contribute to the anisotropy of permeability in basalt.

2.2.1.6 Soils and Ash Beds

Clay-rich horizons, which tend to have low permeability, can form in two main ways. The first is as soils that develop on top of a lava flow. The second is by weathering of ash beds deposited on lava flows. These clay-rich units can be extensive and serve as horizontal aquitards that can be buried by subsequent lava flows.

2.2.1.7 Mineralization

Mineralization plugs (or partially plugs) fractures and other voids within a lava flow. Mineralization hence causes permeability in basalts to decrease. As mineralization develops over time, mineralization will tend to be most pronounced in older and deeper flows. Mineralization can involve hydrothermal minerals (e.g., sulphur) as well as nonhydrothermal minerals.

2.2.1.8 Preservation of High-Permeability Features by Lava

As new lavas erupt and bury older lava flows, they also bury any features in the older lava flows. This can result in the preservation, in the subsurface, of high-permeability features that formed at the surface. For example, partial collapses of the rock along fault scarps result in accumulations of talus blocks as large as several meters at the base of the scarps. Passageways large enough to walk through occur in some of these talus accumulations. In at least some places, subsequent lava flows that covered these fault-scarp talus deposits solidified against the outer surface of the deposits, leaving an unfilled interconnected network of large voids within the buried talus deposits. As a second example, some lavas have flowed over open vertical fissures with apertures of at least a few decimeters without flowing into the fissures and filling them. Once covered, these covered fissures would retain their high permeability. Finally, many buried features can be reactivated. For example, in *many* places, faults were buried by lavas, only to be later reactivated (Martel and Langley 2006; Kaven and Martel 2007).

2.2.2 Structures at Kilauea

Two major structures exist at Kilauea and many other large volcanoes in Hawai‘i: calderas and rift zones (Figure 15). Calderas are collapse features located at a volcano summit. Active calderas, such as Kilauea, commonly host lava lakes. The summit caldera at Kilauea overlies a magma

reservoir complex which, according to Poland, Miklius, and Montgomery-Brown (2014), includes at least two storage zones, a shallow zone at 1–2 km depth and a deep zone at a depth of 3–5 km. Rift zones radiate from the calderas. Kilauea contains two active rift zones, the ERZ and the Southwest Rift Zone. We describe the surficial characteristics of these major structures in more detail below.

In addition to the major structures, the basalt flows of Hawai‘i contain networks of smaller structures: vertical cooling cracks (Figure 16a). These vertical cooling cracks bound prisms of basalt and are perpendicular to the nearly horizontal boundaries of the lava flows. The cracks form polygonal patterns in map view at a broad range of scale. The polygons range in width from centimeters to hundreds of meters. The cooling cracks themselves have apertures of less than a millimeter to more than a decimeter. The structures associated with the calderas and rift zones develop in basalt flows that already have a well-connected network of cooling cracks.

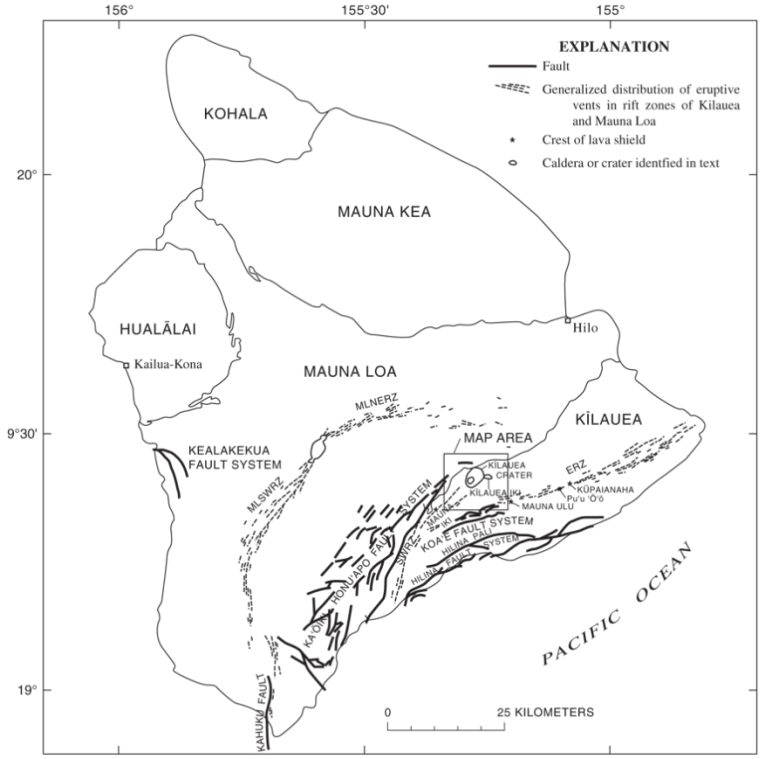

Figure 15. Map of major geologic structures on Kilauea Volcano.

Source: Neal and Lockwood (2003)

(a) (b)

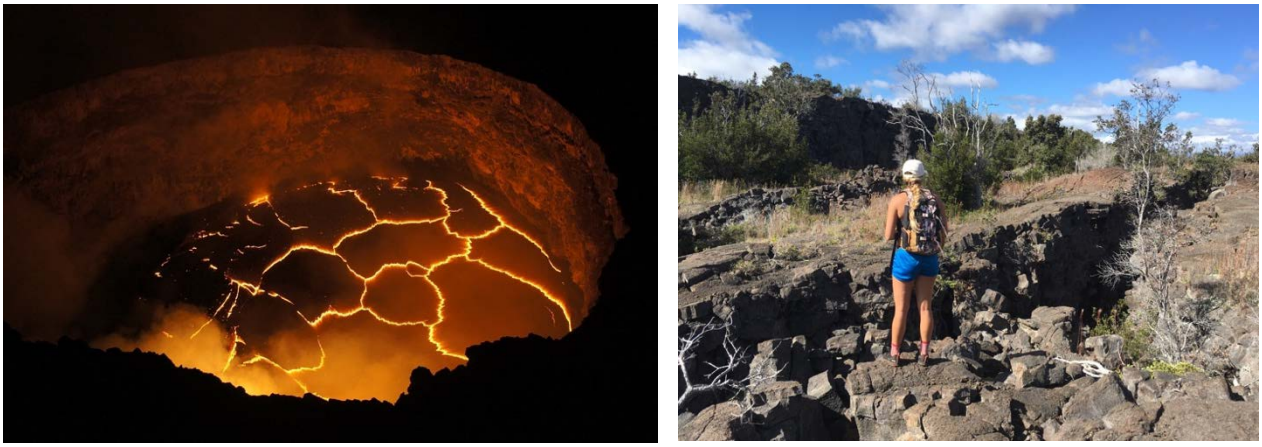

Figure 16. Examples of fractures at Kilauea. (a) Polygonal cooling fractures, shown here in a lava lake in Halemaumau. (b) Gaping fissure from the Koae fault system. Steep fractures such as this characteristically parallel the traces of faults and eruptive fissures on Kilauea.

2.2.2.1 Calderas

Caldera are collapse features that are nearly circular or elliptical in map view, with walls that can be hundreds of meters tall (Figure 17). Kilauea caldera has had a radius of 1–2 km. The caldera atop Mauna Loa is ~2.5 km wide and 6 km long. Calderas are bounded by steeply dipping normal faults we call ring faults. Some ring faults branch out away from the caldera into the surrounding basalt. The floor of Kilauea subsided by ~500 m in 2018 (Segall et al. 2019), so the major ring faults extend at least that far down-dip. Segall et al. (2019) treat the ring faults as extending 2 km down-dip.

A series of fissures border the ring faults at Kilauea (Figure 17). The traces of the fissures in map view roughly parallel the traces of the ring faults. These fissures are especially prominent outside of the main ring fault bounding Kilauea caldera.

2.2.2.2 Rifts

Rift zones are the longest structures in Hawai‘i. The ERZ of Kilauea extends more than 100 km away from the caldera, with most of the exposed rift zone being below sea level (Figure 14). The Southwest Rift Zone extends about 40 km away from the caldera, with most of the exposed rift zone being above sea level.

The subsurface structure along the ERZ is intricate (Figure 18). Records of seismicity indicate that at Kilauea many blade-like dikes propagate laterally away from Kilauea caldera along the ERZ in the subsurface, at depths of a few kilometers (Rubin and Pollard 1987). However, a swarm of seismicity along the ERZ during the 2018 eruptive episode extended to a depth of 6–12 km (Flinders et al. 2020), indicating that some dikes along the ERZ extend down-dip all the way (or nearly all the way) to where Kilauea volcano rests on the oceanic crust. The Hawaiian rift zones dilate as they accommodate the dikes, with the rock in the rift above the dikes being stretched, and the rock to either side of the rift zone contracting.

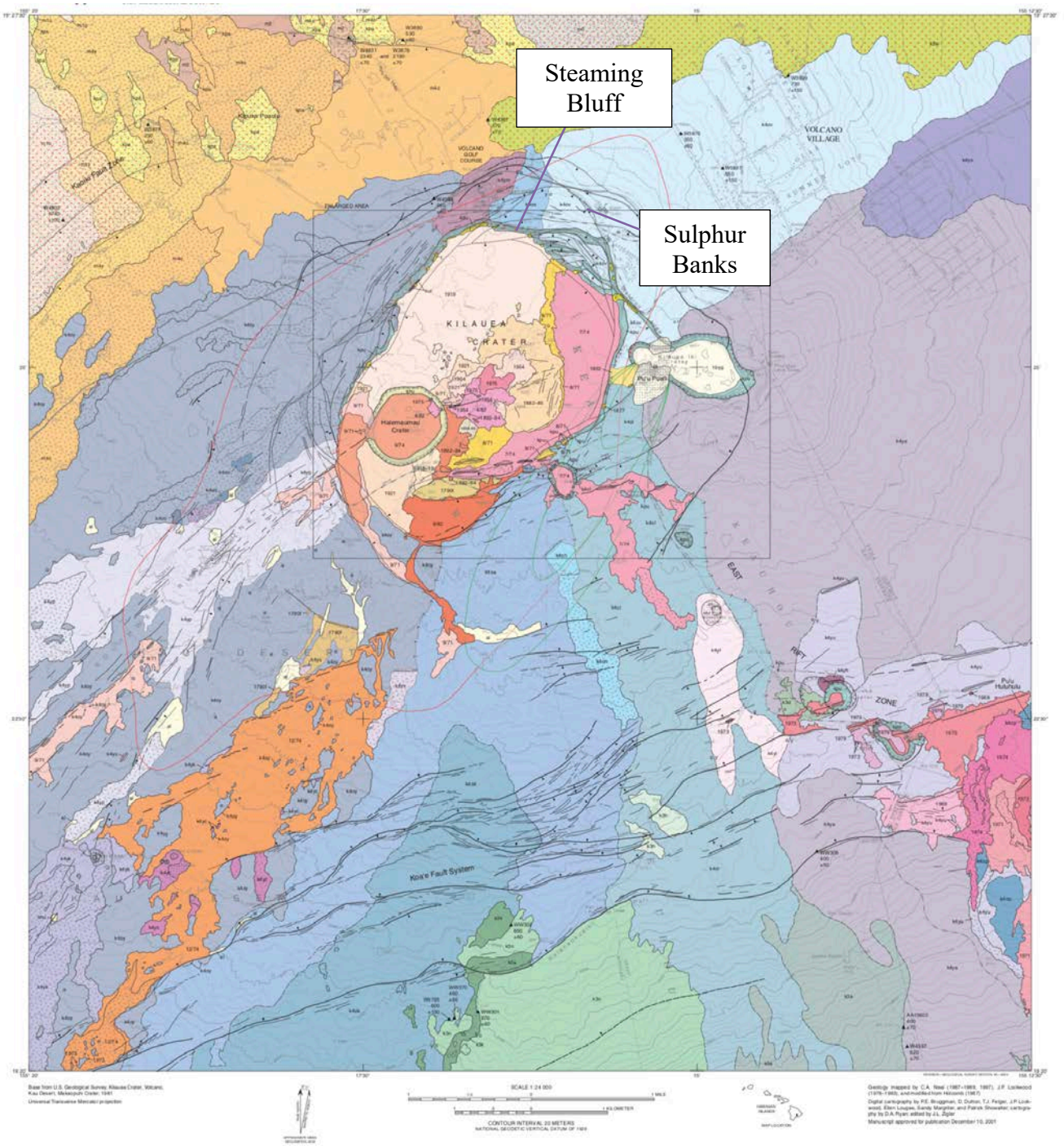

Figure 17. Geologic map showing the traces of faults and gaping fractures around Kilauea Caldera (in northern part of map) and along the Koae fault system (in southern half of map). Normal fault traces are marked by the heaviest black curves, with balls on the down-dropped side of the fault. Gaping fissures are marked by thin black curves. Steaming Bluff and Sulphur Banks are prominent hydrothermal features (see Figure 18). The colored units are volcanic units (predominantly lava flows) of different age.

Source: Neal and Lockwood (2003)

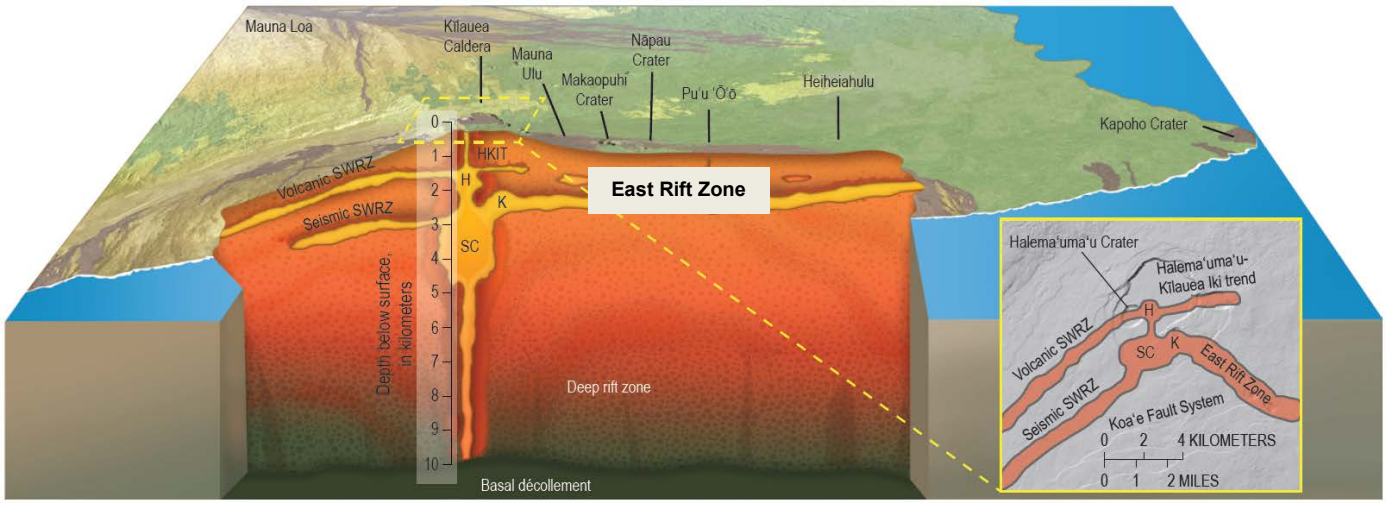

Figure 18. Illustration of proposed structure of Kilauea's subsurface magma plumbing system. The schematic cut-away shows a cross section through Kilauea's summit and rift zones. The sizes of magma pathways and storage areas are exaggerated for clarity. H, Halema'uma'u reservoir; K, Keanakāko'i reservoir; SC, south caldera reservoir; SWRZ, Southwest Rift Zone. Plan view gives the relations of magma pathways to surface features and topography in the vicinity of Kilauea Caldera.

Source: Poland, Miklius, and Montgomery-Brown (2014)

Along the surface, the rift zones on Kilauea display numerous steeply dipping normal faults, steep gaping fissures, as well as additional fissures from which lava erupted. All of these strike parallel to the rift. The occurrence and orientation of these structures are consistent with stretching of the rock across a rift.

Excellent exposures of the faults and fissures along a rift occur within the Koae fault system, about 5 km south of Kilauea caldera (Figure 16b, Figure 17, and Figure 18). A series of nested grabens occur there, with gaping fissures near the normal faults. These fissures opened in response to bending of the ground surface that accompanies the faulting (Martel and Langley 2006; Kaven and Martel 2007; Martel, Stock, and Ito 2014). Networks of these fissures strike parallel to the normal faults along the full extent of normal faults in the rift zone. Some of the gaping fissures have apertures of a few meters or more (Figure 16b). The largest of these gaping fissures extend at least several tens of meters below the ground surface, and perhaps much deeper.

2.2.3 Hydrologic and Hydrothermal Implications

Gaping fissures are associated with the ring faults at calderas and with the normal faults along rift zones. The apertures of the gaping fissures, coupled with their length and depth, indicate that these fissures can transmit fluids at high rates. The localized occurrence of steam vents along fissures at Steaming Bluff on the northern edge of Kilauea caldera (Figure 17 and Figure 20a) and the localized occurrence of fumaroles along a ring fault north of Kilauea caldera (Figure 17 and Figure 20b) prove that the fissures and faults there are hydraulically conductive and enhance the permeability of the basalt. We expect that the superposition of the faults and fissures on basalt that already contains cooling cracks results in a highly conductive fracture network, with the greatest permeability parallel to the faults and the lowest permeability perpendicular to the faults (Figure 21).

(a)

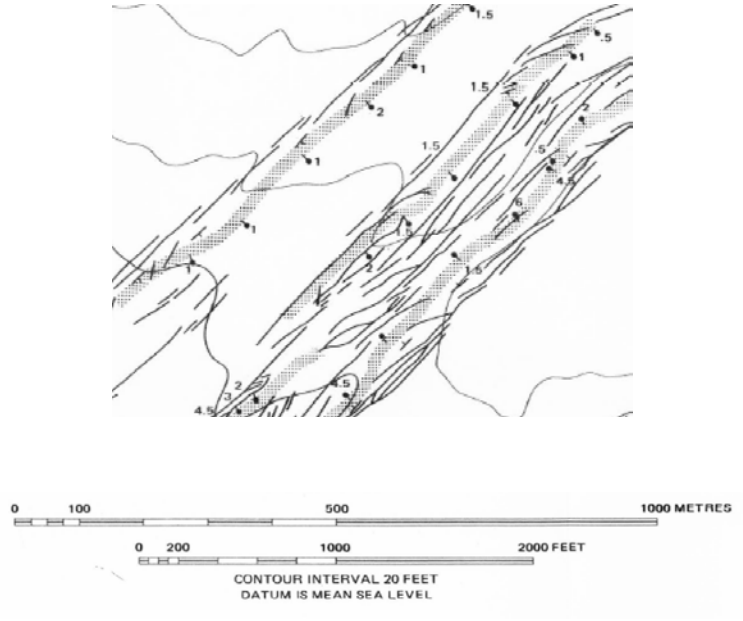

(b)

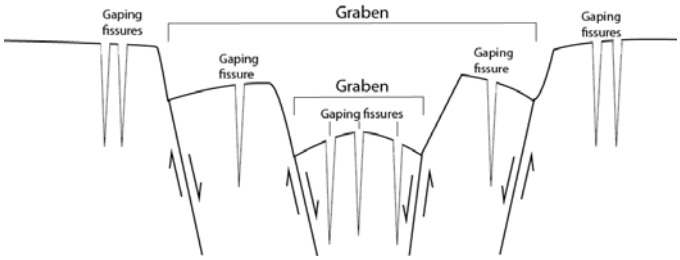

Figure 19. (a) Map of part of a rift zone within the Koae fault system. The scarps of normal faults are stippled, the numbers indicate estimated scarp heights (in meters), and the balls are on the down-dropped sides of the faults. Black curves mark traces of gaping fissures. (b) Idealized cross section across a rift zone.

Source: Duffield (1975)

(a)

(b)

Figure 20. Examples of hydrothermal activity along ring faults of Kilauea caldera. (a) Steaming Bluff at the northern edge of Kilauea caldera. (b) Sulphur Banks, showing fumarolic activity and sulphur deposition along a normal fault scarp a few meters tall. See Figure 17 for the locations of these features.

Sources: (a) https://www.nps.gov/havo/learn/nature/steam-vents.htm;
(b) https://www.nps.gov/thingstodo/walk-to-haakulamanu.htm

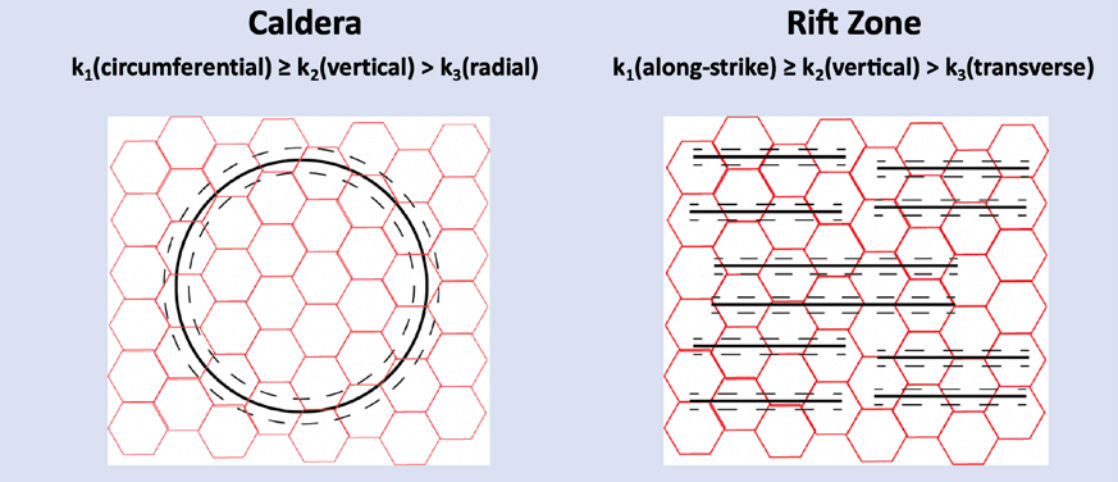

Figure 21. Diagrams showing idealized fracture networks in map view along a caldera ring fault (left panel) and along a rift zone (right panel). Fault traces are shown in heavy black lines, gaping fissures in thin black lines, and cooling fractures by red polygons. The highest permeability is inferred to parallel the faults, with the lowest permeability being perpendicular to the fault traces.

2.2.4 Effects of the Stress Field on Permeability

The permeability of fractured rock is sensitive to the stresses in the rock. This is because the stresses can close or open fractures, and the permeability is highly sensitive to fracture aperture (the permeability varies as the cube of the facture aperture). We briefly review how the directions and magnitudes of the principal stresses tend to affect the permeability of fractured rock. We use a convention where tensile stresses are positive.

2.2.4.1 Effect of Principal Stress Directions on Permeability

The principal stresses are three normal stresses that act in three mutually perpendicular directions. The principal stresses can have different magnitudes, where σ_1 is the most tensile (least compressive) stress, σ_3 is the least tensile (most compressive) stress, and σ_2 is the intermediate principal stress. Where one of the principal stresses is perpendicular to a planar fracture, the fracture can open or close depending on whether the fluid pressure in the fracture exceeds the ambient compressive stress perpendicular to the fracture. Where one of the principal stresses is oblique to a planar fracture, then the surfaces of a fracture might shear (i.e., slip). If a fracture were perfectly planar and had perfectly smooth surfaces, then this slip would not cause a change in fracture aperture. Fractures in rock, however, are not perfectly planar, and their surfaces are rough, so slip can increase the aperture of a real fracture in some places and decrease its aperture in others.

The effect on fracture aperture usually is most pronounced if either σ_1 is perpendicular to the fracture (causing the fracture to be most open) or if σ_3 is perpendicular to the fracture (causing the fracture to be most closed). In a fractured mass with multiple fractures of varied orientation, the fractures perpendicular to the most compressive stress will tend to be the most closed, whereas the fractures perpendicular to the most tensile stress will tend to be most open. As a result, the principal stresses tend to cause the permeability to be anisotropic in a fractured rock mass, with the direction of greatest permeability being perpendicular to the most tensile stress (σ_1) and parallel to the most compressive stress.

2.2.4.2 Effect of Stress Magnitudes on Permeability

To illustrate the impact stresses have on fractured rock permeability, we start by examining the effect of stresses on fracture aperture. The maximum aperture of an isolated planar fracture is proportional to the driving pressure, the difference between the normal stress perpendicular to a fracture and the fluid pressure in the fracture (Pollard and Segall 1987). Even in complexly fractured rock with multiple fractures, a uniform change in the fluid pressure can induce an approximately uniform change in the driving pressure, provided that the fractures do not grow. Both theory and field tests can relate changes in the fluid pressure to changes in the permeability of a fractured rock mass. A decrease in the fluid pressure corresponds to an increase in the effective stress in the rock. Data from pump tests at the Multiwell Test Site in Colorado (Figure 22) show that changes in the effective stress of 2,000 psi can cause the permeability (k) of a fractured rock mass to change by approximately two orders of magnitude relative to its reference permeability (k_0). The permeability response to stress changes at any particular site depends on both the ambient stresses there and the stress changes.

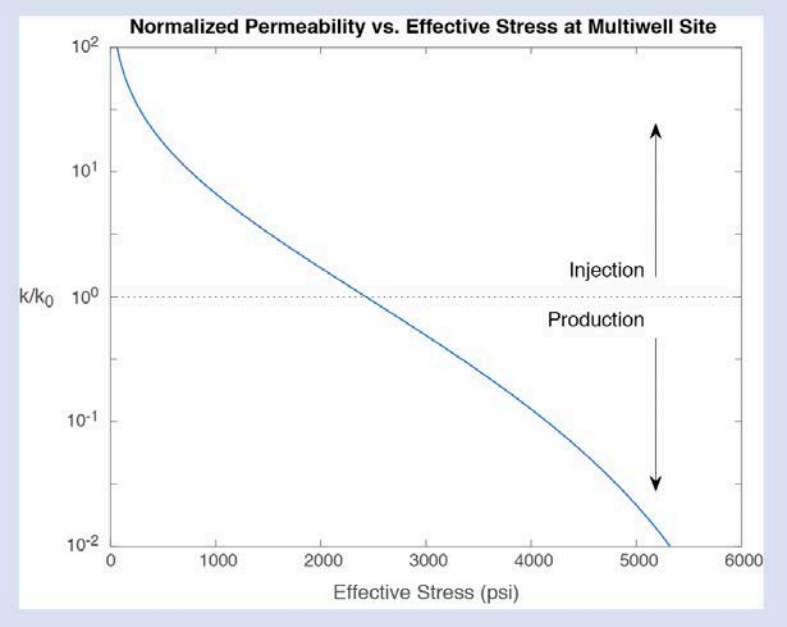

Figure 22. Normalized permeability vs. changes in effective stress at the Multiwell Test Site.

Source: Warpinski (1991); National Research Council (1996)

2.2.5 The Stress Field Near the Topographic Surface at Kilauea

2.2.5.1 Geologic Constraints

We do not have quantitative stress measurements at Kilauea, but geologic information allows us to infer certain characteristics of the ambient regional stress field near the topographic surface. We explore the LERZ first; then we consider the area around Kilauea caldera.

The LERZ strikes ~60° (structure east-northeast of ERZ in Figure 15), as do the nearly vertical eruptive fissures within it. These fissures are opening mode fractures, which characteristically develop in planes perpendicular to the least compressive principal stress (σ_1). Thus, along the LERZ, σ_1 is nearly horizontal and trends ~150°/330°. The other two principal stresses (σ_2 and σ_3) must lie in vertical planes that contain the eruptive fissures, and one of those principal stresses must be essentially vertical (i.e., perpendicular to the nearly horizontal ground surface). The most compressive stress (σ_3) is likely to be vertical and result from the weight of the rock. Whereas the principal stresses are mutually perpendicular, σ_2, the intermediate principal stress, would be horizontal and trend ~60°/240°, parallel to the strike of the ERZ.

The geologic structure is more complicated around Kilauea caldera (Figure 17) than along the ERZ (Figure 15). This suggests that the stress field exhibits more spatial heterogeneity near the caldera. Along the Koa'e fault system, which strikes 70°, the faulting is essentially pure dip-slip. This means that σ_1 there is nearly horizontal and trends ~160°/340°, that the most compressive stress (σ_3) is likely to be vertical, and that σ_2 would be horizontal and trend ~60°/240°, parallel to the strike of the ERZ. These stresses do not account for the observed normal slip on the curved ring faults around the caldera, however, which reinforces our conclusion that the orientations of the principal stresses in the vicinity of the caldera exhibit considerable spatial heterogeneity.

The magnitudes of the ambient principal stresses are not well constrained. Given the relatively gentle slopes on Kilauea, we are confident that the most compressive principal stress (σ_3) essentially equals the stress arising from the weight of overburden. Accordingly, $\sigma_3 = -\rho_b g d$, where ρ_b is the density of basalt (~2900 kg/m^3), g is gravitational acceleration (9.8 m/sec^2), and d is the depth below the surface (in meters). The minus sign reflects our use of a tension-positive (compression-negative) stress convention. We are unaware of geologic data that place strong constraints on the magnitude of the horizontal stresses either at the topographic surface or in the subsurface.

2.2.5.2 Insight from 2D models

We gain additional insight into the stress field within Kilauea volcano by considering 2D solutions for stresses beneath topographic surfaces. For example, 2D boundary element (BEM) solutions can account for gravity, topography of arbitrary shape, and regional tectonic stresses (Martel 2000). These numerical solutions compare quite favorably to exact 2D solutions for the stresses beneath bell-shaped topography (Savage, Swolfs, and Powers 1985). For cosinusoidal topography of low relief that is affected only by gravity (Figure 23), the 2D BEM solutions show that the most compressive stress (σ_2), which is nearly vertical, increases nearly linearly with depth. In contrast, the most tensile stress (σ_1), which is nearly horizontal, varies in a much less regular fashion. The same conclusions arise from analytical 2D approximations for the stresses beneath sinusoidal topography of low relief (Martel 2016), based on Boussinesq's solution (Barber 2002). The 2D analytical approximations (Figure 24) match the 2D BEM solutions (Figure 23) quite well.

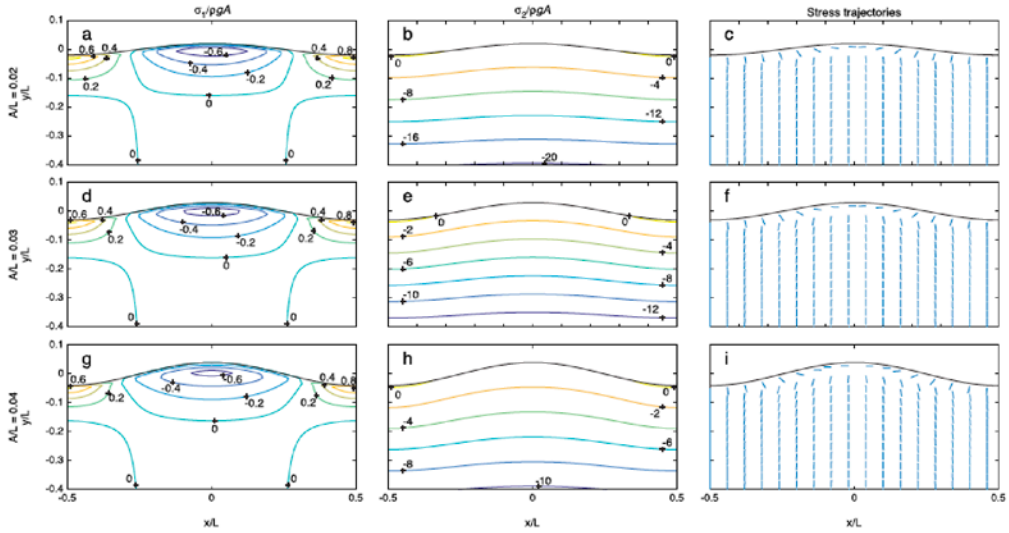

Figure 23. Contour plots of normalized stress components and stress trajectories below cosinusoidal topography subject just to gravity, for various A/L ratios (in rows): $\sigma_1 \rho g A$ (left column); $\sigma_2 \rho g A$ (center column); and trajectories perpendicular to the most tensile stress (right column). First row: A/L = 0.02. Second row: A/L = 0.03. Third row: A/L = 0.04 (A: amplitude, L: wavelength). Solutions are determined using the boundary element method.

Source: Martel (2016)

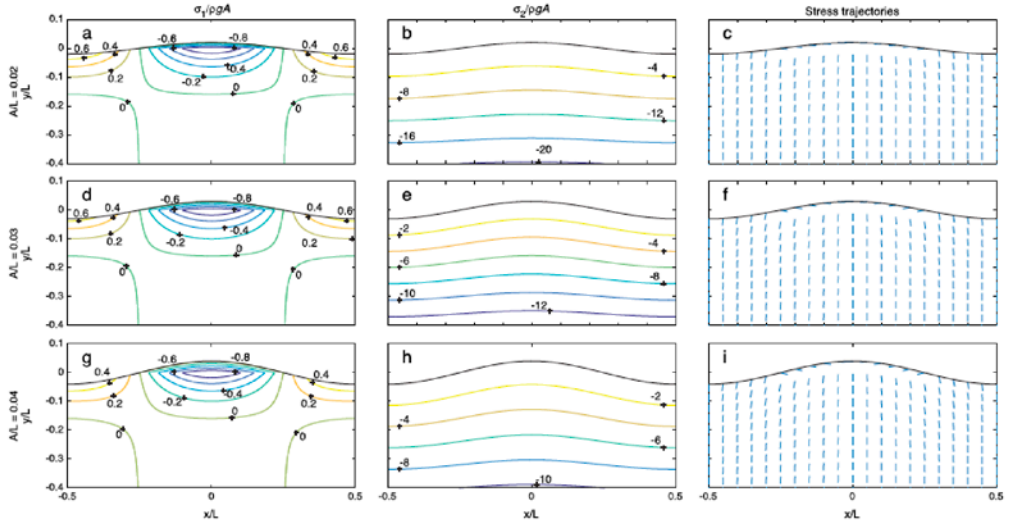

Figure 24. Contour plots of normalized stress components and stress trajectories below cosinusoidal topography subject just to gravity, for various A/L ratios (in rows): $\sigma_1 \rho g A$ (left column); $\sigma_2 \rho g A$ (center column); and trajectories perpendicular to the most tensile stress (right column). First row: A/L = 0.02. Second row: A/L = 0.03. Third row: A/L = 0.04 (A: amplitude, L: wavelength). Solutions are determined using the 2D analytical method. Note that the results are consistent with the plots generated using BEM (Figure 23).

Source: Martel (2016)

2.2.5.3 Insight From Existing 3D models

Further insight into the stress field beneath topographic surfaces can be gained by considering 3D solutions. We know of no analytical solutions for 3D topography, but numerical solutions do exist. For example, Moon et al. (2017) have extended the 2D BEM solution method of Martel (2000) to three dimensions. Like the 2D BEM approaches, the 3D BEM method can account for topography of arbitrary shape, gravity, and regional tectonic stresses.

In addition, Lautze et al. (2020) introduced a fast, approximate 3D solution method, based on Boussinesq's solution, and applied it to synthetic conical volcanoes with gentle slopes (Figure 25) as well as to volcanoes of arbitrary shape. An inspection of Figures 23–25 shows that the fast, approximate 3D solution reveals the same kind of spatial variations in the stresses as the 2D approaches. Figure 25c also shows the failure potential ϕ, a scalar stress invariant that can be used as a proxy for gauging fracture permeability ($\phi = |([(\sigma_1 - \sigma_3)/([(\sigma_1 + \sigma_3)|$). The fast, approximate 3D solutions, however, have not yet been verified against the 3D boundary element solutions.

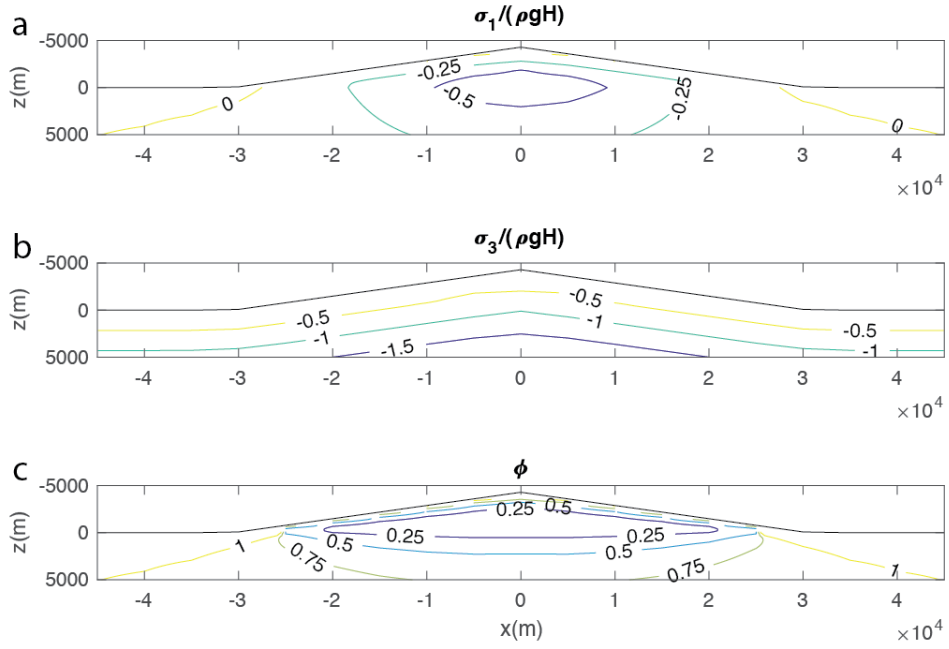

Figure 25. Fast, 3D approximate solutions for (a) maximum (σ_1) and (b) minimum (σ_3) normalized tensile stresses in a conical subaerial volcano with 8° slopes, with stresses normalized by ρgH, where H = 4.3 km is the height of the volcano. (c) Failure potential (ϕ): high values indicate places where fracture-permeability would be greatest.

Source: Lautze (2020)

2.2.5.4 Conclusions

The absence of publicly available data on the stress magnitudes at Kilauea substantially compromises our ability to understand how permeability varies laterally as well as with depth. Stress measurements from a deep borehole would improve our understanding of the stress field at Kilauea. However, if data from just a single deep borehole were available, that information would

not be sufficient to understand how the stress field varies in three dimensions. In order to better understand the stress field at Kilauea, we propose to model the stress field in three dimensions.

2.2.6 Proposed Research and Next Steps

We propose to model the stress field at Kilauea in three dimensions. We consider the total stress field in a region (σ^T) to be the sum of an ambient "base" stress field (σ^a) and perturbations to the stress field ($\Delta\sigma$): $\sigma^T = \sigma^a + \Delta\sigma$. We expect that the ambient stress field within one of the Hawaiian islands is primarily due to gravity. Bending stresses associated with the flexure of the oceanic plate beneath the islands of Hawai‘i might contribute to the ambient stresses as well. We do not expect tectonic stresses observed in continents to play a role given the setting of Hawai‘i in the middle of the Pacific Plate. We also will model the stress perturbations associated with M_w 6.9 earthquake near the base of Kilauea on May 4, 2018 (Bai et al. 2018) to evaluate their effect on the ambient field. We will calculate scalar stress invariants that can serve as proxies for the permeability in the subsurface. We will incorporate the stress invariants into the machine learning procedure for detecting hidden groundwater and geothermal resources.

The proposed research has three main tasks.

2.2.6.1 Task 1: Boundary Element Modeling of the Ambient Field

We will model the ambient stress field in three dimensions using a 3D boundary element method based on triangular displacement discontinuities. The team has experience (Martel and Boger 1998; Martel 2004) using the boundary element code POLY3D of Thomas (1993), but for the proposed research we will use a new version of this code written in Matlab by Davis (2021). Davis revised the code to eliminate problematic artifacts in the original solutions of Yoffe (1960) for triangular dislocations. Those artifacts resulted in stress singularities along lines normal to the triangular elements that extend through the triangle vertices. Those artifacts could be avoided in models of planar faults (Martel and Boger 1998), but it would have been awkward to contend with given the varied orientations of the triangular elements needed to model a topographic surface (Figure 26). To prepare for using the code of Davis (2021), one of our team members has dissected this code and rewritten parts of it to better tailor it to the proposed work, in correspondence with Davis. With the 3D BEM code, we will calculate the ambient stresses due to gravity beneath the topographic surfaces of Kilauea.

We will calculate scalar stress invariants from the model results that can serve as proxies for permeability and incorporate them into the machine learning analyses. We will calculate three stress invariants: (1) the failure potential (ϕ); (2) the mean normal stress [$\overline{\sigma} = (\sigma_1 + \sigma_2 + \sigma_3)/3$]; and (3) the most tensile stress (σ_1). The failure potential addresses both the opening and shearing of fractures, whereas the mean normal stress and the most tensile stress most directly address the opening of fractures. By examining different permeability proxies, we expect to gain a better understanding of the robustness of our overall results.

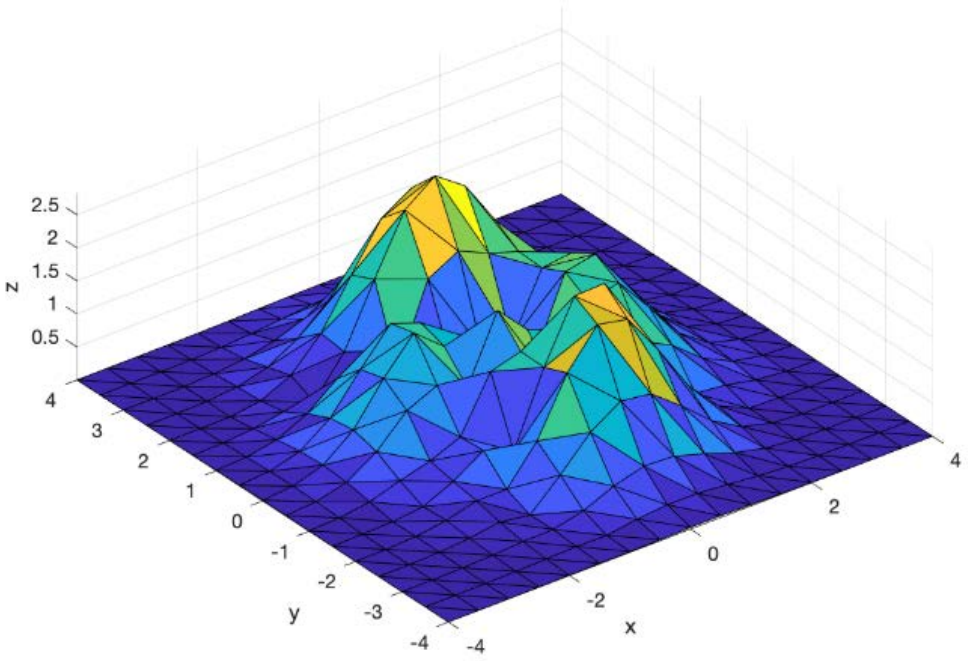

Figure 26. A coarse triangular mesh simulating the topographic surface of an irregularly shaped volcano.

2.2.6.2 Task 2: Verifying the Fast, 3D Approximations Against 3D BEM Solutions

Although the boundary element method has proven to be accurate, it can also be slow to run for modeling the stresses beneath topography. For example, some of the modeling runs of Moon et al. (2017) took days to run on a personal computer. In contrast, the fast, 3D approximate solutions used to model the stresses within Hawaiian volcanoes (Lautze et al. 2020) took only minutes. We will verify the accuracy of the fast, 3D approximate solutions by comparing them with 3D BEM solutions.

2.2.6.3 Task 3: Evaluating the Stress Perturbations due to Faulting on May 4, 2018

One major question we will addresses is how sensitive the stress field at Kilauea is to perturbations from earthquakes. The May 4, 2018 M_w 6.9 earthquake on the south flank of Kilauea occurred very early in the eruptive episode of 2018 at Kilauea, albeit the day *after* fissure eruptions commenced on the LERZ. An unresolved puzzle is whether the earthquake in some way helped trigger the eruptions after May 4. Bai et al. (2018) solved for the fault plane orientation and the slip distribution over the fault during the May 4 earthquake, and they have shared their solutions with us. We will use their solutions to calculate the stress perturbation produced by faulting. Then, by comparing the stress perturbations with the ambient field calculations, we will evaluate whether the earthquake might have helped promote the eruptions after May 4. We will use the 3D BEM code of Davis to model the stress perturbations for two scenarios: (1) a flat, horizontal ground surface (the standard assumption); and (2) a topographic surface that mimics the actual topography at Kilauea. We have nearly completed modifications of the code of Davis to better tailor it to this task. We also

have coded up a Delauany triangulation method that improves on Matlab's method for dividing a planar fault up into triangular elements.

2.3 Multimodal Machine Learning for 3D Characterization of Hidden Groundwater and Geothermal Resources[1]

In this study, we present a MML workflow to assimilate and predict the distribution of numeric and categorical modalities (called feature types in machine learning parlance) along a groundwater-geothermal continuum. Success of the MML workflow relies on a transductive learning algorithm that uses mutual information (measure of entropy describing mutual dependence among random variables) to project disparate and incomplete field observations onto a single embedding space (hypersurface), thereby fusing the features. Features can include any combination of measured (point field) and derived (multiphysics-based numerical model inversions, data-driven machine learning, and multiphysics-informed) machine learning. The aim of this study is to demonstrate efficacy in using the MML workflow for identifying hidden geothermal (and coupled groundwater) resources and attendant geologic features in Hawai'i. We hypothesize that the MML can assimilate and predict heterogeneous and incomplete features for locating hidden resources by exploiting mutual information in multimodal field observations. To test this hypothesis, the proposed MML workflow was applied to subsets of Hawai'i Play Fairway project modalities and predicts subsurface geophysical, geologic, and hydrogeologic features across the Islands of Lāna'i and Hawai'i. The successful application of the MML workflow achieves the following objectives: (1) develop open community data sets, (2) identify data acquisition targets with high value for future work, (3) identify new signatures to detect hidden groundwater and geothermal resources, and (4) foster new capabilities for characterizing subsurface temperature and permeability. This study extends the work of Friedel (2016) who applied a MML workflow to construct a continuous set of hydrostratigraphic units for characterizing shallow (<200 m) groundwater systems, and Vesselinov et al. (2020) who used an unsupervised machine learning methodology (factor analysis) to discover hidden signals in field data and extract their dominant attributes in a shallow (<200 m) hydrothermal system.

2.3.1 Methods

The MML workflow involves the application of three primary steps to local feature types: (1) feature selection, (2) feature prediction, and (3) feature clustering.

2.3.1.1 Feature Selection

The identification of suitable features (observation types) for building the MML model is undertaken using the nonlinear wrapper approach called learn heuristics with feature constraints. The wrapper model requires one predetermined learning algorithm in feature selection and uses its performance to evaluate and determine which features are selected (Yu and Liu 2003). In this regard, the learn heuristics reflect the machine learning algorithm that is introduced into the Metaheuristics algorithm (Buscema, Breda, and Lodwick 2013). The machine learning algorithm is generalized to multiple learning algorithms that are evaluated, including Backpropagation, K-Nearest Neighbor, or Naïve Bayes, inside a genetic algorithm (metaheuristic). Constraints on the learn heuristic approach typically involve features such as one or more response variables. Given

[1] A summary of the machine learning data discussed in this section was originally presented at the 2022 Stanford Geothermal Conference. Please see Friedel et al. (2022) for more information.

that the genetic algorithm converges to a global minimum surface (not a single vector), the process is randomly reinitiated and run until the subset of optimal features can be identified based on how well they predict variables at unsampled locations.

2.3.1.2 Feature Prediction

A Modified Self-Organizing Map (MSOM) procedure is used to impute feature vectors at unsampled locations in order to inform predictions of geothermal indicators. The method is sufficiently robust to cope with feature vagaries due to sample size and extreme data insufficiency, even when >80% of the data are missing (Friedel and Daughney 2016). The transductive MSOM procedure involves the sequential application of competitive learning (Self-Organizing Map) and estimation (minimization of a two-component objective function by competitive learning). The architecture of MSOM involves an input layer (signals from the environment) and an output layer (competitive feedback to the environment). The input layer comprises a set of nodes (neurons) that are connected to one another through a rectangular topology (rows by columns). The connections between inputs (data vectors) and nodes have weights, so a set of weights corresponds to each node.

In implementing the MSOM procedure, the competitive learning process iteratively modifies weights during the training phase so that the self-organized output pattern becomes consistent, meaning that the input pattern produces the same output pattern. In doing so, the MSOM iteratively maps each data sample as a vector (each variable is characterized as a cloud of data vectors) across a hypersurface on which data vectors closer to each other are more related (self-similar) than data vectors farther away. The learning algorithm may be summarized as follows (Kohonen 2001):

1. Generate initial values including weights, radius, and learning parameter values.
2. Select input vector from data set.
3. Identify winning node, which is the closest node to the input vector using the Euclidean distance metric.
4. Identify the neighborhood with the given radius using a Gaussian function.
5. Update the weights for the winning node and all the nodes in the same neighborhood.
6. Repeat steps 2 to 6 until the weight vectors reach a converged state.
7. The estimation of missing values (sometimes referred to as imputation) is done simultaneously for all variables across the hypersurface (Kalteh, Hjorth, and Berndtsson 2008).

Feature prediction is undertaken for each new instance, x, by searching through the MSOM best-matching unit vectors for the K most similar instances (Wang 2003; Riese 2019). To determine which of the K instances in the training dataset are most like the new instance, the Euclidean distance metric is used while iteratively minimizing the sum of quantization and topographical error vectors as part of the competitive learning process (Kalteh, Hjorth, and Berndtsson 2008).

Training and testing of the MSOM model are carried out using a split-sample validation approach. In this approach, the data records are randomly shuffled and split with 80% set aside for training and 20% set aside for testing. In total, the original data set is shuffled and split using this procedure N times. Each split characterizes a fold used in computing the N-fold cross-validation statistics to assess generalizability of the unsupervised machine learning algorithm when presented

independent field data. The metrics used to evaluate model performance include R^2 (a statistical measure representing the proportion of variance for the observed variable that is *explained* by the estimated variable) and mean squared error (predictive success) for continuous features; and accuracy (predictive success) and Cohen's Kappa (comparison between the observed accuracy and the agreement expected due to chance) for categorical (present or absent) features (Cohen 1960). Cohen suggested the Kappa result for categorical features be interpreted as follows: values ≤ 0 as indicating no agreement and 0.01–0.20 as none to slight, 0.21–0.40 as fair, 0.41–0.60 as moderate, 0.61–0.80 as substantial, and 0.81–1.00 as almost perfect agreement.

2.3.1.3 Feature Clustering

Grouping statistically meaningful features across the self-organized hypersurface utilizes k-means clustering (Vesanto and Alhoniemi 2000). The best partitioning for each number of clusters is determined based on the Euclidian distance criterion and interesting merges are defined using the Davies-Bouldin validity index (Davies and Bouldin 1979). In this study, the optimal number of clusters is determined as the mode by repeating the k-means process to avoid convergence at local minima. The Davies-Bouldin validity index is selected as a matter of convenience, but other validity measures could be used.

2.3.2 Case Studies

The MML study focuses on the Islands of Lānaʻi (Friedel et al. 2022) and Hawaiʻi, as described in the following sections on the study region, feature types, feature selection, feature prediction, and feature clustering. The MML framework was initially tested for application to the Island of Lānaʻi by means of a generous donation from the Pulama Lānaʻi to Lautze through the University of Hawaiʻi Foundation and using data gathered during the Hawaiʻi Play Fairway project through a GTO grant under award number DE-EE0006729. Knowledge gained from the Lānaʻi work was used in developing and testing the subsequent MML framework for application to the Island of Hawaiʻi through this project.

2.3.2.1 Island of Lānaʻi

The Island of Lānaʻi and adjacent Pacific Ocean are located about 96 km southeast of Honolulu, Oahu (Figure 27). Lānaʻi is a cashew-shaped island with a maximum width of 29 km in the longest direction. The highest point on Lānaʻi is 1026 m with a land area of 364 km^2. The geology of Lānaʻi is described as an eroded extinct basaltic volcano that developed during one period of activity (Stearns 1940). Structurally, the island has three primary rift zones (Northwest Rift Zone, Southwest Rift Zone, and South Rift Zone) and caldera located in the Pālāwai Basin (Figure 28). The summit plateau resulted from collapse along the Northwest Rift Zone (Stearns 1940). Lānaʻi island has fault breccias and dike complexes that lie in the rift zones radiating from the Pālāwai Basin. Relatively low permeability dikes crosscut porous lavas of relatively high permeability, forming local compartmentalized reservoirs (Stearns 1940). Basaltic rocks exposed along the west coast are thinly bedded and considered the most permeable rocks due to cavities and fractures within and between lava flows and are thought to permit the landward intrusion of sea water. Groundwater temperatures measured in a well on the rim of the Pālāwai Basin during Play Fairway Phase 3 vary from ~21°C at the land surface to ~65°C at a depth of 1 km. Little is known about the subsurface groundwater-geothermal system outside these locations, although temperatures at the Moho (~13 km depth) are likely to be in the range of 444°C to 892°C (Schutt, Lowry, and Buehler 2018). Therefore, understanding the occurrence of groundwater and geothermal resources requires knowledge of the spatial distribution and characteristics of these basalt-dike systems.

2.3.2.2 Feature Types

Feature types used in the Lānaʻi case study represent a subset of those data assembled and/or collected during the Hawaiʻi Play Fairway project, funded by GTO. This data set includes geologic, groundwater, and geophysical observations relevant to subsurface heat, fluid, and permeability collected at the island of Lānaʻi (Lautze et al. 2020). For example, the geologic data include information on subaerially erupted basalt and dike rocks identified at the surface and in drill cores. Groundwater data collected in boreholes include physical properties (water level and specific capacity), aqueous chemistry (major ions, nutrients, and metals), and aqueous parameters (dissolved oxygen, specific conductivity, and temperature). These data sets reflect field sampling from the surface to a maximum borehole depth of ~1 km (Figure 28). To connect this sample region to greater depths, uncollated surface gravity and MT measurements were collected and deterministically inverted to estimate 3D distribution of density and electrical resistivity values across Lānaʻi over depths of more than 14 km (Lautze et al. 2020).

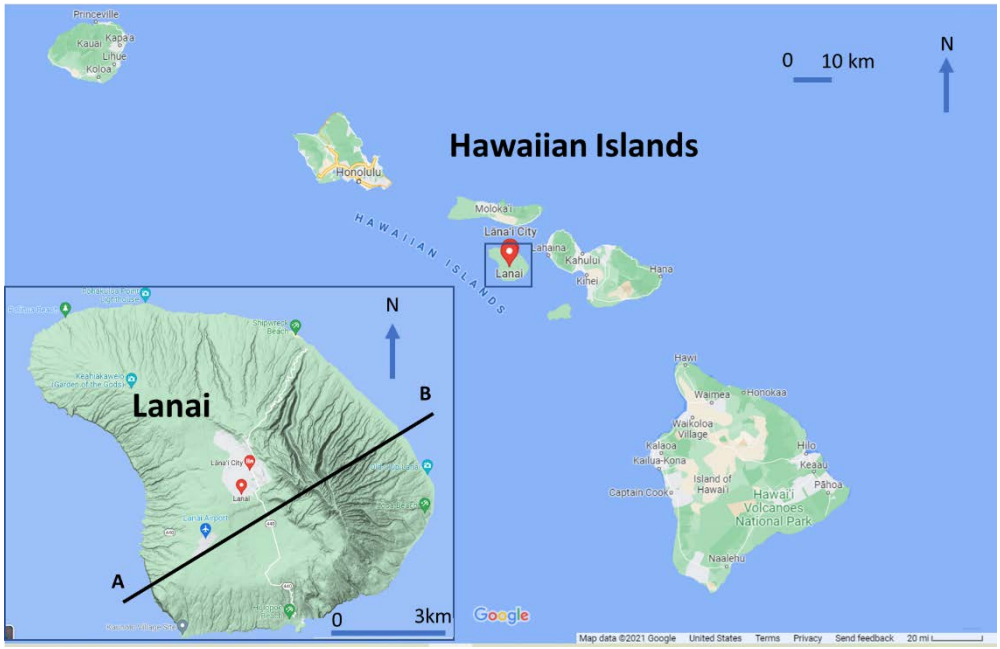

Figure 27. Lānaʻi study map showing proximity of Lānaʻi to the Hawaiian Islands and Lānaʻi cross-section (inset) for which MML results are extracted (from the surface to 15 km) for evaluation and construction of the conceptual model.

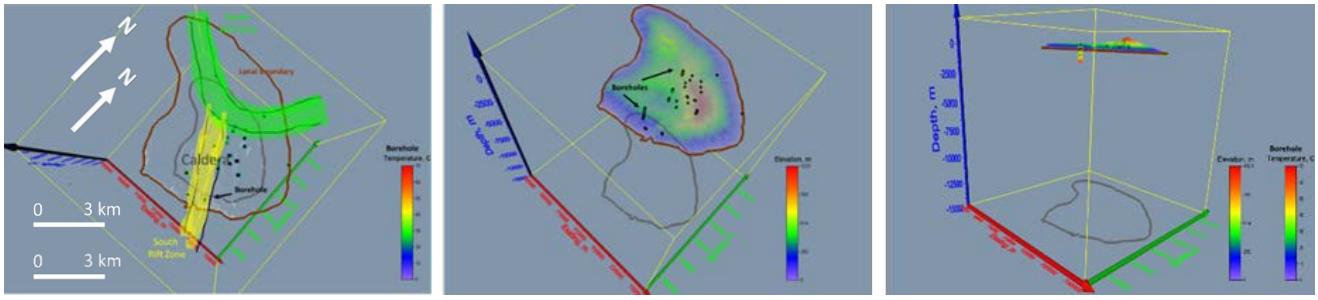

Figure 28. Study map and model framework showing Lānaʻi coastal boundaries at sea level (brown) and projections at 15km depth (gray); left panel includes primary rift zones: north (green) and south (yellow); caldera, borehole/well locations (shown as dots with color indicating temperature); middle and right panels show location of borehole/well locations with respect to elevation.

2.3.2.3 Island of Hawaiʻi

The Island of Hawaiʻi, also referred to as the "Big Island," is largest of the Hawaiian Islands (Figure 29). At its greatest dimension, the island is 150 km (93 mi) across with a total land area of 10,432 km^2 (4,028 mi^2). The Big Island has five subaerial (above sea level) volcanoes: Hualalai, Kilauea, Kohala, Mauna Loa, and Mauna Kea. Of these volcanoes, Kohala is extinct and the oldest with an estimated age of 1 million years (Stearns 1940). In contrast, Hualalai and Mauna Kea are dormant, and Mauna Loa and Kilauea are active. The most recent eruption of Mauna Loa occurred in 1984 whereas Kilauea has been erupting regularly since 1983. The highest point on the Big Island is the dormant volcano Mauna Kea 4,205 m (13,796 ft).

The geology of the Big Island reflects four stages of volcanism (Stearns and MacDonald 1946) as identified from surface and subsurface rock samples. Specifically, during the initial submarine stage (stage 1) small vents or fissures open in the ocean floor and erupt pillow lavas that have higher relative abundances of sodium and potassium than the tholeiitic basalts of the shield-building stage. Continued volcanism produces a shield volcano. As the top of the volcano approaches sea level (stage 2), the water pressure at the volcano summit drops, allowing water in contact with lava to turn to steam, resulting in explosions that form tephra and hyaloclastite rocks. In the subaerial shield-building stage, aa and pahoehoe erupt from the summit area and rift zones, resulting in growth of the volcano. In the subaerial landslide stage (stage 3), large volumes of unstable volcanic rock move seaward from the coastal edges of the volcano under their own weight, eventually failing as a landslide and/or debris flow into the adjacent ocean (Moore, Norark, and Holcomb 1994). Kilauea appears to be in this stage with the largest of Hawaiʻi's historic earthquakes resulting from displacement of the Hilina slump in south Hawaiʻi. In the capping stage (stage 4), alkalic basalt fills the summit caldera and produces a steep-sided cap at the summit of the volcano. Cinder cones develop from lava ejected from a single vent. Mauna Kea is an example of a volcano with multiple steep-sided (25–33 degree) cinder cones.

Structurally, Hawaiʻi Island has four primary rift zones: the Southwest Rift Zone and Northeast Rift Zone (referred to collectively herein as the Mauna Loa Rift), and the Southwest Rift Zone and ERZ (referred to collectively herein as the Kilauea Rift). Both the Southwest Rift Zone and ERZ bound the north side of the Hilina fault system. The Hilina fault system is considered the northern boundary of the Hilina Slump, a 19,800 km^3 (4,760 mi^3) section of the south slope of the Kilauea volcano which is moving away from the island (Denlinger and Morgan 2014). The Hilina Slump,

on the southern flank of the Kilauea Volcano on the southeast side of the island of Hawai‘i, extends from the Hilina Fault zone approximately south of the ERZ to the edge of deep water (Denlinger and Morgan 2014).

The rocks of Hawai‘i Island are considered highly permeable, resulting in rainfall infiltrating rapidly into the subsurface (Stearns and MacDonald 1946). Perennial streams are present only on the western slopes of Kohala Mountain and Mauna Kea. Most of the water infiltrates rapidly to the basal water table, where the freshwater floats on salt water according to the Ghyben-Herzberg principle. Basal water discharges in springs at or near sea level all along the coast. Only a very small proportion of this groundwater is recovered in wells. Along the western coasts, the basal water is of good quality and large supplies await development. Along the eastern coasts, most of the basal water is brackish.

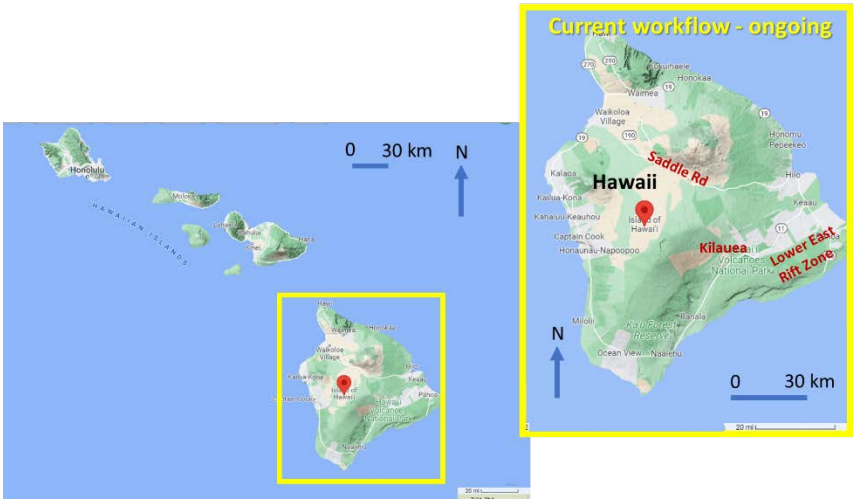

Figure 29. Hawai‘i study map showing (left) proximity of the Island of Hawai‘i to the Hawaiian Islands, and (right) the Saddle Road, Kilauea, and LERZ study areas for which MML is used to assimilate and predict features locally (individual areas), regionally (three areas) and island wide (at the three designated study areas and random locations of pseudo-boreholes from surface to 40 km depth).

2.3.2.4 Feature Types

Feature types used in the Hawai‘i case study represent a subset of the data assembled and/or collected during the Hawai‘i Play Fairway project, funded by GTO, along with publicly available seismic data (IRIS 2022) and various published and contractor reports (Jerran et al. 2019, State of Hawai‘i 1990). This data set includes observations from four feature categories: location (e.g., easting, northing, and elevation); state variable (e.g., temperature) (Putrika 1997; Lautze et al. 2020); geology (this includes structures such as the Halima, Kahuku, Kaoiki, Kealakekua, Koae, and Kohala fault systems; Kilauea and Mauna Loa rift zones [Lipman, Rhodes, and Dalrymple 1990; Wolfe and Morris 1996; Trusdell, Wolfe, and Morris 2006]; rock designations such as basalt erupted subaerially, oceanic crust, underplated rock, mantle [Leahy et al. 2010]); and physical properties (Lautze et al. 2010) such as density, resistivity, p-wave velocity, s-wave velocity, and earthquake magnitude.

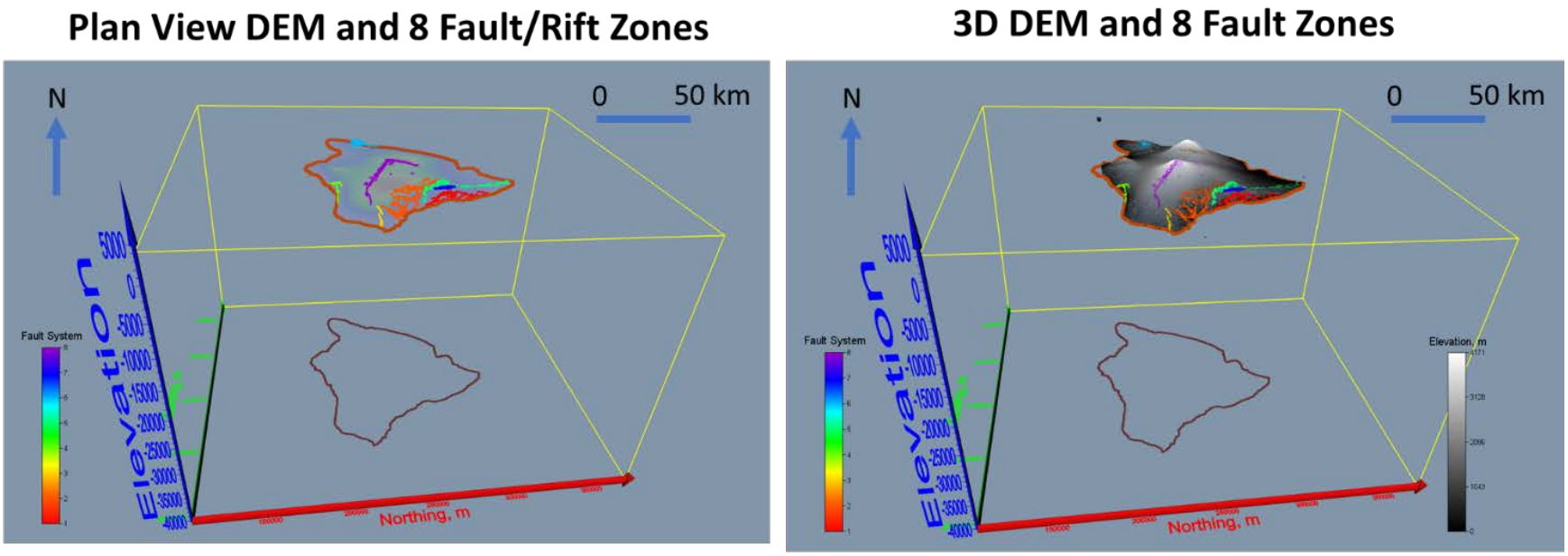

Figure 30. Study map and model framework showing Hawai'i coastline at sea level (orange) and its projection at 40 km depth (brown); left panel includes primary fault/rift systems 1 to 8 and layered on plan view DEM; the right panel includes primary fault zones draped onto the DEM from 0 m (sea level) to 4,171 m.

The Hawai‘i temperature data reflect measurements collected from shallow (generally 25–100 m) groundwater wells (N=32) along the island coast, and geothermal boreholes along the Saddle Road (N=2), at Kilauea (N=1), and along the LERZ (N=9) (Lautze et al. 2020). The groundwater well data reflect field sampling from the surface to a maximum borehole depth of about 1 km (Figure 28), whereas the geothermal wells yield measurement depths as great as 3 km. To connect the groundwater and geothermal samples to greater depths, uncollated surface gravity, MT, and seismic measurements were collected and deterministically inverted to estimate 3D distribution of density, electrical resistivity, and velocity values across study areas to depths as great as 40 km. A spatial overview of sample locations for these study areas is presented in Figure 31a.

At the Saddle Rd study area (Figure 1.31b), surface AMT and MT measurements were recorded and *deterministically* inverted to provide 1D density and 1D resistivity profiles (Constable, Parker, and Constable 1987) at 31 stations (12PT, 13PT, 15PT, 16PT, 1PT1, 2PT1,3PT1, 4PT1, 5PT1, 6PT1, 7PT1, 8PT1, 9PT1, HH01, HH02, HH03, KK01, KK02, KM01, MK1, ML01, ML02, MM13, OR01, PK01, PK02, Pk03, PK04, PK05, REF1, and WF01). The profiles extend from the surface to a depth of 3 km. The same measurements also were inverted using a *stochastic* inversion scheme developed as part of this project to provide 1D resistivity profiles spanning deciles from the surface to a depth of 3 km. Another deterministic inversion was undertaken using the same MT measurements to provide 1D resistivity profiles to a depth of 40 km, ensuring the project had coverage spanning the Moho (Leahy et al. 2010). A separate deterministic gravity inversion (UBC 2013) provided density measurements along surface stations to a depth of 3 km. In addition to surface measurements, other temperature, velocity, and resistivity measurements, recorded to a depth of 1.5 km from the PTA2 and KMA1 boreholes, were also used in this study.

At the Kilauea study area (Figure 31c), surface MT measurements were recorded and deterministically inverted (Constable, Parker, and Constable 1987) to provide 1D resistivity profiles at 16 stations (g1sta03rrhkml, g1ta04rrhkml, g1sta05rrhkml, g1sta19rrhkml, g2sta13rrhkml, g2sta1rrhkml, g3sta12rrhkml, g4sta01rrpark, g4sta06rrpark, g4sta08rrpark, g5sta07rrpark, g5sta11rrpark, g6sta09rrpark, g6sta101rrpark, g6sta17rrpark, and g6sta18rrpark) from the surface to a depth of 40 km. Other seismic measurements located within 150 m of the MT stations were recorded and inverted as part of this project to obtain discrete p-wave and s-wave velocities to depths exceeding 40 km. A single borehole sponsored by National Science Foundation (Keller-NSF) provided temperature measurements to a depth of 1.5 km.

At the LERZ study area (Figure 31c), surface MT measurements were recorded and deterministically inverted (Constable, Parker, and Constable 1987) to provide 1D resistivity profiles at nine stations (km01, km02, ps02, ps08, ps09, ps11, ps12, and ps19) from the surface to a depth of 40 km. Seismic measurements located within 150 m of the MT stations were inverted as part of the project to obtain p-wave and s-wave velocities to depths exceeding 40 km. Measurements from several geothermal boreholes (Ashida 1, Geothermal 1, Geothermal 2, HGP-A, KS-1, KS-2, Lanipuna-1, SOH1, SOH2, Geothermal 4, SOH4, Keauohana 1, and Malam Ki) provided temperatures from the surface to a depth of about 1.5 km (Jerran et al. 2019; Stolper, DePaolo, and Thomans 2009; Sorey and Colvard 1994; PGV 1991; State of Hawai‘i 1990; Campbell and Gardner 1981; Kihara et al. 1977; Kingston Reynolds Thom & Allardice Ltd. 1976). In addition, measurements from a single geothermal well north of the LERZ near Hilo (Stolper, DePaolo, and Thomans 2009) provided temperatures at the coastal boundary.

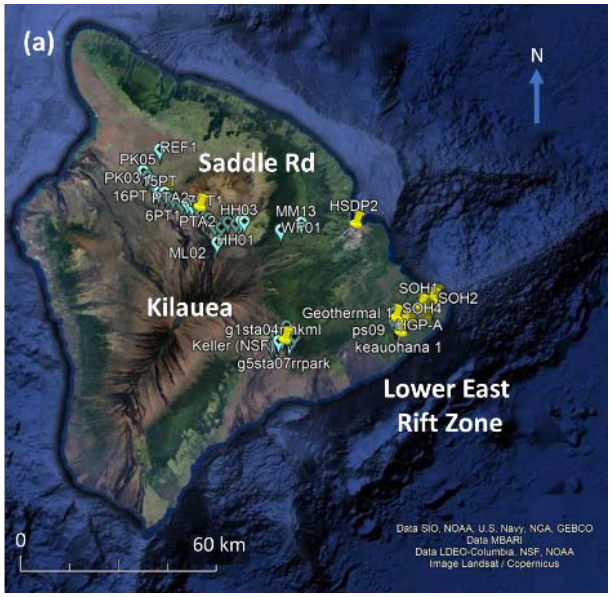

Figure 31. The local study regions on the island of Hawai‘i include Saddle Road, Kilauea, and LERZ: (a) The distribution of geothermal wells (shown in yellow) and geophysical stations (light blue) across Hawai‘i. (b) Station and well detail in the Saddle Road area. (c) Station and well detail in the Kilauea and LERZ areas.

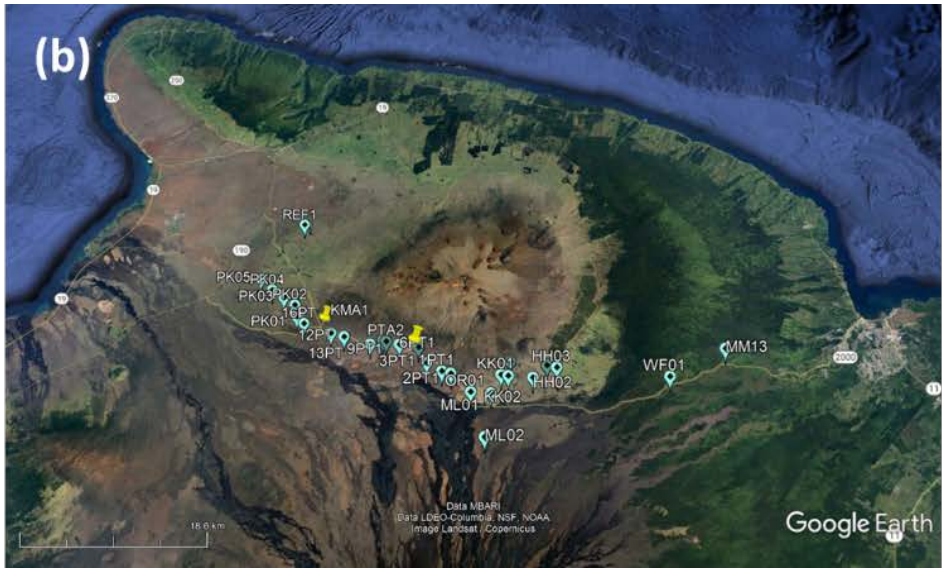

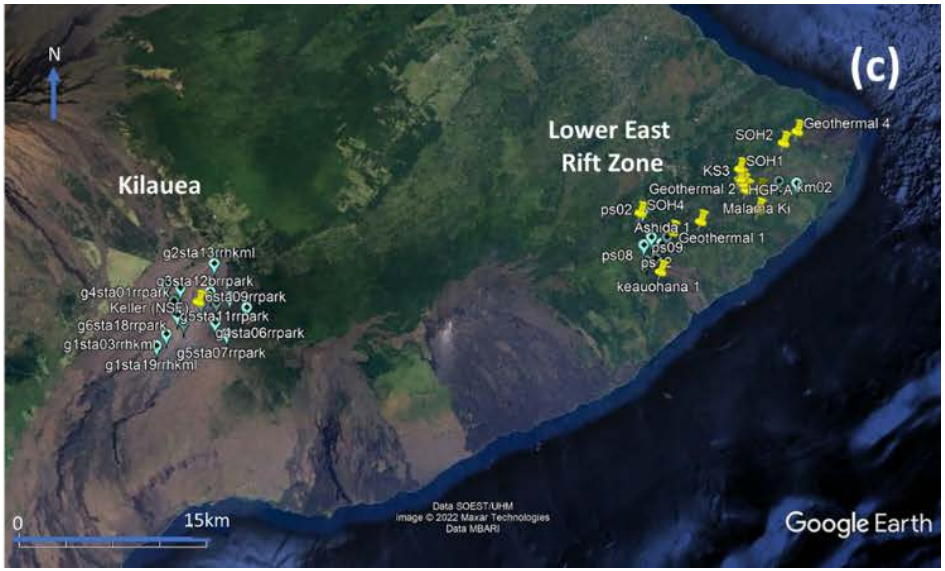

2.3.3 Preliminary Results

2.3.3.1 Island of Lāna'i

2.3.3.1.1 Feature Selection

Of the original number of predictor variables (N = 54), the learn-heuristic feature selection process identified an optimal global set of variables (N = 27) suitable for predicting features beneath Lāna'i (Table 2). These variables are used in building the unsupervised learning-based models. Important predictors that appear common to all three state variables include water (i.e., the ocean); geology (basalt erupted subaerially and dikes), physical properties (density, resistivity, specific capacity); aqueous properties (specific conductivity, oxygen reduction potential, and pH); and aqueous chemistry (HCO3, NO3, PO3, SO4, r, F, Fe, K, Na, Si, Sr, and Ca/Mg ratio).

Table 2. Summary of Features Determined to be Informative Using the Learn Heuristics Approach Constrained to the State Variables of Head (m), Temperature (°C), and Chloride Concentration (mg/l)

Constraints on learn heuristics

Informative features

		Type		Observation		Support
Category	Features	Discrete	Continuous	Measured	Derived	Point
State variables	Head, m		X	X		X
	Temperature, C		X	X		X
	Chloride concentration, mg/l		X	X		X
Water	Ocean	X		X		X
Geology	Basalt	X		X		X
	Dike	X		X		X
Physical properties	Density, kg/m3		X		X	
	Resistivity, ohm-m		X		X	
	Specific capacity, m3/d/m		X		X	
Aqueous properties	Specific conductivity		X	X		X
	Oxygen reduction potential, mv		X	X		X
	pH		X	X		X
Aqueous chemistry	HCO3, mg/l		X	X		X
	NO3, mg/l		X	X		X
	PO4, mg/l		X	X		X
	SO4, mg/l		X	X		X
	Br, mg/l		X	X		X
	F, mg/l		X	X		X
	Fe, mg/l		X	X		X
	K, mg/l		X	X		X
	Na, mg/l		X	X		X
	Si, mg/l		X	X		X
	Sr, mg/l		X	X		X
	Ca/Mg		X	X		X

Physical properties: resistivity (ohm-m), specific capacity (m3/d/m); Aqueous properties: specific conductance (uM/s), oxygen reduction potential (mv); Aqueous chemistry: Br = bromide, (mg/l), F = Fluoride (mg/l), Fe = iron (mg/l), HCO3 = bicarbonate (mg/l), K = potassium (mg/l), Na = sodium (mg/l), NO3 = nitrate (mg/l), PO4 = phosphate (mg/l), Si = silica (mg/l), SO4 = sulfate (mg/l), Sr = strontium (mg/l), Ca/Mg = calcium-magnesium ratio.

2.3.3.1.2 Feature Prediction

Prior to training of the MSOM, features (field variables) were normalized by their data variance and randomly assigned (presenting the input vectors to the map sequentially using a randomly sorted database) as an initial set of map weight vectors. Application of the MSOM network to training data is done using a single fixed number of neurons and topological relations. The selected neural map shape (148 rows by 140 columns) is a toroid (wraps from top to bottom and side to side) with hexagonal neurons. Training of the map was conducted using both rough and fine

phases. The rough training phase involved 20 iterations using a Gaussian neighborhood with an initial and final radius of 204 units and 51 units, respectively, within a neural map shape of 20,720 units (148 rows by 140 columns). The fine training involved 400 iterations using a Gaussian neighborhood with an initial and final radius of 51 units and 1 unit, respectively. The initial and final learning rates of 0.5 and 0.05 decayed linearly down to 10^{-5}, and the Gaussian neighborhood function decreased exponentially from a decay rate of 10^{-1} iteration to 10^{-3}, providing reasonable convergence evidenced by similarity in their low quantization (q_e=0.073) and topographic (t_e=0.076) errors.

Testing and validation of the trained MSOM model are reflective of the five split sets previously described. The cross-validation statistics further reveal that the MSOM model has a moderate ability (kappa values >0.53) to predict dikes and basalt erupted subaerially with strong prediction accuracies (accuracy values >0.99). For the sake of brevity, summary statistics and scatterplots are presented for independent observations and predictions of selected features that include temperature, chloride concentration, resistivity, and density (Figure 32). Note that the metrics for temperature predictions are reflective of those measured in the upper 1 km, because the magnitude of increasing temperatures at greater depths is unknown. In general, the cross-validation statistics (Table 3) reveal similar observed to predicted values (minimum, average median, and maximum) with reasonable prediction accuracies (standard deviation/square root of count): resistivity = 0.32 ohm-m, density = 1.2 kg/m3, temperature = 0.002 C, chloride concentration = 1.16 mg/l. The associated scatter plots (Figure 32) of observed versus predicted values for these features have varying R^2 values: resistivity, ohm-m = 89.9%; density, kg/m3 = 99.9%, chloride, mg/l = 68.8%; temperature, C = 92.8%. To show the whole picture (not just the summary metric of R^2), the scatter plot of observed and predicted values (Figure 32) demonstrates the bias at smaller values. Although resistivity has a relatively high R^2 value, there is a wide spread of predicted versus observed. The bias at small values for density, conductivity, and chloride concentration is attributed to challenges in predicting these features at the ocean-basalt interface given the large voxels used during deterministic inversions and moderate ability to predict the presence or absence of basalt erupted subaerially. Future studies may benefit by introducing higher frequency AMT measurements to improve near-surface estimates of resistivity at the coastal boundary and shallow depths. Likewise, the prediction of small density values may be reflective of the inability of MSOM to resolve density at the ocean-coastal boundary due to grid resolution.

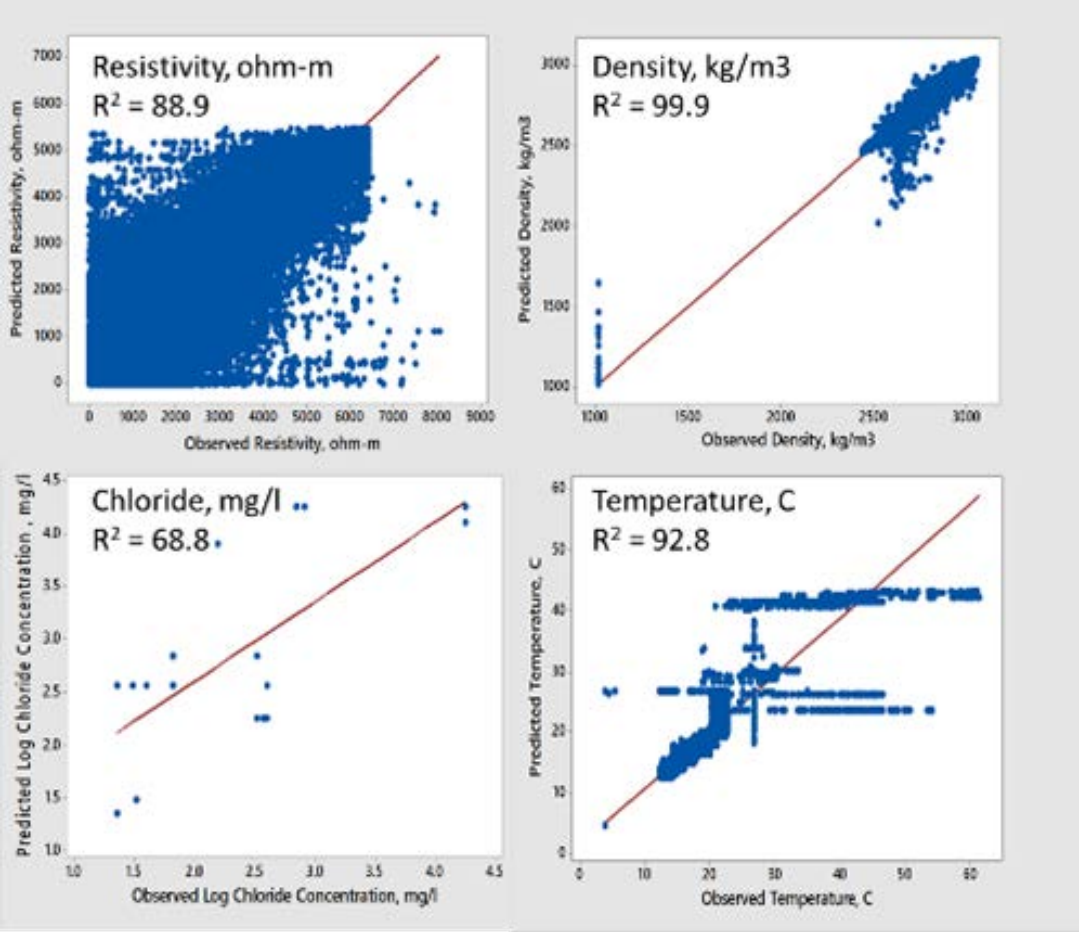

Figure 32. Scatterplots showing observed versus predicted values for selected features with fitted line and R^2 values (%): resistivity, density, chloride concentration, and temperature.

Table 3. Summary Statistics for Observed and Predicted Features: temperature (°C), chloride concentration (mg/l), resistivity (ohm-m), and density (kg/m^3)

Temperature, C

Statistic	Observed, C	Predicted, C	Error, C
Minimum	4.00	4.00	0.00
Average	22.5	23.4	0.34
Median	22.4	23.4	0.03
Maximum	61.4	61.3	30.4
Standard deviation	4.69	8.19	1.22
Count	213824	1044532	213824

Chloride, mg/l

Statistic	Observed, mg/l	Predicted, mg/l	Error, mg/l
Minimum	23.0	23.0	0.0
Average	17999	12956	1.3
Median	18000	18000	0.0
Maximum	18000	18002	17670
Standard deviation	157.7	7974	533.3
Count	212919	1044530	212919

Resistivity, ohm-m

Statistic	Observed, ohm-m	Predicted, ohm-m	Error, ohm-m
Minimum	0.10	0.14	-86.5
Average	516	385	130
Median	100	35.1	25.4
Maximum	8066	5470	7181
Standard deviation	940	786	288
Count	799480	1044530	799480

Density, kg/m3

Statistic	Observed, kg/m3	Predicted, kg/m3	Error, kg/m3
Minimum	1020	1020	0.00
Average	1129	2016	21.9
Median	1020	2617	0.00
Maximum	3055	3037	2029
Standard deviation	420.6	862.4	182.6
Count	227176	1044530	227176

Note that statistics for the temperature are confined to those measured in the upper 1 km given that temperatures at the Moho are assumed to be ~758C.

Source: Schutt et al. (2018)

A natural outcome when using the trained MSOM model is the simultaneous prediction of all model features. Given the large number of available features, a reduced number of features is selected for presentation that include state variables (temperature, chloride concentration), physical properties (specific capacity—a surrogate for permeability), geology (basalt and dike), and geothermal stratigraphic units (GSU). Each of these features represent predicted values extracted from the 3D data cube along the cross-section A-B. Cross-section A-B (Figure 33) strikes SW-NE along a profile that begins at the Pacific Ocean on the west, crosses the caldera dike system, the point of highest elevation, and ends at the Pacific Ocean on the east. Collectively, Figure 33–Figure 37 reveal a heterogeneous groundwater-geothermal system. Note that the model domain boundary is indicated as having poor resolution given the lack of available field data in these regions. In the balance of the model domain, testing reveals that the prediction process preserves reasonable population statistics for the geologic, hydrogeologic, and geophysical features, but the individual feature predictions reflect a random process (statistics change for different split sets). For this study, the cross-validation statistics demonstrate the ability of the MSOM to generalize when estimating continuous features from sparse field data characterizing the different support volumes.

This section presents a subset of features predicted while using the trained MSOM and five sets of independent observations. For example, the 3D density and 3D resistivity predictions are presented in Figure 33. Some general spatial observations are that both density and resistivity are heterogeneous through the region. The interpreted density anomalies include minimum values associated with the ocean and greatest density inland at the caldera and to a depth of about 15 km. The predicted resistivity also appears heterogenous through the region, with features at sea level displaying more resistive character at and below the region of greatest elevation, and conductive

features similar in magnitude to the ocean but decreasing landward in areas located at the northernmost point and southwestern point (toward point A on the cross section). Another slightly deeper region of high conductivity (low resistivity) appears at the eastern boundary of the island (toward point B on the cross section). These areas suggest regions of landward intrusion of sea water, with decreasing gradients, over ~5 km from the coast. In the area of maximum elevation, the resistivities are greatest, possibly due in part to groundwater recharge of freshwater. Below about 1 km, the anomalies appear as vertical rectangular regions of alternating medium-to-high resistivity values.

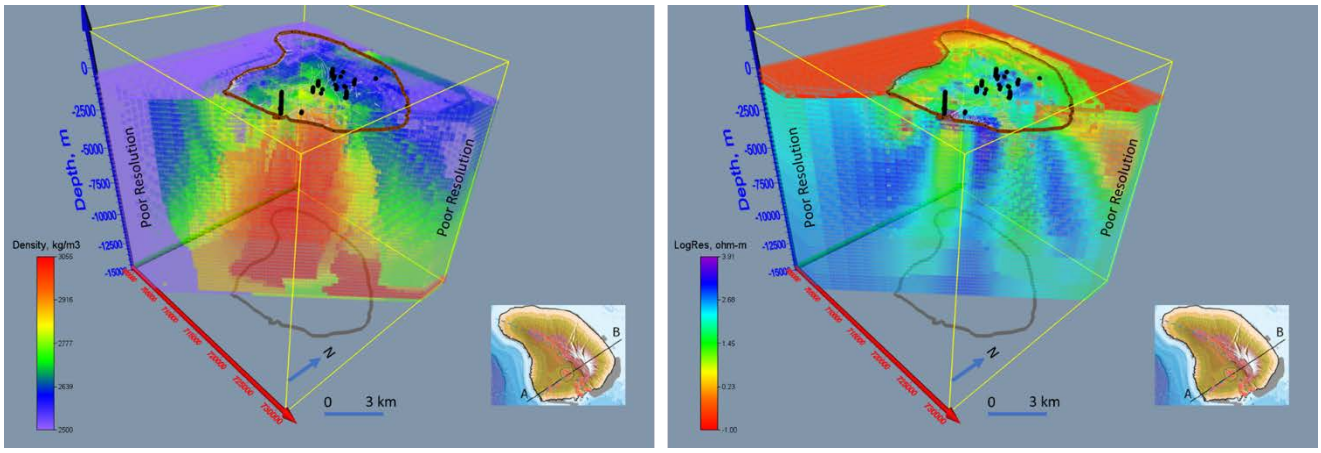

Figure 33. Inverted 3D geophysical property distributions sliced horizontally at sea level and vertically along A-B: (left) density, kg/m^3 (density >2500 kg/m^3), and (right) log resistivity, ohm-m. Regions of poor resolution reflect limited field data available to inform the model.

The predicted spatial occurrence of subaerially erupted basalt, referred to as "basalt" (left), and submarine basalt and dikes, referred to as "dike" (right), are shown in Figure 34. The basalt is prominent from the surface to depths as great as about 10 km. We note that the "basalt" *appears* to be draped over a region indicated as not being "basalt." The "nonbasalt" region most likely represents an intrusive complex consisting in part of dikes, sills, and laccoliths with several interesting features. This dome-shaped feature appears to have roots that extend below the Moho, located at about 12.5 km depth. The change in character below the complex is interpreted as the possible location of the Moho. Other vertical features are interpreted as dike swarms rising on the west side of the pluton (between 5 and 8 km depth) and at the top of the intrusion below the caldera region (from sea level to about 1 km depth). The later dike swarms correspond to the region denoted as a dike zone by Malahoff and Woollard (1966) based on airborne total field magnetic anomalies. Lastly, dikes of the western swarm rose vertically to a depth of about 5 km below the surface where they feed what appears to be a sill or a laccolith.

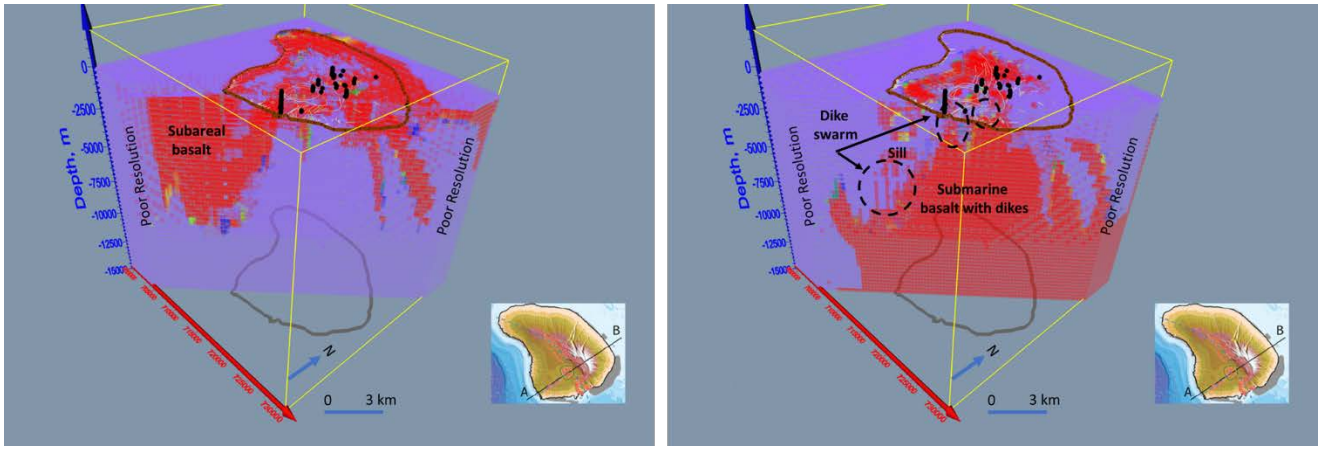

Figure 34. Predicted 3D geology distribution (95% likelihood to be present or absent) sliced horizontally at sea level and vertically along A-B: subaerial basalt, referred to as basalt (left), and submarine basalt and dikes, referred to as dike (right). Dike image includes likely dike swarms, sill, and Moho (about 12.5 km). The locations of shallow dike swarms correspond to airborne dipole magnetic anomalies (Malahoff and Woollard 1966). Regions of poor resolution reflect limited field data available to inform the model.

The predicted spatial occurrence of the ocean (left) and specific capacity (right) are shown in Figure 35. The ocean appears correctly located adjacent to the island and increases in depth to the western and eastern boundary of the model. That said, the ocean at the western edge appears to extend to the bottom of the model domain. In fact, the actual ocean depth in this region is known to be about 6 km, thereby revealing the apparent lack of resolution in resistivity and gravity information near the domain boundary to inform the MSOM model. Improvements in predictions for this region of the model would likely require the addition of related properties derived possibly from shipborne and/or ocean bottom geophysical measurements. The specific capacity predictions in this study represent the analog to permeability. In general, there is a trend characterized by low specific capacity at the eastern boundary increasing toward the west. This trend follows from an earlier discussion indicating that the most permeable basaltic rocks are located at the western edge of Lānaʻi. Also, the western dike swarm (between 5 and 8 km depth) is characterized as medium specific capacity, whereas the adjacent region to the east is characterized as low specific capacity.

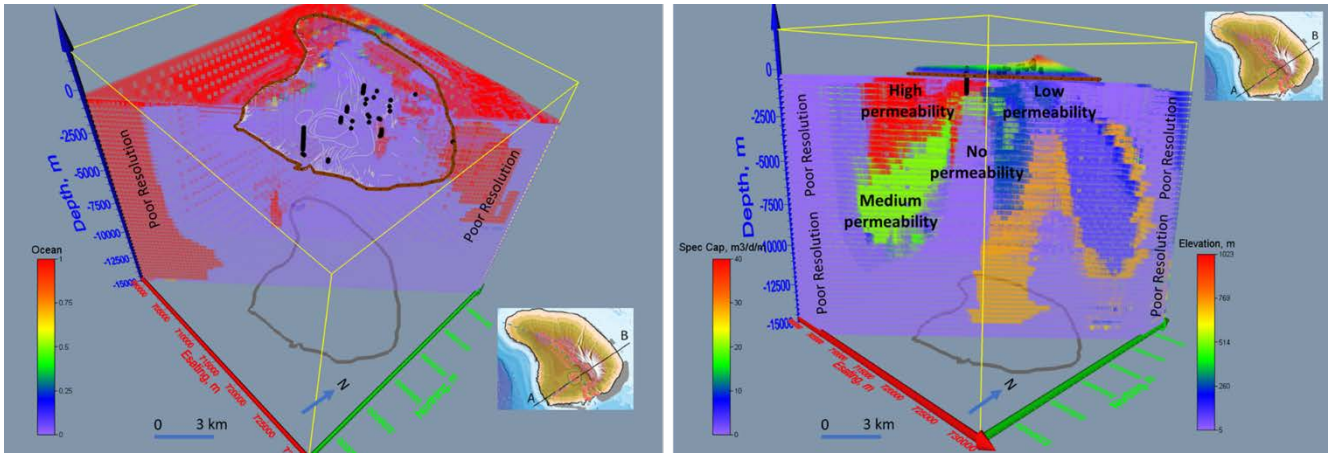

Figure 35. Predicted features sliced horizontally at sea level and vertically along cross section A-B: (left) 3D ocean character (present/absent), (right) specific capacity (permeability analog). This figure reveals a trend where low specific capacity at the eastern boundary increases toward the west. This trend follows from an earlier discussion indicating that the most permeable basaltic rocks are located at the western edge of Lānaʻi. Well locations are black dots and regions annotated as poor resolution reflect limited field data available to inform the model.

The predicted spatial distribution of temperature is over the range of 5°C to 758°C as shown in Figure 36. The upper left panel reveals the plan view temperature distribution at sea level with the digital elevation model overlying the island. The deep ocean at the model boundary reveals the coldest temperatures of about 5°C. The upper right panel reveals the plan view temperature distribution at sea level with no digital elevation model. Noteworthy are the cool temperatures near 20°C (blue) in the region of highest elevation and warm temperatures near 65°C (orange) in and around the caldera region. The lower left panel interprets regions of downward groundwater recharge from the region of highest elevation and cool temperatures. There is likely upward convective transport from the 758°C source at the Moho through the inferred dike swarm and sill region of medium specific capacity (surrogate for permeability) toward the warm 65°C region near the deepest well. The region directly below this well and adjacent to the inferred region of convective transport is predicted to have no specific capacity (no permeability), thereby supporting plausible convective transport through the more permeable region with conductive heat transfer away from the convective heat transport pathway. The lower right panel identifies two geothermal prospects. The first geothermal prospect has predicted temperatures of about 65°C to 108°C and is located between 1 and 2 km depth in the vicinity of the caldera. The second and preferred geothermal prospect has predicted temperatures of about 149°C to 275°C, located between 3 and 6 km depths in the vicinity of the western dike swarm and sill.

The predicted spatial distribution of chloride concentration sliced horizontally at sea level and vertically along A-B is shown in Figure 37. The left linear concentration plot spans 23 mg/l (freshwater or no water) to 18,000 mg/l (ocean water). The log chloride concentration plot on the right reveals heterogeneous water types that include freshwater, brackish water, and saline water. Two potential freshwater resource zones are indicated with circles. These freshwater resource zones have similar specific capacity but the zone to the west (closer to the caldera) has elevated temperatures, whereas the zone to the east has cooler temperatures. Figure 38 shows a conceptual groundwater system based on chloride concentration, geology, and temperature predictions. Two potential freshwater resources are present. The resources have similar permeability, but the zone to

the west (closer to the caldera) has elevated temperatures, whereas the zone to the east has cooler temperatures.

2.3.3.1.3 Feature Clustering

The joint interpretation of information across the MSOM network involves applying stochastic k-means clustering. We consider the mode of k-means clusters as the best way to aggregate information. The clustering of similar information at various locations characterizes the variability of parameters associated with these GSUs. The distribution of GSUs mapped along the cross-section A-B on Lānaʻi reveal five basic groups, shown in Figure 39: (1) ocean (purple), (2) salinized subaerial basalt (blue), (3) subaerial basalt, called basalt (green), (4) basalt-dike transition, called dike + basalt (orange red), and (5) basalt and dike, called dike (red). Each GSU is characterized by univariate and spatial statistics that describe the physical and chemical properties comprising the geothermal model (Table 4). Other interpreted features include possible underplating and possibly the Moho at a depth of ~13 km (Leahy et al. 2010).

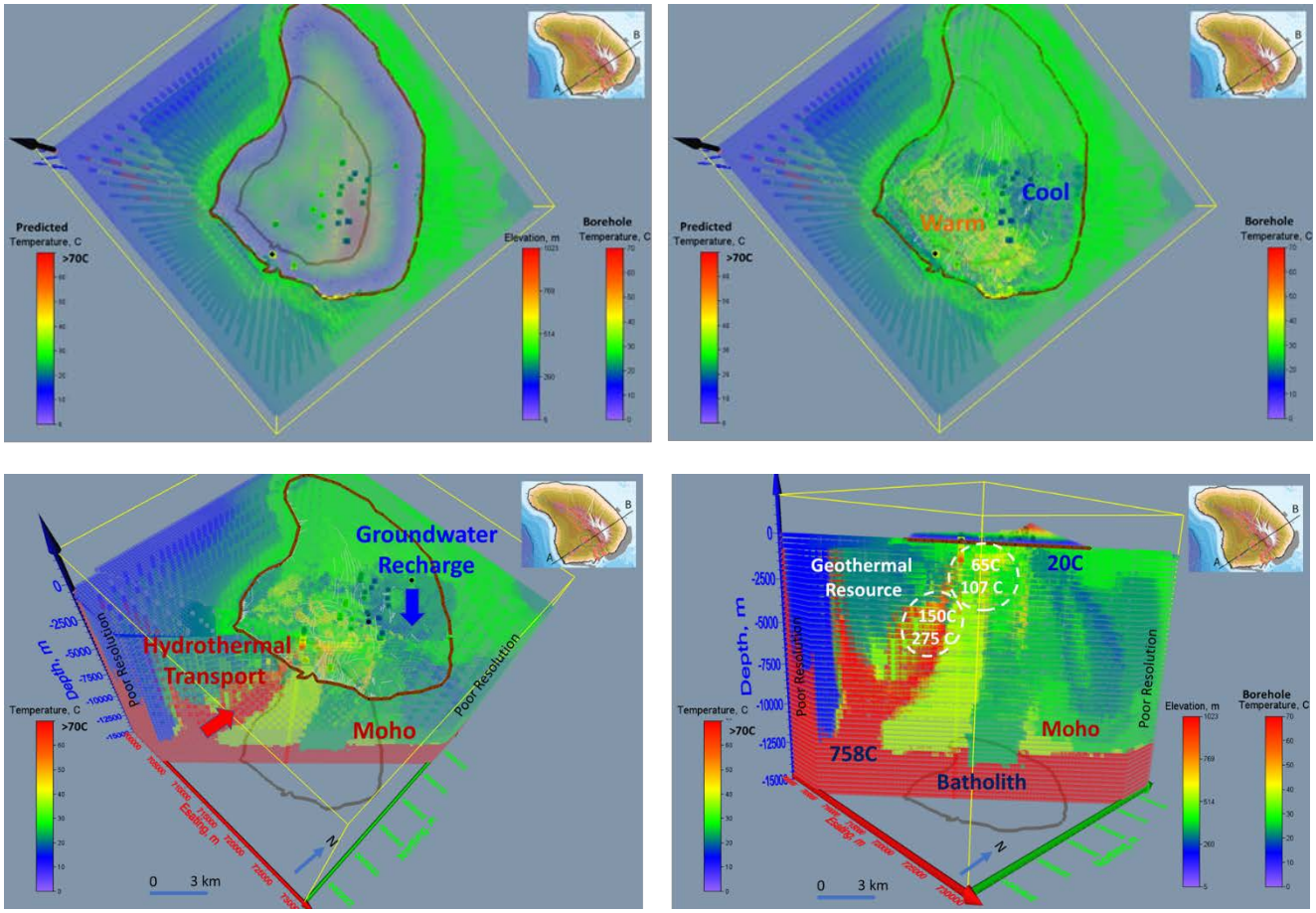

Figure 36. Predicted temperature over the range of 20° to 758°C. Upper left: plan view temperature distribution at sea level with the digital elevation model. Upper right: plan view temperature distribution at sea level with no digital elevation model (lower left). Noteworthy are the cool temperatures (blue) attributed to recharge at high elevation and warm temperatures in and around the caldera region. Lower left: interpreted regions of groundwater recharge from the region of highest elevation and hydrothermal transport from the region below the Moho. Lower right: two prospective geothermal resources. The first is about 65°C to 107°C between 1 and 2 km depth in the vicinity of the caldera. The second is about 149°C to 275°C between 3 and 6km in the vicinity of the western dike swarm and sill. Regions of poor resolution reflect limited field data available to inform the model.

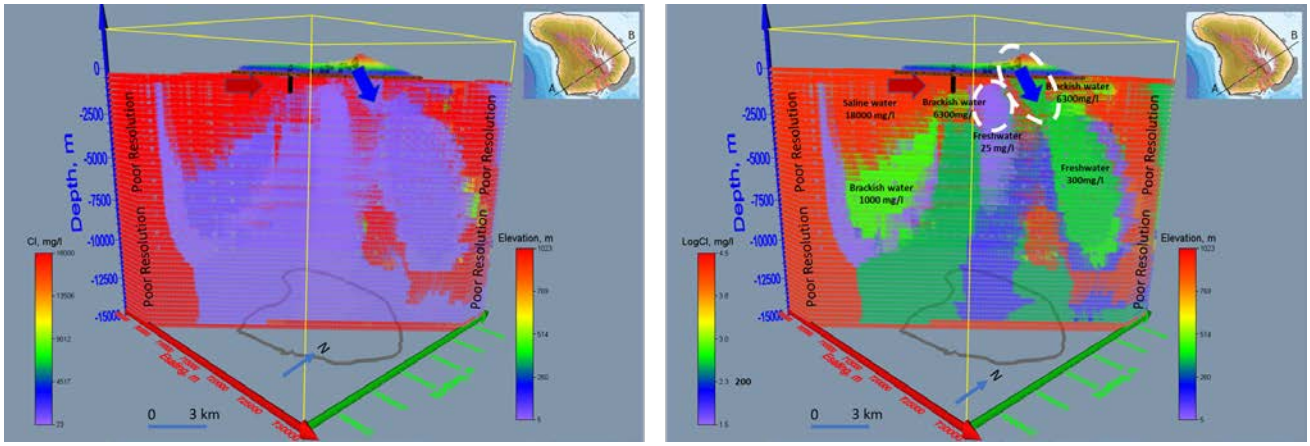

Figure 37. Predicted chloride concentration sliced horizontally at sea level and vertically along cross section A-B. Left: linear concentration plot (23 mg/l (freshwater or no water) to 18,000 mg/l (seawater). Right: log chloride concentration plot showing heterogeneous water types that include freshwater, brackish water, and saline water. Two potential freshwater resources are outlined by white circles. The resources have similar permeability but the zone to the west (closer to the caldera) has elevated temperatures, whereas the zone to the east has cooler temperatures.

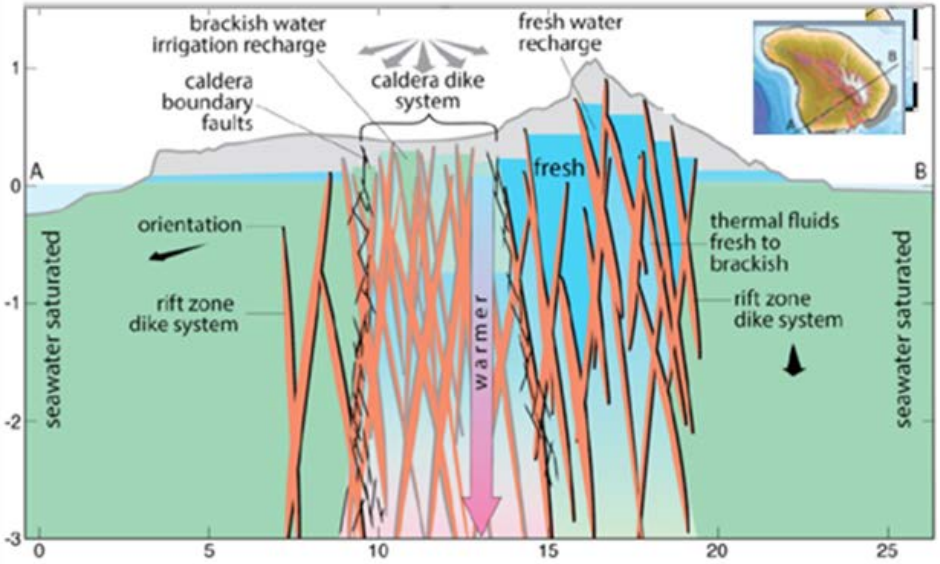

Figure 38. Conceptual model which agrees with MML predictions of continuous features along cross-section A-B.

Source: Lautze and Thomas (2022; in review)

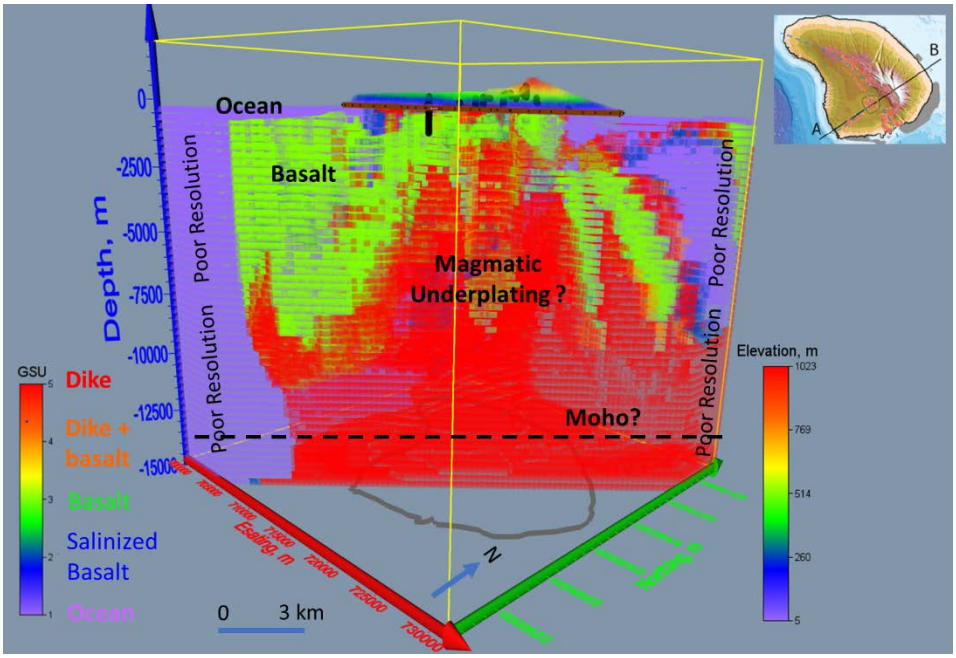

Figure 39. Predicted 3D GSUs sliced horizontally at sea level and vertically along A-B reveal five basic groups: (1) ocean (purple); (2) salinized subaerial basalt (blue); (3) subaerial basalt, called "basalt" (green); (4) submarine basalt-dike transition called dike-basalt (orange); and (5) submarine basalt and dikes, called "dike" (red). Each GSU is characterized by univariate and spatial statistics describing all the physical and chemical properties comprising the model (Table 4). Well locations appear as black dots. Other interpreted features include magmatic underplating and Moho (Leahy et al. 2010).

Table 4. Summary Statistics for Selected Properties Associated With Geothermal Stratigraphic Units

Group		Summary	Location			Water	Geology		State Variables			Physical properties			Aqueous properties		
GSU	Description	Statistic	Easting, m	Northing, m	Elev, m	Ocean	Dike	Basalt	Head, m	Temp, C	Cl, mg/l	SpeCap, m3/d/m	Density, kg/m3	Res, ohm-m	Cond, uM/s	ORP, mv	pH
1	Ocean	minimum	698886	2286203	-14745	1.00	0.00	0.00	0.0	4.0	16593	0.0	1020	0.1	0	51.9	8.00
		average	712723	2300699	-2042	1.00	0.00	0.00	0.0	58.0	17999	0.0	1325	119	47961	111.3	8.00
		median	709822	2299659	-319	1.00	0.00	0.00	0.0	24.4	18000	0.0	1020	0	48000	88.5	8.00
		maximum	730986	2318303	2055	1.00	0.01	0.01	0.1	758.0	18000	0.0	2960	3628	48000	283.1	8.00
		Standard deviation	10501	10412	3955	0.00	0.00	0.00	0.0	157.0	21	0.0	645	353	1267	55.0	0.00
2	Salanized basalt and dikes	minimum	700086	2286803	-14745	0.00	0.00	0.00	0.0	19.8	164	0.0	1020	0.1	0	52.1	7.95
		average	713052	2306872	-1822	0.45	0.29	0.25	10.6	49.9	17611	0.0	2062	60	46523	112.3	8.00
		median	711256	2309303	-945	0.36	0.03	0.00	0.0	26.8	18000	0.0	2515	2	48000	88.5	8.00
		maximum	730986	2318303	2055	0.98	1.00	1.00	465.1	758.0	18000	7.3	2948	3818	48000	283.1	8.00
		Standard deviation	8740	8012	3216	0.39	0.39	0.38	59.6	130.0	2102	0.3	716	319	7339	58.9	0.00
3	Basalt	minimum	700756	2287403	-11445	0.00	0.00	0.01	0.0	18.9	23	0.9	2478	4	0	52.1	7.14
		average	714600	2300283	-3573	0.00	0.01	0.99	42.9	29.5	5901	19.6	2717	445	1365	150.9	7.87
		median	713886	2298203	-2145	0.00	0.00	1.00	0.9	28.1	708	20.0	2703	233	166	196.2	7.90
		maximum	730986	2318303	855	0.00	0.99	1.00	484.2	73.0	18000	41.0	3011	4424	48000	283.1	8.00
		Standard deviation	7806	7622	3165	0.00	0.10	0.10	95.4	10.1	8072	13.3	96	516	6207	54.8	0.13
4	Dikes and Basalt	minimum	702786	2290103	-10245	0.00	0.00	0.00	0.0	18.9	31	1.4	2614	3	0	52.1	7.14
		average	723764	2298945	-3448	0.00	0.53	0.47	263.8	28.1	7623	25.1	2769	244	856	151.7	7.86
		median	724986	2298803	-2445	0.00	0.57	0.43	224.0	24.5	400	29.0	2747	34	167	196.2	7.91
		maximum	730986	2318303	306	0.25	0.99	0.99	484.3	46.0	18000	41.0	3048	4933	22370	227.4	8.00
		Standard deviation	5428	5197	2537	0.02	0.41	0.41	172.7	9.2	8823	14.9	92	603	1558	58.2	0.20
5	Dikes	minimum	698886	2286503	-14745	0.00	0.00	0.00	0.0	18.9	23	0.0	1020	0.1	0	52.1	7.14
		average	717025	2304238	-7022	0.00	0.83	0.17	229.3	182.3	6416	4.7	2768	748	14322	153.7	7.79
		median	717186	2304259	-7245	0.00	1.00	0.00	246.3	26.8	543	0.0	2807	237	2036	135.3	8.00
		maximum	730986	2318303	2055	0.80	1.00	1.00	485.6	758.0	18000	41.0	3055	8066	48000	283.1	8.00
		Standard deviation	7819	8007	4903	0.01	0.37	0.37	179.8	297.8	8376	8.9	262	1166	20843	58.2	0.34

Group		Summary	Location			Water	Geology		Aqueous chemistry										
GSU	Description	Statistic	Easting, m	Northing, m	Elev, m	Ocean	Dike	Basalt	HCO3, mg/l	NO3, mg/l	PO4, mg/l	SO4, mg/l	Br, mg/l	F, mg/l	Fe, mg/l	K, mg/l	Na, mg/l	Si, mg/l	Sr, mg/l	Ca/Mg
1	Ocean	minimum	698886	2286203	-14745	1.00	0.00	0.00	139.0	0.70	0.10	2.65	60.97	1.38	0.02	357.1	9200	1.0	0.02	0.31
		average	712723	2300699	-2042	1.00	0.00	0.00	140.0	0.70	0.10	2.65	64.00	1.40	0.02	380.0	10000	1.0	1.04	0.31
		median	709822	2299659	-319	1.00	0.00	0.00	140.0	0.70	0.10	2.65	64.00	1.40	0.02	380.0	10000	1.0	0.38	0.31
		maximum	730986	2318303	2055	1.00	0.01	0.01	140.0	0.70	0.12	2.67	64.00	1.40	0.02	380.0	10000	1.1	2.66	0.32
		Standard deviation	10501	10412	3955	0.00	0.00	0.00	0.0	0.00	0.00	0.00	0.04	0.00	0.00	0.3	11	0.0	1.11	0.00
2	Salanized basalt and dikes	minimum	700086	2286803	-14745	0.00	0.00	0.00	103.6	0.62	0.10	2.65	7.51	0.59	0.01	27.4	311	1.0	0.04	0.31
		average	713052	2306872	-1822	0.45	0.29	0.25	139.8	0.70	0.10	2.65	63.19	1.40	0.02	376.8	9896	1.0	0.74	0.32
		median	711256	2309303	-945	0.36	0.03	0.00	140.0	0.70	0.10	2.65	64.00	1.40	0.02	380.0	10000	1.0	0.34	0.31
		maximum	730986	2318303	2055	0.98	1.00	1.00	140.0	0.72	1.51	3.81	64.00	1.40	0.02	380.0	10000	27.9	2.60	0.67
		Standard deviation	8740	8012	3216	0.39	0.39	0.38	1.7	0.00	0.05	0.05	4.70	0.04	0.00	22.8	713	0.9	0.84	0.01
3	Basalt	minimum	700756	2287403	-11445	0.00	0.00	0.01	52.5	0.48	0.00	2.65	0.06	0.00	0.00	1.9	16	1.0	0.04	0.31
		average	714600	2300283	-3573	0.00	0.01	0.99	84.9	1.69	2.25	27.11	3.78	0.11	0.17	22.6	526	1078	0.21	1.05
		median	713886	2298203	-2145	0.00	0.00	1.00	83.0	0.64	2.58	6.40	0.14	0.04	0.00	2.7	23	880	0.06	1.13
		maximum	730986	2318303	855	0.00	0.99	1.00	146.4	4.24	4.84	151.20	64.00	1.40	0.78	380.0	10000	1650	0.74	1.22
		Standard deviation	7806	7622	3165	0.00	0.10	0.10	25.9	1.63	2.12	33.57	13.69	0.30	0.31	80.8	2135	418	0.17	0.21
4	Dikes and Basalt	minimum	702786	2290103	-10245	0.00	0.00	0.00	52.5	0.48	0.00	2.65	0.06	0.00	0.00	1.9	16	1.0	0.04	0.31
		average	723764	2298945	-3448	0.00	0.53	0.47	71.5	0.90	2.05	11.49	0.65	0.04	0.06	4.7	74	1037	0.23	1.08
		median	724986	2298803	-2445	0.00	0.57	0.43	83.0	0.64	2.58	7.20	0.14	0.04	0.00	2.1	22	1130	0.38	1.13
		maximum	730986	2318303	306	0.25	0.99	0.99	142.8	4.26	3.87	76.00	64.00	1.40	0.78	380.0	10000	1650	0.74	1.22
		Standard deviation	5428	5197	2537	0.02	0.41	0.41	16.9	0.97	1.76	18.53	4.49	0.11	0.21	26.0	677	259.4	0.16	0.15
5	Dikes	minimum	698886	2286503	-14745	0.00	0.00	0.00	52.5	0.48	0.00	2.65	0.06	0.00	0.00	1.9	16	1.0	0.04	0.31
		average	717025	2304238	-7022	0.00	0.83	0.17	122.2	2.19	1.64	26.37	24.25	0.71	0.07	186.0	4842	645	0.57	0.66
		median	717186	2304259	-7245	0.00	1.00	0.00	140.0	0.70	0.10	6.40	1.88	0.13	0.02	12.7	127	842	0.38	0.84
		maximum	730986	2318303	2055	0.80	1.00	1.00	146.4	7.59	5.81	151.20	64.00	1.40	0.78	380.0	10000	1650	2.61	1.22
		Standard deviation	7819	8007	4903	0.01	0.37	0.37	26.5	2.56	2.31	38.14	29.35	0.67	0.20	186.8	4961	654	0.79	0.35

Location: Elev = elevation (m). State variables: Head = hydraulic head (m), cl = chloride concentration (mg/l), Temp = temperature (°C). Physical properties: Res = electrical resistivity (ohm-m), SpecCap = specific capacity, (m3/d/m). Aqueous properties: Cond = specific conductance, uM/s, ORP = oxygen reduction potential (mv) Aqueous chemistry: Br = bromide, F = flouride, Fe = iron, HCO3 = bicarbonate (mg/l), K = potassium, Na = sodium, NO3 = nitrate (mg/l), PO4 = phosphate (mg/l), Si = silica, SO4 = sulfate, Sr = strontium, Ca/Mg = calcium-magnesium ratio.

2.3.3.2 Island of Hawai‘i

2.3.3.2.1 Feature Selection

The feature selection process undertaken using learn heuristics (wrapper method) is constrained by the state variable temperature (Jerran et al. 2019; Stolper, DePaolo, and Thomans 2009; Sorey and Colvard 1994; PGV 1991; State of Hawai‘i 1990; Kihara et al. 1977; Kingston, Reynolds, Thom & Allardice Ltd. 1976) shown in the purple box in Table 5. Informative features appearing in the green box are determined to be associated with geology (e.g., various fault systems and basalt, oceanic crust, underplating, and mantle layering) and geophysical properties (e.g., density, resistivity, p-wave and s-wave velocity, and earthquake magnitudes). The following sections cover three parts: (1) local assimilation and prediction; (2) regional feature assimilation and prediction; and (3) island-wide assimilation and prediction.

Of the original predictor variables available for consideration (N = 36), the learn-heuristic based feature selection process identified an optimal set of global variables (N=21) suitable for predicting features beneath the island of Hawai‘i (Table 5). These numeric and categorical features are used in constructing, training, and testing the MML models. Twenty numeric features that appear informative to the state variable (temperature) include location (easting, northing, elevation), and geophysical properties (density, resistivity, p-wave velocity, s-wave velocity, and earthquake magnitude). Categorical features that appear informative to the state variable (temperature) include geology (Hilina, Kahuku, Kaoiki, Kealakehua, Kohala, and Koae fault systems; Kilauea and Mauna Loa rifts [Lipman, Rhodes, and Dalrymple 1990, Wolfe and Morris 1996; Trusdell, Wolfe, and Morris 2006]; and basalt, oceanic crust, and mantle layers [Leahy et al. 2010]). Unlike the Lāna‘i study, no aqueous properties, aqueous chemistry, or stable isotopes were included during Phase 1 of this study.

Table 5. Summary of Features Deemed Informative Using the Learn Heuristics Approach Constrained to the State Variables Temperature (°C) in Three Categories: Location, Geology, and Geophysical Properties

Constraints on learn heuristics

Informative features

		Type		Observation		Support	Location		
Category	Features	Deterministic	Stochastic	Measured	Derived	Point-1D	Borehole	Surface	Source
Location	Easting, m	X		X		X			
	Northing, m	X		X		X			
	Elevation, m	X		X		X			
State variable	Temperature, C	X		X	X	X			Lautze et al., 2020; Putrikia, 1997
Geology	Hilina Fault	X		X		X			Lipman et al., 1990;
	Kahuku Fault	X		X		X			Wolfe and Morris, 1996;
	Kaoiki Fault	X		X		X			Trusdell et al., 2006
	Kealakekua Fault	X		X		X			
		X		X		X			
	Koae Fault	X		X		X			
	Kohala Fault	X		X		X			
	Kilauea Rift	X		X		X			
	Mauna Loa Rift								
	Basalt Layer	X			X	X			Leahy et al., 2010
	Oceanic Crust	X			X	X			Leahy et al., 2010
	Under plating	X			X	X			Leahy et al., 2010
	Mantle	X			X	X			Leahy et al., 2010
Physical properties	Density, kg/m3	X			X	X			Lautze et al., 2020
	Resistivity, ohm-m	X	X		X	X	X	X	Lautze et al., 2020
	P-wave velocity, km/s	X			X	X		X	Lautze et al., 2020
	S-wave velocity, km/s	X			X	X		X	Lautze et al., 2020
	Vp/Vs	X							
	Earthquake, magnitude	X				X		X	Lautze, et al., 2020

Prior to training, we normalized the elevations (spanning depths from 4.1 to -40 km) to produce a vector of values spanning the range of 0 to 1. The remaining numeric features are normalized by their data variance and randomly assigned (presenting the input vectors to the map sequentially using a randomly sorted database) as an initial set of map weight vectors. Application of the

MSOM network to training data is done using a single fixed number of neurons and topological relations which differ for each model and appear in the following sections: local assimilation and feature prediction (simple), regional assimilation and feature prediction (intermediate in complexity), and island-wide assimilation and feature prediction, briefly described next.

2.3.3.2.2 Local Assimilation and Feature Prediction

In this section, we present local (separate) feature assimilation and prediction results for the Saddle Road and LERZ areas. The aim is to assess the quality of sparse measurements to inform local predictions. The objectives are to: (1) predict Saddle Road resistivity at MT/AMT stations (blue) and boreholes (yellow); and (2) predict temperature at LERZ (right) boreholes (yellow).

At Saddle Road, the resistivity model is developed using location (easting, northing, elevation), density, and resistivity (deterministic layered earth inversions to 40 km depth performed by personnel at UH, and stochastic layered earth inversions to 3 km depth conducted by personnel at PNNL; see Section 3). The MSOM shape (26 rows by 20 columns) is a toroid (wraps from top to bottom and side to side) with hexagonal neurons. Training of the map is conducted using both rough and fine phases. The rough training phase involved 20 iterations using a Gaussian neighborhood with an initial and final radius of 33 units and 9 units, respectively; and the fine training involved 400 iterations using a Gaussian neighborhood with an initial and final radius of 9 units and 1 unit, respectively. The initial and final learning rates of 0.5 and 0.05 decay linearly down to 10^{-5}, and the Gaussian neighborhood function decreases exponentially from a decay rate of 10^{-1} iteration to 10^{-3}, providing reasonable convergence, as evidenced by similarity in their low quantization (q_e=0.21) and topographic (t_e=0.145) errors.

Figure 40 presents log-resistivity prediction results for station 12PT. This figure presents: (a) the location map highlighting resistivity station 12PT; (b) observed (deterministically inverted 1D layer earth resistivity values) and predicted resistivity values (minimum, median, and maximum values determined using 30 trials and a leave-one-out cross-validation strategy); (c) a plot of the deterministic log resistivity (LogRho) versus median stochastic log resistivity (LogQ50); and (d) prominent resistive and conductive features from the surface to 40 km based on the deterministic inversion. We note a slight bias in the prediction of resistivity associated with conductive zones, suggesting the potential need to increase the number of model trials, increase the network size, and/or add additional features to better constrain the prediction. The strong correlation coefficient (0.92) between LogRho (UH resistivity values to depths of 40 km) and median LogQ50 (PNNL resistivity values to 3 km) supports the ability to assimilate shallow, higher-frequency resistivity information with deeper, lower-frequency resistivity information (Figure 40c).

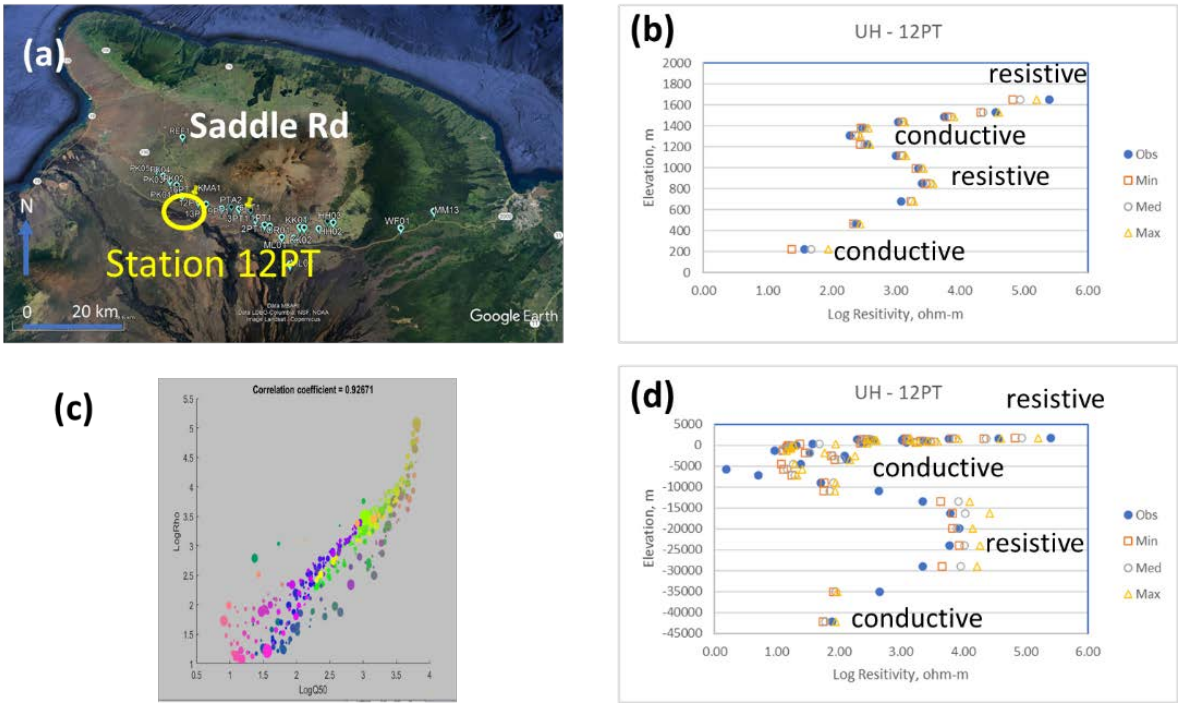

Figure 40. Predicted Saddle Road 1D resistivity features: (a) The location map highlighting resistivity station 12PT. (b) Observed and predicted resistivity values at station 12PT. (c) Plot of the deterministic log resistivity (LogRho) versus median stochastic log resistivity (LogQ50). (d) Prominent resistive and conductive features from the surface to 40 km based on the deterministic inversion.

The LERZ temperature model utilizes location information (easting, northing, and elevation) and sparse temperatures from geothermal wells across the area. In this regard, the MML workflow functions as a nonlinear multivariate 3D interpolator. The neural map shape (22 rows by 16 columns) is a toroid (wraps from top to bottom and side to side) with hexagonal neurons. Training of the map used both rough and fine phases. The rough training phase involved 20 iterations using a Gaussian neighborhood with an initial and final radius of 28 units and 7 units, respectively. The fine training involved 400 iterations using a Gaussian neighborhood with an initial and final radius of 7 units and 1 unit, respectively. The initial and final learning rates of 0.5 and 0.05 decayed linearly down to 10^{-5}, and the Gaussian neighborhood function decreased exponentially from a decay rate of 10^{-1} iteration to 10^{-3}, providing reasonable convergence, as evidenced by similarity in their low quantization (q_e=0.10) and topographic (t_e=0.14) errors (Figure 41).

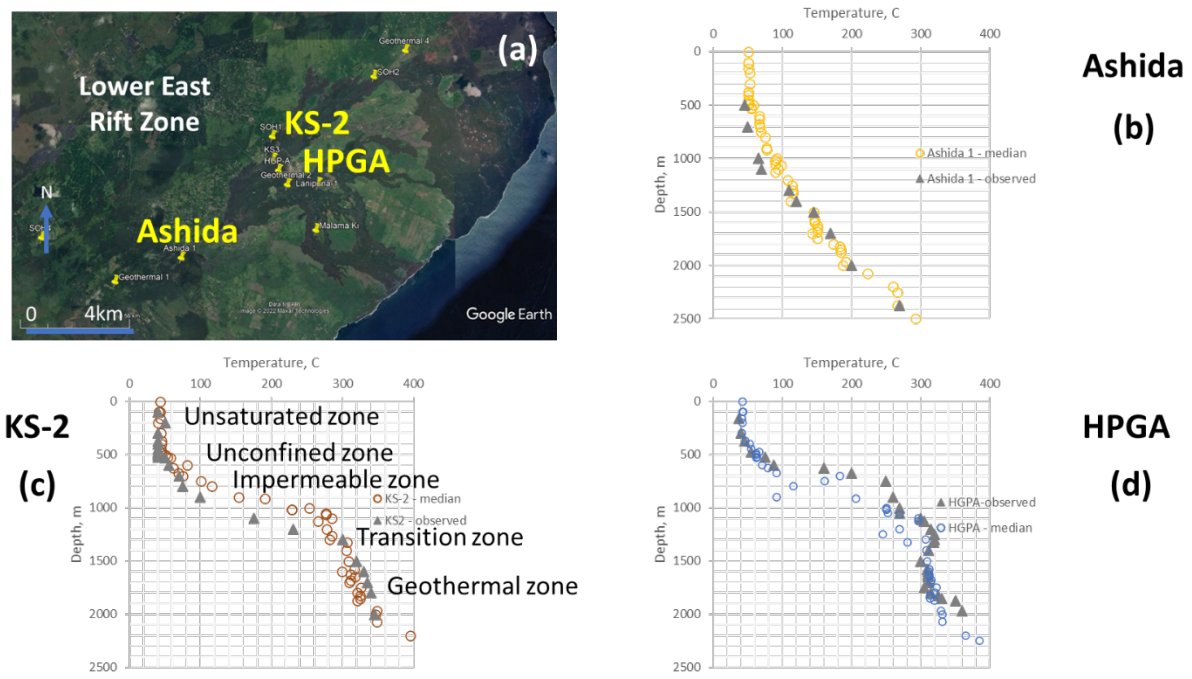

Figure 41. Predicted LERZ temperature predictions: (a) Location map for three geothermal wells (yellow): Ashida, KS-2, and HPGA. (b) Observed and median prediction temperatures at the Ashida well. (c) Observed and median prediction temperatures at the KS-2 well. (d) Observed and median prediction temperatures at the HPGA well. The observed temperatures appear as triangles and median predictions appear as circles. The median prediction values are computed following 30 random trials using a leave-one-out cross-validation strategy. The KS-2 temperature profile is interpreted as having five zones: unsaturated, unconfined, impermeable, transition, and geothermal. Similar zonation can be identified in the HPGA well but not in the Ashida well.

Figure 41 shows comparative temperature profiles for three geothermal wells in the LERZ. The location map (Figure 41a) shows the wells, and the other subfigures present the measured and predicted temperature profiles for (b) Ashida, (c) KS-2, and (d) HPGA geothermal wells. Triangles mark observed temperatures, and circles designate median predictions. The median prediction values are computed following 30 trials using a leave-one-out cross-validation strategy. In general, the observations and median prediction values correspond at these geothermal wells. Note that these plots appear in order of increasing thermal complexity despite their proximity (less than 3 km separation). Of these profiles, the KS-2 temperature plot characterizes well-defined hydrologic zones that are classified as unsaturated, unconfined, impermeable, transition, and geothermal. These classes might provide an additional set of categorical constraints in future studies with the aim of identifying hidden groundwater resources. Other available categorical measurements available to constrain feature predictions include subsurface geologic information, such as subaerial, shallow marine, transition, and deep marine environments (Campbell and Gardner 1981).

2.3.3.2.3 Regional Assimilation and Prediction

This section presents regional feature assimilation and prediction results using combined data from the Saddle Road, Kilauea, and LERZ areas. The aim is to identify potential 2D hidden geothermal resources, 2D lithospheric flexure under volcanic loading, and 2D geologic layering. The objectives are twofold: (1) predict geophysical (numeric) features (e.g., temperature, density, resistivity, Vp, and Vp/Vs ratio); and (2) predict geologic (categorical) features (e.g., velocity layers basalt, crust, underplating, and mantle).

The regional model developed herein incorporates information from these numeric and categorical features. The map shape (72 rows by 66 columns) is a toroid (wraps from top to bottom and side to side) with hexagonal neurons. Training of the map was conducted using both rough and fine phases. The rough training phase involved 20 iterations using a Gaussian neighborhood with an initial and final radius of 98 units and 25 units, respectively. The fine training involved 400 iterations using a Gaussian neighborhood with an initial and final radius of 25 units and 1 unit, respectively. The initial and final learning rates of 0.5 and 0.05 decayed linearly down to 10^{-5}, and the Gaussian neighborhood function decreased exponentially from a decay rate of 10^{-1} iteration to 10^{-3}, providing reasonable convergence as evidenced by their reasonably low quantization (q_e=0.053) and topographic (t_e=0.34) errors. Given that all three split sets (folds 1, 2, and 3) have similar error vectors, future studies might consider increasing the network size to reduce the topographic error vector (the proportion of all data vectors for which first and second best-matching units [BMUs] are not adjacent units) to the same magnitude as the quantization error (the average distance between each data vector and its BMU is a measure of map resolution). This approach has been shown by Friedel et al. (2020) to reduce uncertainty and bias, thereby improving feature predictions.

The component planes plot, shown in Figure 42, presents the converged weights for the first 20% subsample (fold-1) of records across the MSOM network by numeric (location: easting, northing, elevation), state variable (temperature), geophysical (density, log resistivity, V_P, V_P/V_S, and earthquake magnitude) and categorical (fault systems: Hilina, Kahuku, Kaoiki, Kealakekua, Koae, and Kohala; rifts: Kilauea and Mauna Loa; and geologic layers: basalt, oceanic crust, underplating, and mantle) properties. Similar pattern and colors imply high spatial correlation (e.g., temperature and V_P), whereas the same pattern with opposite colors implies high negative spatial correlation (e.g., temperature and elevation). Variations among feature weights with the state variable is preferable to highly correlated features which would increase the non-uniqueness in predictions and therefore uncertainty.

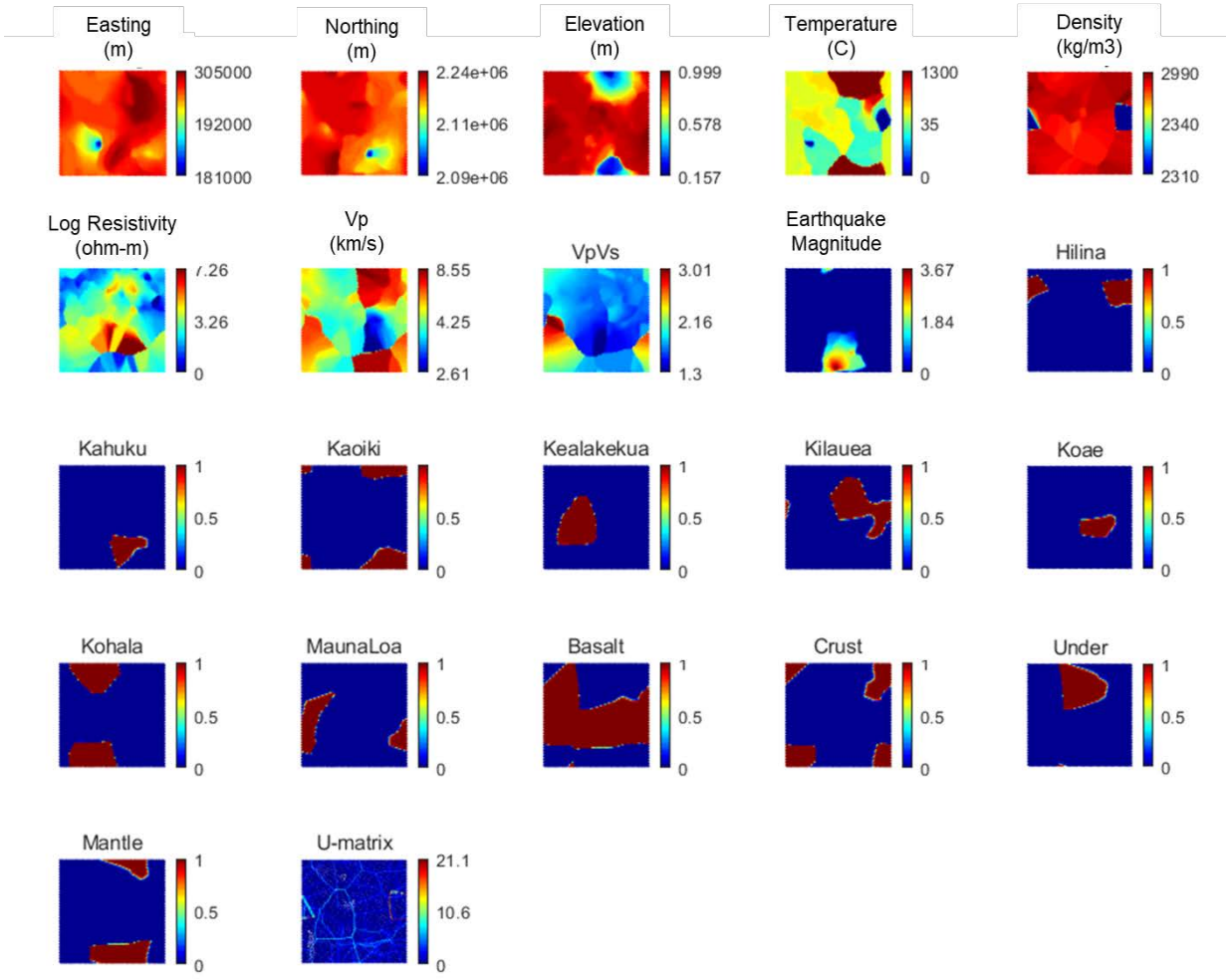

Figure 42. Component planes plot shows the converged weights of the first 20% subsample (fold-1) of records across the MSOM network by numeric (location: easting, northing, elevation), state variable (temperature), geophysical (density, log resistivity, V_P, V_P/V_S, and earthquake magnitude), and categorical (fault systems: Hilina, Kahuku, Kaoiki, Kealakekua, Kilauea, Koae, Kohala, Mauna Loa; and geologic layers: basalt, oceanic crust, underplating, and mantle) properties.

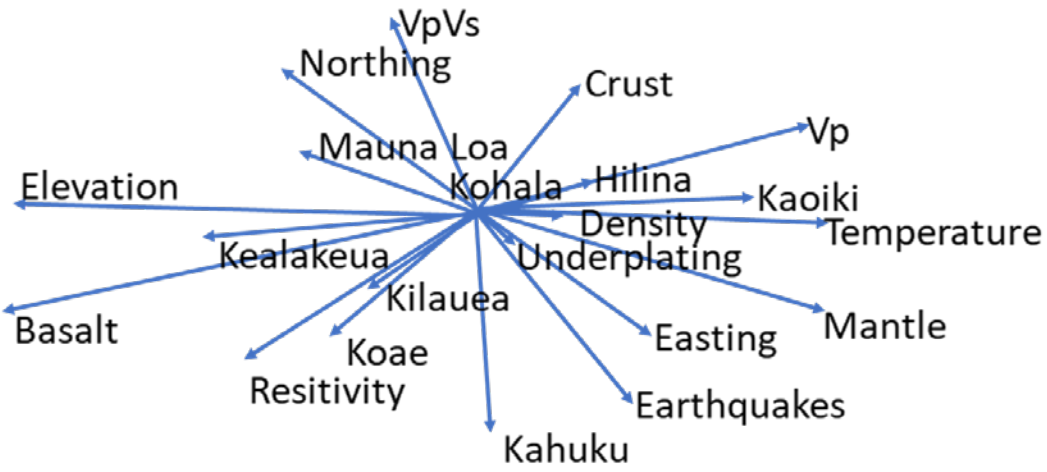

Figure 43. Principal component planes projection of median feature weight vectors (Vesanto 1999) following the fold-1 split. Features on opposite sides of the plat are anticorrelated, whereas the features that group together are more likely to be positively related.

Testing and validation of the trained MSOM model are reflective of the three split sets previously discussed, where each k-fold represents a random sampling of shuffled records split (80/20) from the original data set. Table 6 provides summary statistics, following independent testing, for predicted temperature, density, resistivity, p-wave velocity, and s-wave velocity. For the sake of brevity, we present cross-plots and their associated R^2 values for temperature for each fold in Figure 44 and Table 7. In these figures, the independent observations appear along the horizontal axis, and predicted observations along the vertical axis. The high R^2 values provided in the table for each fold suggest that the model generalizes well when presented with independent data. Note that in contrast to the Lānaʻi study, the metrics for temperature predictions reflect those *measured* in the upper 3 km, and those *applied* as a linear boundary condition (based on regressed temperature values determined using thermobarometry (Putrika 1997) at depths from 20 to 40 km.

In addition to statistical summaries for the independent testing of numeric features, we provide tables of kappa statistics for the independent testing of categorical features (Table 8). These tables present kappa statistics that reveal a reasonably high level of independent model performance when predicting categorical k-fold layer features such basalt, oceanic crust, magmatic underplating, and mantle for three different folds (subsample splits). In general, the independent model layer predictions range from moderate to almost perfect across the three independent split sets (folds).

Table 6. Summary Statistics Following Independent Testing of Selected Features Predicted Using the Trained Machine Learning Network. Each K-Fold Reflects a Random Sampling of Shuffled Records Split (80/20) From Original Data Set.

Fold-1	Statistic									
Feature	N	N*	Mean	SE Mean	StDev	Minimum	Q1	Median	Q3	Maximum
Temperature Observed, C	3960	14235	232	6.32	398	17.2	63.9	71.5	98.8	1301
Temperature Predicted, C	18195	0	188	2.58	348	14.9	59.1	72.9	101.7	1299
Density Observed, kg/m3	223	17972	2690	4.92	73.5	2499	2637	2678	2747	2993
Density Predicted, kg/m3	18195	0	2650	0.86	116	2314	2628	2659	2718	3012
Log Resisitivity Observed, ohm-m	412	17783	2.54	0.06	1.17	-0.80	1.65	2.43	3.37	6.87
Log Resisitivity Predicted, ohm-m	18195	0	2.65	0.01	1.14	-0.68	2.17	2.55	3.05	7.64
Vp Observed, km/s	3453	14742	4.90	0.02	1.24	2.69	4.04	4.43	5.25	8.60
Vp Predicted, km/s	18195	0	4.79	0.01	1.30	2.67	4.04	4.33	5.13	8.46
Vs Observed, km/s	3451	14744	2.67	0.01	0.75	1.53	2.29	2.39	2.52	4.90
Vs Predicted, km/s	18195	0	2.64	0.01	0.77	1.61	2.17	2.42	2.64	4.84

Fold-2	Statistic									
Feature	N	N*	Mean	SE Mean	StDev	Minimum	Q1	Median	Q3	Maximum
Temperature Observed, C	3857	14337	237	6.50	403.6	16.7	63.9	70.2	100.7	1301
Temperature Predicted, C	18195	0	260	3.16	426.7	15.2	63.0	74.0	100.8	1294
Density Observed, kg/m3	212	17872	2675	5.28	76.8	2467	2631	2658	2736	2857
Density Predicted, kg/m3	18195	0	2650	0.86	116.3	2314	2628	2659	2718	3012
Log Resisitivity Observed, ohm-m	356	17839	2.53	0.06	1.09	0.00	1.65	2.46	3.42	5.46
Log Resisitivity Predicted, ohm-m	18168	27	2.65	0.01	1.14	-0.68	2.17	2.55	3.04	7.64
Vp Observed, km/s	3397	14794	4.91	0.02	1.27	2.56	4.03	4.42	5.25	8.55
Vp Predicted, km/s	18195	0	4.79	0.01	1.30	2.67	4.04	4.33	5.13	8.46
Vs Observed, km/s	3393	14798	2.69	0.01	0.77	1.53	2.30	2.39	2.54	4.89
Vs Predicted, km/s	18195	0	2.64	0.01	0.77	1.61	2.17	2.42	2.64	4.84

Fold-3	Statistic									
Feature	N	N*	Mean	SE Mean	StDev	Minimum	Q1	Median	Q3	Maximum
Temperature Observed, C	3957	14238	228.5	6.27	394.7	17.2	63.5	69.9	98.6	1301
Temperature Predicted, C	18195	0	205.8	2.76	372.5	16.7	62.5	69.1	98.9	1299
Density Observed, kg/m3	211	17984	2683	5.24	76.10	2495	2629	2663	2749	2975
Density Predicted, kg/m3	18195	0	2669	0.87	117.9	2314	2641	2698	2737	2998
Log Resisitivity Observed, ohm-m	399	17796	2.58	0.06	1.18	-0.62	1.66	2.49	3.42	6.87
Log Resisitivity Predicted, ohm-m	18195	0	2.92	0.01	1.27	-0.17	2.23	2.82	3.41	7.71
Vp Observed, km/s	3476	14719	4.91	0.02	1.25	2.69	4.04	4.43	5.27	8.60
Vp Predicted, km/s	18195	0	4.80	0.01	1.27	2.58	4.07	4.38	5.34	8.48
Vs Observed, km/s	3472	14723	2.69	0.01	0.76	1.53	2.30	2.39	2.54	4.90
Vs Predicted, km/s	18195	0	2.65	0.01	0.73	1.59	2.26	2.39	2.69	4.85

Table 7. Summary of Independent Testing on Numeric Model Features Following Development of (80/20) Split Sets

Fold	Model	R-squared
1	Temperature, C	99.0%
	Density, kg/m3	100.0%
	Resistivity, ohm-m	83.1%
	P-wave velocity, km/s	99.1%
	S-wave velocity, km/s	99.1%

Fold	Model	R-squared
2	Temperature, C	99.8%
	Density, kg/m3	100.0%
	Resistivity, ohm-m	66.0%
	P-wave velocity, km/s	99.1%
	S-wave velocity, km/s	95.5%

Fold	Model	R-squared
3	Temperature, C	99.0%
	Density, kg/m3	100.0%
	Resistivity, ohm-m	98.9%
	P-wave velocity, km/s	99.1%
	S-wave velocity, km/s	99.3%

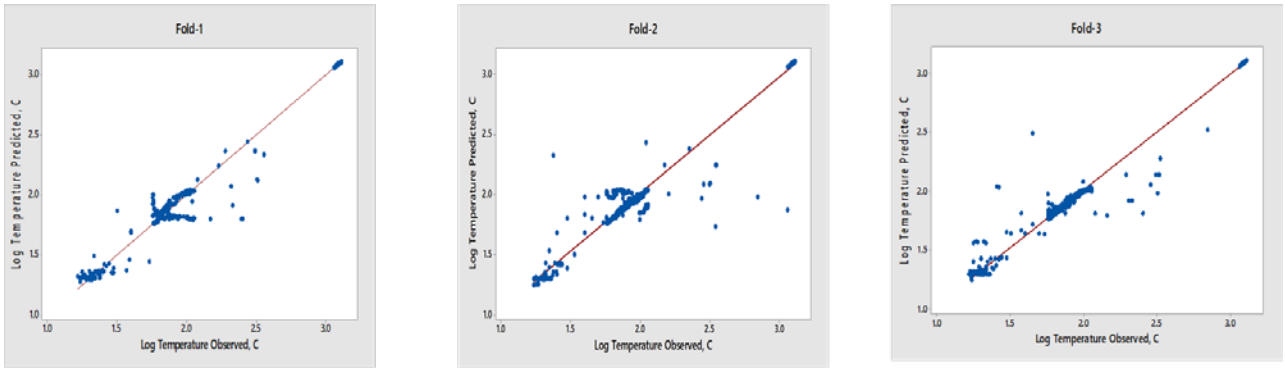

Figure 44. Cross-plots of temperature with observed (horizontal axis) and predicted (vertical axis) revealing good correspondence for each split set (fold).

Table 8. Kappa Statistics (Cohen 1960) When Using Machine Learning to Predict Subsurface Geologic Features

Geologic Feature	K-fold	Summary	Statistic	Performance
Basalt Layer	1	n	1498	
		Kappa	0.441	Moderate
		Accuracy	0.650	
	2	n	1498	
		Kappa	0.440	Moderate
		Accuracy	0.641	
	3	n	1498	
		Kappa	0.430	Moderate
		Accuracy	0.648	

Geologic Feature	K-fold	Summary	Statistic	Performance
Under plating	1	n	1498	
		Kappa	0.613	Substantial
		Accuracy	0.926	
	2	n	1498	
		Kappa	0.664	Substantial
		Accuracy	0.928	
	3	n	1498	
		Kappa	0.461	Moderate
		Accuracy	0.907	

Geologic Feature	K-fold	Summary	Statistic	Performance
Oceanic Crust	1	n	1498	
		Kappa	0.887	Almost perfect
		Accuracy	0.979	
	2	n	1498	
		Kappa	0.588	Moderate
		Accuracy	0.928	
	3	n	1498	
		Kappa	0.869	Almost perfect
		Accuracy	0.975	

Geologic Feature	K-fold	Summary	Statistic	Performance
Mantle	1	n	1498	
		Kappa	0.926	Almost perfect
		Accuracy	0.981	
	2	n	1498	
		Kappa	0.908	Almost perfect
		Accuracy	0.976	
	3	n	1498	
		Kappa	0.905	Almost perfect
		Accuracy	0.976	

Presence and absence of geologic features based on velocity model of Leahy et al. (1999)

Given that the testing results support the ability of MSOM to generalize to independent data, we use the algorithm to simultaneously predict regional numeric and categorical features across the Saddle Road, Kilauea, and LERZ areas. Figure 45 presents the set of numeric and categorial feature predictions as viewed from the north looking across the Saddle Road, Kilauea, and LERZ study areas. The numeric predictions include geophysical features (e.g., temperature, density, resistivity, V_P, and V_P/V_S ratio), with the aim of potentially identifying hidden geothermal resources, lithospheric flexure under volcanic loading, and geologic layering.

The temperature predictions indicate no near-surface high temperature geothermal resources below the Saddle Road profile (Figure 45a). In contrast, temperature predictions indicate localized high-temperature geothermal anomalies beneath the Kilauea and LERZ areas. While anomalous geothermal temperatures were known and exploited in the LERZ, use of the trained model might identify new drilling prospects there. In the next section, we consider whether geothermal resources might be identified across the whole island using a randomly located set of pseudo-boreholes (characterized by empty cells from the surface to 40 km depth) and surface points to develop quasi-3D subsurface images of these same features and various fault systems.

Other geophysical anomalies coincide with machine learning predictions at the Saddle Road, Kilauea, and LERZ areas. For example, notable medium-high density anomalies occur in the right half of the Saddle Road image from sea level to about 7 km depth (Figure 45b). Other medium-high density anomalies appear at deeper depths in the Kilauea and LERZ areas. In contrast, the Kilauea and LERZ areas reveal large lateral low-density anomalies from sea level to a depth of about 7 km and adjacent medium-high density densities to greater depths.

The predicted background resistivity across the study areas (Figure 45c) is intermediate in value (green in color), with heterogenous high and low resistivity anomalies superimposed from sea level to the model base. For example, one group of predicted medium-low resistivity anomalies occurs from sea level to about 3 km depth. Additional predicted medium-low resistivity anomalies occur below the Saddle Road at depths of about 4–8 km, below Kilauea at depths of 4–7 km, and at the western edge of the LERZ at depths of 7–12 km. The bottom of the last anomaly is adjacent to a medium-high resistivity anomaly that extends to about 17 km. At this same depth is a medium-low resistivity anomaly that extends to a depth of ~20 km where the anomaly changes to low-resistivity character. These low resistivity predicted anomalies, considered in conjunction with geophysical anomalies, might represent high conductive features associated with geothermal processes.

The predicted p-wave velocity (V_P) at the study areas ranges from 3.5 to 8.5 km/s (Figure 45d). In general, the upper 1–2 km displays low velocities, but the velocities progressively increase with depth. The velocity structure of Kilauea and the LERZ are similar, characterized loosely as four horizontal layers with velocities less than 4.8 km/s, from 4.8 km/s to 6.2 km/s, from 6.2 km/s to 7.3 km/s, and from 7.3 km/s to greater than 8 km/s. Leahy et al. (2010) and Zhong and Watts (2013) identified similar velocity layers and referred to the layers as volcanic, oceanic crust, underplating, and mantle. In contrast to the velocity layering at Kilauea and LERZ, the velocity character at Saddle Road appears to bend downward, possibly reflecting downward flexure due to volcanic loading by Mauna Loa and Mauna Kea. Predictions using alternate sets of independent data result in the same (or very similar) velocity structures across these three study areas.

The predicted background V_P/V_S ratio ranges from 1.5 to 3 (Figure 45e). V_P/V_S ratios of ~3 commonly indicate soil layers. The predominant V_P/V_S ratio in Figure 45e of ~1.75 probably

represents competent elastic rock. In contrast, a heterogeneous distribution of high and low V_P/V_S ratios appear laterally adjacent to each other beneath the Saddle Road and Kilauea areas to depths of about 3 km. In the Saddle Road area, an extensive V_P/V_S anomaly of magnitude 2.0 crosses the western third of the Saddle Road profile at depths from ~3 km to 15 km. Additional V_P/V_S anomalies of magnitude 1.5–1.6 appear at or near surface locations along profiles of each study area. We interpret these near-surface anomalies as marking gaseous fluids, such as those discussed at the LERZ (Nugraha et al. 2016). The low V_P and low V_P/V_S anomalies in the upper 2 or 3 km at Kilauea and the LERZ may be caused by the presence of steam (PGV 1991) or volatiles (Lin et al. 2015). Anomalies at much greater depths, such as below ~17 km at Saddle Road and ~23 km at LERZ, where V_P and V_S are high and V_P/V_S anomalies are greater than 1.8, may indicate the presence of partial or molten magma. This is particularly true toward the west and across the first third of the Saddle Road images.

In the next section, we use the trained MSOM algorithm to simultaneously predict categorial features. We present the results from the same north looking perspective across the Saddle Road, Kilauea, and LERZ study areas (Figure 46). The preliminary categorical feature predictions focus on geologic features, such as basalt, (oceanic) crust, and underplating, with the aim of potentially identifying 2D lithospheric flexure under volcanic loading and 2D geologic layering. From these results, we interpret the boundary between the predicted magmatic underplating and mantle to be the Moho. Based on this interpretation, the depth to the Moho under Kilauea and LERZ is ~13 km, but under Mauna Loa and Mauna Kea, its depth is estimated to vary between 13 km (edge of flexure) to 23 km (bottom of flexure).

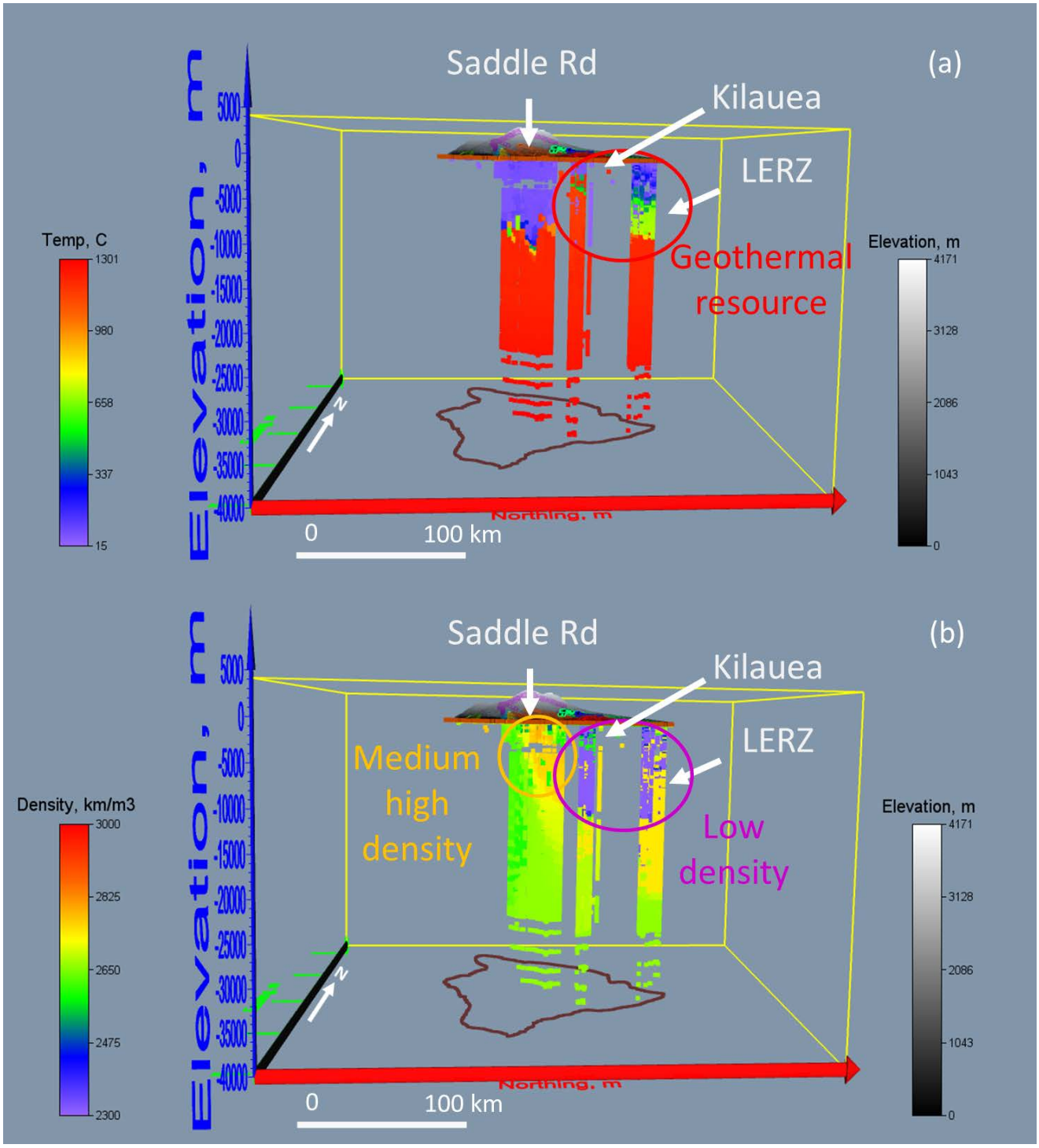

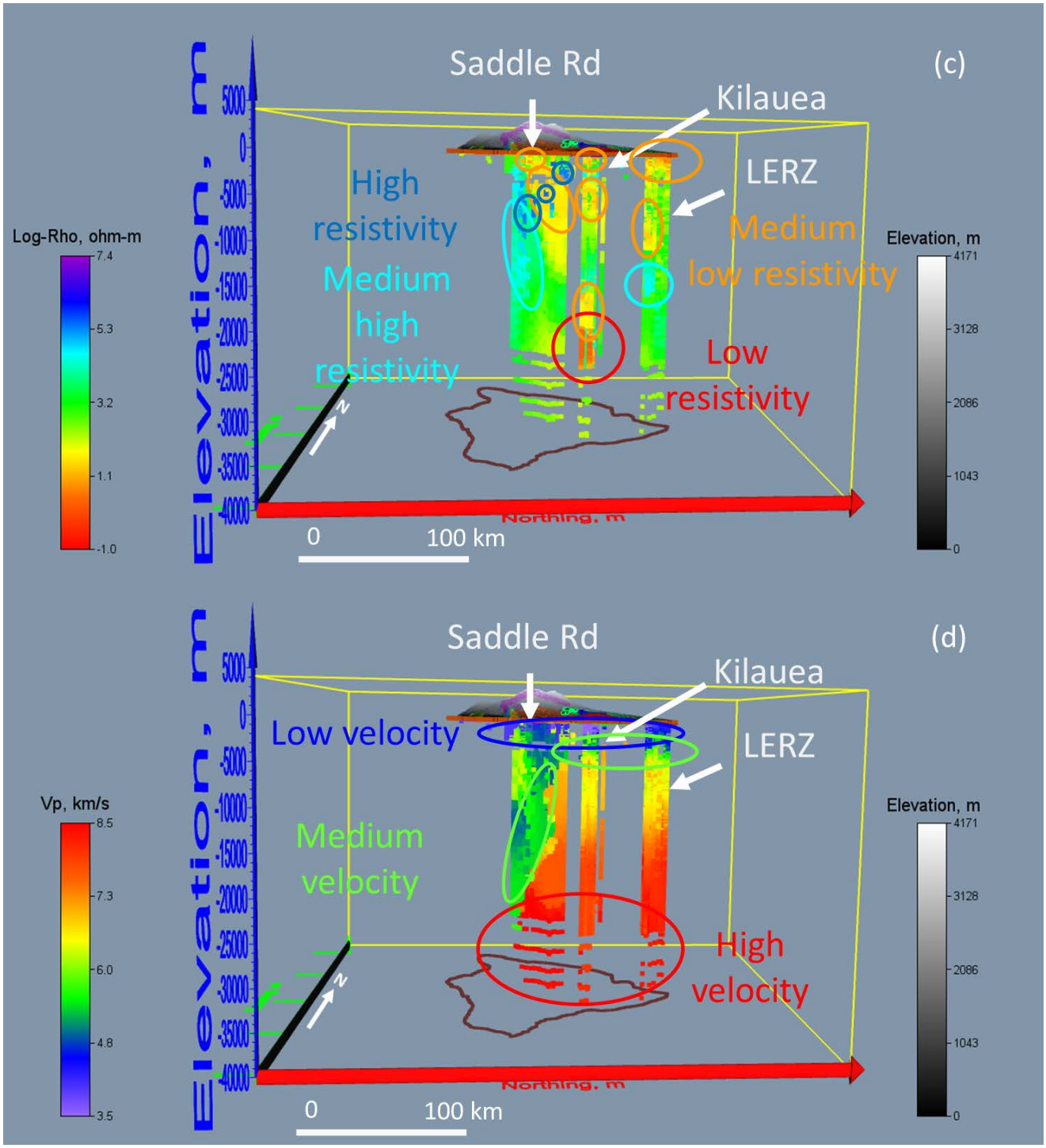

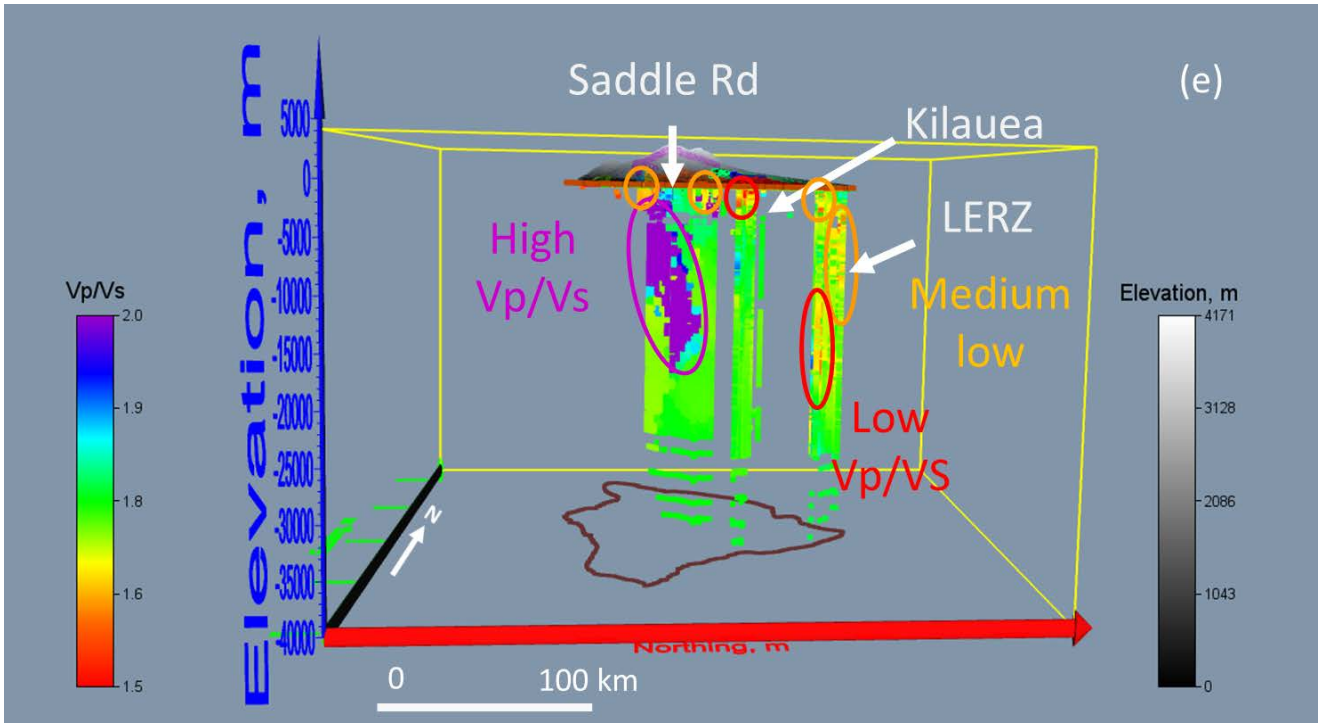

Figure 45. Regional simultaneous feature predictions across Saddle Road, Kilauea, and LERZ, using the third independent split set (fold-3): (a) temperature, C; (b) density, kg/m3; (c) log-resistivity (ohm-m), (d) Vp, km/s; and (e) V_P/V_S ratio. Low anomalies and high anomalies are annotated in each of the plots.

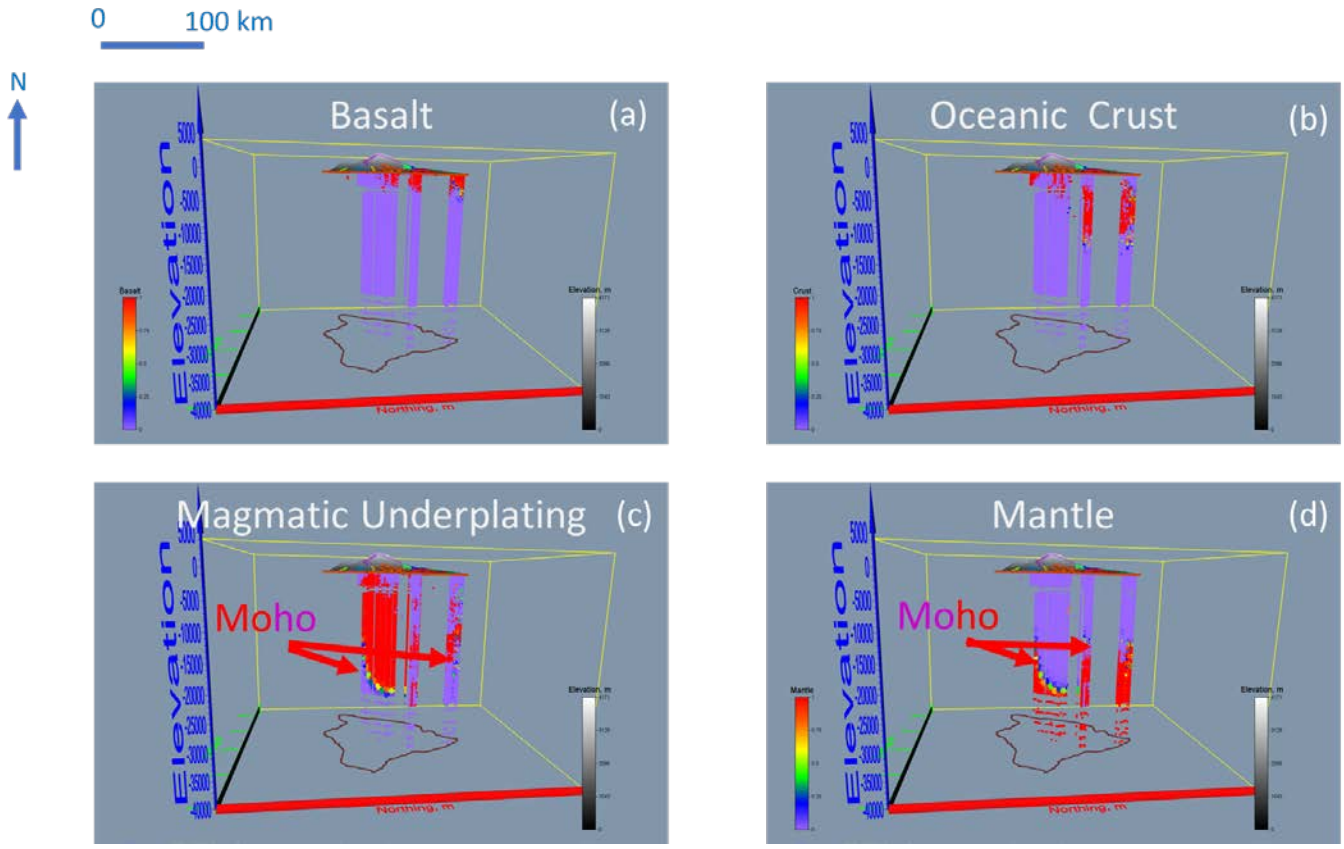

Figure 46. Simultaneous categorical feature predictions across Saddle Road, Kilauea, and LERZ, using the first independent split set (fold-1): (a) Temperature, °C. (b) Density, kg/m^3. (c) Log-resistivity (ohm-m). (d) V_P, km/s; and (e) V_P/V_S ratio. The interpreted location of the Moho is consistent across the Kilauea and LERZ but appears to be much deeper beneath the Saddle Road profile. The increased depth of the Moho beneath Saddle Road might be attributed to volcanic loading of Mauna Kea and Mauna Loa.

2.3.3.2.4 Island-Wide Assimilation and Prediction

In this section, we present results for the independent island-wide assimilation and prediction of features. We use the Saddle Road, Kilauea, and LERZ area records together with 2,500 randomly located surface sites and 150 random randomly located pseudo-boreholes scattered across the island. The pseudo-boreholes are represented by empty cells that extend from the surface to a depth of 20 km, below which a linear temperature gradient is applied (Putrika 1997). The aim of this section is to identify hidden geothermal resources, lithospheric flexure under volcanic loading, geologic layering, and earthquake-fault associations, and to characterize faults, all in 3D. The objectives are to: (1) predict geophysical (numeric) features, e.g., temperature, density, resistivity, V_P, V_P/V_S ratio; and (2) predict geologic (categorical) features (e.g., velocity layers basalt, crust, underplating, and mantle). The feature predictions are presented as a single independent set (fold-3) in plan-view together with (a) eight prominent island fault systems, (b) regional feature predictions, (c) island-wide feature predictions below sea level, and (d) island-wide feature predictions below and above sea level. The fault systems and rifts on Hawai‘i are numbered and color coded as follows:

Fault systems:

- Hilina=1 (red)
- Kahuku =2 (red-orange)
- Kaoiki = 3 (orange)
- Kealakekua = 4 (dark green)
- Koae = 6 (dark blue)
- Kohala = 7 (light blue).

Rifts:

- Kilauea = 5 (light green)
- Mauna Loa = 8 (purple).

The inclusion of regional feature predictions in each figure provides a means to visually evaluate the continuity among features when extending the regional application to the whole island using randomly placed pseudo-boreholes and surface sites. Given that the Phase 2 and Phase 3 data sets will be improved by application of 3D and joint inversions, the results presented herein are considered preliminary with the focus on identifying anomalies with minimal interpretation.

The first set of figures present independent temperature predictions over the range of 10°–1,300°C (Figure 47) and over the range of 10°–>350°C (Figure 48). In both sets of figures, the continuity of temperature predictions at the regional level and below-sea-level island-wide temperature suggests that the extension of feature prediction using simulated boreholes may be useful in future studies. Also, several temperature anomalies are present. Those temperature anomalies at the LERZ area are known and geothermal energy is being produced there. The geothermal anomalies beneath Kilauea caldera and the area southeast of the caldera correspond to recent and ongoing eruptions of lava. In addition to the LERZ and Kilauea anomalies, temperature anomalies occur on the east and west flanks of Mauna Kea, as well as one southwest of Mauna Loa near the Mauna Loa fault system.

Independent density predictions are presented over the range of 2,300–3,000 kg/m^3 in Figure 49. The island-wide prediction process reveals a prominent low-density feature (2,300 kg/m^3) around the LERZ area that extends southwest parallel to the coast, as well as north of the Hilina fault system. Other relatively high-density anomalies (2,800 kg/m^3) occur at and above sea level beneath Mauna Kea and Mauna Loa. The density anomaly of the greatest magnitude (3,000 kg/m^3) appears near the surface, directly below Mauna Kea caldera.

Several log-resistivity anomalies occur across the island. The most prominent low-resistivity (high-conductivity) features appear within 3 km of the surface at the LERZ and Kilauea areas (Figure 50). A medium-to-low-resistivity anomaly occurs along the western end of Saddle Road. Other low-resistivity features are located south of the Saddle Road beneath the northwest and southwest flanks of Mauna Loa; both are west of Mauna Loa fault system. Various spatially large resistivity features (0.1 to 100,000 ohm-m) are apparent in the island-wide prediction sets. The largest high-resistivity (purple) feature on the Big Island is associated with the Kaoiki fault system. This feature appears in the above-sea-level island-wide predictions. The second largest medium-high resistivity anomaly (dark blue) also appears only in the above-sea-level predictions and along the Mauna Loa fault. The presence of both these features in the above-sea-level prediction sets may indicate that the associated parts of the Kaoiki and Mauna Loa fault systems may be relatively shallow.

The prediction of V_P is extended from the regional study areas across the Big Island (Figure 51). The velocity predictions presented in Figure 51b–d reveal a spatially variable gradient when studying the region from Kilauea southeast toward the coast; other investigators have observed this as well (Park et al. 2007; Lin et al. 2014). Implementation of the island-wide prediction process resulted in increasing the anomalous velocity (relative to prediction of individual regions) below the Saddle Road from 3.5 km/s to about 6 km/s. This revised upward V_P prediction is indicative of oceanic crust which seems consistent with published discussions on Big Island volcanic loading and downward flexure of the oceanic crust reaching a minimum between the Mauna Kea and Mauna Loa volcanoes as described by others (Leahy et al. 2010; Zhong and Watts 2013; Klein 2016). Further supporting this hypothesis is the change from layer-cake velocity structure (low velocity layers at the surface that increase to highest velocity at the model domain bottom) beneath Kilauea and LERZ to a downward and compressed velocity trend reaching a minimum point south of the Saddle Road and west of Mauna Loa fault. West of this region there are no simulated boreholes and therefore no V_P predictions to define the likelihood of structural symmetry with possible rising flexural limb reflective of the layer cake structure east of Mauna Loa fault.

The prediction of V_P/V_S ratio is extended from the regional study areas across the Big Island (Figure 52). Multiple high and low V_P/V_S anomalies exist (1.5–2.0) that can be combined with V_P and low log-resistivity anomalies to better understand spatial geothermal resources on the Big Island. For example, at shallow depths (upper 2–3 km) near the LERZ and Kilauea areas, the anomalously low V_P/V_S ratio and correspondingly low log-resistivity might be interpreted as the presence of gaseous fluids. The presence of steam in the HPGA and other geothermal wells of the LERZ are examples of this behavior (PGV 1991). A similar anomalous region in the vicinity of the Koae Fault zone can be interpreted likewise. Also, an increase in the V_P/V_S ratio can reflect a decrease in the stiffness of the geologic material. In this case, the high V_P and V_P/V_S ratios together with low log-resistivity may be reflective of a partial melt. One example is at lower depths beneath the LERZ, where the combination of high V_P, high V_P/V_S, and low log-resistivity might be associated with the upward flow of partially molten magma. Another deeper region of anomalously high V_P, high V_P/V_S ratio, and low log-resistivity at depths below about 17 km beneath Saddle

Road and southward under Mauna Loa might be interpreted as the location of partially molten magma.

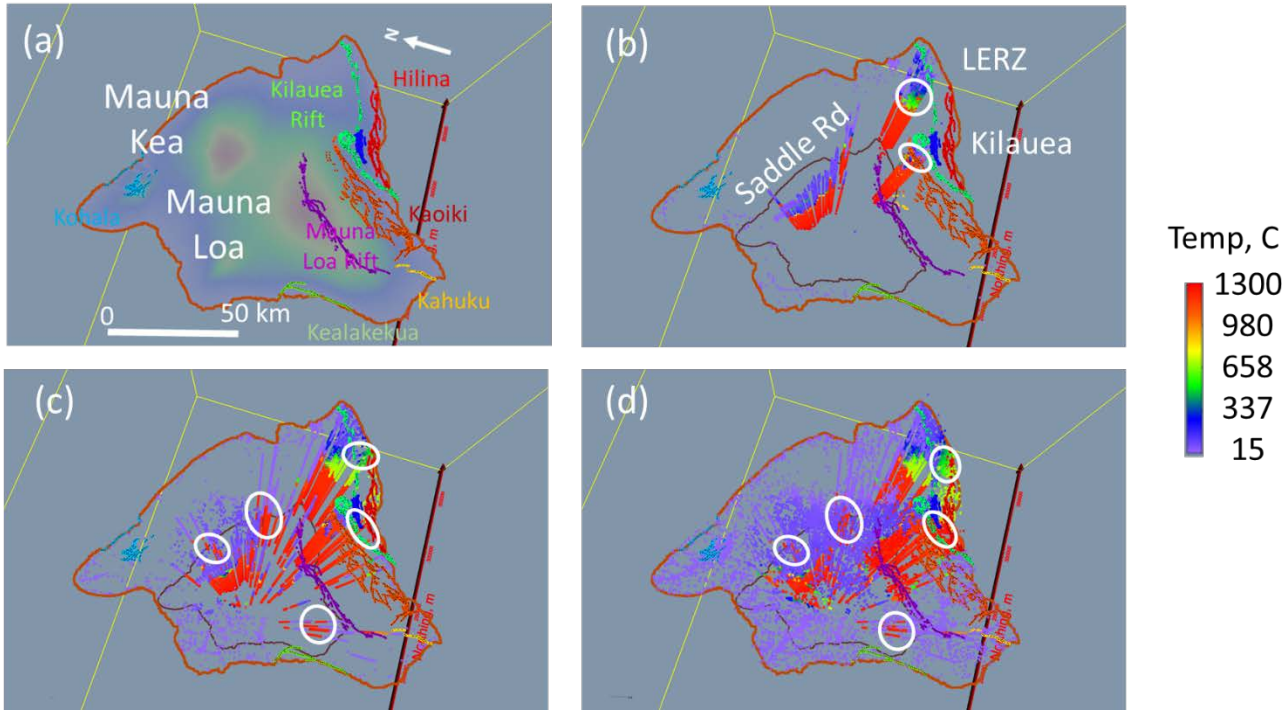

Figure 47. Comparison of temperature (10°–1,300°C) predictions at the regional and island scales: (a) Fault systems: Hilina = 1 (red), Kahuku = 2 (red-orange), Kaoiki = 3 (orange), Kealakekua = 4 (dark green), Koae = 6 (dark blue), Kohala = 7 (light blue), and rifts: Kilauea = 5 (light green), Mauna Loa = 8 (purple); (b) Independent (fold-3) regional below sea level temperature predictions across Saddle Road, Kilauea, and LERZ areas. (c) Independent island-wide below-sea-level temperature predictions based on assimilation of regional features and 100 random pseudo-boreholes. (d) Independent island-wide above- and below-sea-level temperature predictions based on assimilation of regional features, 100 random pseudo-boreholes, and 2,500 random surface locations. Geothermal anomalies are identified by white circles.

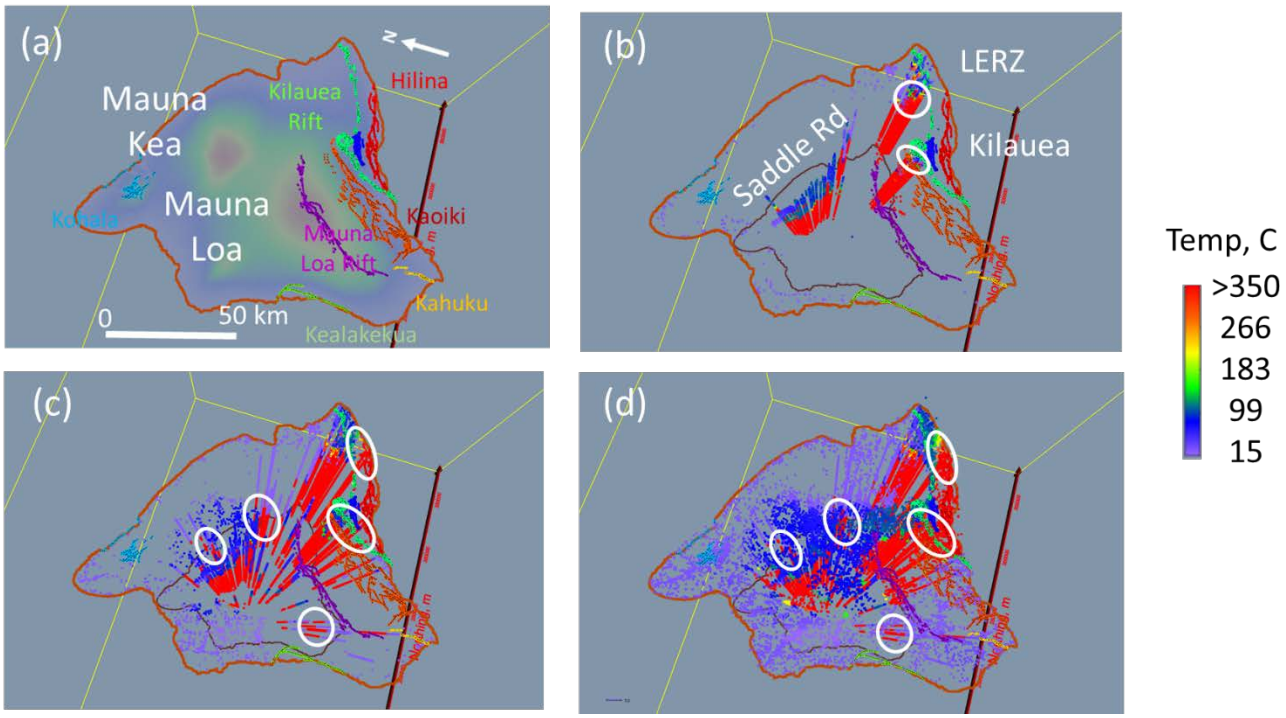

Figure 48. Comparison of temperature (10°– >350°C) predictions at the regional and island scales: (a) Fault systems: Hilina = 1 (red), Kahuku = 2 (red-orange), Kaoiki = 3 (orange), Kealakekua = 4 (dark green), Koae = 6 (dark blue), Kohala = 7 (light blue), and rifts: Kilauea = 5 (light green) and Mauna Loa = 8 (purple). (b) Independent (fold-3) regional below sea level temperature predictions across Saddle Road, Kilauea, and LERZ areas. (c) Independent island-wide below-sea-level temperature predictions based on assimilation of regional features and 100 random pseudo-boreholes. (d) Independent island-wide above- and below-sea-level temperature predictions based on assimilation of regional features, 100 random pseudo-boreholes, and 2,500 random surface locations. Hot colors represent high-temperature areas and cool colors represent low-temperature areas.

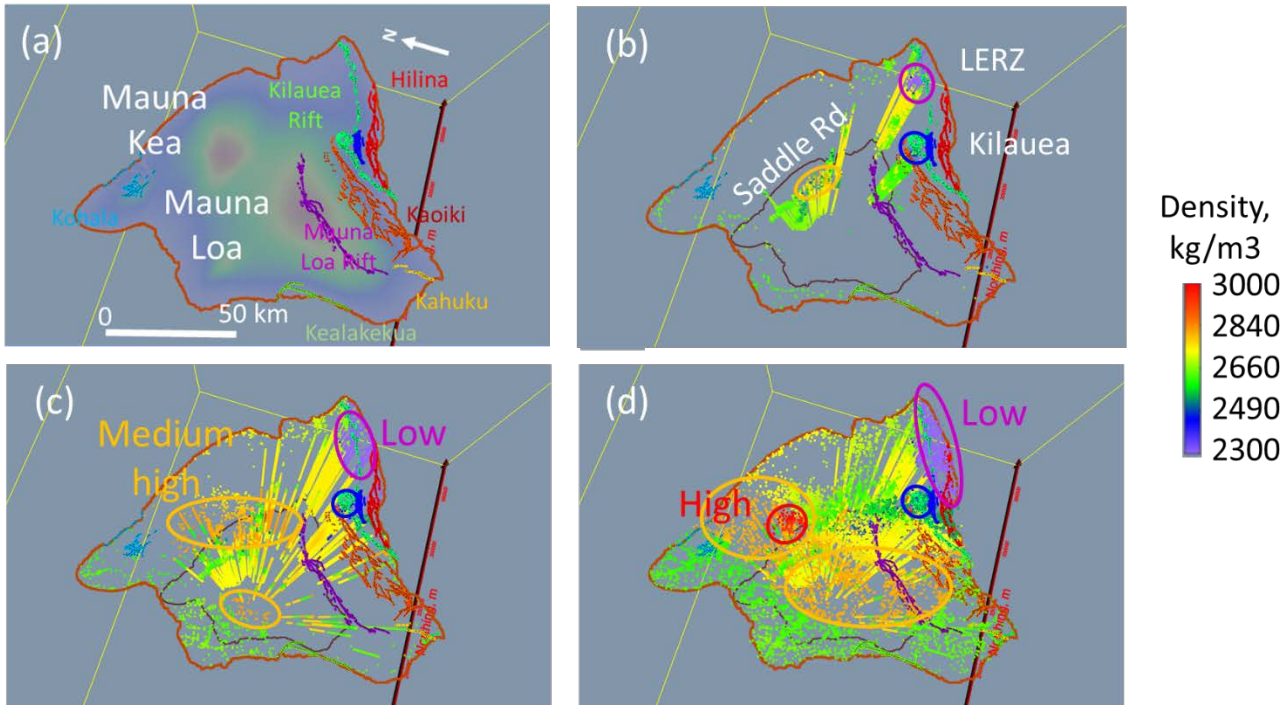

Figure 49. Comparison of density (2,300–3,000 kg/m^3) predictions at the regional and island scales: (a) Fault systems: Hilina = 1 (red), Kahuku = 2 (red-orange), Kaoiki = 3 (orange), Kealakekua = 4 (dark green), Koae = 6 (dark blue), Kohala = 7 (light blue), and rifts: Kilauea = 5 (light green) and Mauna Loa = 8 (purple). (b) Independent (fold-3) regional below-sea-level density predictions across Saddle Road, Kilauea, and LERZ areas (c) Independent island-wide below-sea-level density predictions based on assimilation of regional features and 100 random pseudo-boreholes. (d) Independent island-wide above- and below-sea-level density predictions based on assimilation of regional features, 100 random pseudo-boreholes, and 2,500 random surface locations. Hot colors represent high-density areas and cool colors represent low-density areas.

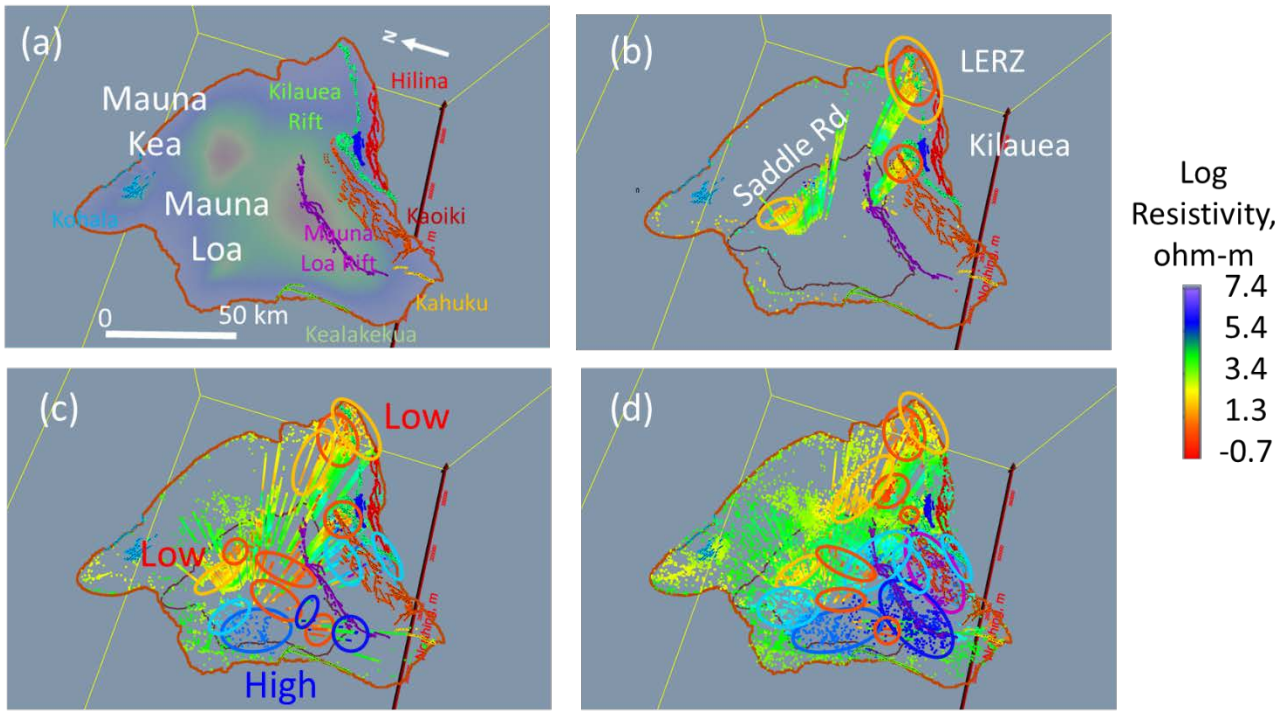

Figure 50. Comparison of Log resistivity (-0.7 to 7.7 ohm-m) predictions at the regional and island scales: (a) Fault systems: Hilina = 1 (red), Kahuku = 2 (red-orange), Kaoiki = 3 (orange), Kealakekua = 4 (dark green), Koae = 6 (dark blue), Kohala = 7 (light blue), and rifts: Kilauea = 5 (light green) and Mauna Loa = 8 (purple). (b) Independent (fold-3) regional below-sea-level log-resistivity predictions across Saddle Road, Kilauea, and LERZ areas. (c) Independent island-wide below-sea-level log-resistivity predictions based on assimilation of regional features and 100 random pseudo-boreholes. (d) Independent island-wide above- and below-sea-level log-resistivity predictions based on assimilation of regional features, 100 random pseudo-boreholes, and 2,500 random surface locations. Hot colors represent low-resistivity (high-conductivity) areas and cool colors represent high-resistivity (low-conductivity) areas.

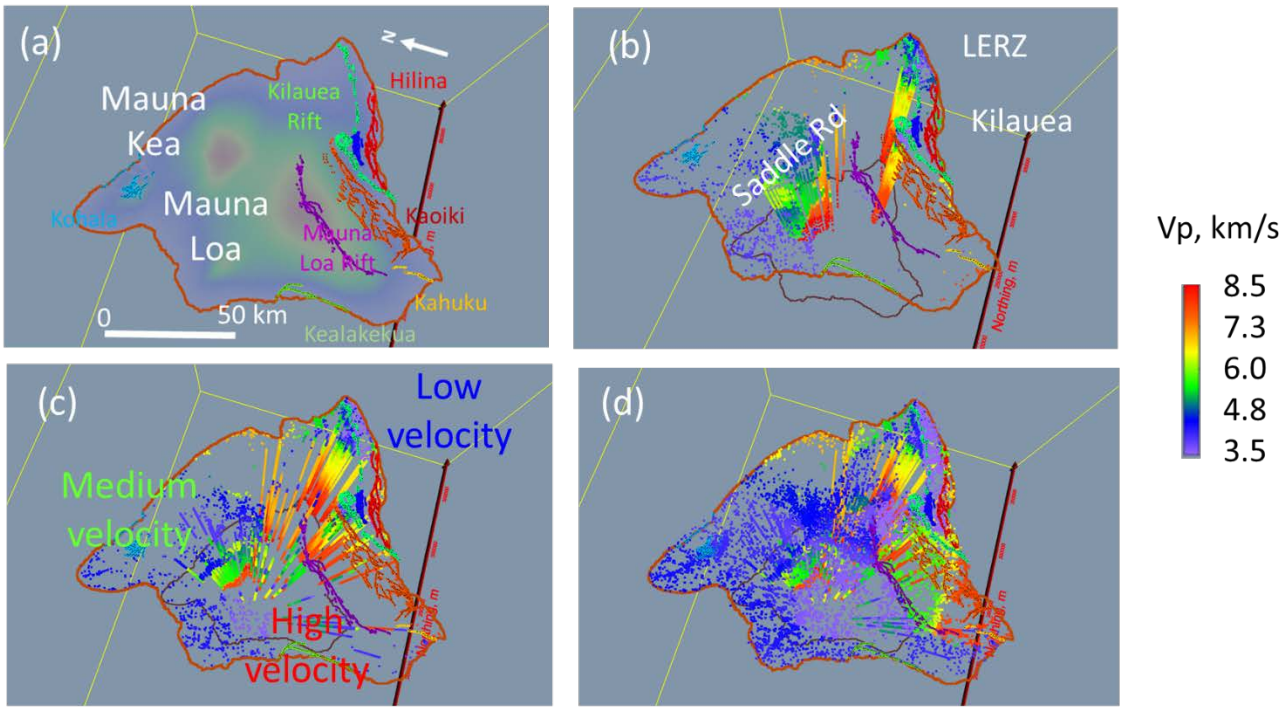

Figure 51. Comparison of V_P (3.5 to 8.5 km/s) predictions at the regional and island scales: (a) Fault systems: Hilina = 1 (red), Kahuku = 2 (red-orange), Kaoiki = 3 (orange), Kealakekua = 4 (dark green), Koae = 6 (dark blue), Kohala = 7 (light blue), and rifts: Kilauea = 5 (light green) and Mauna Loa = 8 (purple). (b) Independent (fold-3) regional below-sea-level V_P predictions across Saddle Road, Kilauea, and LERZ areas. (c) Independent island-wide below-sea-level V_P predictions based on assimilation of regional features and 100 random pseudo-boreholes. (d) Independent island-wide above- and below-sea-level V_P predictions based on assimilation of regional features, 100 random pseudo-boreholes, and 2500 random surface locations. Hot colors represent high values of V_P and cool colors represent low values of V_P ratio. The velocity predictions in panels b–d reveal a spatially variable gradient described by others when studying the region from Kilauea southeast toward the coast (Park et al. 2007; Lin et al. 2014).

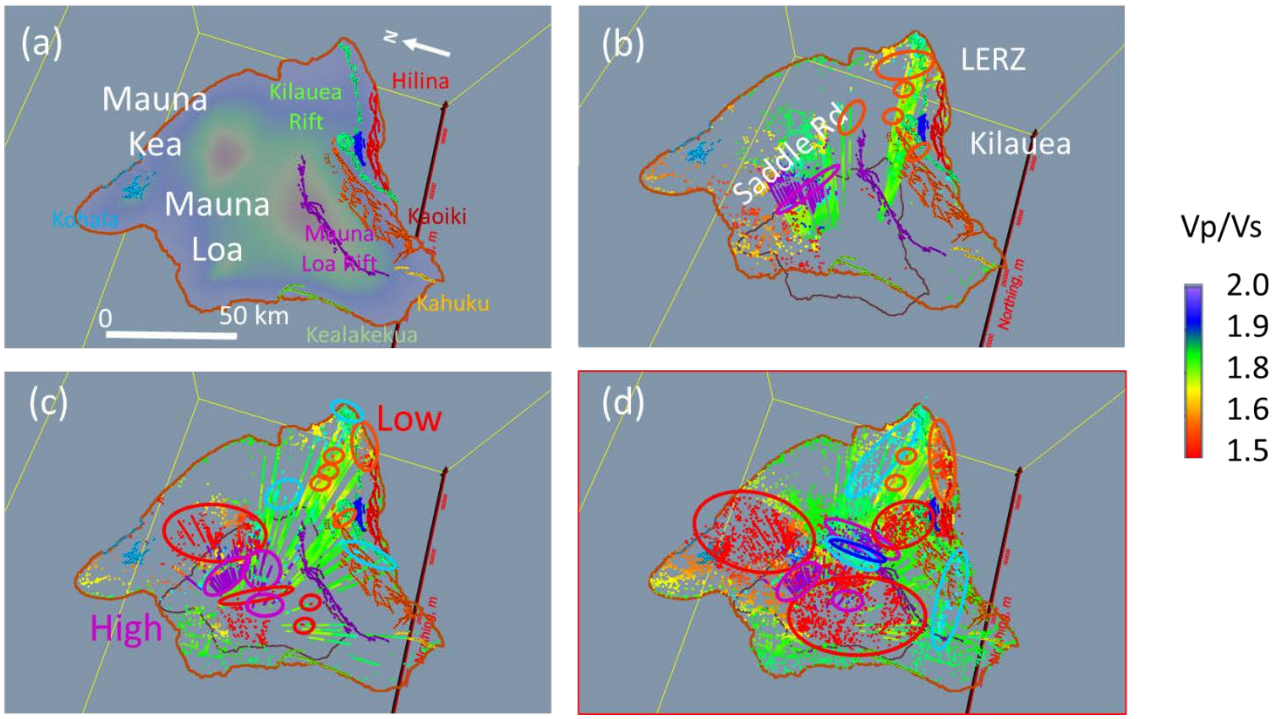

Figure 52. Comparison of V_P/V_S ratio (1.5 to 2.0) predictions at the regional and island scales: (a) Fault systems: Hilina = 1 (red), Kahuku = 2 (red-orange), Kaoiki = 3 (orange), Kealakekua = 4 (dark green), Koae = 6 (dark blue), Kohala = 7 (light blue), and rifts: Kilauea = 5 (light green) and Mauna Loa = 8 (purple). (b) Independent (fold-3) regional below-sea-level V_P/V_S predictions across Saddle Road, Kilauea, and LERZ areas. (c) Independent island-wide below-sea-level V_P/V_S predictions based on assimilation of regional features and 100 random pseudo-boreholes. (d) Independent island-wide above- and below-sea-level V_P/V_S predictions based on assimilation of regional features, 100 random pseudo-boreholes, and 2,500 random surface locations. Hot colors represent low values of V_P/V_S ratio and cool colors represent large values of V_P/V_S ratio.

The predictions of quasi-3D geologic layering using categorical constraints based on known and predicted velocity are presented in Figure 53. The simultaneous prediction of basalt, oceanic crust, magmatic underplating and mantle layers appear in different viewing perspectives (Figure 53a, b). These figures further support the notion of oceanic flexure under the Hawaiian volcanic load (Leahy et al. 2010, Zhong and Watts 2013, Klein 2016).

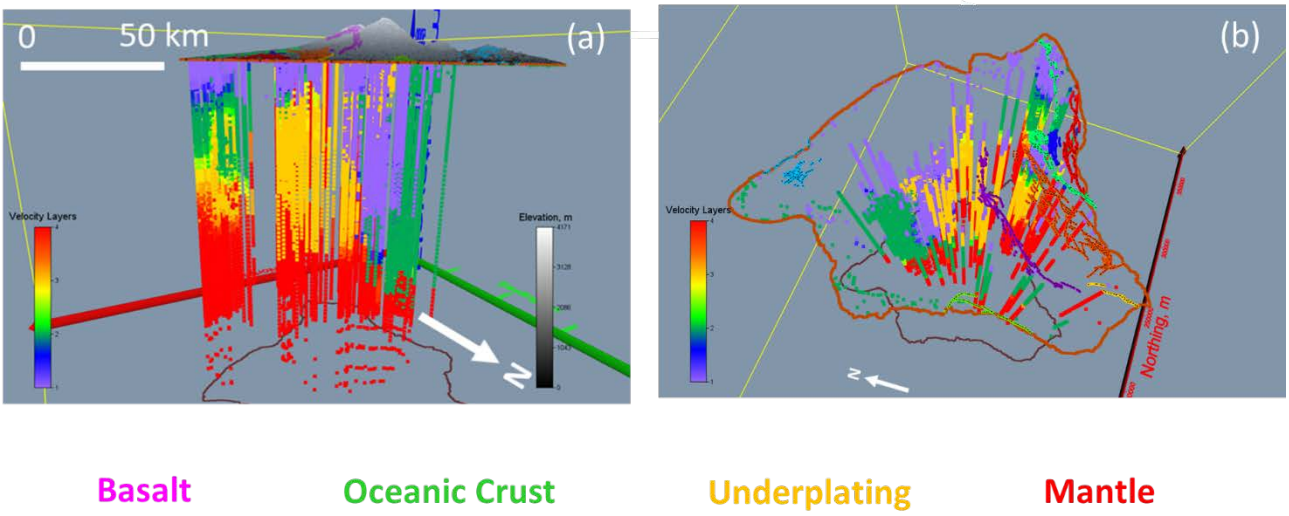

Figure 53. Predicted 3D geologic layering using categorical constraints based known and predicted velocity.

The predicted 3D earthquake-fault system associations are presented in Figure 54. Some of the prominent features include the association of earthquakes with distinct fault systems and rifts. Note that the earthquake and fault systems are predicted simultaneously, so their association is indicated by the same color. For example, earthquake clusters are associated with the Hilina fault system (1, red), the Kaoiki fault system number (3, orange), the Kilauea rift (5, light green), and the Koae fault system (6, blue). The most prominent shallow earthquakes appear to be associated with the Kilauea rift system; the intermediate deep earthquakes appear to be associated with the Hilina fault system; and the deepest earthquakes appear to be associated with the Kaoiki fault system.

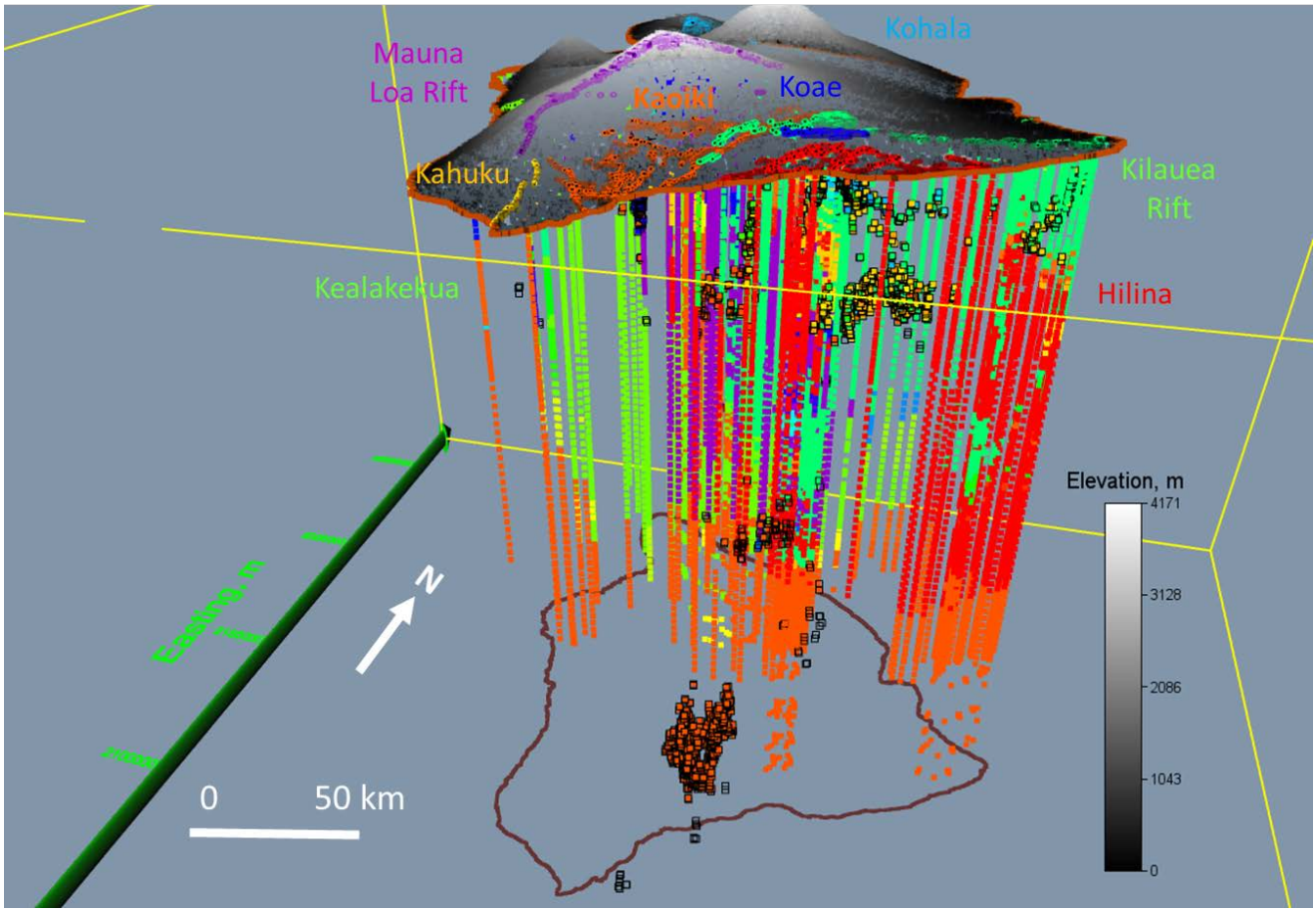

Figure 54. 3D fault-earthquake characterization predictions for the eight fault systems. Some of the prominent features include the association of earthquakes with distinct fault systems as indicated by the same color.

Predicted characteristics of selected faults on the Big Island are presented in Figure 55. The two left panels (a and c) provide top views (of the region below sea level) that reveal an approximately northeast-striking Kaoiki fault system and approximately northward-striking Kahuku fault system. The right two panels (b and d) are side-looking-northwest views toward the Kilauea-LERZ coastline. These figures reveal modeled fault aspects including the depths and trends of the Koae and Hilina fault systems. The Hilina fault system appears to start midway along the coast and strike northeast towards the Puna ridge, whereas the Koae fault appears to maintain a shallow profile trending toward the southwest.

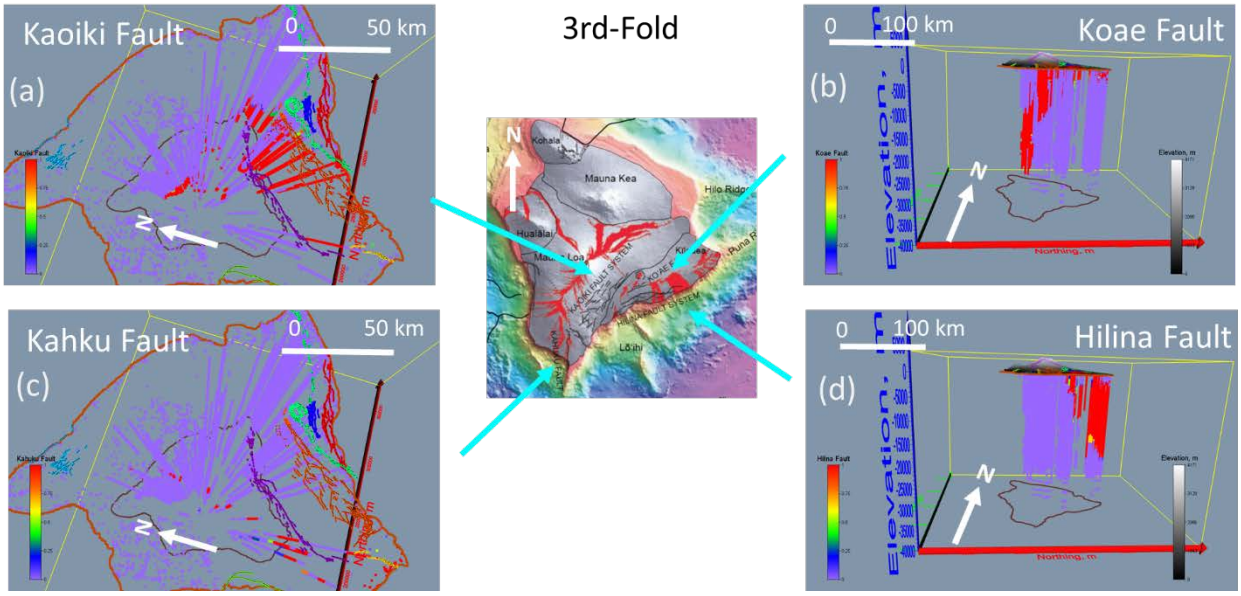

Figure 55. Predicted characteristics of selected faults on the Big Island. The two left panels show top views that reveal an approximately northeast trending Kaoiki fault system and approximately northward trending Kahuku fault system. The right two panels are looking northwest toward the Kilauea-LERZ coastline. These figures reveal modeled aspects including the depths and trends of the Koae and Hilina fault systems. For this case, the Hilina fault appears to start midway along the coast trending northeast in the direction of the Puna ridge, whereas the Koae fault appears to maintain a shallow profile trending toward the southwest.

2.3.4 Summary

In this study, an MML workflow is proposed, features selected, and an MSOM algorithm trained and tested for studying groundwater and geothermal characteristics at the island of Lāna‘i and geothermal characteristics at the island of Hawai‘i. Although each case study uses different subsets of the Hawai‘i Play Fairway hydrogeologic, geothermal, and geophysical data, the trained models both generalize to independent test data (randomly shuffled data sets split with 80% for training and 20%) despite being characterized as sparse, spatially limited with different support volumes, and uncertain.

In the Lāna‘i study, we use the trained model to predict continuous 3D features, which we in turn use to characterize five 3D GSUs. The predicted features include state variables (such as hydraulic head, temperature, chloride concentration), physical properties (such as density, resistivity, and specific capacity—a permeability surrogate), geology (basalt erupted subaerially and dikes—where “dikes” represent igneous intrusions), aqueous chemistry (major ions, metals, isotopes), and aqueous properties (pH, specific conductance, dissolved oxygen). Inspection of the predicted features reveals possible geologic attributes, such as basalt flows, igneous intrusions, and the Moho; possible groundwater features, such as downward groundwater recharge and saltwater intrusion; heterogenous chloride concentrations, such as zones of freshwater, brackish water, and saline water; and geothermal features, such as zones of upward convective hydrothermal transport along a gradient from the Moho (758°C) to the near surface (20°–65°C). Based on this information, two freshwater resources are identified from the surface to a depth of ~1 km: (1) a warm water (50°–65°C) region with intermediate specific capacity, low chloride concentration (<50 mg/l); and (2) a cool water (~20°C) region with low specific capacity and low chloride concentration (<300 mg/l). Two geothermal resources are identified by their associated characteristics. The first is a

warm (65°C) water resource, near the caldera, that extends from near the surface warmer down to ~1 km depth. The second is a very hot hydrothermal plume being transported upward from the Moho (about 750°C) to commercially viable drilling depths of ~2.0 km to 6 km, where the temperatures are ~107°C to 275°C. The ability to determine GSUs from independent sets of hydrogeologic, geothermal, and geophysical measurements supports their potential use in simultaneous characterization of combined groundwater and geothermal resources. Further, this novel approach affords the possibility for direct assignment of GSUs and their features to numerical model cells (or nodes). This minimizes ambiguity in the conceptualization-to-numerical-modeling process, including in identifying initial parameter values, boundary conditions, and geostatistical constraints in support of the calibration process. The MML workflow techniques used herein are novel in this application and their initial success warrants further research. The performance metrics in the Lānaʻi case study provide encouragement to continue this line of groundwater-geothermal research as part of the new ISLAND HEAT project.

In the second case study, the trained Hawaiʻi model is first used to simultaneously predict regional numeric and categorical features across the Saddle Road, Kilauea, and LERZ areas. The set of numeric and categorial predictions included geophysical features (e.g., temperature, density, resistivity, V_P, and V_P/V_S ratio) which appear to reveal hidden geothermal resources, lithospheric flexure under volcanic loading, and geologic layering in the subsurface. Next, the regional model is extended island-wide by introducing 2,500 random surface locations and 150 pseudo-boreholes randomly scattered across the island to predict 3D geophysical (numeric) features (e.g., temperature, density, resistivity, V_P, V_P/V_S ratio) and 3D geologic (categorical) features (e.g., subaerially erupted basalt, oceanic crust, underplating materials, and mantle rocks). These characteristics point to hidden geothermal resources, lithospheric flexure under the volcanoes, geologic layering, earthquake-fault associations, and fault characteristics—all in 3D. Despite success in achieving the aim and objectives of this case study, the model can be improved in ways suggested as next steps in Phase 2 and Phase 3.

2.3.5 Proposed Research and Next Steps

We propose the following next steps to improve and advance the efficacy of the MML framework for developing open community data sets, identifying data acquisition targets with high value for future work, identifying new signatures to detect hidden groundwater and geothermal resources, and foster new capabilities for characterizing subsurface temperature and permeability.

1. Expand the availability and improve the quality of numeric data for assimilation and prediction. Improving numerical data will focus on (a) expanding field data collection to areas not yet surveyed; (b) providing higher-frequency data sets to improve near-surface information; (c) perform 3D geophysical inversion (deterministic, stochastic, and hybrid) using electromagnetic, gravity, self-potential, and velocity measurements; (d) perform joint multiphysics inversions and multiphysics-informed machine learning (resistivity and density, density and velocity, resistivity and velocity) to improve estimates and thereby mutual information available to inform the prediction process. Other numeric data sets that are being considered include ocean bathymetry, temperature, aqueous chemistry, and resistivity; and aqueous subsurface chemistry for characterizing samples from groundwater and geothermal wells.

2. Increase the availability and quality of categorical data for assimilation and prediction. Improving categorical data will focus on introducing surface and borehole rock type, age, and environments (subaerial, transition, submarine).
3. Cross-validation statistics will be computed for numeric and categorical features predicted across Hawai‘i Island. In addition to evaluating the effect of multiple independent samples on the feature prediction uncertainty, other approaches based on data augmentation using unsupervised deep learning will be considered.
4. GSUs will be computed across Hawai‘i to summarize and promote the joint interpretation of multimodal information.

3 Hawai‘i Island Gravity and Magnetotelluric Geophysical Inversion Update

The ISLAND HEAT project is intended to reduce the risks, costs, and uncertainty of geothermal exploration and improve the success rate of well drilling through optimization of an innovative, multiattribute synthesis calibrated via proven heat and permeability. The aim of this multigeophysics inversion task is to advance subsurface imaging by developing and integrating inversion from multiphysics. Standard single property inversions are undertaken with property estimates used for physical interpretation and as initial or prior values in the joint inversion effort.

In Phase 1, the PNNL team developed the forward and inverse models for the multigeophysics measurements, including gravity and AMT/MT data, and provided inversion outputs as spatial maps of density and electrical resistivity to the machine learning and data synthesis teams for physics-based interpretation and conceptual model development. The AMT/MT 1D layering inversion study covers the PGV (the northwest region of the Hawai‘i Island), while the 3D gravity inversion covers the northwest region with the topographically corrected data from UH. The resulted density model can be used to provide prior information (e.g., structures or layering) for interpretation or joint inversion. The AMT/MT data were screened and cleaned for inverting 1D layering resistivity and interpolated to generate 2D spatial maps, which are to be used as priors for 3D AMT/MT inversion. In Phase 2, the developed 3D AMT/MT inversion will be conducted for both the northwest and LERZ areas, and 3D gravity inversion will be completed for LERZ.

This section summarizes the gravity, MT, and AMT data availability and data quality, the development of inversion code, and the inverted resistivity and density maps.

3.1 Well-Log, Gravity, and AMT/MT Data

Figure 56 shows the Hawai‘i Island and the three main subregions of interest: Northwest, Kilauea, and LERZ. In the northwest subregion, the available facies and resistivity and temperature well log data can provide initial information for multigeophysics inversion.

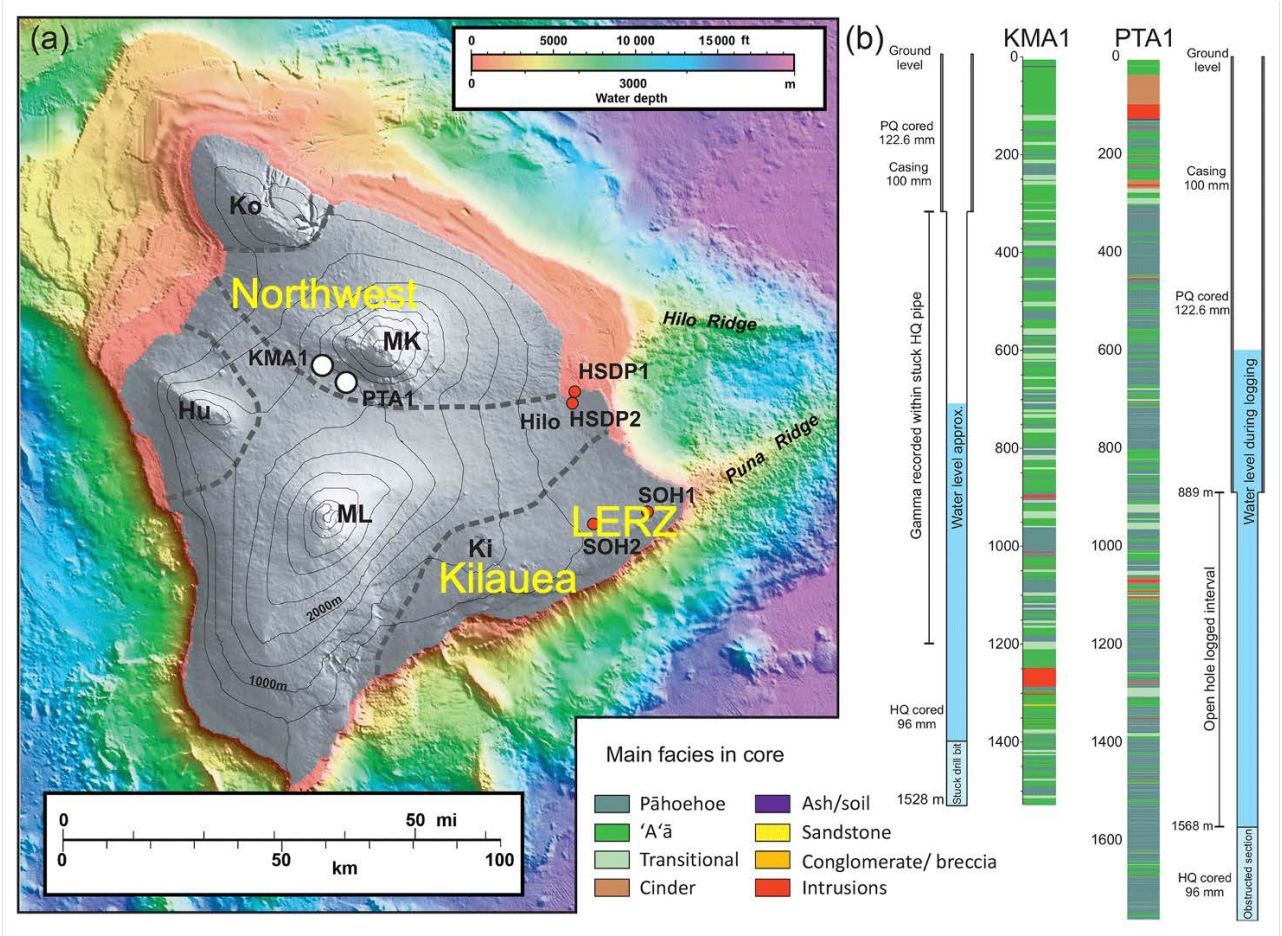

Figure 56. The study areas (Northwest, Kilauea, and LERZ). (a) Water depth map. (b) Facies and water levels in the wells KMA1 and PTA1.

A series of MT geophysical surveys have been performed that span the Mauna Loa/Mauna Kea Saddle Region, the Kilauea region, and the LERZ on Hawai'i Island. These surveys can provide electrical resistivity profiles and resistivity maps at several elevations along the axis of the field measurements that can yield information on the subsurface geological structure. The AMT/MT survey transect in the northwest region is shown in Figure 57.

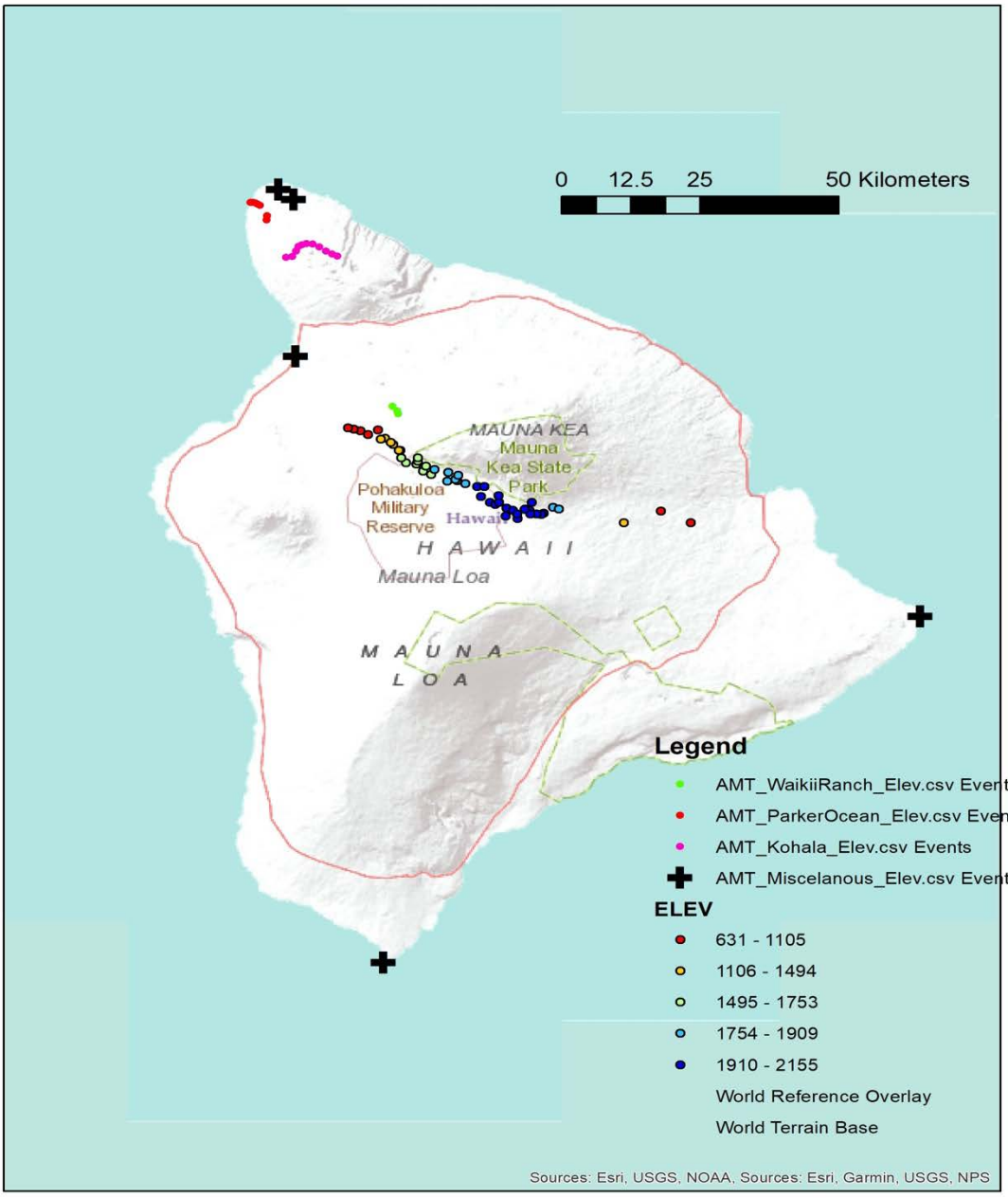

Figure 57. The AMT/MT transect in the northwest region of Hawai'i Island.

Gravity data, on the other hand, is easier to obtain and covers the entire island, as shown in Figure 58.

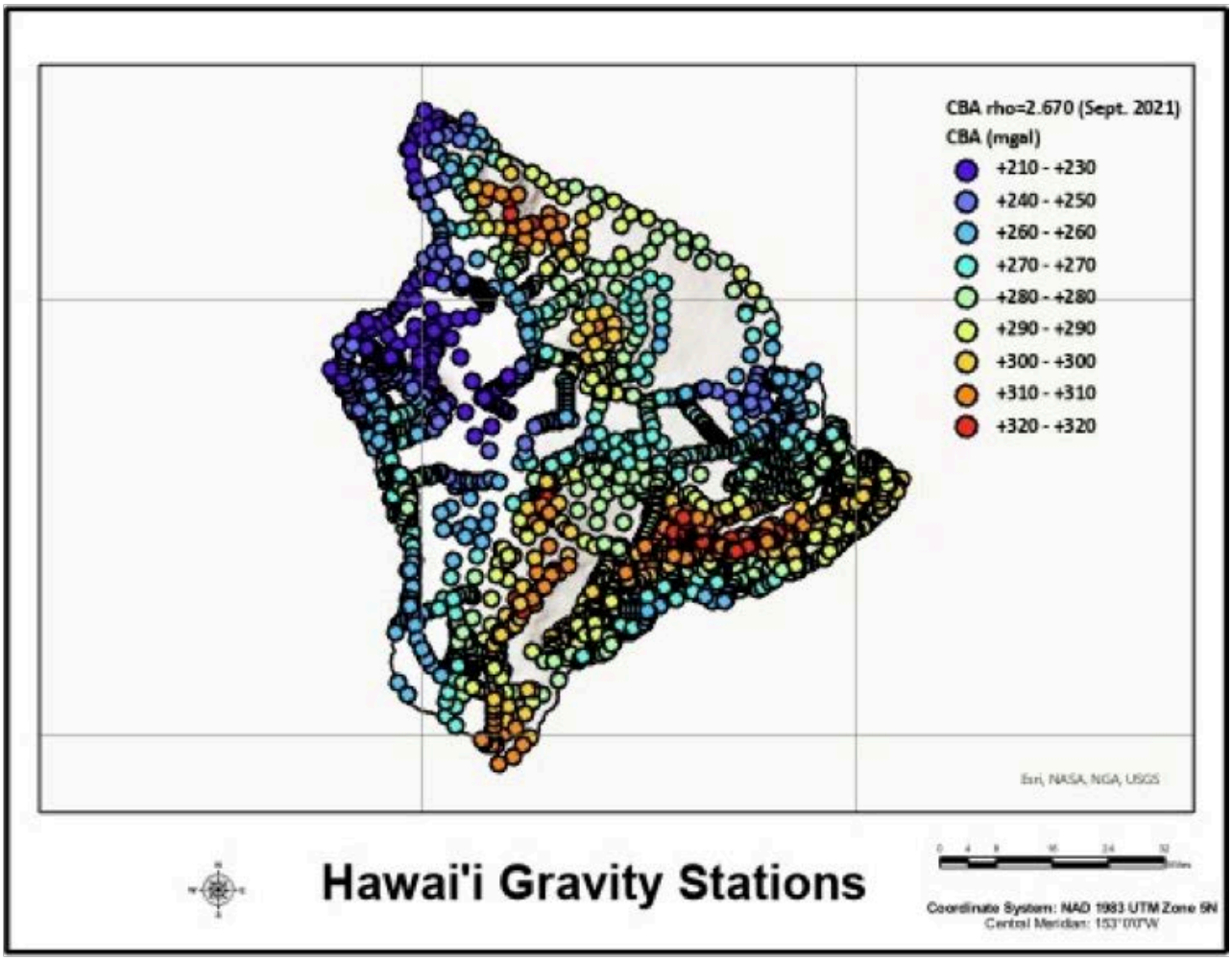

Figure 58. The distribution of gravity stations on Hawai‘i Island.

The gravity data, collected from a series of surveys, are subject to uncertainty due to inconsistency in topographic correction, which has been fixed by the UH team. There are also inconsistency issues in the AMT/MT data, which has been checked by visualizing the apparent resistivities and impedance. The sites with consistent AMT/MT data in the northwest Saddle Region are shown in Figure 59. Such a long transect allows integration of layering inversion results to produce resistivity maps in the Saddle Road area.

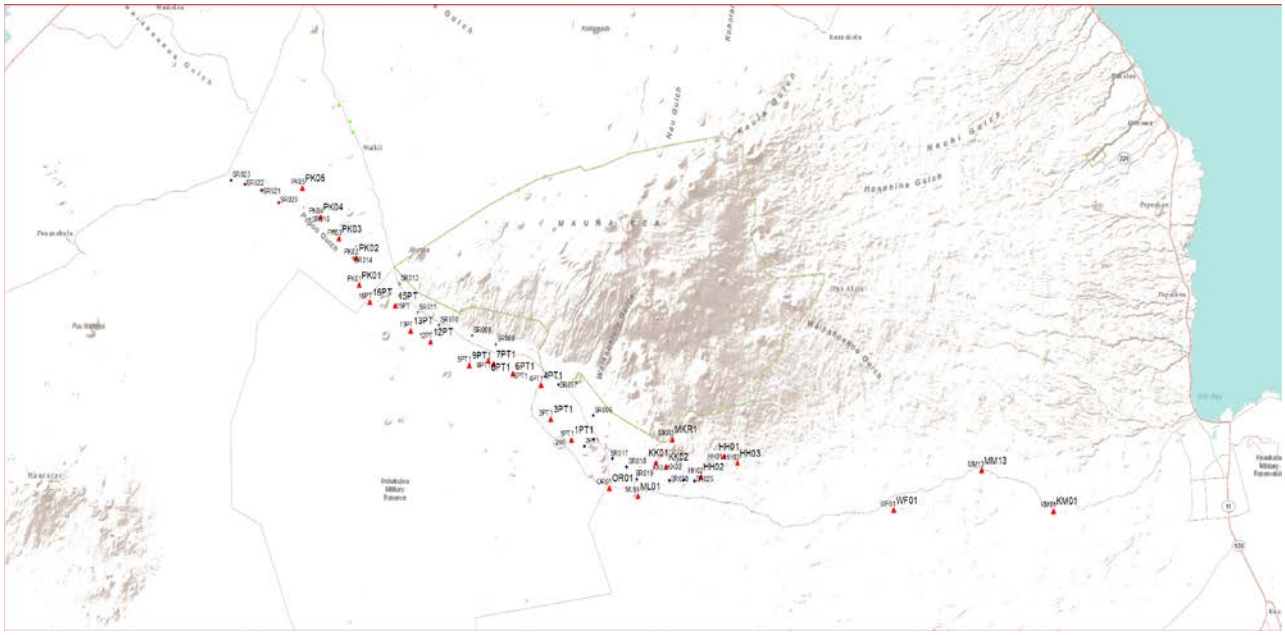

Figure 59. The AMT/MT stations with consistent data in the Saddle Road area.

3.1.1 Stochastic and Deterministic Inversion

Conventional geophysical inversions are usually gradient-based deterministic methods, such as Gauss-Newton methods (Pratt, Shin, and Hicks 1998), conjugate gradient methods (Newman and Alumbaugh 2000), and steepest descent techniques (Roy 2002). However, the solutions obtained using these methods often depend on the choice of initial values and thus might represent a local best fit model rather than the global best fit model. Additionally, the deterministic methods provide very limited uncertainty information on the estimated parameters (Chen et al. 2012). Stochastic inversion methods can (1) quantify the uncertainty about unknown parameters; (2) provide inversion results that are almost independent of initial values and therefore global and robust; and (3) provide guidance on optimal inversion setup with bounds violation check. When the forward models are expensive, or the unknown are of high dimension, surrogate reduced order models or dimensional reduction may be needed as stochastic inversion often needs to run forward model thousands of times or more for high-dimensional unknown parameter space.

The PNNL team developed a general-purpose Markov Chain Monte Carlo (MCMC) sampler in a Bayesian framework, which produces posterior samples with quantified uncertainty. The inversion framework can be used for 1D/2D/3D AMT inversion or joint inversion (with common unknowns). There are several derivatives of the MCMC sampler (Brooks et al. 2011) to improve the accuracy and efficiency of the inversion process:

- Metropolis-Hastings algorithm (symmetric random walk proposal)
- Metropolis-Hastings with mixtures and blocks (mixing global and local distributions, or dividing state vectors into blocks with separate updating)
- Gibbs sampling (component-wise proposal)
- DRAM (delayed rejection adaptive metropolis): partial local adaptation of the proposal within each time step; covariance matrix of the Gaussian proposal distribution is adapted on the fly

- DREAM (differential evolution adaptive metropolis): multiple different simultaneous chains for global exploration; automatically tunes the scale and orientation of the proposal distribution in randomized subspaces
- Differential Evolution MCMC with snooker update and sampling from past states (DEzs).

In order to optimize and finalize the inversion model, we evaluated the effectiveness of the inversion code via synthetic tests by comparing:

- DEzs vs. Differential Evolution Adaptive Metropolis (DREAM)-MCMC
- Noise-free vs. random noise data
- Subsurface conductivity fields with gradually increasing or decreasing or alternating conductivity values
- Likelihood functions defined for AMT magnitudes with vs. without logarithmic transform
- Single chain vs. multiple chains.

Figure 60 shows an example of the MCMC-Bayesian inversion testing results using a synthetic data set with known layered subsurface conductivity (i.e., 1/resistivity). Conductivity is measured in Siemens per meter (S/m), while resistivity is its reciprocal, measured in Ohm-meters (Ohm-m). Overall, the posterior modes match the true values very well at all layers. As expected, we observe much narrower posterior uncertainty in the top layers, while the uncertainty bounds increase with depth because the bottom layers' properties can only be detected in the low-frequency, low-resolution electromagnetic field observed at the surface. This also justifies the use of stochastic inversion for adding uncertainty measures of the inversion. Instead of a single set of unknown parameter estimates (e.g., from deterministic inversion), the posteriors can be used to derive quantiles to be used in machine learning analysis or integrated data interpretation.

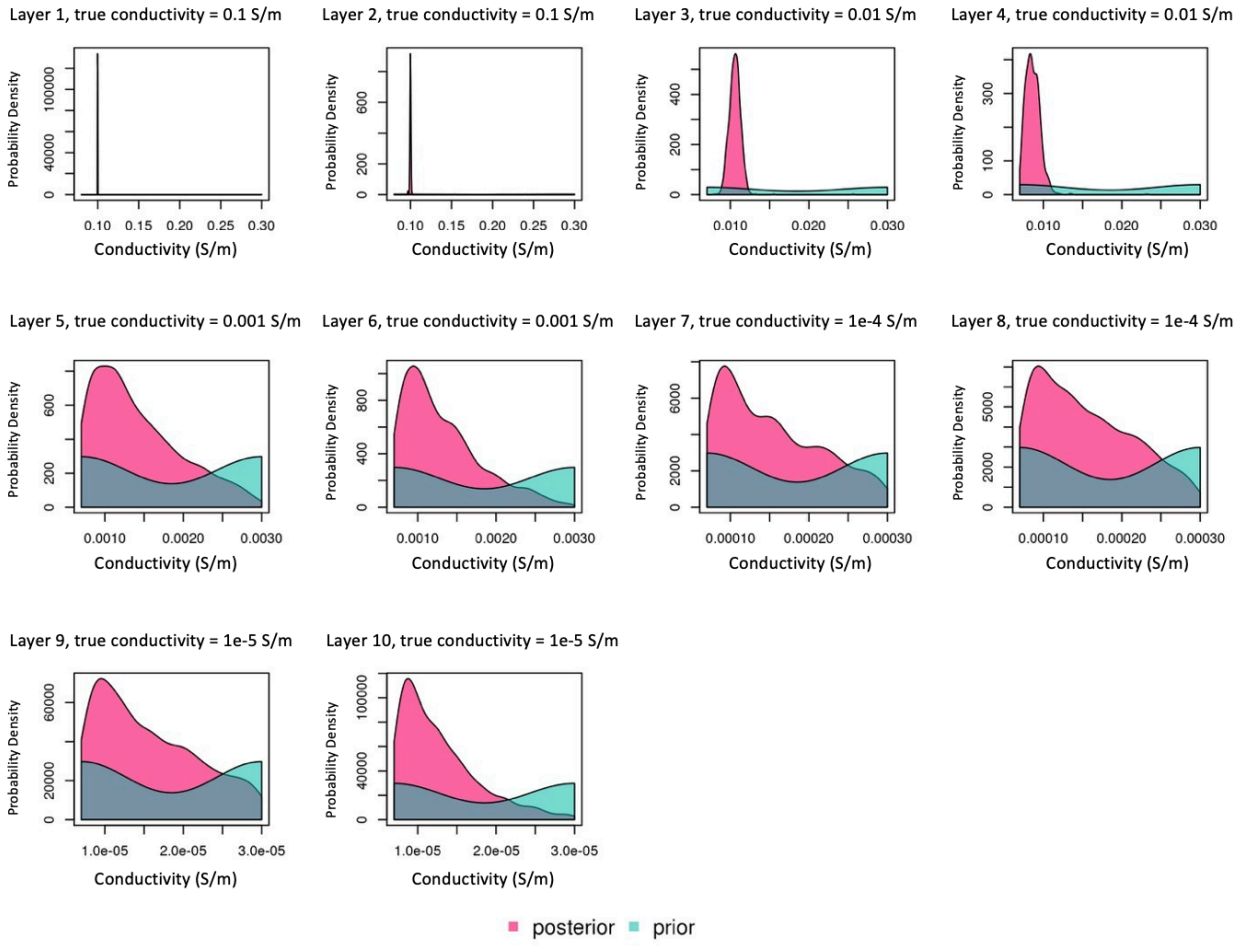

Figure 60. Example MCMC-Bayesian posterior pdfs of the conductivity (S/m) of 10 subsurface layers.

The synthetic tests yield the following summary:

- Better results can be achieved with logarithmic transformation of MT magnitudes; single chain and multi-chain results are comparable and consistent;
- Without noise, the top four layers and the bottom two layers can be resolved at very high accuracy and precision;
- Inversion accuracy varies for the middle layers depending on the noise level; with 5% noise, DREAMzs sampling is better than the DEzs approach; even with noises, the modes of top four layers and bottom two layers match well to the truth conductivity values;
- The optimized setup is applied to the real-world data (e.g., AMT/MT).

3.1.2 AMT/MT Inversion

The MT method is a passive electromagnetic exploration method that measures orthogonal components of the electric and magnetic fields on the Earth's surface. The source field is naturally generated by variations in Earth's magnetic field, which provide a wide and continuous spectrum of electromagnetic field waves. These fields induce currents into the Earth, which are measured at the surface and contain information about subsurface resistivity structures (Spies and Frischknecht 1991; Simpson and Bahr 2005). The AMT method records and processes frequencies that range from about 10 to about 100,000 Hz, while the MT method records and processes signals in the

frequency range of 0.0007 to 357 Hz. The AMT method (Zonge and Hughes 1991) offers a more detailed image of the subsurface resistivity beneath a receiver station and can collect an adequate data set for an individual station in a few hours, but its depth of penetration is limited to about 1 km. The MT method provides a much greater depth of penetration, up to several tens of kilometers, but its use of a lower frequency range requires a much longer data collection period at individual stations.

The general-purpose MCMC-Bayesian inversion is performed at the sites with available AMT/MT data. Figure 61 shows the real and imaginary impedance calculated from the posterior samples of the inverted subsurface resistivities, as a function of frequency. The observed impedance (shown as red asterisks in the plots) are well located within the bounds derived from the posterior samples of inverted resistivities.

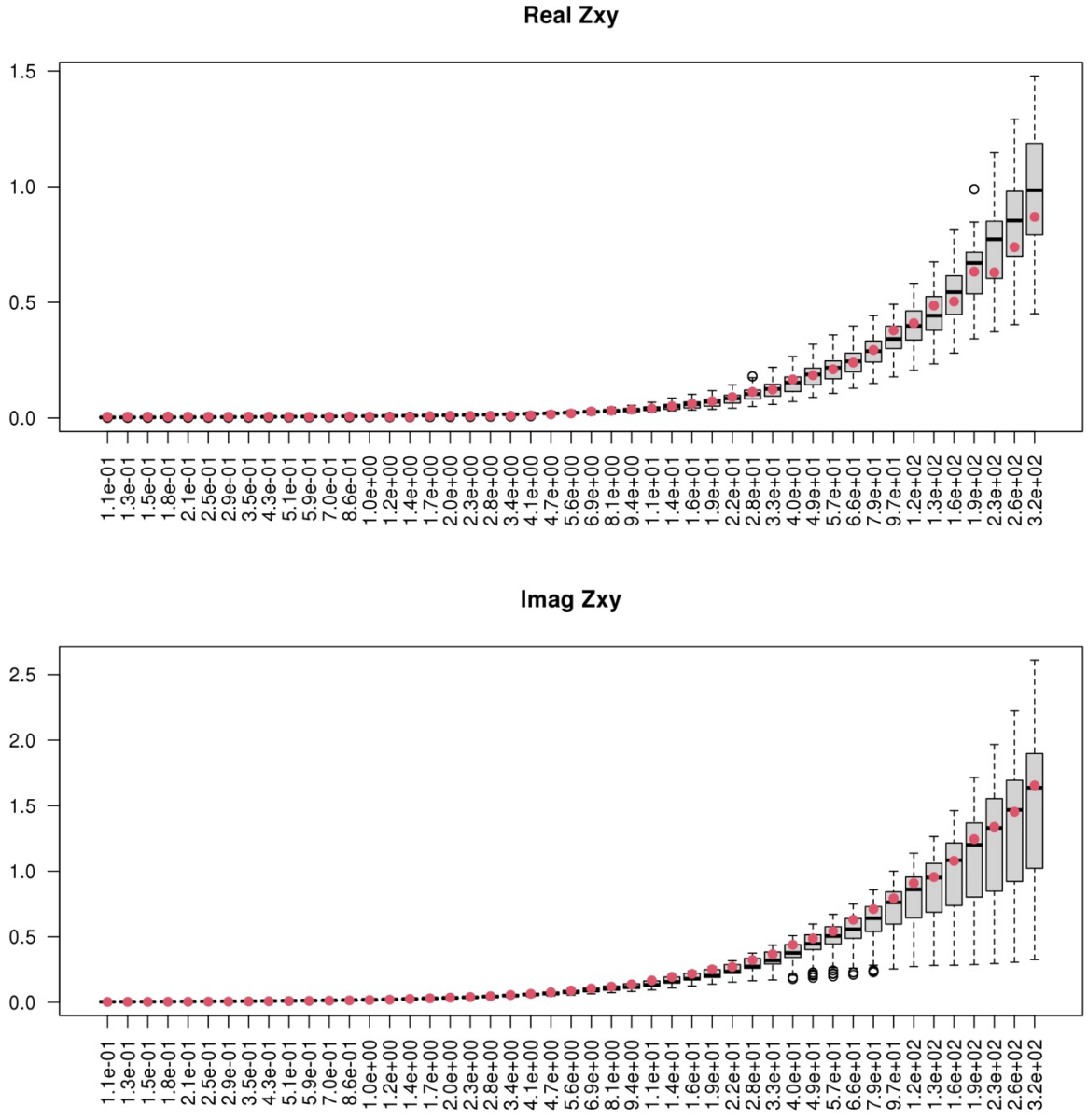

Figure 61. The observed real and imaginary impedance at site 9PT1, vs. the calculated impedance from the posterior estimates of subsurface resistivities.

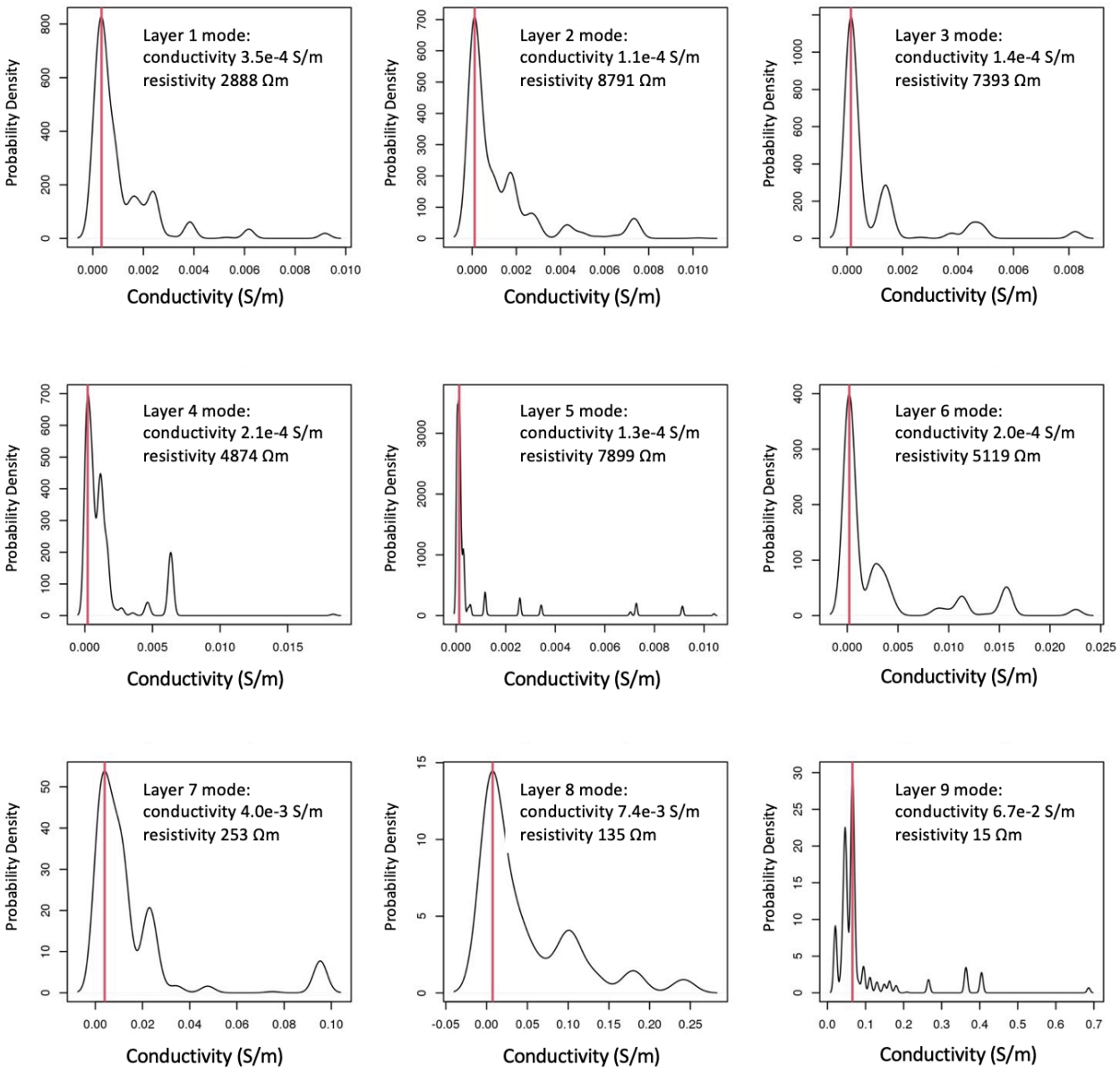

Figure 62. The posterior pdfs of subsurface conductivities (1/resistivities) in the top layers at site 9PT1.

Figure 62 shows the posterior pdfs of the resistivities of the subsurface layers at site 9PT1. In general, the deeper layers correspond to larger uncertainty bounds. Layers 7–9 correspond to a conductive zone at an elevation of approximately 500 m, which is quite consistent across the sites, as can be seen in Figure 63. The plot is looking north with west to the left and east to the right. Warm colors are resistive, and cool colors are conductive. Distances and elevations are in meters. The inversion results are consistent with what was found in a previous USGS study by Pierce and Thomas (2009).

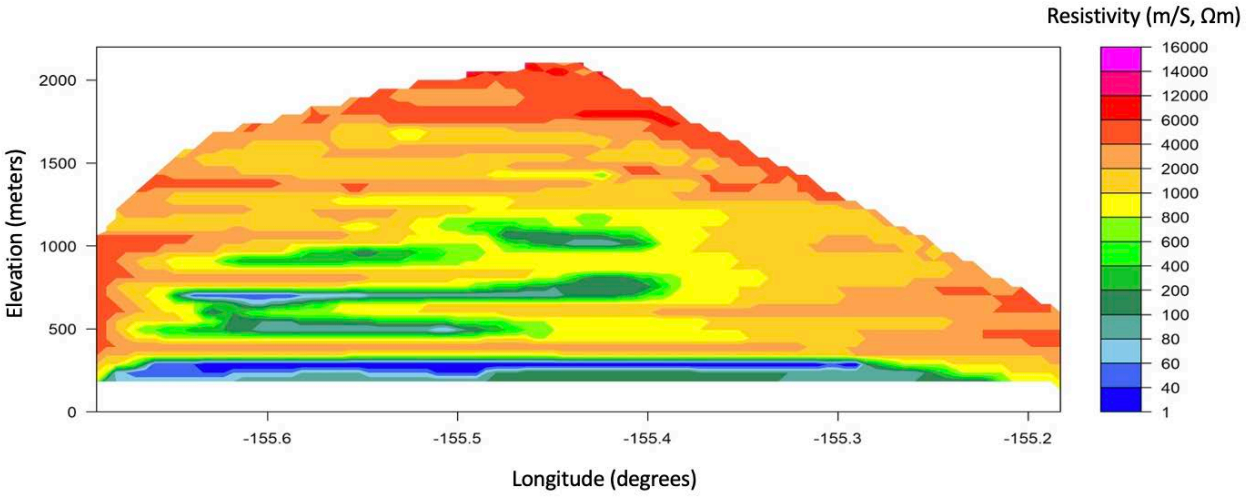

Figure 63. Resistivity map using the modes of the inverted resistivity for shallow layers.

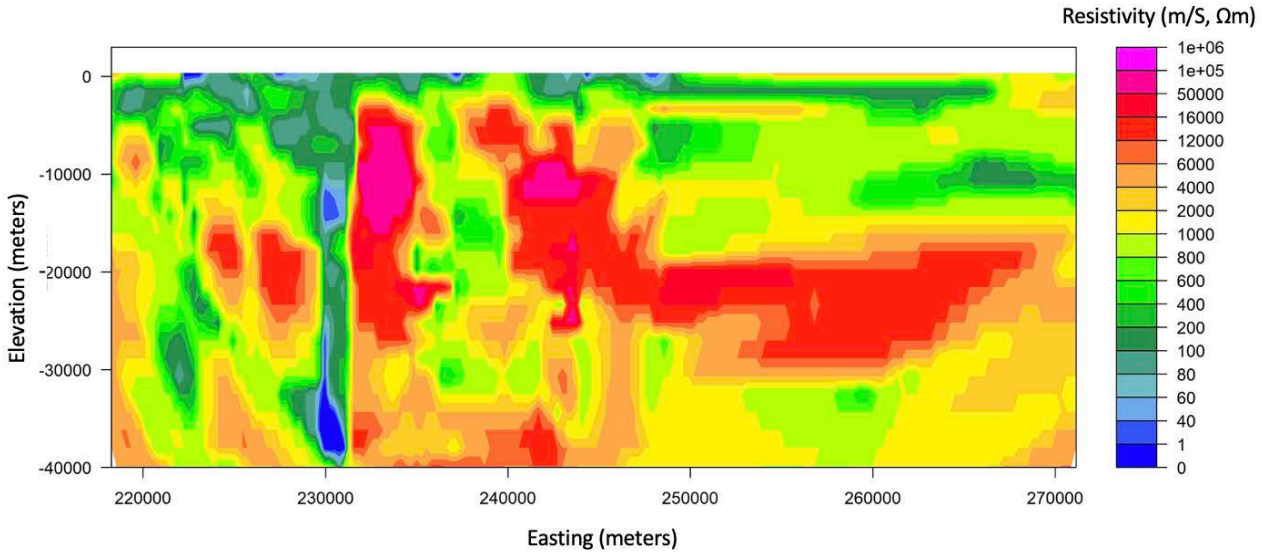

Figure 64. Extended resistivity map using the modes of the inverted resistivity for layers extended to 40km depth.

The very low frequency component of the observed MT data may reflect resistivity information at much larger depth, for example, up to 40 km. Therefore, we added more layers to have an extended inversion domain in an attempt to identify other important geological zones or discontinuity layers (e.g., the Moho). In Figure 64, a resistivity map shows some discontinuities around the depths of 16 km and 25 km. Interestingly, it also identifies a connected conductive zone (i.e., at easting 230,000 m), which could be an artifact due to measurement errors at a single local site.

The statistical moments, modes, quartiles from the posterior estimates are archived and passed on to the machine learning team for data integration and interpretation.

3.1.3 Gravity Inversion

Gravity inversion allows us to constrain the interior mass distribution of a planetary body using the observed shape, rotation, and gravity. A gravity experiment involves measuring the vertical components of the gravity field produced by anomalous (either excess or deficient) mass beneath the surface (Jacoby and Smilde 2009). A distribution of anomalous mass, characterized by anomalous density $\rho(x, y, z)$, produces its own gravity field, gs, which is superimposed on the ambient gravity field. By measuring the resultant field and removing the ambient field from the measurements through numerical processing, one obtains the field due to the anomalous mass.

The coordinate system for all the gravity data is NAD 1983 UTM zone 5N. The UH team provided the CBA data using a density correction of 2.67 g•cm^{-3}, which was then incorporated in an ArcGis project (Figure 65).

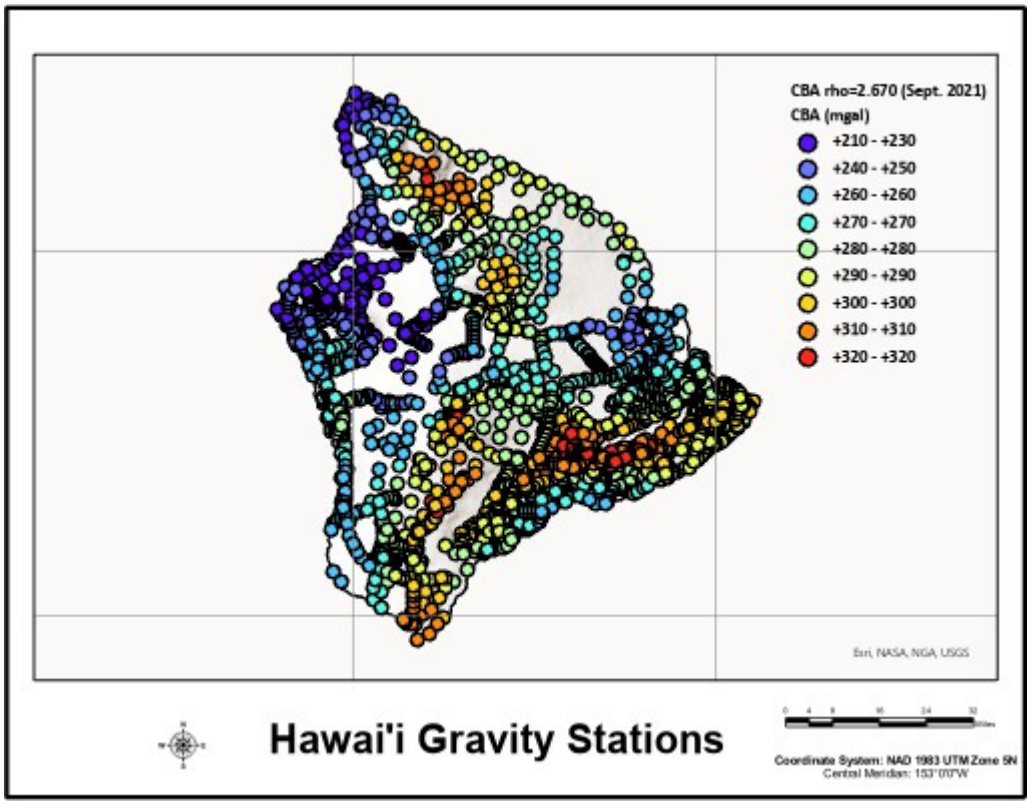

Figure 65. Gravity stations.

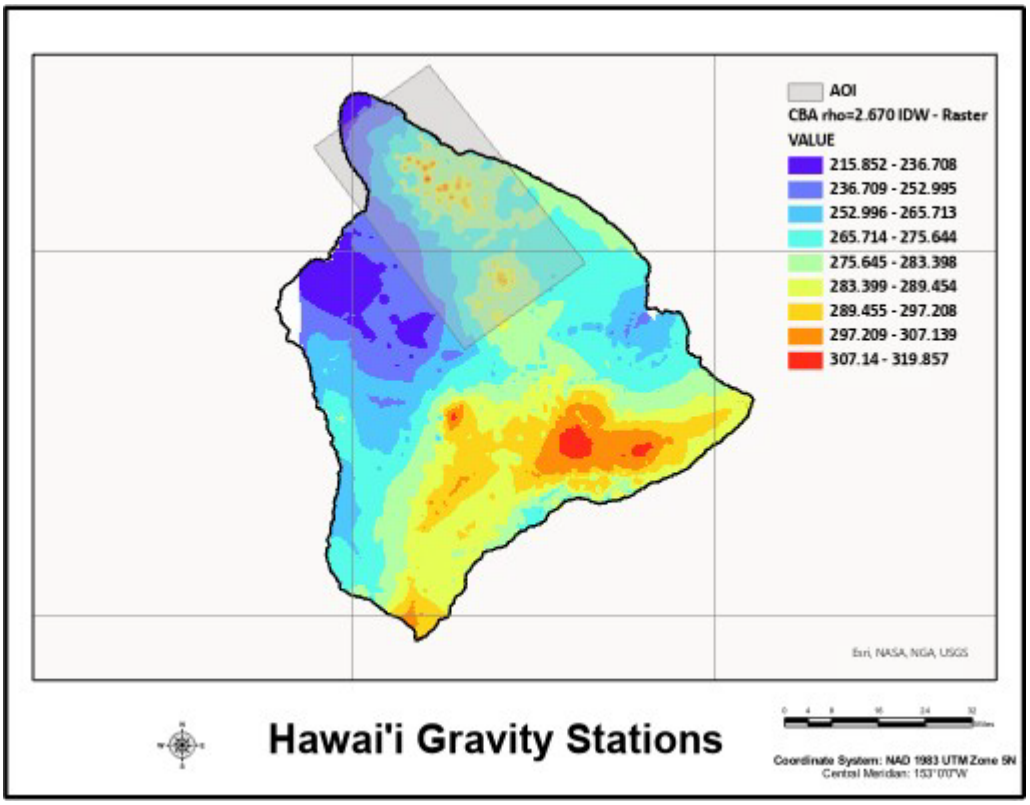

Figure 66. CBA map with the area of interest superimposed as light blue rectangle.

In a second step, a subdomain of the gravity and topography data sets was extracted (Figure 66). This is the domain used for the gravity inversion.

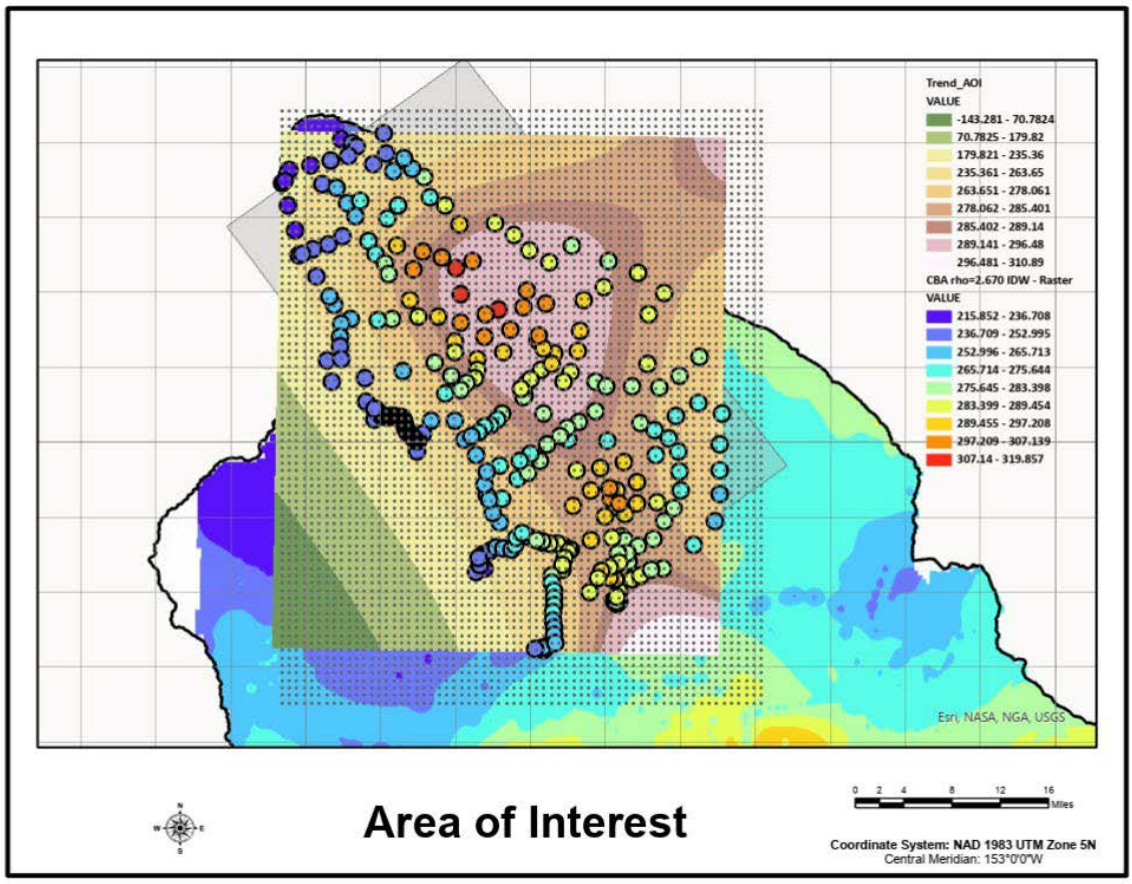

Figure 67. The subregion of interest is indicated by the gray rectangular box.

In this domain, a gravity regional is computed using a third-degree polynomial (Figure 67) and then the residual is obtained by subtracting the regional signal to the observed CBA. The inversion is made on this residual CBA.

This subregion is then decomposed in prisms to build the 3D grid (Figure 67) that is used for the gravity modelling (UBC Grav3D) software (UBC 2013).

The result is a grid of relative density values in g/cm^{-3} (Figure 68) that is used to compute the gravity anomaly compared to the observed residual CBA (Figure 69). The residuals are close to 0, particularly in the regions of our interest. The absolute density values are obtained by adding the constant value of 2.67 g/cm^{-3}.

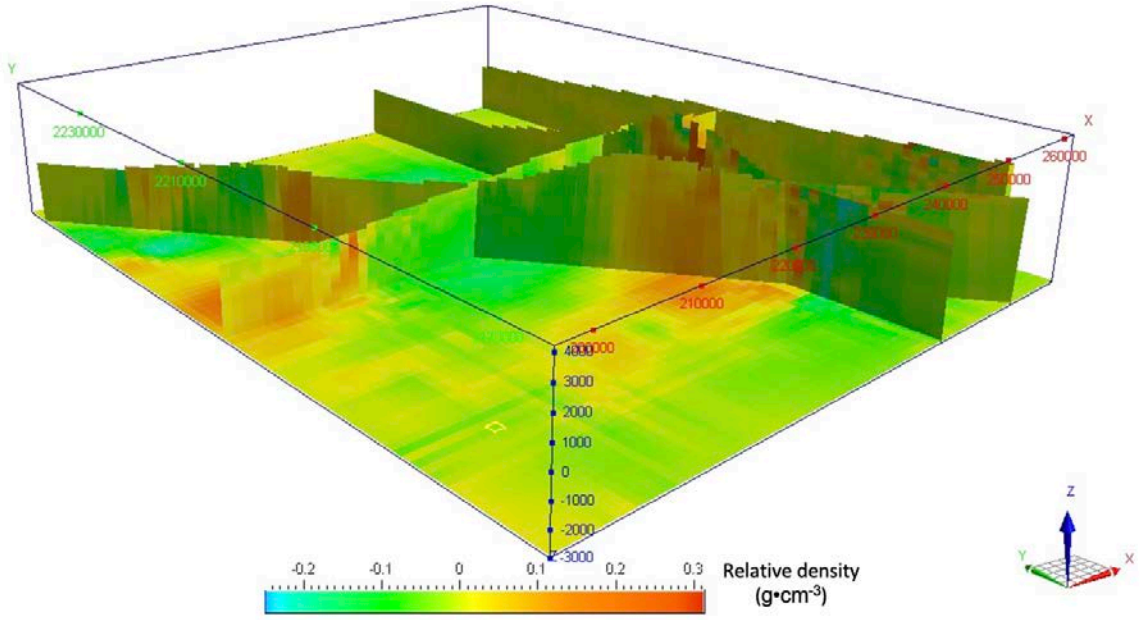

Figure 68. 3D distribution of relative density (g•cm^{-3}) after 12 iterations of the inversion.

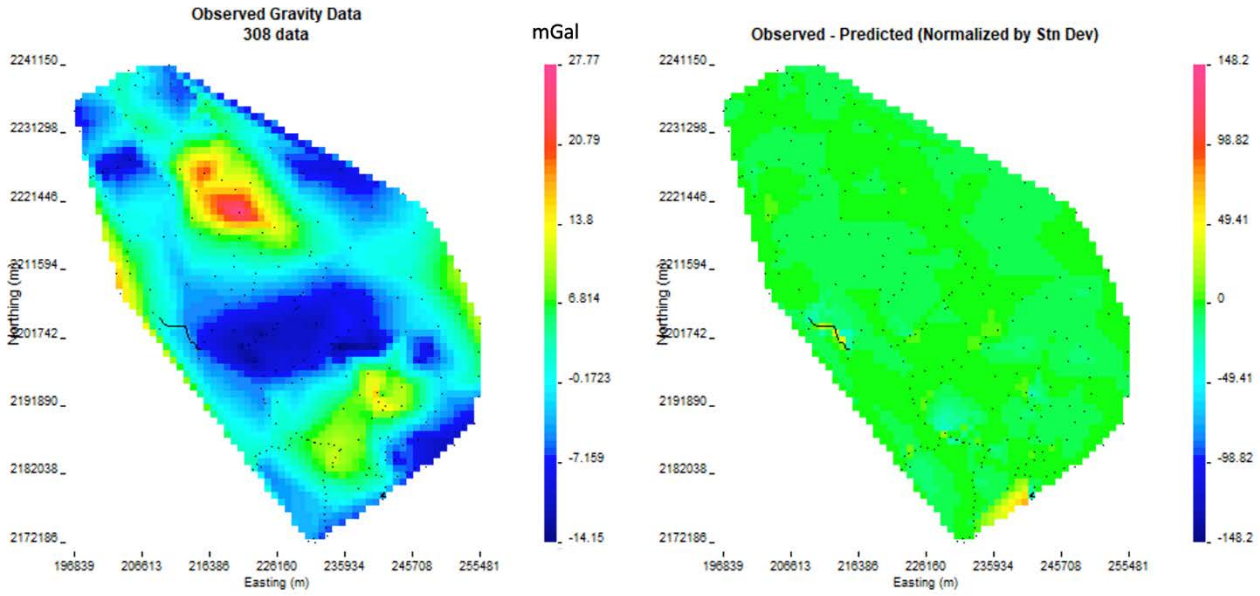

Figure 69. Comparison of the gravity anomaly predicted by the inversion and the observed residual CBA.

3.1.3.1 Density Profile at the MT Stations

For each MT station along the Saddle Road, the closest node of the modelled density grid was determined, and a density profile was extracted (absolute density vs. elevation). The results are summarized in a spreadsheet named "Density_Profiles_MTstations.xlsx," which can be used for comparing with or providing prior information for AMT/MT inversion.

3.2 Summary

In summary, in Phase 1, the PNNL team has made the following progress:

- Developed, tested, and implemented gravity 3D inversion for the PGV a process that can be migrated to LERZ
- Developed, tested, and implemented 1D AMT/MT inversion; results will be used as priors for 3D inversion
- 3D AMT/MT forward and inverse code has been developed and is ready to implement.

The research plan in Phase 2 will include:

- 3D gravity inversion covering LERZ
- 1D inversion at additional LERZ stations
- 3D AMT/MT inversion for all newly archived data
- 3D gravity/MT/seismic integration with structural coherence regulation.

4 Seismic Imaging

The island of Hawai‘i is very seismically active. Seismicity is not just limited to volcanic eruption centers but distributed throughout, and offshore from, the entire island. The seismicity represents various processes including volcanic events, dike intrusion, tectonic movement, and rebalance of crustal stresses from high erosion rates. Seismicity related to geothermal and volcanic fluid processes can have particularly distinct signatures, such as swarm type behavior. Analyzing statistical parameters of seismicity such as clustering can enable classification of seismicity and help to understand links to a potential geothermal resource.

The goals of this task included collecting, processing, and tomographically imaging passive seismic earthquake data from seismic stations in the vicinity of Kilauea volcano, the Southwest Rift Zone and ERZ, and the PGV. The objectives included the compilation of a database with seismic waveform data from 2012 to 2021, the processing of P- and S-wave phase arrival information, and the development of a 3D model of P- and S-wave velocity distribution, V_P/V_S ratio, and hypocenter locations of the processed seismicity. The relocated hypocenters clearly delineate the locations of the Kilauea caldera and its associated rift zones as well as a small cluster of seismicity below the PGV. Additionally, a deep cluster of seismicity located in the upper mantle between 30 km and 40 km depth is visible below the coastline, where the Southwest Rift Zone converges with the ocean.

The results of the velocity inversion are intended to reveal the delineation of tectonic features at depth that control the dynamics of the volcanic system, and to aid in the development of the 3D conceptual model. The results clearly show the structural boundaries of the Kilauea caldera with higher seismic velocities than the surrounding region from shallow to mid crustal depth, representing the magmatic intrusions that are ascending from lower crustal and upper mantle depths. At the same time, V_P/V_S ratio reveals lower than typical values in the near surface region, likely affected by gas in the shallow fracture system, and higher than usual values at mid-crustal depth, which may indicate molten magmatic intrusions in the volcanic system. While the Hilina Fault zone in the upper East Rift Zone does not reveal anomalous V_P/V_S ratio, the Koae Fault zone to the north reveals lower V_P/V_S values at shallow depth, again delineating the potential presence of gas in the shallow fracture system. The upper and lower East Rift Zones are characterized by a gradual increase in P- and S-wave velocities with depth and a discontinuous horizontal anomaly at 6 km depth with a pronounced increase to mantle velocities. This anomaly may represent the pathway of the magma along its way to the LERZ during the 2018 Kilauea eruption. An interesting feature is a high V_P/V_S anomaly below the PGV. This anomaly extends from mid-crustal to shallow depths below the PGV and may represent molten intrusions ascending from depth. This feature could be a potential target for future expansion of the geothermal resource.

4.1 Seismic Data Collection and Data Processing

For the current project, a study region was defined that included the Kilauea caldera, the Southwest and East Rift Zones and the PGV area. The study region is represented by the black rectangle in Figure 70, which shows the island of Hawai‘i, the distribution of permanent seismic stations on the island, and the preliminary hypocenter locations of 21,500 earthquakes that have been analyzed during the present study.

During this task, 24 GB of seismic waveform data from January 2012 to June 2021 for 96 seismic stations in the area of interest were collected from the IRIS Data Management Center. Data collection commenced with obtaining the USGS catalog for events in the study area from January 2012 to June 2021. This was followed by using Obspy (Beyreuther et al. 2010), requesting 40-second time windows of waveform data for all stations in the study area from the IRIS Data Management Center. The waveform data, in miniSEED format, were subsequently uploaded to the Data Foundry on Open EI.

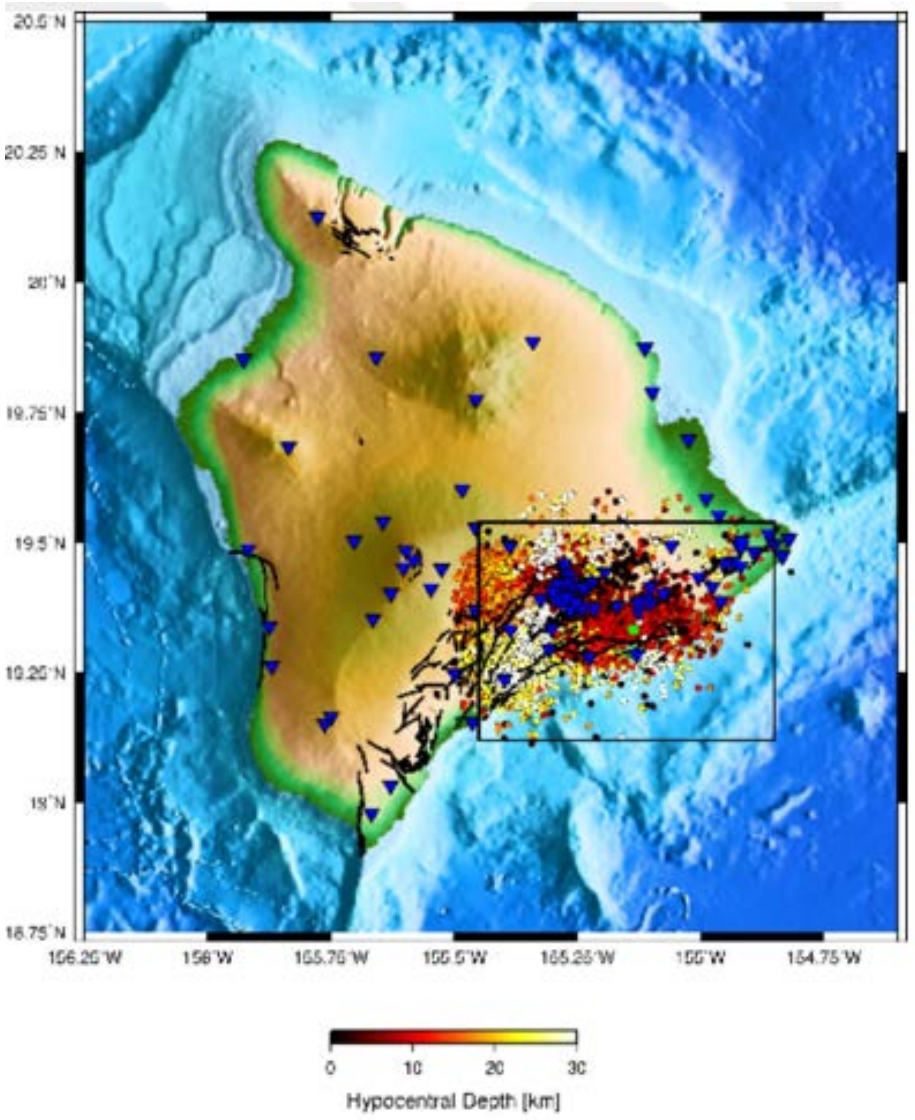

Figure 70. Map of the island of Hawai‘i with permanent seismic stations (blue triangles), the area of interest of the current study (black rectangle), and preliminary hypocenter locations of 21,500 earthquakes, color-coded by depth (colored circles).

Seismic data processing was based on PhaseNet (Zhu and Berosa 2019), a deep-neural-network-based seismic arrival-time picking method, and the Rapid Earthquake Monitoring & Analysis System (REMAS) code developed by Hutchings et al. (2011). PhaseNet uses three-component seismic waveform data as input and generates probability distributions of P arrivals and S

arrivals as output, based on thousands of analyst picks of California earthquake network data. The maxima in the probability distributions provide accurate arrival times for both P and S waves. PhaseNet has been shown to be applicable to earthquakes in areas other than California (Zhu 2022, personal communication) The REMAS software was subsequently applied to the PhaseNet output to perform event association, preliminary event location, moment magnitude, and estimation of phase travel time. All parameters were subsequently loaded into a database and input files were generated for tomographic imaging with the inversion code tomoFDD (Zhang and Thurber 2003; Gritto, Yoo, and Jarpe 2013). In addition to these input files, waveform cross correlations between events are computed for differential travel times and included in the inversion. The details of the processing are described in Figure 71 below.

The magnitude distribution of the processed events is presented in Figure 72. The magnitudes of most events range from M_w 1.0–4.0, with the maximum number of events at M_w = 2.3. The hypocenter depths of the preliminarily located events is presented in Figure 73a, while the depth of the relocated events is presented in Figure 73b. The preliminary locations were based on a simple location method assuming a 1D velocity model. After 3D inversion, the events exhibit a tri-modal distribution, with most events located from 0 km–5 km depth, intermediate events from 5 km–10 km depth, and deep events from 30 km–40 km depth. The latter group of events belongs to the Pāhala cluster, situated along the southern coast of Hawai‘i. It will be revisited in a latter section.

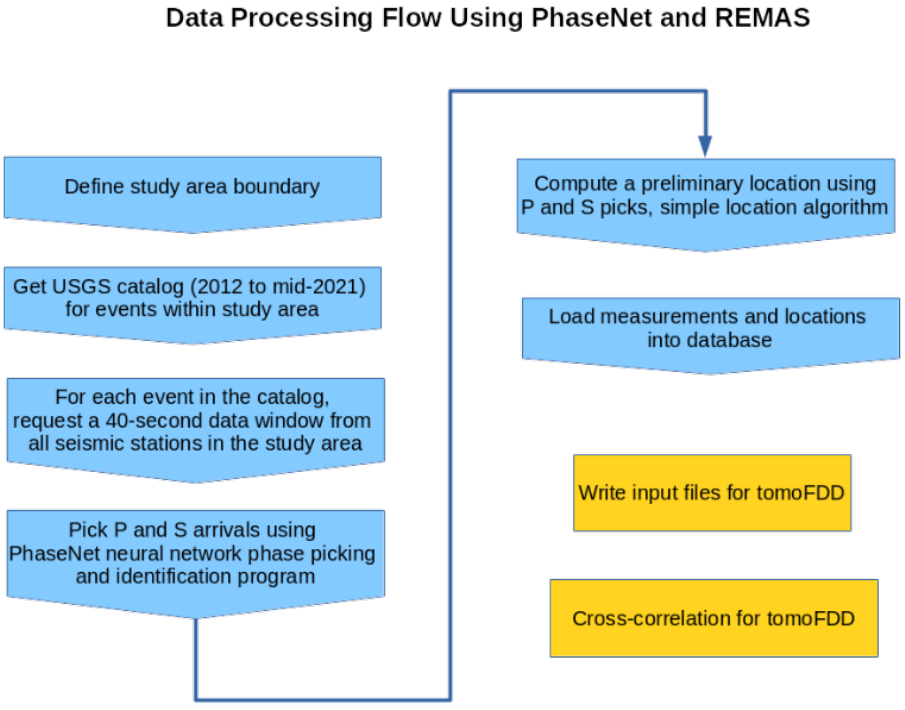

Figure 71. Schematic flow of seismic data processing with the software packages PhaseNet and REMAS.

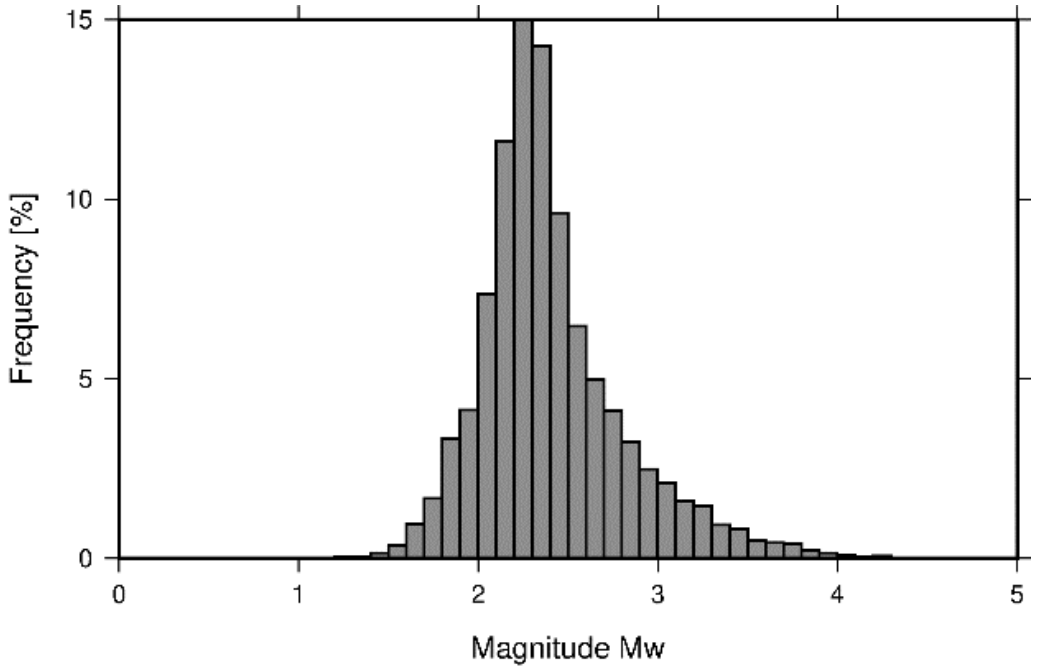

Figure 72. Histogram of the moment magnitude M_w of 21,500 events processed from January 2012 to June 2021.

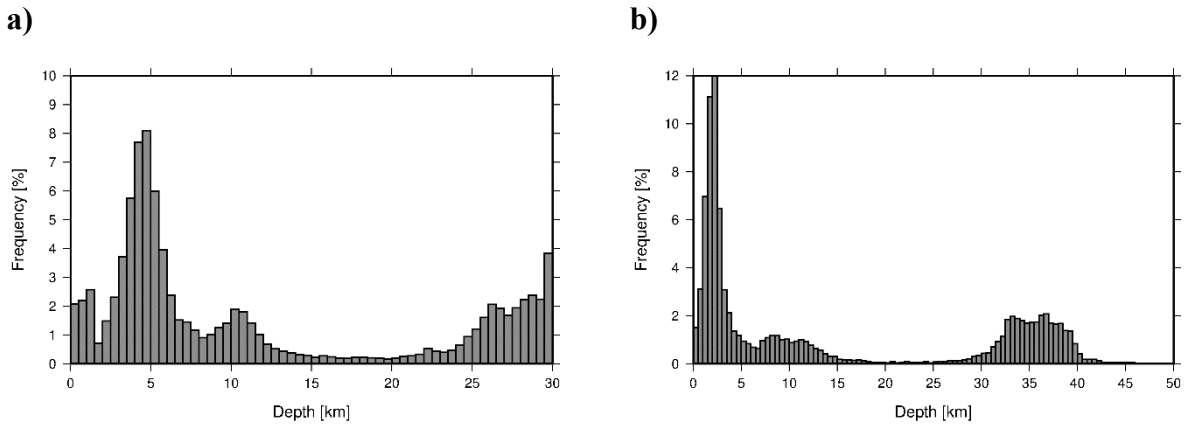

Figure 73. Hypocenter depths of 21,500 events processed between January 2012 and June 2021. (a) Preliminary event locations. (b) Post-inversion event locations.

4.2 Seismic Imaging

The phase data and preliminary earthquake locations are subsequently used to perform 3D joint inversion for P- and S-wave velocity structure, V_P/V_S ratio, and hypocenter locations. The inversion code tomoFDD takes advantage of dynamic memory allocation, which enables allocation and deallocation of memory for any field or array as they are accessed during computation. The advantage is that larger data arrays can be assigned during the inversion, because most are not accessed simultaneously. This is important for seismic imaging where high volumes of seismic travel time data from tens of thousands of earthquakes are typically

processed (Gritto, Yoo, and Jarpe 2013). Dynamic memory allocation and the use of the fast finite difference eikonal solver (Podvin and Lecomte 1991) make tomoFDD well suited for the current project where the combination of a high number of stations, a high volume of recorded earthquake data, and a high number of inversion nodes pose great demands on computer memory and CPU speed. The inversion of the current project is based on a node spacing of 1 km, while the forward modeling is based on a node spacing of 250 m (see below).

4.2.1 Starting Model

An appropriate starting model is important for the success of any data inversion campaign. In the current case, a 3D P- and S-wave velocity model, developed by Lin et al. (2014) for the Mauna Loa and Kilauea volcanoes, was utilized to generate a starting model for the study area. The node spacing of the Lin et al. (2014) model was 3 km, which was interpolated to 1 km in the current study because of the higher number of events and stations in the study area. A map of the study area including node spacing for the current inversion is presented in Figure 3.5. The map shows the study area denoted by the black rectangle along the southeastern coast of Hawai‘i. The locations of seismic stations, used in the current study, are shown by the blue triangles, while the locations of the Kilauea caldera and the PGV are marked by the yellow and green diamond, respectively. As mentioned above, the node spacing for the inversion step is 1 km, which is represented by the black dots in Figure 74. During the inversion, the forward modeling is based on a fast eikonal solver (Podvin and Lecomte 1991), which allows for a denser sampling of the 3D space, such that the node spacing for this step was chosen to be 250 m (represented by red dots in Figure 74). After the last iteration of the inversion, the final velocity models are interpolated from 1 km to 250 m to yield a smoother representation of the model. However, the resolution of the velocity estimates is still 1 km or larger. The dashed lines on the map represent transects along which the results of the velocity inversion will be shown in vertical direction in a later section.

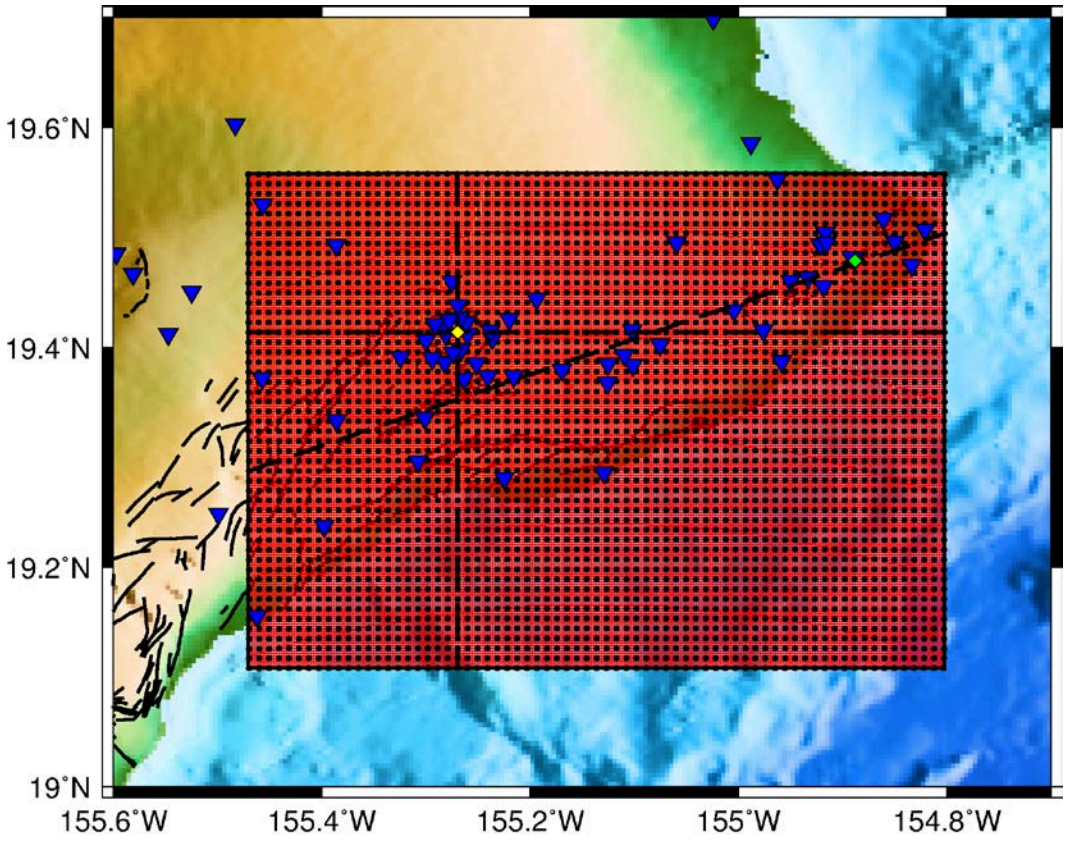

Figure 74. Map of the study area with node locations for the 3D inversion (black dots) and node locations for the forward modeling (red dots). The locations of the seismic stations used in the inversion are represented by the blue triangles, while the location of the Kilauea caldera and the PGV are given by the yellow and green diamond, respectively. The transects of vertical cross sections, along which the results of the seismic imaging will be shown in a later section, are given by the black dashed lines.

4.2.2 Model Resolution

After the node spacing is defined, the preliminary hypocenter locations of the earthquakes are known, and the locations of the seismic stations are given, the model resolution needs to be appraised. Model resolution is a measure of certainty with which a parameter is estimated relative to its neighbor. Model resolution depends on station and earthquake geometry, the node spacing, the number of unknowns (i.e., V_P and V_S estimates at each node, hypocenter coordinates of earthquakes, and event origin times) and the number of knowns (i.e., the travel time observations). As mentioned above, a node spacing of 1 km was selected and it must be determined how well this grid can resolve velocity features given the geometry of earthquake and recording stations for the current data set. To evaluate the resolution, a checkerboard test with ± 5% velocity contrast in P-wave (5 km/s ± 0.25 km/s) and S-wave (3 km/s ± 0.15 km/s) velocities was performed for neighboring squares. The length of each checkerboard square was 2 km, and each square was sampled by 4 nodes (2x2). Map views of the checkerboard models are presented in Figure 75, while cross sections along the transects A-A", B-B", and C-C" are shown in Figure 76. The cells along transect A-A" are not symmetrical, because the cross section traverses the regular-spaced cells at an oblique angle of 18°.

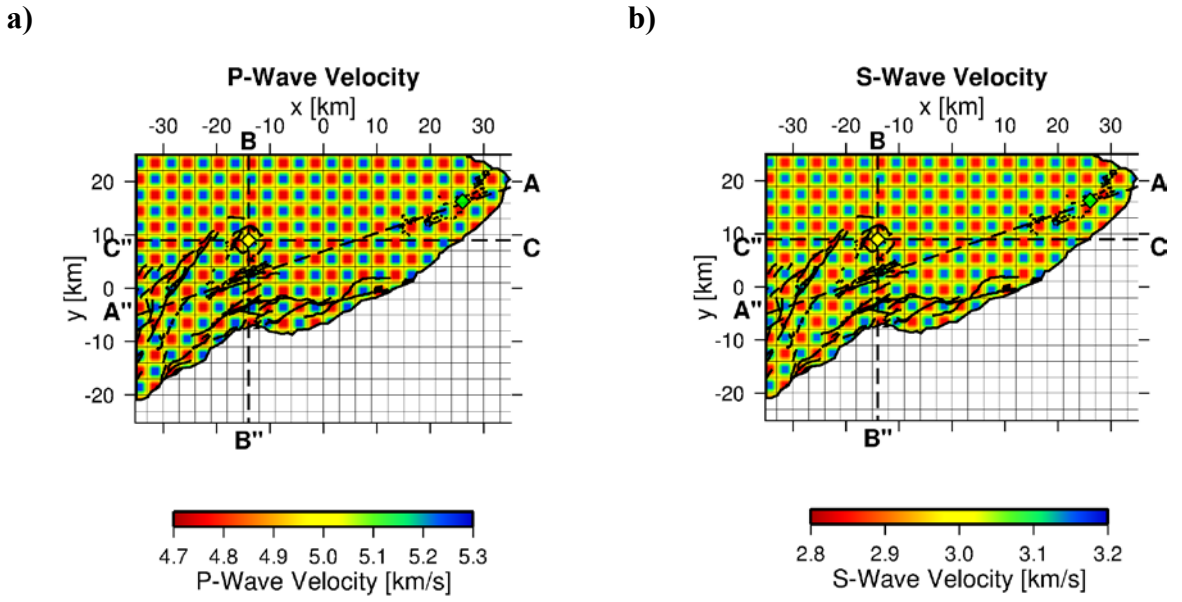

Figure 75. Map views of the Checkerboard model of the Study area. (a) P-wave velocity model. (b) S-wave velocity model.

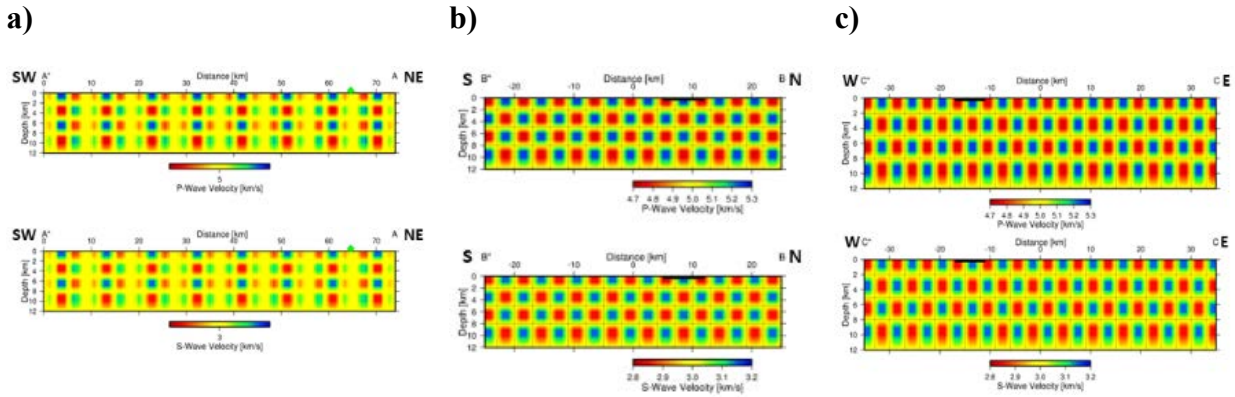

Figure 76. Cross-sectional views of the Checkerboard model of the study area. (a) Along transect A-A" in Figure 75. (b) Along transect B-B" in Figure 75. (c) Along transect C-C" in Figure 75.

For each observed P- and S-wave travel time pick associated with an earthquake and a recording station, theoretical travel times were calculated using the checkerboard as a starting model. Gaussian distributed noise of $\delta t = 0.025$ s (representing a picking error of approximately ¼ wavelength) was added to the data, while the standard deviation was set to $\sigma = 0.01$ s. The synthetic travel times were subsequently inverted in an attempt to recover the checkerboard pattern. The starting velocity model during this inversion step was a homogeneous model for both P- and S-waves at 5 km/s and 3 km/s, respectively.

The results of the inversion test are presented in Figure 77 and Figure 78 in horizontal slices at varying depth intervals from 1 km to 30 km. The results of the 3D velocity inversion are best resolved where the ray density is highest. Conversely, results are poorly or not resolved where

the ray density is low or zero, which results in yellow shading, i.e., the starting velocity model (V_p = 5.0 km/s and V_s = 3.0 km/s) is not updated during the inversion. Even though the number of P-wave phase picks is ~ 30% higher that of the S-waves, their spatial distribution is similar, which is reflected in the checkerboard results. The best-resolved regions are in the central study area, around Kilauea caldera and to the south towards the coast. The region north of Kilauea is not resolved due to the paucity of seismicity and seismic stations (see Figure 70). The best resolution is obtained between 10 and 15 km, where the ray density is specifically high, due to the P- and S-waves being refracted across the Moho discontinuity. It is noted that the amplitudes of the velocity estimates are relatively well recovered for both P- and S-waves.

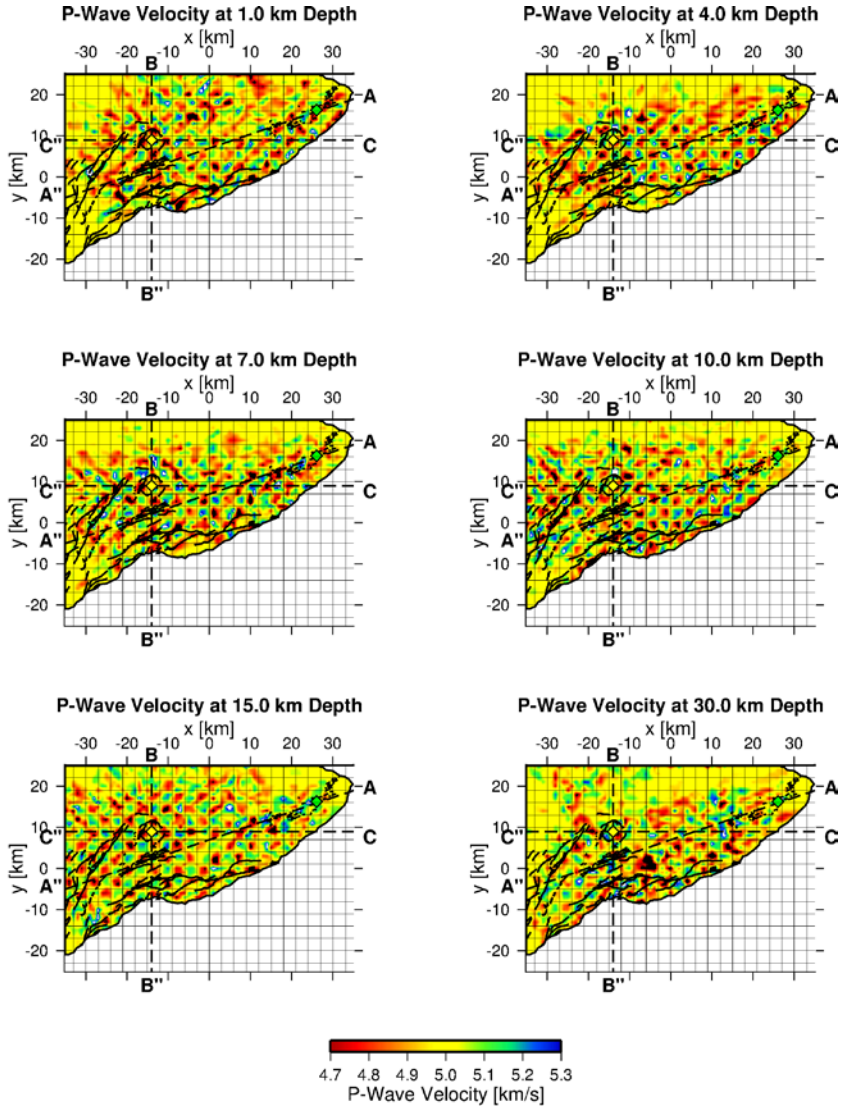

Figure 77. Map view of the checkerboard inversion results for the P-wave velocity in the study area.

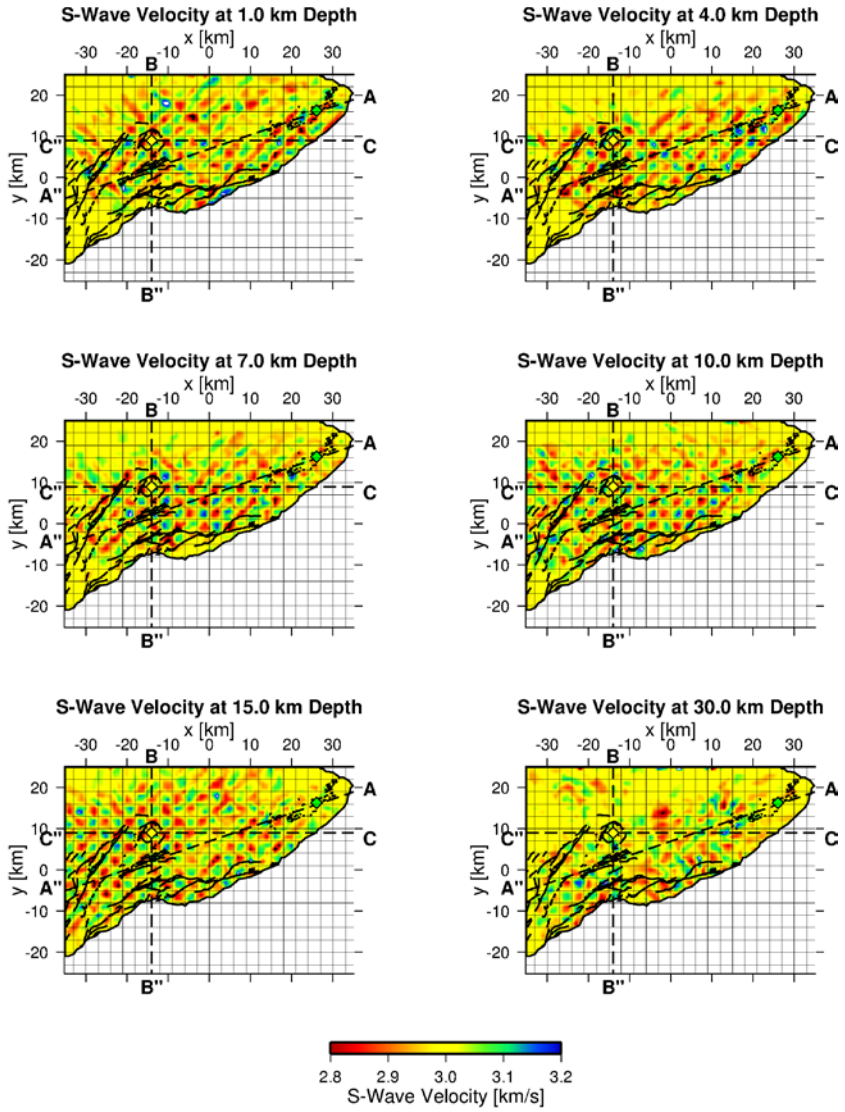

Figure 78. Map view of the checkerboard inversion results for the S-wave velocity in the study area.

The results of the inversion test in cross-sectional view are presented in Figure 79. Again, regions with a lack of seismicity or seismic stations are not resolved, resulting in yellow colors. This effect can be seen in Figure 79b, where the northern section has neither seismicity nor seismic stations, while the southern section is off the coast (see Figure 78). Despite the low resolution along the margins of the study area, the changing pattern from positive to negative anomalies in neighboring cells can be traced across the checkerboard model. The results of the checkerboard test reveal streaking between the red cells containing low-velocity anomalies. This is caused by the propagation of the seismic waves through the model, which tend to follow the fastest path from the earthquake to the seismic station (i.e., the blue cells). As a consequence, the cells with high-velocity anomalies are favored by the rays, while the low-velocity cells are less favored, which caused lower resolution in the latter case.

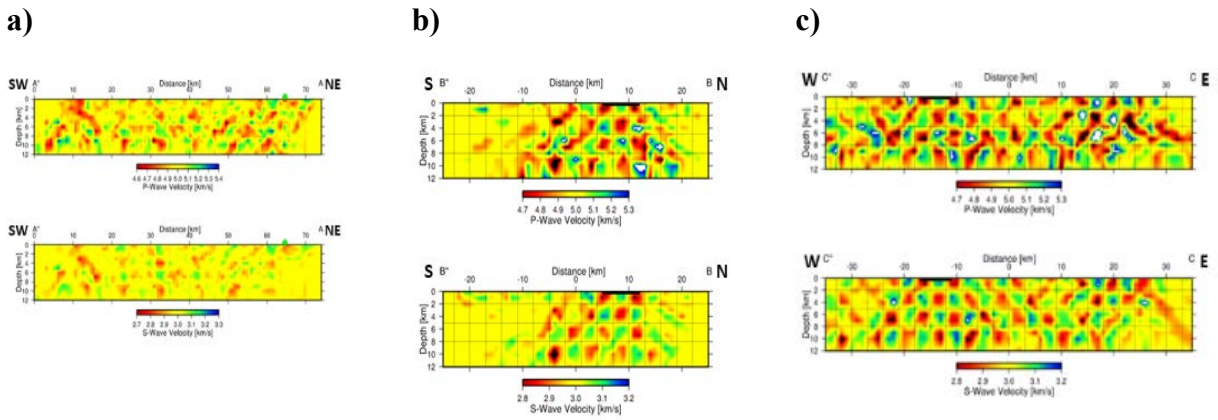

Figure 79. Cross-sectional views of the checkerboard inversion results in the study area. (a) Along transect A-A" in Figure 75. (b) Along transect B-B" in Figure 75. (c) Along transect C-C" in Figure 75.

4.2.3 Seismic Inversion

4.2.3.1 Misfit Function

The inversion program tomoFDD uses damped least-squares to solve the inverse problem. During the inversion, the program computes the differences between theoretically computed and observed travel times and minimizes the misfit in a least-squares sense. This is done iteratively based on the starting velocity model. After each iteration the program updates the earthquake location, origin time, and velocity models until a sufficiently small misfit between theoretically computed and observed travel times is achieved. The goal is a velocity model that is smooth in a geological sense, which is achieved by halting the inversion when the misfit does not change much between iterations. The misfit curve of the current inversion is presented in Figure 80. The four curves represent the absolute and weighted misfits of the mean and the variance. The misfit of each parameter decreases quickly, such that the inversion is stopped after four iterations. The fast decrease in misfit can be attributed to the 3D starting model, which is a good representation of the geology and tectonics in the study area.

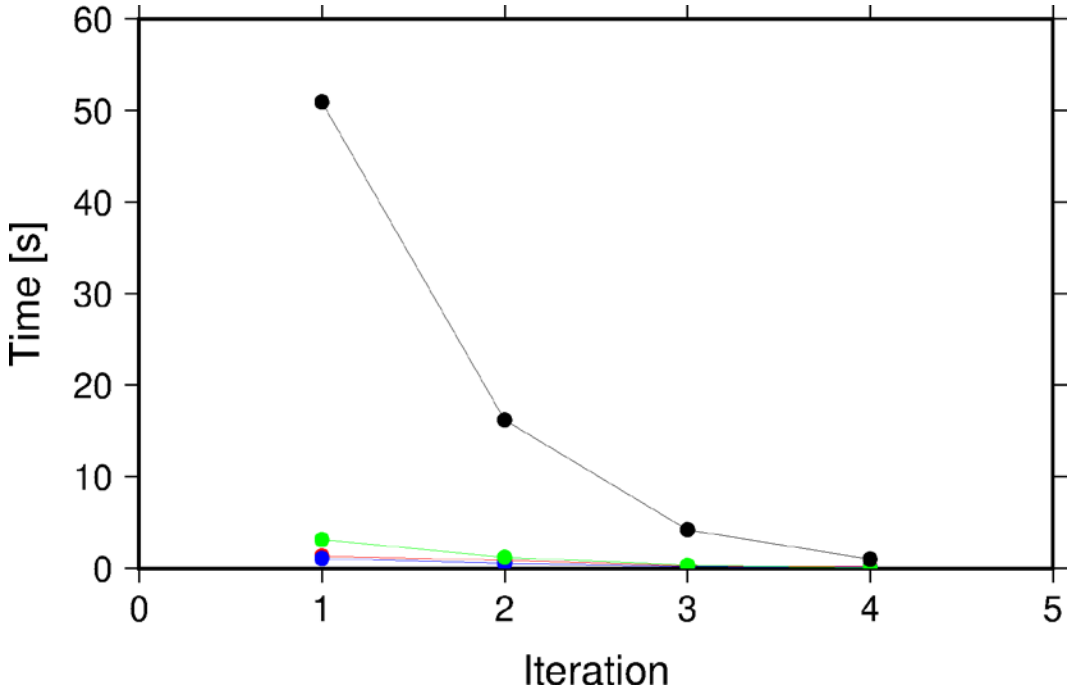

Figure 80. Weighted travel time misfit between theoretically computed and observed travel times as a function of number of iterations. The curves represent misfit of absolute mean (red), misfit of weighted mean (blue), misfit of absolute variance (black), and misfit of weighted variance (green).

4.2.3.2 Earthquake Hypocenter Relocation

The 3D seismic inversion jointly solves for hypocenter locations and the P- and S-wave velocity structure. The earthquake locations are presented in Figure 81, which shows a map view of the study area with major tectonic features. The black dots represent the epicentral distribution of the preliminary and post-inversion earthquake locations derived from the processing of waveform data. It can be seen that the events are spatially associated with the tectonic features. The Kilauea caldera is demarked by a high rate of seismicity, as are the various surrounding rift and fault zones. The most noticeable difference between the pre- and post-inversion event locations is the cluster of events in the southwestern corner of the study area. This is the deep Pāhala cluster which was visible in the histogram of focal depth in Figure 73b. It is located between 30 km and 40 km depth below the coast of Hawai‘i. Also noticeable is the lack of seismicity around the PGV, which will be revisited later.

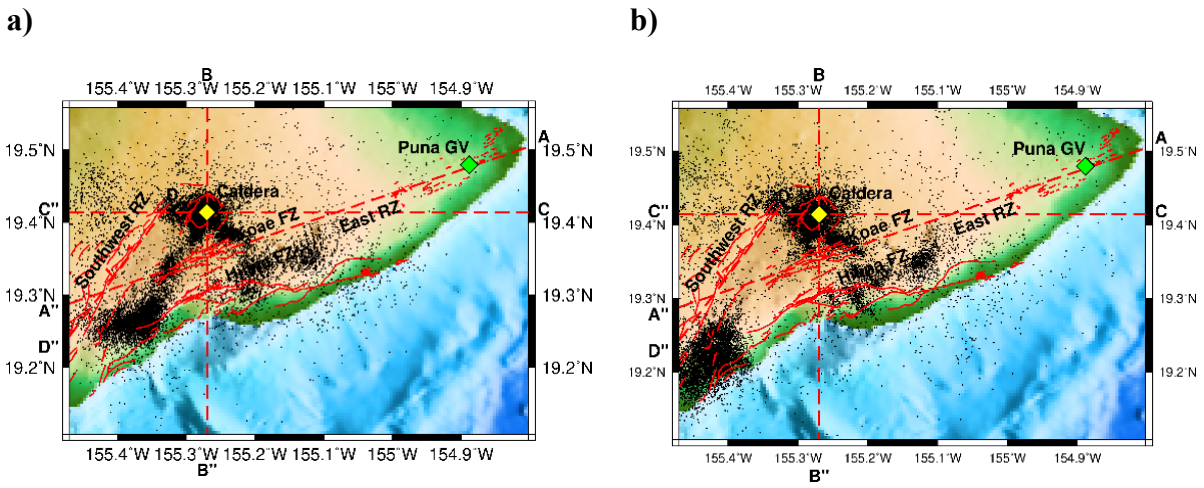

Figure 81. Map view of the study area with major tectonic features and earthquake locations (black dots). Transects of cross section are shown by red dashed lines, and Kilauea caldera and PGV by the yellow and green diamonds, respectively. (a) Preliminary location. (b) Post-inversion locations.

4.2.3.3 Application of V_P/V_S-Ratio in Past Studies

Seismic tomography studies have been used in the past to delineate geological and tectonic structure in various tectonic settings. In those studies, images of P- and S-wave velocities typically delineate the large-scale structure of such regions. In addition, the ratio between P- and S-wave velocity (V_P/V_S) can be used to map regions of gaseous versus liquid saturation. The V_P/V_S ratio of a perfectly elastic rock without fractures has a value of approximately 1.73. If fractures are introduced and these fractures are saturated with a liquid fluid such as water, or the rock is partially molten as in volcanic magma, the S-wave velocity decreases due to the reduced rigidity, and V_P/V_S increases. However, if the fractures are filled with a gaseous liquid such as steam in geothermal reservoirs or air-filled fault zones in the near subsurface, the P-wave velocity decreases strongly due to the reduced compressibility of the gaseous fluid and V_P/V_S decreases. It is typically assumed that $V_P/V_S > 1.8$ indicates the presence liquid fluids, while $V_P/V_S < 1.6$ indicates the presence of gaseous fluids.

Applications of studies using V_P/V_S include imaging fluids such as oil, water, and CO_2 in second and tertiary oil recovery (Gritto, Romero, and Daley 2004), tracing the movement of fluids associated with volcanic swarms (Dahm and Fischer 2013), imaging fluids in fault zones (Lin and Shearer 2007) and mapping the presence of liquid and gaseous fluids in geothermal reservoirs (Lin and Shearer 2009; Gritto, Yoo and Jarpe 2013; Gritto and Jarpe 2014). A compilation of studies in volcanic and sedimentary setting, where V_P/V_S has been used to map gaseous fluids in the subsurface, is compiled in Table 9. The fluids include water and steam in geothermal settings, melt and CO_2 in volcanic settings, and water and supercritical CO_2 in an oil and gas reservoir. These applications show the usefulness of V_P/V_S ratio in distinguishing between liquid and gaseous fluid in the subsurface. In the following, the V_P/V_S ratio will be used to interpret the seismic imaging results of Kilauea volcano and its surrounding tectonic regions.

Table 9. Compilation of Studies in Volcanic Regions Where V_P/V_S Is Used to Identify Gaseous Fluids. Yellow Highlighted References Denote Studies that Have Been Conducted in Volcanic Regions.

Study	Location	Purpose	Fluid
Julian et al., 1996	The Geysers, CA	Geothermal	Steam
Gunasekera et al., 2003	The Geysers, CA	Geothermal	Steam
Gritto et al., 2004	Lost Hills, CA	Oil Recovery	CO_2 (supercritical)
Husen et a., 2004	Yellowstone, WY	Volcanism	Melt/Gas
Lin and Shearer, 2007; 2009	Southern California, CA	So. Cal/San Andreas Fault	Water
Dahm and Fischer, 2013	Western Bohemia, CZ	Volcanism	Melt/CO_2
Lin, 2013	Long Valley, CA	Volcanism	CO_2 (degassing Mammoth Mt.)
Gritto et al., 2013	The Geysers, CA	Geothermal	Water/Steam
Zhang and Lin, 2014	Coso, CA	Geothermal	Water/Steam
Gritto and Jarpe, 2014	The Geysers, CA	Geothermal	Water
Bachura and Fischer, 2016	Western Bohemia, CZ	Volcanism	Melt/CO_2
Lin and Wu, 2018	The Geysers, CA	Geothermal	Steam

4.2.3.4 Seismic Tomography Results From Processing of Waveform Data

The first 3D inversion of seismic data was performed with P- and S-wave phase arrival times obtained through processing the seismic waveform data from 2012 to 2021. The processing resulted in 21,500 earthquakes, 310,000 P-wave phase arrivals, and 210,000 S-wave phase arrivals. The data were subsequently used to perform a 3D joint inversion to derive earthquake hypocenter locations and distributions of the 3D P- and S-wave velocity structure.

The results of the 3D velocity inversion are presented in map view for selected depth intervals in Figure 82. As before, the transects of vertical cross sections are denoted by red dashed lines, while the locations of the Kilauea caldera and the PGV are indicated by the yellow and green diamonds, respectively. At shallow depth (1 km), Kilauea caldera and its surrounding areas are delineated by higher P-wave (2.5 km/s) and S-wave (1.5 km/s) velocity estimates compared to background values. At 3 km depth, the Hilina Fault zone and the Southwest Rift Zone are recognized by lower-than-average velocities (V_P = 4.0 km/s; V_S = 2.5 km/s). At a mid-crustal depth of 6 km, the Kilauea volcano and associated magmatic flows are characterized by upper mantle velocities (V_P >7.0 km/s; V_S = 4.5 km/s), which indicates the presence of magmatic intrusions from the lower crust or upper mantle. The magmatic flows trend in a northwest direction and along the upper ERZ. The V_P/V_S ratio reveals low estimates (1.5) in the Kilauea caldera and in the Koae Fault zone at 1 km depth. These may be associated with gases that dissolve from the magmatic intrusions during their ascension from depth. At greater depth (3 km and 6 km), V_P/V_S exhibits higher values (1.9) below Kilauea and the Koae Fault system. Similar to the estimates of the seismic velocities, these values may indicate the presence of melt.

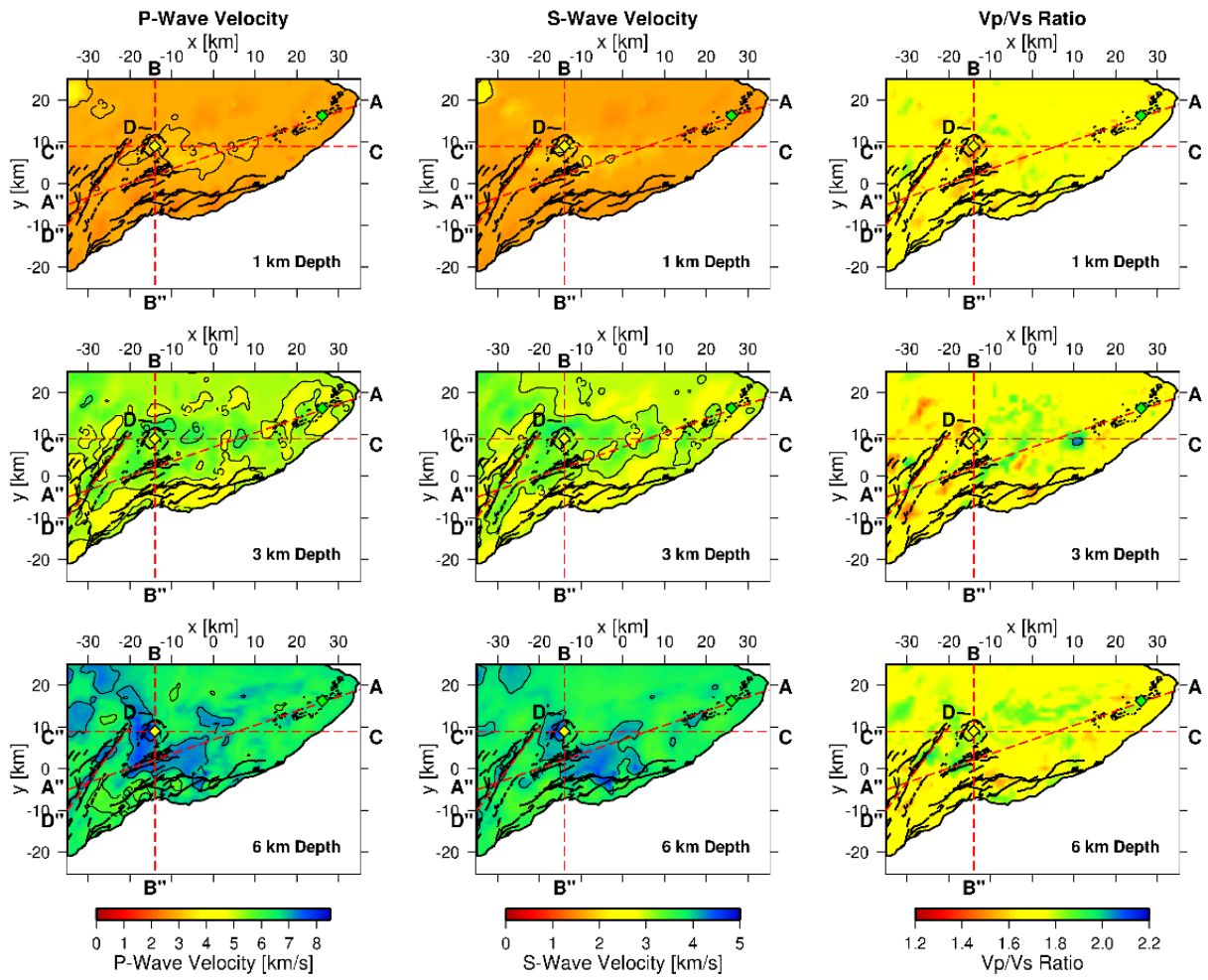

Figure 82. Map view of the seismic inversion results from processing of waveform data at selected depth intervals.

The results of the inversion in cross-sectional view are presented in Figure 83. The location of the cross sections are given by the red dashed lines in Figure 82. Figure 83a shows the results for the ERZ. The major tectonic features are noted at the top of the cross section. The P- and S-wave velocities are characterized by a gradual increase from surface to depth. The locations of the Southwest Rift zone, the Koae Fault zone, and the PGV reveal lower estimates (V_P = 2.5 km/s, V_S = 1.5 km/s) than the surrounding areas. At mid-crustal depth (6 km) both P- and S-wave velocities show anomalous highs (V_P >7.0 km/s, V_S = 4.5 km/s) below the Southwest Rift zone and below the Koae Fault zone. They may represent the presence of magmatic intrusions into these fault systems. The V_P/V_S ratio reveals low values (1.5) below the Koae Fault zone at shallow depth (1km), while the Southwest Rift zone does not display anomalous estimates. However, at mid-crustal depth (6 km) the V_P/V_S ratio shows high values (1.9) below the Southwest Rift zone, below the Koae Fault zone and further to the east. A faint high V_P/V_S anomaly (1.9) is visible below the PGV at mid-crustal depth. These high V_P/V_S anomalies support the interpretation of the presence of magmatic melt throughout the ERZ. The cross sections through Kilauea caldera in north-south direction are presented in Figure 83b. It can be seen that at shallow depth (1 km), Kilauea caldera is represented by velocity values (V_P = 4.5 km/s, V_S = 2.5 km/s), which are higher than in the surrounding region, whereas the Koae and

Hilina Fault zones are characterized by low velocity values (V_P = 2.5 km/s, V_S = 1.5 km/s). At mid-crustal depth below Kilauea caldera and Koae Fault zone, V_P and V_S show the same distinct high velocity values that were already visible in the map views in Figure 82. The V_P/V_S ratio shows a distinct low (1.5) below the caldera and the Koae Fault system at shallow depth (1 km) and an anomalous high (1.9) below the caldera at mid-crustal depth. Finally, the cross sections through Kilauea caldera in east-west direction are presented in Figure 83c. The results confirm the previous observations of higher-than-normal velocities throughout the caldera at shallow depth (1 km) and a distinct high-velocity anomaly at mid-crustal depth. The Southwest Rift Zone is recognized by low velocity anomalies in the shallow crust at 1 km depth. The V_P/V_S ratio shows low estimates (1.5) at shallow depth below the caldera, underlain by higher values (1.9) at mid-crustal depth.

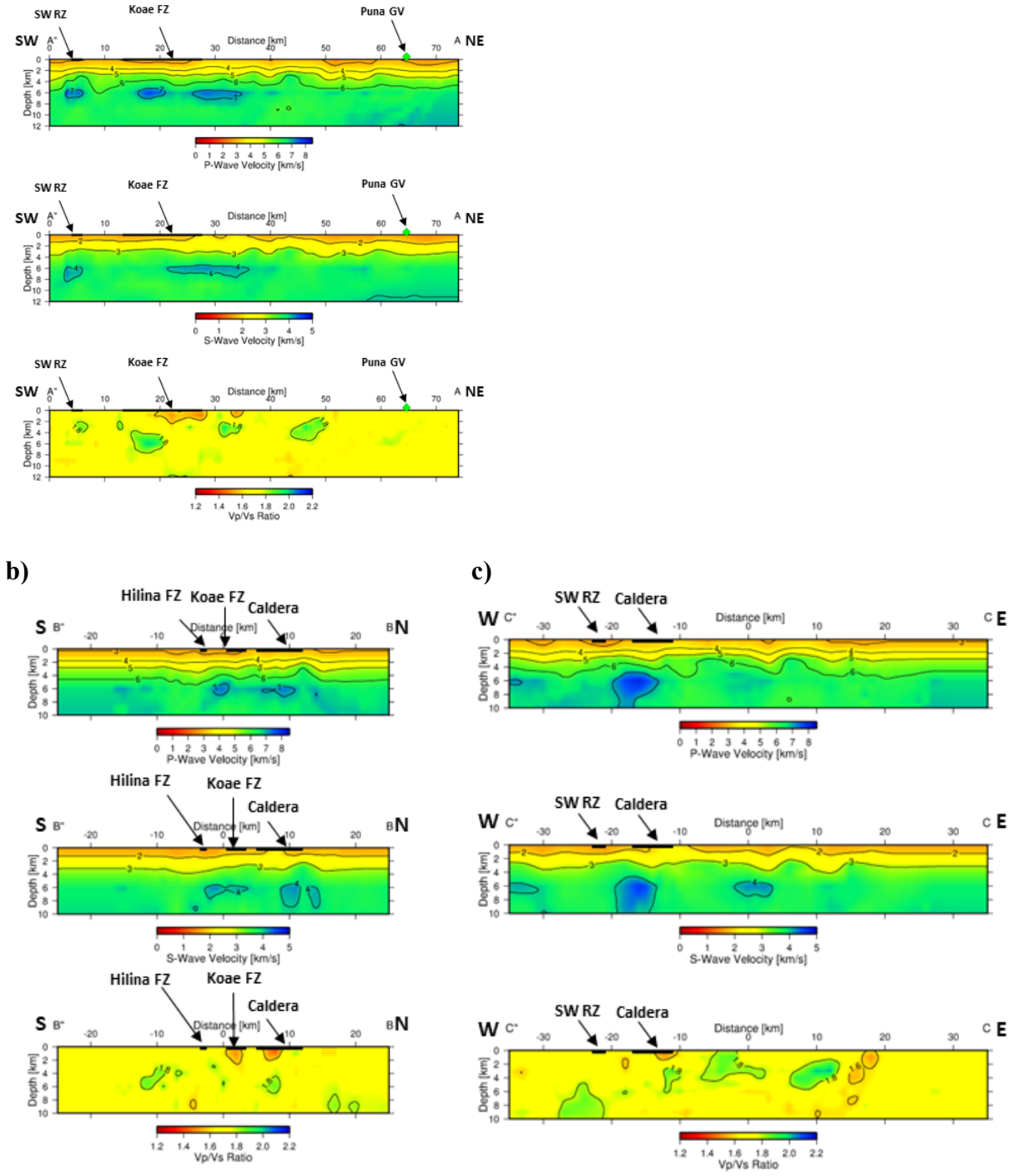

Figure 83. Cross-sectional views of the seismic inversion results from processing of waveform data in the study area. (a) Along transect A-A" in Figure 82. (b) Along transect B-B" in Figure 82. (c) Along transect C-C" in Figure 82.

4.2.3.5 Seismic Tomography Results From Processing of Hawaiian Volcano Observatory Catalog Data

A 3D seismic inversion was conducted using HVO catalog data to independently confirm the results obtained from the analysis of waveform-derived travel time data presented in the last section. The HVO data offer the advantage that the event locations are analyst reviewed and that some of these events are located in the LERZ, close to the PGV, thus supplementing the seismic coverage in this particular area of interest. The HVO data consist of 8,300 events with 180,000 P-wave and 60,000 S-wave phase arrival times. The event locations after 3D inversion are shown in Figure 84. Although there are fewer events in comparison to the results in Figure 81b, the event locations clearly delineate the Kilauea caldera and potential zones of magmatic intrusion extending radially from the caldera in southwest and southeast directions. Additional events along the LERZ, and particularly to the northeast of the PGV, will improve the resolution of the seismic inversion results.

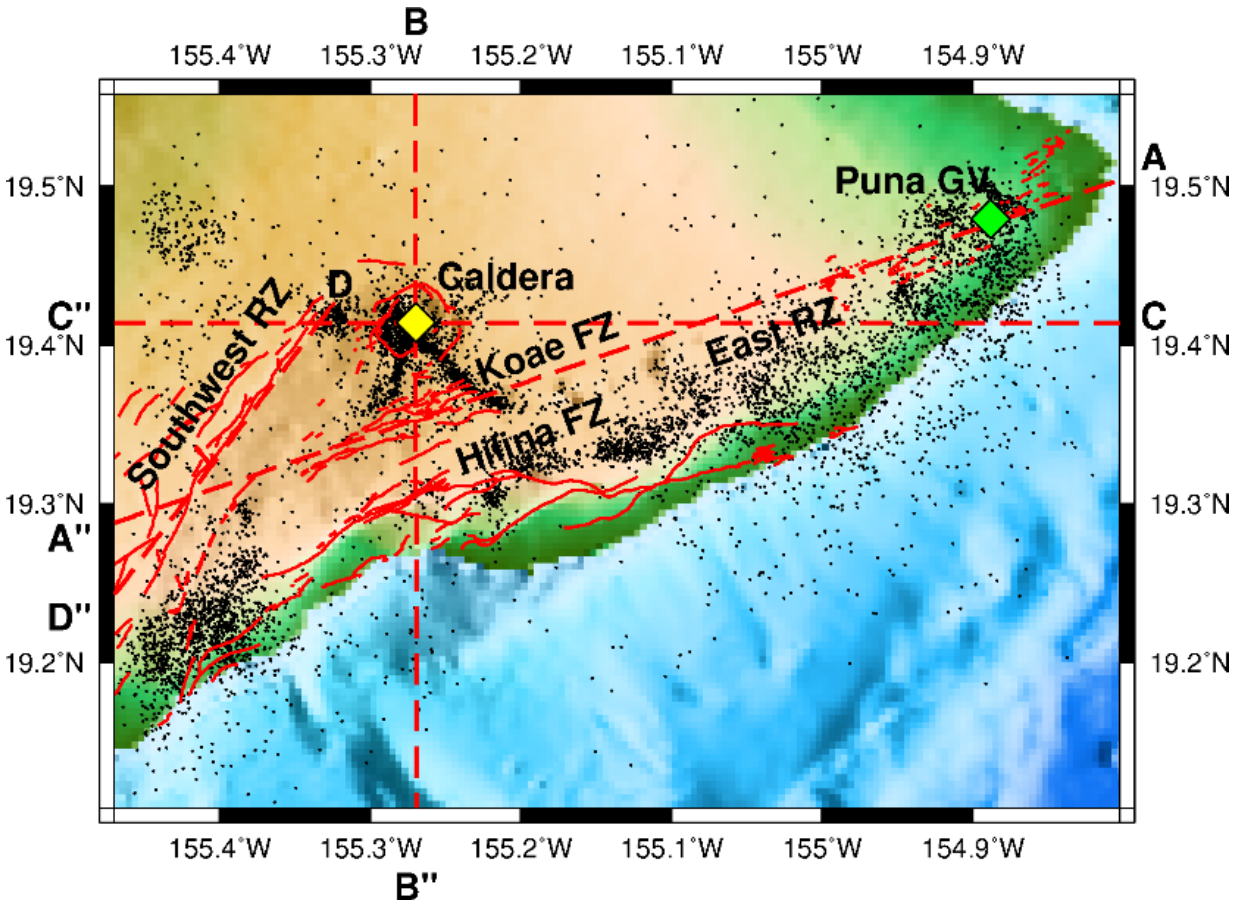

Figure 84. Map view of the study area with major tectonic features and post-inversion earthquake locations (black dots) derived from HVO catalog data. Transects of the cross section are shown by red dashed lines; the Kilauea caldera and PGV are shown by the yellow and green diamonds, respectively.

The results of the 3D velocity inversion of HVO catalog data are presented in Figure 85 in map view for selected depth intervals. The results mimic those derived from the inversion of processed waveform data, with anomalies of similar magnitude located in the same locations. Some of the high velocity anomalies at 6 km depth around the Kilauea caldera, in the Southwest Rift zone, and particularly in the ERZ appear more expansive, owing to the higher number and more concentrated locations of the earthquakes in these areas (see Figure 81b and Figure 84).

The results of the inversion of HVO catalog data in cross-sectional view are presented in Figure 86. As before, the major tectonic features are denoted along the top of the profiles. Overall, the anomalies shown in the cross sections are similar in amplitude and location to those derived from the inversion in Figure 83. However, there are some differences in the amplitude of the anomalies along the ERZ (Figure 86a). The high anomalies in P- and S-wave velocity (V_P >7.0 km/s, V_S = 4.5 km/s) at 6 km depth are more pronounced than in Figure 83a. In the P-wave velocity panel, below the Koae Fault zone, a vertical anomaly appears from lower-crustal depth joining the horizontally trending anomaly at 6 km depth. A potential interpretation could be that of an upwelling of magmatic intrusions from the upper mantle into the ERZ. The anomalies of the V_P/V_S ratio in Figure 86a appear more pronounced than those in Figure 83a. The increase in magnitude amplifies the high V_P/V_S anomaly (1.9) that is visible below the PGV. It is possible that the anomaly delineates low viscous rock, such as magmatic melt, that ascends from mid-crustal depth to shallower parts of the crust below the PGV. The increase in the amplitude of the anomalies is also visible in the north-south and the east-west and cross sections (see Figure 83b and Figure 86b; Figure 83c and Figure 86c).

Overall, the results of the 3D inversion of processed HVO catalog data independently confirm the results derived from inverting the processed waveform data. In addition, the inversion of HVO data reveals more detail about the magnitude of the anomalies, allowing for a more detailed interpretation of the tectonic structure along the ERZ.

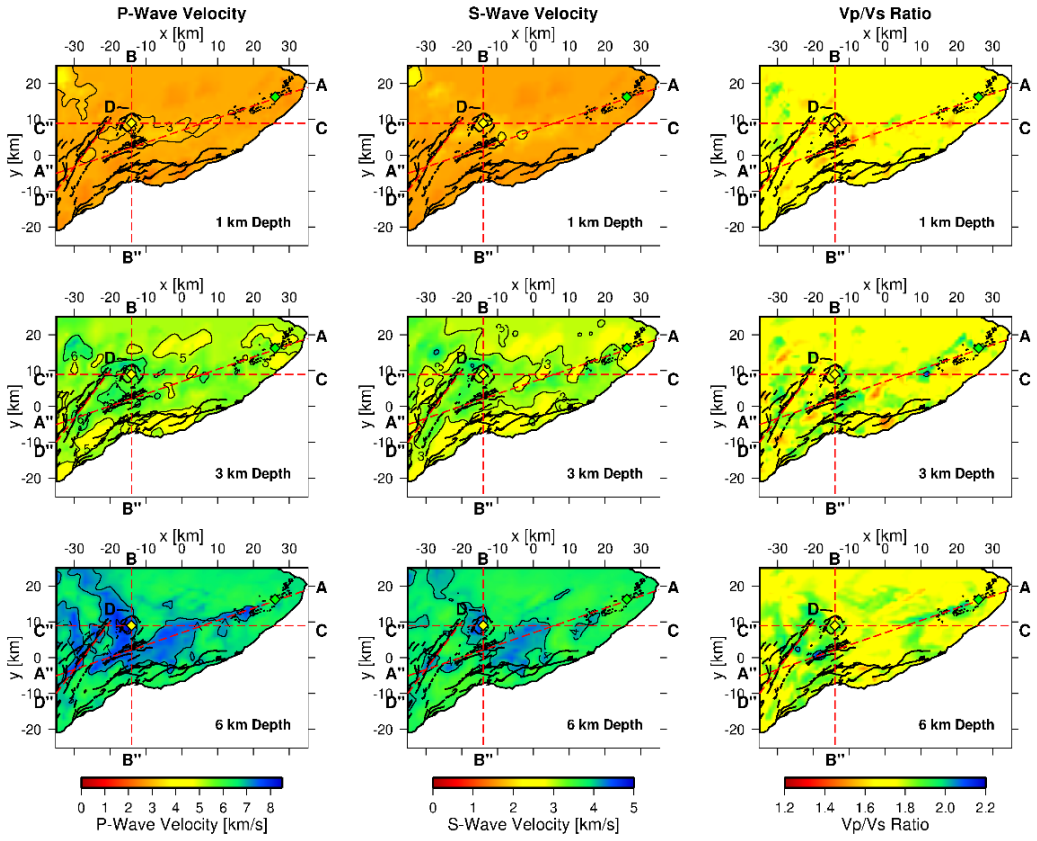

Figure 85. Map view of the seismic inversion results from processing of HVO catalog data at selected depth intervals.

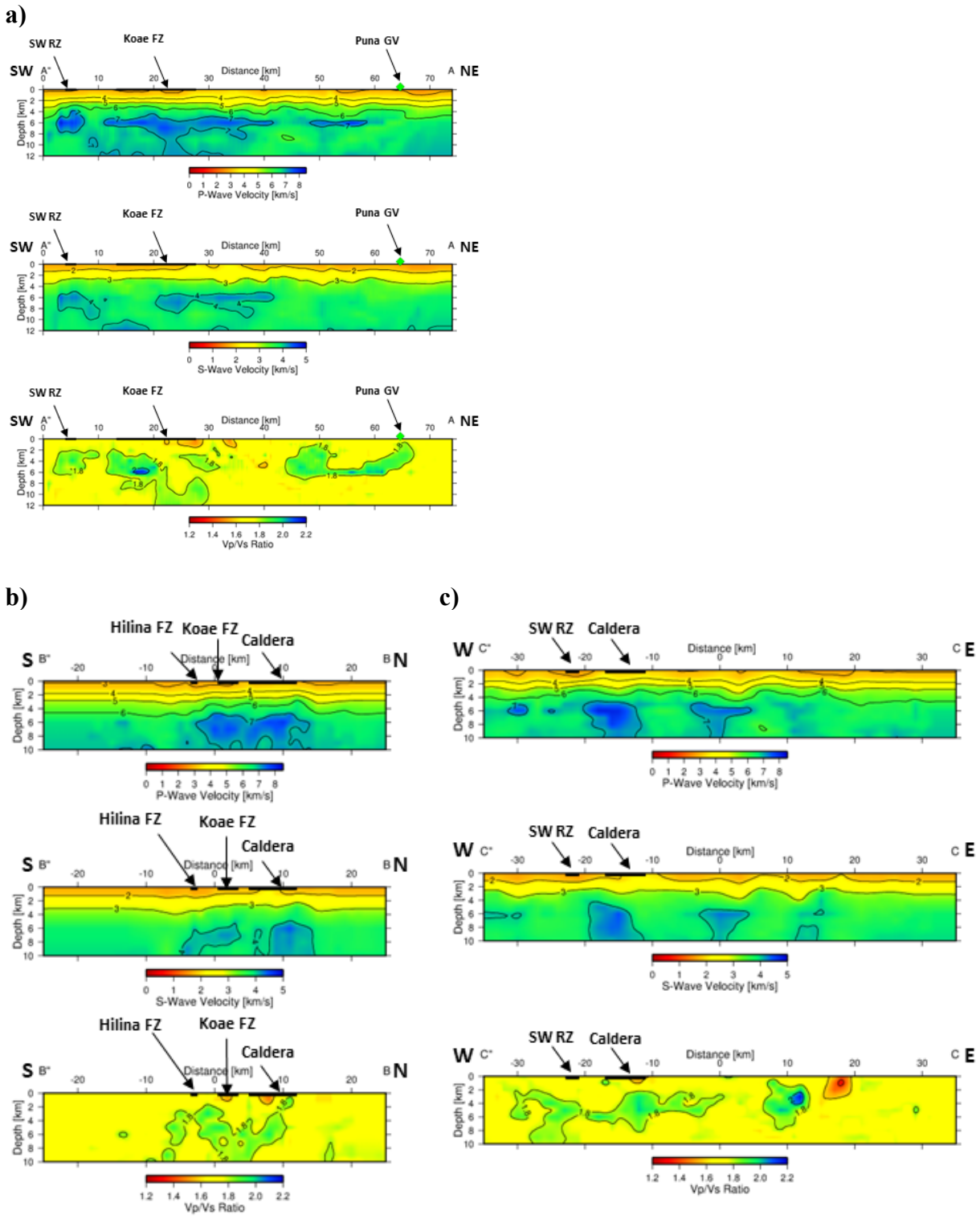

Figure 86. Cross-sectional views of the seismic inversion results from processing of HVO catalog data in the study area. (a) Along transect A-A" in Figure 85. (b) Along transect B-B" in Figure 85. (c) Along transect C-C" in Figure 85.

4.2.3.6 Seismic Tomography Results From Combined Processing of Waveform and Hawaiian Volcano Observatory Catalog Data

In a final step, a 3D seismic inversion was conducted using a combined data set of waveform-derived phase arrivals and HVO catalog data. This inversion is intended to combine the benefits of each data set, which offer good earthquake coverage in various areas. Because the events in each data set had different ID numbers, the event origin times were used to select unique events from both data sets. In this case, only those events were selected that had origin times that differed by a minimum of six seconds. This selection resulted in 25,600 unique events that formed the basis for the inversion of the joint data set.

The relocated events are presented in Figure 87. The seismicity delineates the major tectonic features of the study area, including the Pāhana cluster in the southwest, and the LERZ in the vicinity of the PGV.

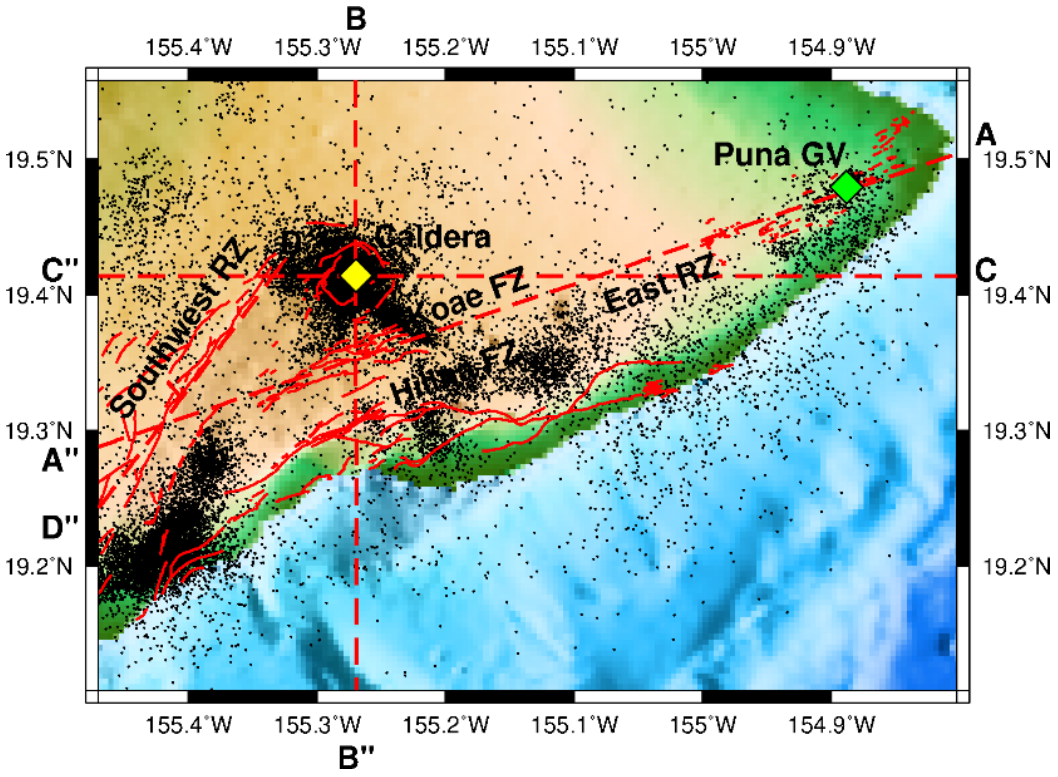

Figure 87. Map view of the study area with major tectonic features and post-inversion earthquake locations (black dots) derived from the joint inversion of phase data from the analysis of waveforms and HVO catalog data. Transects of cross section are shown by red dashed lines, and Kilauea caldera and PGV by the yellow and green diamonds, respectively.

The results of the 3D velocity inversion of the joint data set are presented in Figure 88 in map view for selected depth intervals. The images combine the features visible in the previous inversions (Figure 82 and Figure 85) with similar locations of the anomalies and associated amplitudes.

The results of the inversion of the joint data set in cross-sectional view are presented in Figure 89. There are some differences from the previous inversion result, notably the absence of the

vertical anomaly in the P-wave velocity in the ERZ (Figure 89a) that would indicate a potential upwelling of magmatic material from the lower crust or the upper mantle. Nevertheless, the horizontal high-velocity anomalies in the P- and S-wave velocities are still significant in the cross section along the ERZ (Figure 89a). The high V_P/V_S anomaly trending from mid-crustal to shallower depth below the PGV is still visible, but its amplitude is slightly reduced (Figure 89a). The differences from the previous inversion results are most pronounced in the southeast-northwest cross section along the ERZ because the difference in the number and distribution of earthquakes relative to the previous inversions is most notable here. At the same time, the differences in the north-south and east-west cross sections from the previous inversion results are minimal.

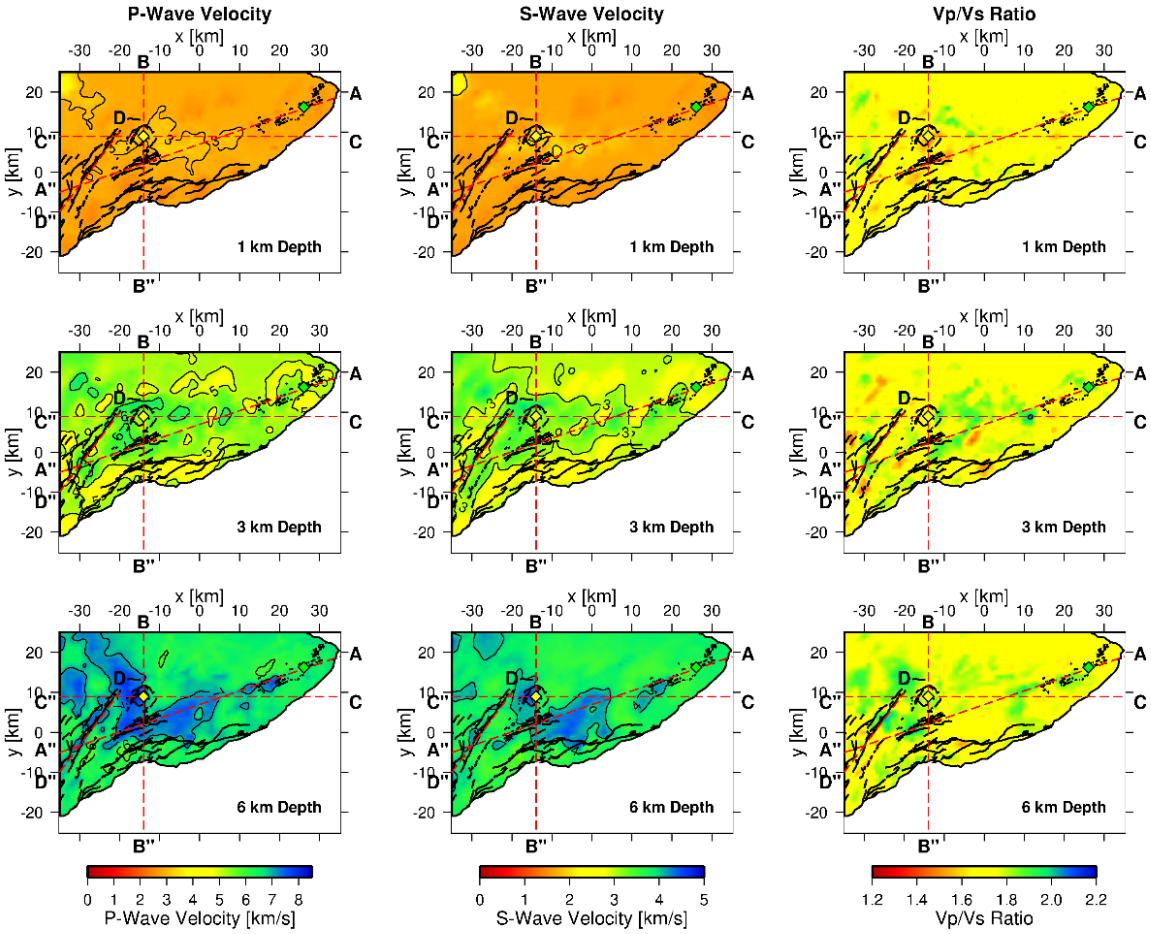

Figure 88. Map view of the seismic inversion results from processing of seismic waveform and HVO catalog data at selected depth intervals.

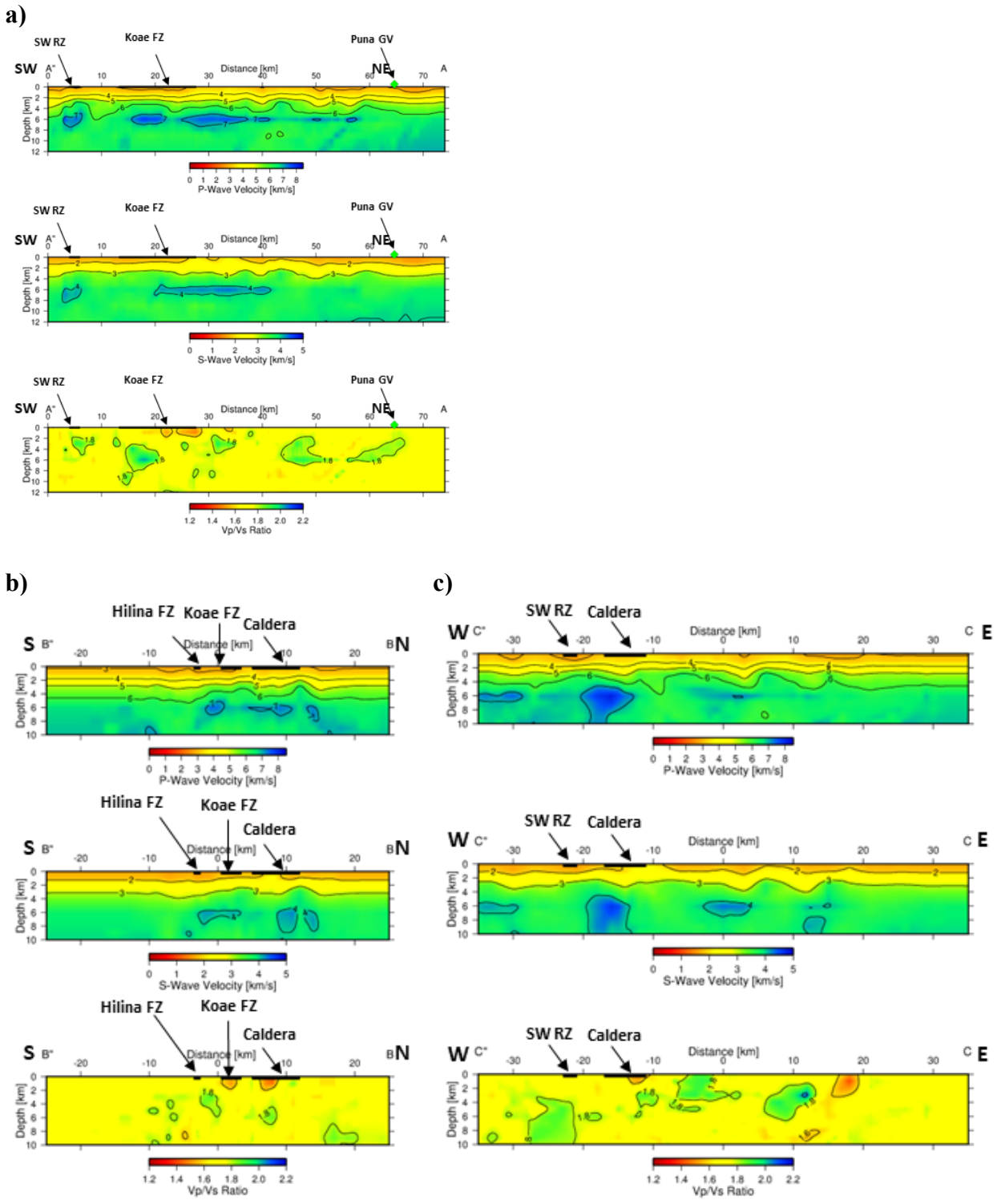

Figure 89. Cross-sectional views of the seismic inversion results from processing of seismic waveform and HVO catalog data in the study area. (a) Along transect A-A" in Figure 88. (b) Along transect B-B" in Figure 88. (c) Along transect C-C" in Figure 88.

4.3 Conclusions

The 3D seismic joint inversion for earthquake hypocenter locations and P- and S-wave velocity structure of Kilauea caldera and surrounding regions produced results that agree with the general known geology in the study region. Both the locations of earthquake hypocenters and the velocity structure delineate tectonic structures such as the Kilauea caldera and the Southwest and East Rift zones at shallow and mid-crustal depths. Additionally, an earthquake cluster was located between 30 km and 40 km depth below the southern coast of Hawai‘i, at the junction of the Southwest Rift zone with the ocean. The volcanic system seems to be dominated by horizontal volcanic intrusions at mid-crustal depth (6 km), which were observed below the caldera as well and along the ERZ. The results of the inversion of HVO catalog data reveal velocity anomalies that may indicate a potential upwelling of magmatic intrusions from the lower crustal or the upper mantle into the ERZ. However, these anomalies are absent in the inversion of travel times derived from waveform data as well as in the inversion of combined travel times from waveform and HVO data. A persistent V_P/V_S anomaly high (1.9) is visible below the PGV, although the extent and magnitude of the anomaly varied slightly depending on the type of data inverted. This anomaly could be a potential target for further development of the geothermal resource at the PGV. The results derived for the ERZ reveal interesting features that warrant further study. Specifically, the anomaly below the PGV would benefit from additional analysis using pre-existing data sets that are not yet publicly available or from the deployment of additional seismic stations that would record earthquakes and ambient noise. Studies of ambient noise enable the development of subsurface S-wave velocity models in the absence of seismicity, which is beneficial in the less seismically active region in the LERZ.

5 Imaging Fault and Fracture Dynamics Using Geodetic and Seismicity Data From the May 2018 Kilauea Eruption

The intrusion of fluids into a fracture can significantly perturb the existing stress field, leading to notable seismicity and deformation in the surrounding host rock (Dieterich, Cayol, and Okubo 2000; Pedersen, Sigmundsson, and Einarsson 2007). The complexity of the in-situ stress field, in conjunction with the variability of existing fractures around the intrusion, can obscure the relationship between the intrusion and the resulting seismicity and contort the resulting deformation field. Thus, while the rate- and state-dependent frictional model can be used to link seismicity and fracture aperture changes (Dieterich 1994), the exact relationship in a realistic Earth model will be complicated by heterogeneity and a host of other unknowns, such as the stress fields that existed in the area prior to the intrusion. As noted by Pedersen, Sigmundsson, and Einarsson (2007), these stress fields are controlling factors in terms of the level of seismicity that is generated by intrusion and associated fracturing.

Because of the uncertain relationship between intrusion-related stress changes and seismicity, we do not use the seismicity data to directly estimate aperture changes in the evolving fracture zone (Vasco, Smith, and Hoversten 2020). Rather, we hypothesize a causal link between the observed seismicity and aperture change, and design a regularization measure that will attempt to put the largest changes in fracture aperture at locations with abundant seismicity. In this way, we hope to improve upon previous estimates of fracture evolution (Kundu et al. 2020). Furthermore, we combine two InSAR satellite systems in order to extract range change from time intervals ending on April 30 and May 1, 2018, allowing us to invert for fracture aperture changes on two successive days of the intrusion.

We will use the model of an evolving fracture and its associated seismicity to study the intrusion and subsequent eruption of magma in the ERZ of Kilauea. It is thought that repeated dike injections and magma intrusions keep the ERZ at a high temperature, close to the melting point of basalt (Montgomery-Brown, Poland, and Miklius 2015). This has implications for both the mechanical and thermal state of the fracture zone. Understanding this mechanism in greater detail is important for the generation of electric power at the existing geothermal plant on the island of Hawai‘i.

5.1 The Kilauea Intrusion and Eruption of 2018

The volcanic complex at Kilauea is dominated by two active rift zones, the ERZ and the Southwest Rift Zone (Kundu et al. 2020). On the ERZ, the Pu'u 'O'o and Kupaianaha vents had been erupting almost continuously between 1983 and 2018 and are thought to be in communication with a magma storage reservoir beneath the summit caldera at Kilauea (Kundu et al. 2020). In addition to the rift zones, there is a major decollement that is thought to dip seaward and lie at a depth of around 8 km.

A major eruption occurred at the ERZ of Kilauea Volcano, starting in April of 2018, and continuing for several months. The event caused significant disruption and resulted in voluminous lava flows. These intrusions and magma movements will have a significant impact on existing and future geothermal resources in the southeastern corner of the island of Hawai‘i.

We will focus on the early events in this long sequence, leading up to the major surface eruptions, in an attempt to understand the evolution of the fracture zone and the intrusive activity just prior to the appearance of magma at the surface.

5.2 Seismic Monitoring

Seismic monitoring has a long history on the island of Hawai‘i, with the establishment of the HVO in 1912 (Okubo, Nakata, and Koyanagi 2014). The seismicity on the island of Hawai‘i has been used extensively for characterization of the subsurface stress and evolution of the magma reservoirs. Logically, seismological observations became one of the main sources of information about the Kilauea eruption in 2018 (Anderson et al. 2019; Neal et al. 2019). As expected, the multiple caldera collapses and movement of the magma were accompanied by intense seismicity; frequent earthquakes with MW~5 occurred from April 11 to August 6, 2018, with the strongest event measuring MW6.9 (Figure 90). However, most of the previous studies of the eruption relied on raw HVO catalog data produced by automatic event detection/location. Such raw catalogs are known to suffer from significant errors in the hypocenter locations, which may impede the geological interpretation of the observed earthquakes.

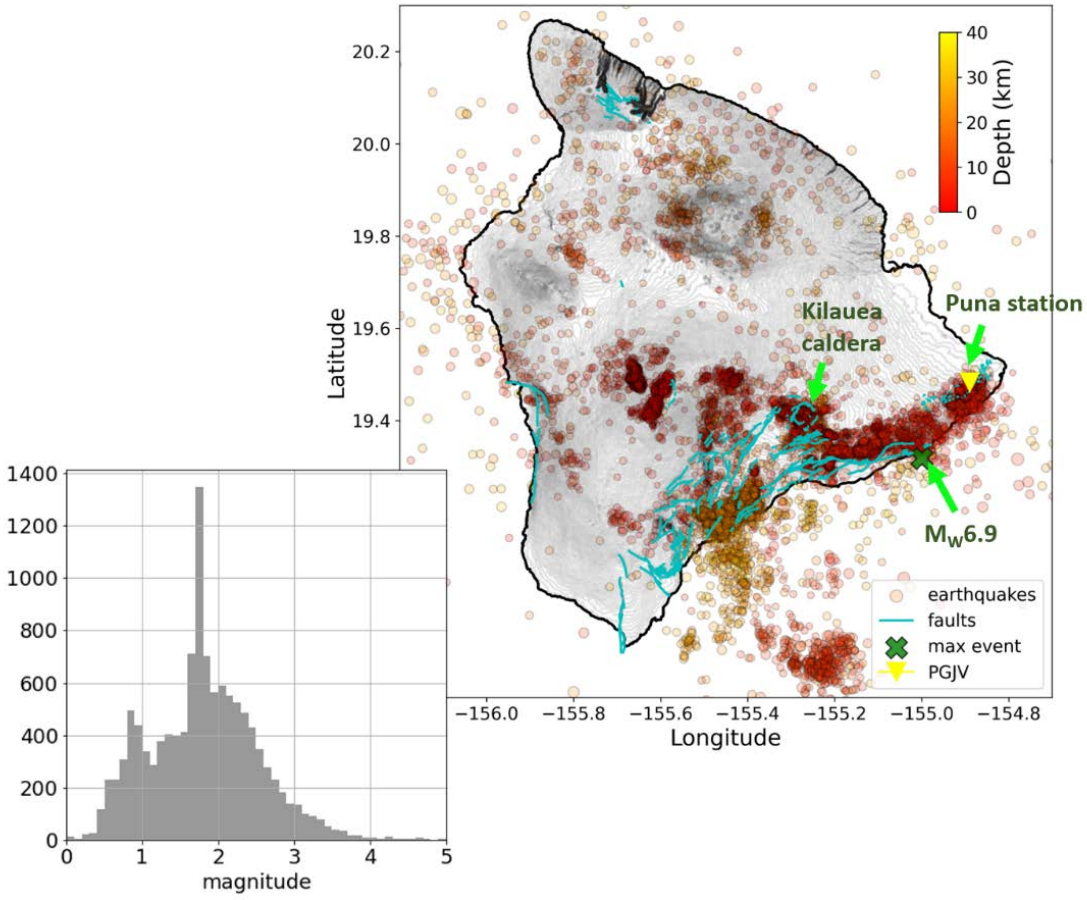

Figure 90. A reviewed catalog of induced seismicity on the island of Hawai‘i between January 1, 2017 and May 1, 2021 retrieved from the USGS ComCat data service (USGS 2020). The inset shows a histogram of the event counts for local magnitude used to pick the high-quality events for our analysis.

5.3 Geodetic Monitoring

Figure 91 shows the location of GPS stations within the ERZ.

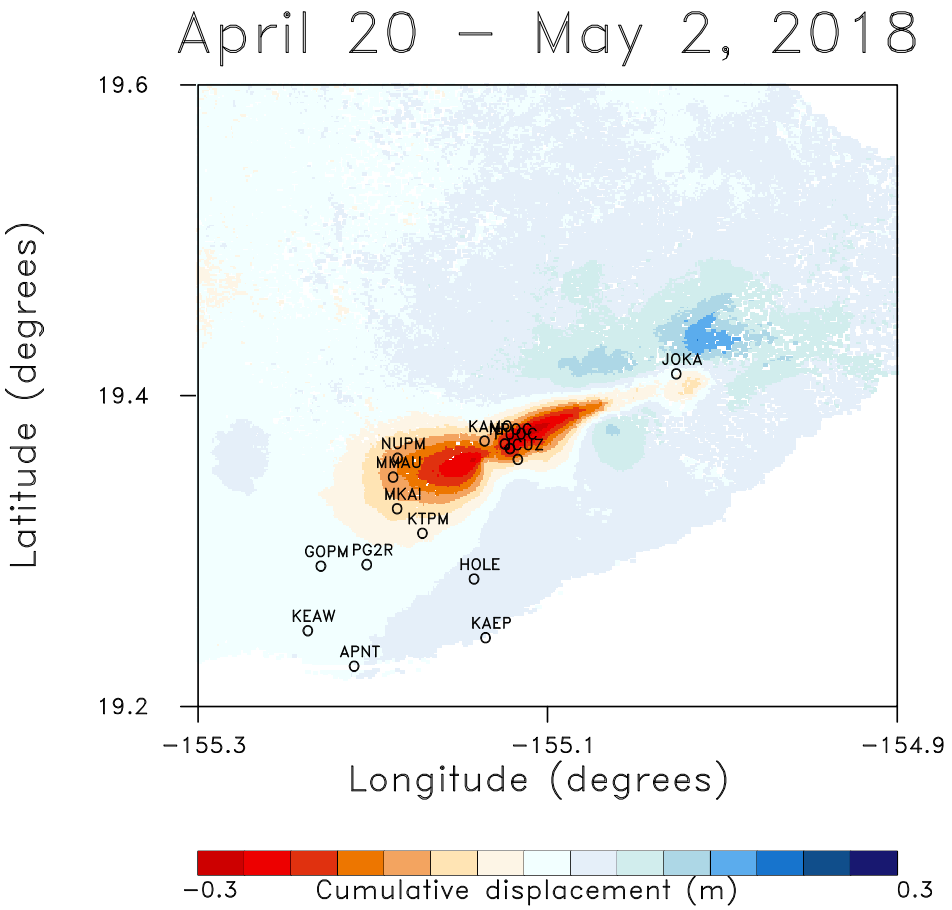

Figure 91. Location of GPS stations around the ERZ of Kilauea Volcano.

5.4 Global Navigation Satellite Systems

Data from the GPS, a Global Navigation Satellite System maintained by the U.S. government, were used to study the temporal variations in ground displacement for a number of points around the ERZ. An extensive set of GPS receivers are deployed around the Mauna Loa and Kilauea volcanic systems, comprising the Hawaiian geodetic network (Montgomery-Brown, Poland, and Miklius 2015). At any given time, there are roughly 57 continuous GPS sites where displacements are estimated at 5-minute intervals. Most of the stations are located around the summit calderas and the station density decreases substantially at the eastern edge of the ERZ (Figure 91). These stations are particularly valuable for the detailed temporal record that they provide. For example, the four time-series in Figure 92 reveal that there is little systematic deformation prior to the sudden activity in late April and early May of 2018. Thus, the changes observed in the InSAR images are primarily due to deformation from April 30 on. These are important complementary observations because, as we discuss next, at best we can only infer InSAR line-of-sight changes over fairly large time intervals. The GPS station distribution is

rather sparse, and the daily displacements change dramatically over rather short distances, perhaps due to highly variable topography and near-surface mechanical properties.

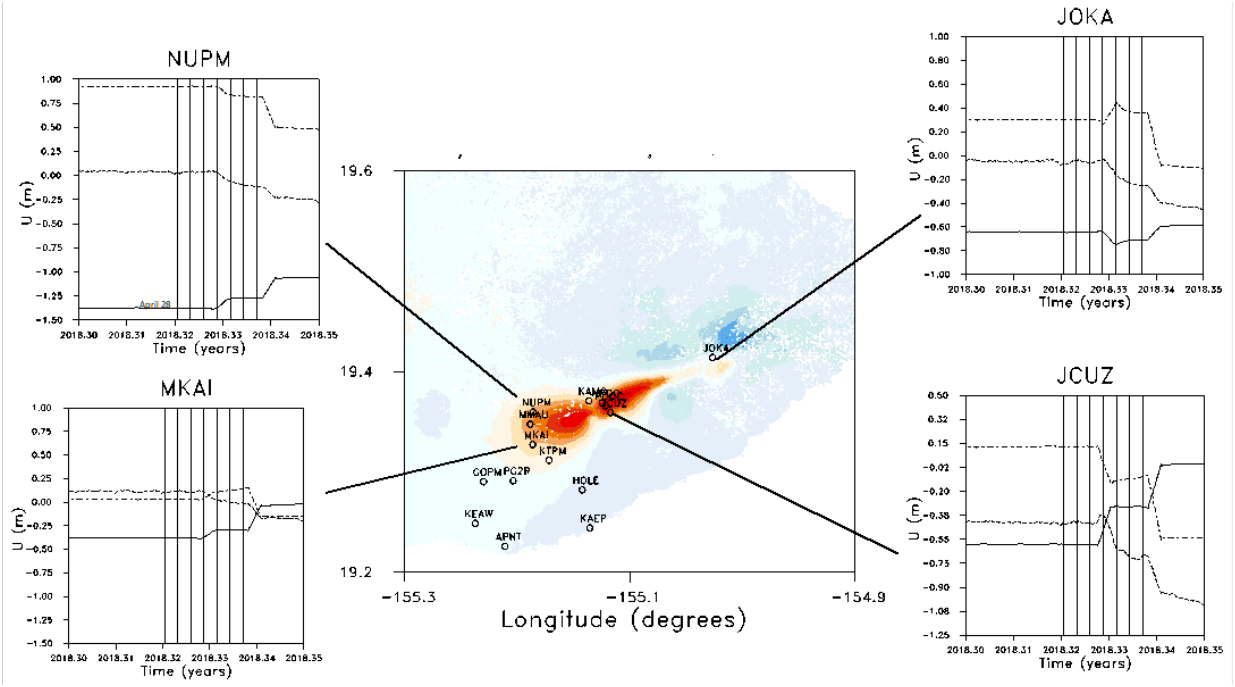

Figure 92. GPS observations for the final days in April and the first few days of May 2018. The vertical bars signify the start of a new day. Color map is Figure 91 showing vertical changes (red negative, blue positive).

5.5 Interferometric Synthetic Aperture Radar

Our main source of information about deformation due to the intrusion is from InSAR observations. These estimates of surface displacement are derived from the propagation time of microwave pulses from orbiting satellites that are reflected off objects on the Earth's surface. The phase differences between reflections from successive orbits is used to compute ground displacements, typically relative to some nearby base point (Ferretti 2014). The InSAR data used in this study came from two sources, the Sentinel-1/2 satellites operated by the European Space Agency and the RadarSat-2 satellites operated by the Canadian government. The orbits used in the calculations of the RadarSat-2 interferograms occurred on April 7, 2018 and May 1, 2018. The satellite heading was 347.8618 degrees, and the incidence angle was 19.1847 degrees. The resulting line-of-sight displacements are plotted in Figure 93.

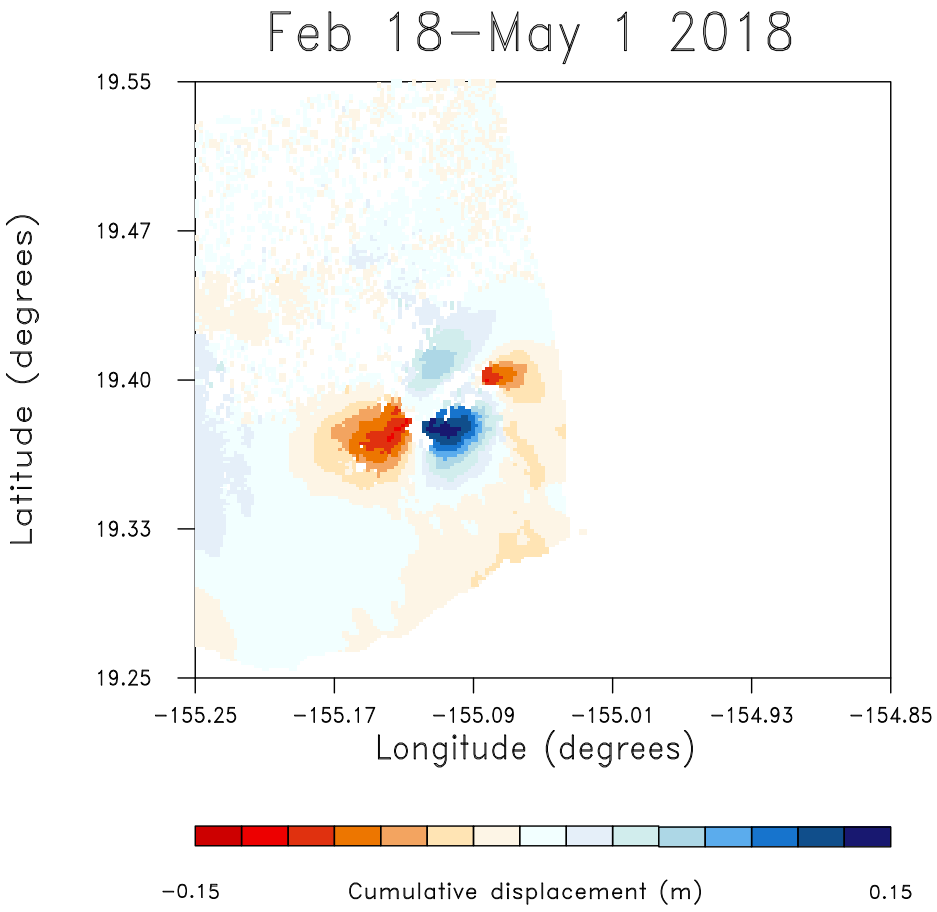

Figure 93. Line-of-sight displacements occurring between April 7 and May 1, 2018, as estimated by RadarSat-2 observations.

For the Sentinel-1/2 interferogram, the baseline orbit was on April 20, 2018 while the follow-up observations were on May 2, 2018. The Sentinel-1/2 satellite heading was -12.2672 degrees, and the incidence angle was 39.6882 degrees. Bi-modal patterns characteristic of deformation above an opening fracture are visible on both images. The pattern in Figure 94 extends further east, indicating an eastward progression for the fracture zone. As we shall see, a similar eastward migration is observed in the seismic event distribution.

5.6 Methodology for Evaluating Seismicity, Deformation, and Fracture Development

Due to the extensive volcanic activity, there are numerous instruments for detecting both seismicity and deformation on and around Kilauea. Most of the monitoring equipment is operated by the HVO. In addition, there are a number of InSAR satellite systems for recording line-of-sight displacement or, equivalently, range change, at a very high spatial resolution. Our goal is to analyze both the seismicity and deformation leading up to the magnitude 6.9 earthquake on May 4 and the subsequent months of eruptions. In particular, we wish to develop a model of fracture evolution that is compatible with both the observed seismicity and measured surface deformation. It is assumed that the main source of the seismicity and deformation is a

dike intrusion along the ERZ at Kilauea. In addition, there may be flow along the fracture zone and areas of closure due to pressure decreases caused by aperture changes elsewhere in the zone.

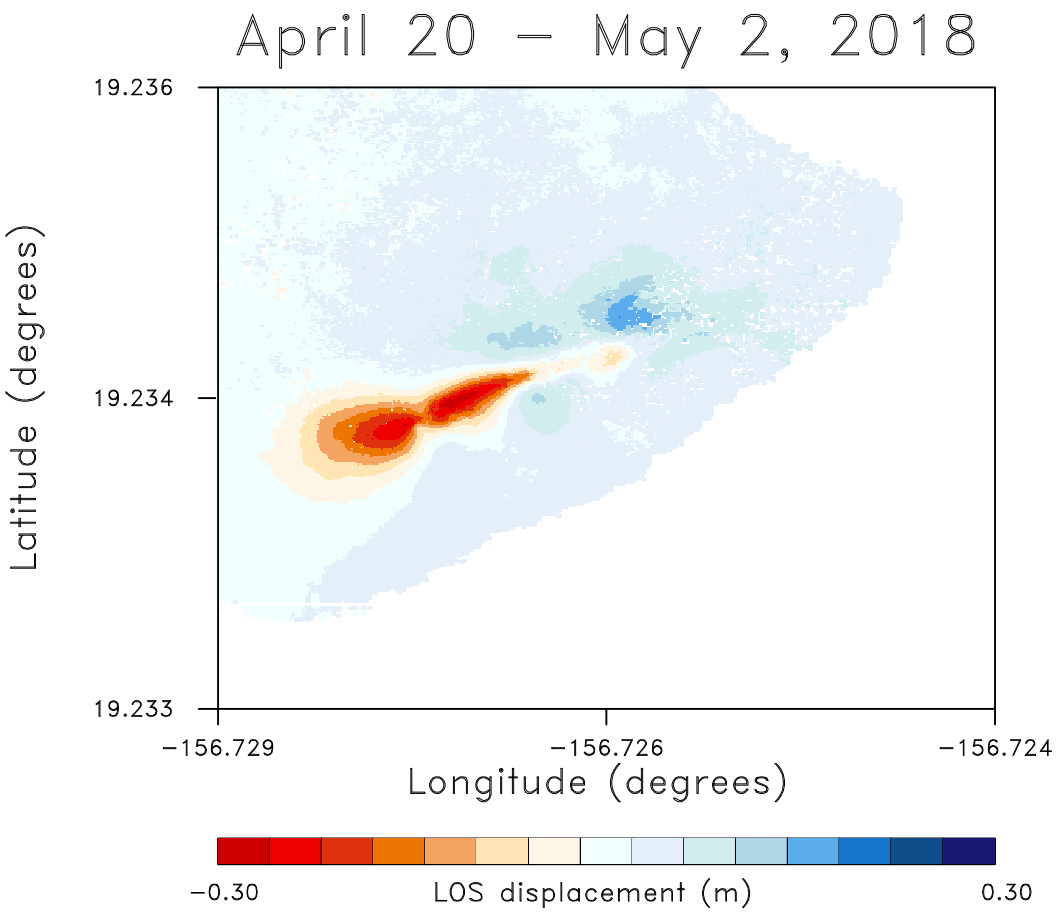

Figure 94. Line-of-sight displacements that occurred between April 20 and May 2, 2018, as estimated from Sentinel-1/2 observations.

5.6.1 Analysis of the Seismological Observations

A standard way to accurately relocate the cataloged events is double-differencing (Waldhauser and Ellsworth 2001). In essence, double-differencing refines the hypocenter inversion by minimizing the mismatch between the events that likely originated at the same subsurface feature. Such an approach proved useful for better imaging of relatively deep faults in Northern California (Waldhauser and Ellsworth 2001) as well as shallow basement faults reactivated by wastewater disposal in the U.S. Midwest (Schoenball and Ellsworth 2017).

We are aware of three existing relocated catalogs that include the Kilauea eruption. Matoza, Okubo, and Shearer (2020) produced the most complete catalog for the island of Hawai‘i to date, containing 275,000 events from 1986 through 2018. Its generality becomes an issue for our purposes—the relocation algorithm will try to reconcile events that originated at different moments in time, whose triggering mechanisms might be completely unrelated. Moreover, legacy catalogs relied on a much sparser seismometer network and less reliable instrumentation,

which increases the overall error rate of the relocation algorithm. To minimize the negative effects of these two factors, Matoza, Okubo, and Shearer (2020) used a one-dimensional velocity model by Klein (1981). On the other hand, Shelly and Thelen (2019) published the results of the fast-track relocation of the seismic events located around the Kilauea caldera during the few months of active eruption. These results do not include the seismicity along the LERZ—the target area for the PGV. The most relevant relocated catalog for our study was produced by Lin and Okubo (2020), which includes 48,000 earthquakes triggered in the vicinity of the LERZ and Kilauea caldera from July 1, 2015 to August 31, 2018, recorded by the HVO seismic stations.

Our relocated catalog aims to augment the catalog by Lin and Okubo (2020) to better constrain the inversion of surface deformations. We retrieved the original reviewed seismic catalog from a USGS data center, ComCat (USGS 2020). It contains P- and S-wave arrivals for more than 65,000 events for the island of Hawai‘i between January 1, 2017 and May 1, 2021. The histogram of the local magnitude (Figure 90) indicates that the magnitude of completeness is somewhere between M_L1.5 and M_L2. As we aim to relocate only those events that are sufficiently strong to have more picked arrivals, in the following we only use events with M_L>1.5. In the vicinity of the LERZ and PGV, we had 11,000 such events.

5.6.2 Relocation Workflow

We implemented a relocation workflow using hypoDD 2.1b software (Waldhauser 2001). The latest version of this software enables the use of three-dimensional velocity models, irregular topography, and sophisticated algorithms for the events clustering. All three features are extremely important for the island of Hawai‘i.

We found that the relocation results for the 3D velocity model by Lin et al. (2014) are superior to the 1D model by Klein (1981). Also, the area has complicated tectonics, with distributed magma bodies, numerous fault/fracture zones, and the basal decollement all generating seismicity. With regard to basal decollement, a lot of near-surface events are relocated above the acquisition surface, identified as ‘airquakes,’ and discarded.

The assumption of a flat acquisition surface would lead to significant depth errors for a relatively wide range of elevations in the vicinity of the LERZ.

Typically, one attributes the events to clusters based on the distance between their hypocenters. However, the errors in the initial catalog reach such high values that the waveforms from the same cluster look very different. Thus, we added the correlation coefficient as an additional parameter for the clustering. Eventually, the clusters have a maximum separation distance of ~5km.

Eventually, our relocation catalog contains ~8,300 events. The rest of the events either have insufficient data quality or could not be attributed to any of the clusters with confidence. Figure 95a shows the relocated events. Figure 95b–d shows that the double-differencing algorithm only rarely moved the hypocenters by more than 2 km. We focused on strong, high-quality catalog events, which have higher probability of accurate initial location, as confirmed by our results.

Figure 95a shows that the relocated earthquakes form sharp lineament going eastward from the Kilauea caldera to the LERZ. However, in the middle and eastern part of the LERZ, the events

clouds look diffuse. This is an expected behavior because these earthquakes were triggered by magma movement, which typically forms laterally extent chambers rather than linear fault-like structures. However, one feature that appears to be rather robust is an eastward progression of seismic events (Figure 96).

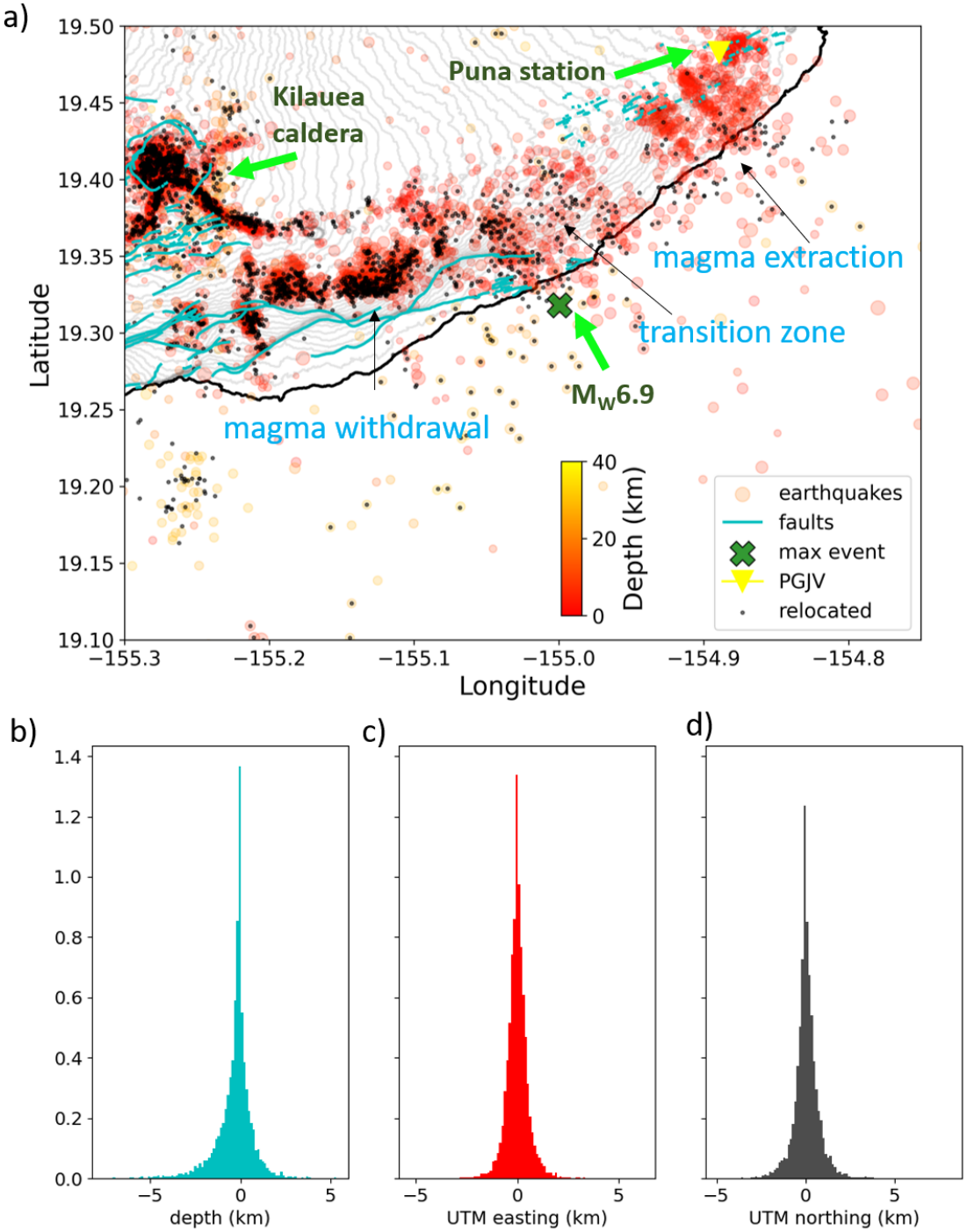

Figure 95. The final catalog of relocated high-quality events (black dots) that likely correspond to pertinent subsurface features (a) compared with the reviewed earthquake catalog shown in Figure 90. Histograms compare magnitude to depth, easting, and northing.

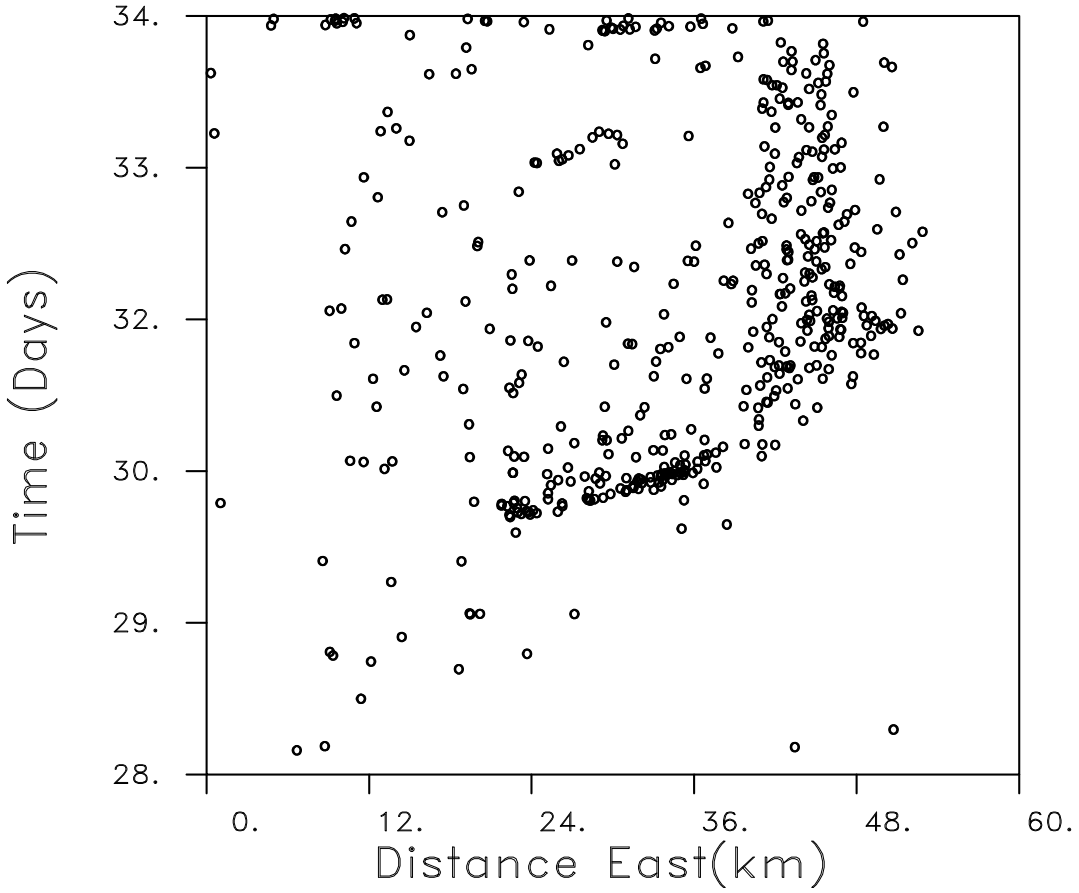

Figure 96. Earthquake east-west position plotted against the origin time of the event. The time is measured in days elapsed since April 1, 2018.

5.6.3 Interferometric Synthetic Aperture Radar Data Analysis

Some of the InSAR data were analyzed using the multidimensional small baseline subset approach (Samsonov and d'Oreye 2012), a variation of the small baseline subset method (Berardino, Fornaro, and Lanari 2002; Lanari et al. 2004; Hooper et al. 2004; Hooper 2008) that can combine multiple synthetic aperture radar data sets with various orbital parameters. In the small baseline approach, orbits with the smallest spatial and temporal differences are used to find the parameters needed to compute the line-of-sight displacements from the InSAR phase changes. The result is an image of the line-of-sight displacements of the Earth's surface, estimated with an accuracy that can approach a few millimeters. As an example, the line-of-sight displacements that occurred between April 7 and May 1, 2018 are plotted in Figure 93, obtained from an analysis of data from the RadarSat-2 satellite system. We also utilized line-of-sight estimates obtained using conventional synthetic aperture radar interferometry (Ferretti 2014), provided by UH (Figure 94).

5.6.4 Estimating Fracture Aperture Changes

As in Vasco et al. (2010) and Rucci, Vasco, and Novali (2013), we subdivide the fracture zone into rectangular subelements and let each element undergo a distinct aperture change over the time interval in question. This approach has been used a number of times to model both dike emplacement in the rift zone at Kilauea as well as to model slip on the basal decollement to the south (Montgomery-Brown et al. 2010; Montgomery-Brown, Poland, and Miklius 2015; Kundu et al. 2020) and will not be described in great detail. A Green's function (Vasco, Johnson, and Goldstein 1988; Okada 1992; Wang, Martin, and Roth 2003) or adjoint approach (Vasco and Mali 2021) is used to compute the sensitivities—the changes in the data due to perturbations in the model parameters—that are needed for the estimation of aperture change of each pixel representing a portion of the fracture. After establishment of a linear system of equations relating the observations, line-of-sight displacements, to the model parameters, fracture aperture changes for each pixel, a least-squares algorithm is used to solve the inverse problem.

Because our resolution of the sources of deformation within the Earth degrades dramatically with depth, the inverse problem of finding aperture changes for a fracture zone with significant vertical extent can be unstable and some form of regularization is required (Vasco et al. 2010).

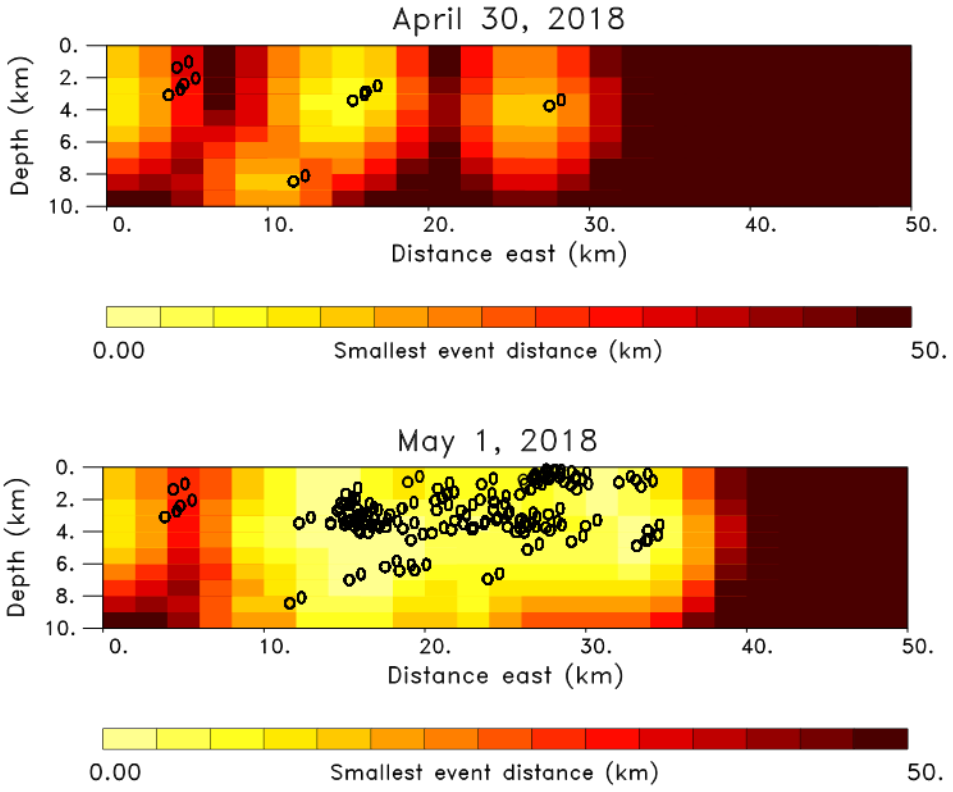

Figure 97. Distance penalty function associating each pixel of the fracture model with the nearest seismic event for events on April 30 and May 1, 2018.

Many forms of regularization, such as a norm penalty or a roughness penalty, have unfortunate consequences when applied to geodetic inverse problems, such as moving the largest anomalies nearest to the surface when minimizing the model norm. Better approaches involve trying to put the largest anomalies nearer to the sources generating the deformation. For deformation due to fluid injection or withdrawal, one can use the distance from the injection points to regularize the inverse problem (Vasco et al. 2010; Vasco et al. 2017; Vasco et al. 2019). However, for many natural sources, one does not know the exact location of fluid influx.

An alternative to regularization methods based upon injection location is to use natural seismicity as a proxy for locations that should correspond to fracture aperture changes. This approach can be based upon the theory rate- and state-dependent friction (Dieterich 1994) and the development of seismicity around a fluid-driven fracture (Vasco, Smith, and Hoversten 2020). As noted by Pedersen, Sigmundsson, and Einarsson (2007), some care must be exercised when applying Dieterich's theory in geothermal and volcanic areas due to the relationship between the current and pre-existing stressing rates. However, the eastward migration of seismicity from the end of April to early May 2018, along with the eastward progression of surface displacement (Figure 93 and Figure 94), does suggest a correlation between the two. Therefore, we constructed a regularization scheme based upon the total daily seismicity (Figure 97). Specifically, we introduce a quadratic penalty term in which the penalty increases as the distance to the nearest event grows. This regularization term will favor solutions with aperture change near seismically active regions. It is possible to use the seismicity in a more direct fashion, as in Vasco, Smith, and Hoversten (2020), but that assumes that the fracture is the sole driver of the seismicity. This might not be true in our case due to the influence of nearby magmatic movement and the influence of the basal decollement (Dieterich, Cayol, and Okubo 2000; Montgomery-Brown et al. 2015).

5.6.5 Application to the Kilauea Intrusion and Eruption in 2018

We implemented the inversion algorithm, using an iterative least squares solver (Paige and Saunders 1982), to solve the regularized minimization of the misfit to the InSAR observations plotted in Figure 93 and Figure 94. The resulting estimates of aperture changes are displayed in Figure 98. There is a clear eastward migration of the fracture between April 30 and the end of May 1, as well as an expansion of the fracture area, in agreement with the seismicity (Figure 97).

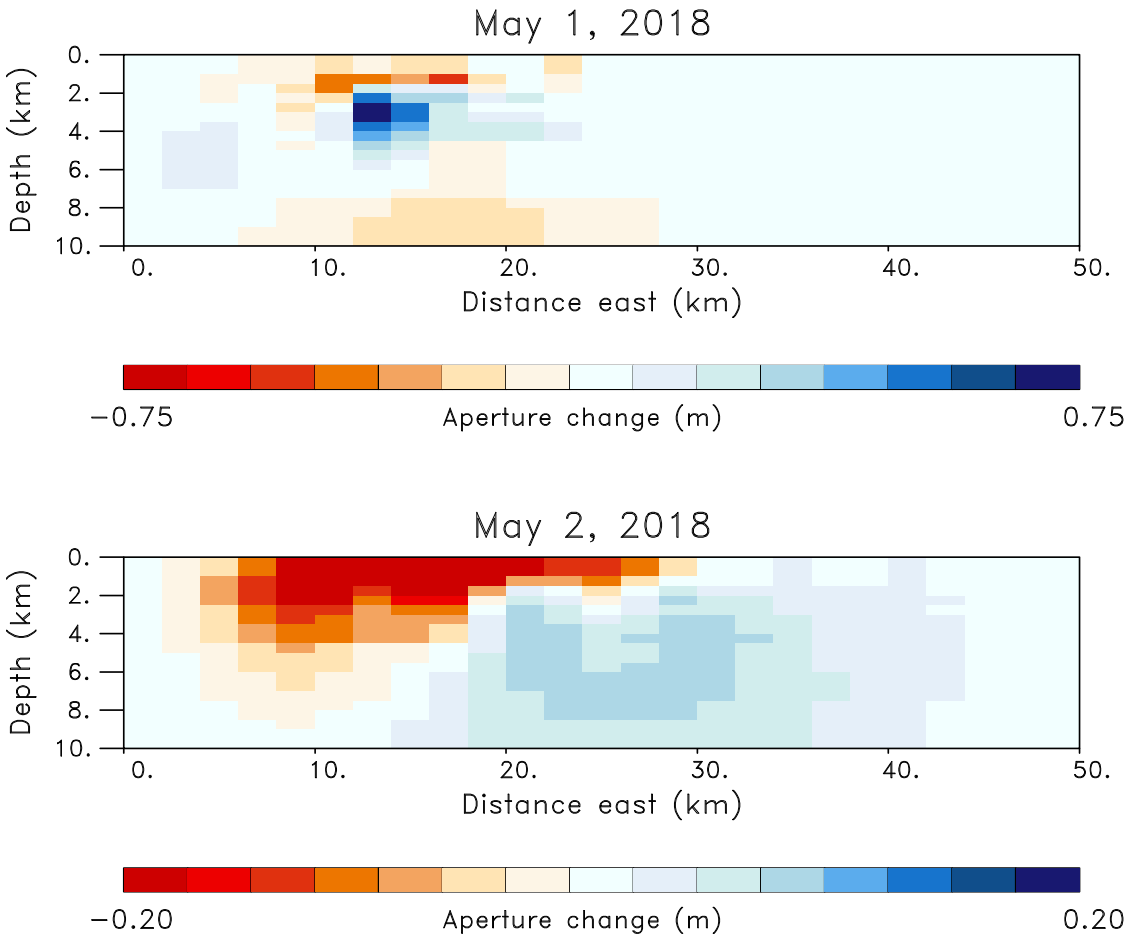

Figure 98. Aperture changes from a baseline day before the start of activity at the end of April until May 1 (top panel) and May 2, 2018 (bottom panel).

The opening of the fracture is rather confined initially and concentrated at a depth of 2 to 4 km. There is further aperture change to the east and to greater depths on the following day. Note that the aperture changes could be due to the upward migration of magma and changes in pressure within the magma, following a rupture leading to the weakening of the rift zone. The decrease in aperture to the west and at shallower depths could be due to magma migration from the region around the caldera. The aperture changes to the east and at depth are in agreement with the later eruption of magma at the surface on the east side of the ERZ and the later 6.9 earthquake on the decollement. In order to evaluate the fit to the observations, we plot the residuals in map view in Figure 99. In general, the residuals are less than an order of magnitude of the observed line-of-sight displacements. However, there is some notable structure within the residuals, suggesting that modeling error, such as an incorrectly located fracture plane or dip, might remain. Other more complicated models, such as curving fracture zones and en-echelon dikes (Montgomery-Brown et al. 2010) are indeed possible. However, such changes in the model are not likely to alter the main features, such as the eastward migration and the expansion of the fracture zone which are so clearly seen in the InSAR observations.

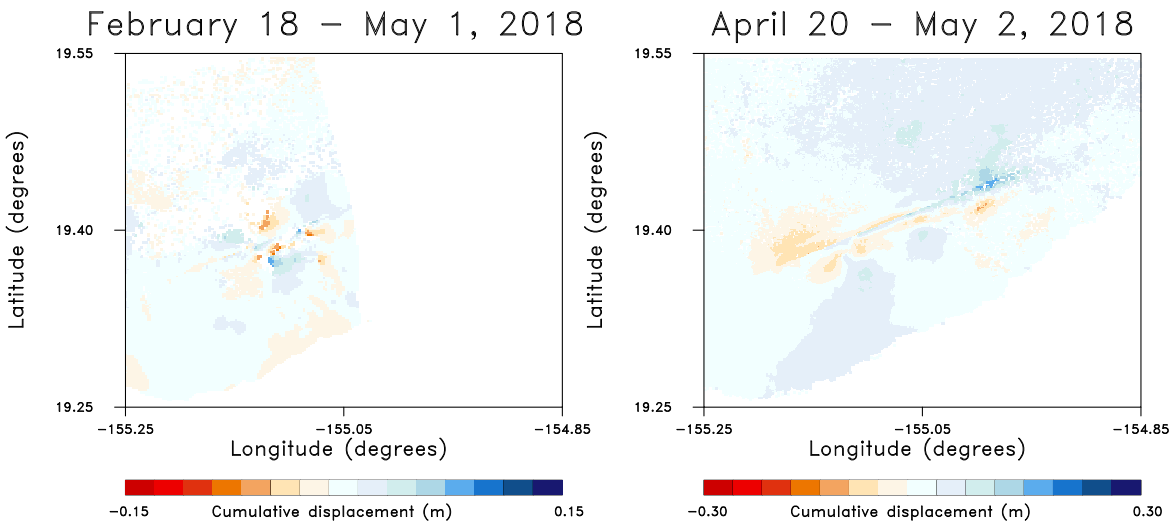

Figure 99. Residuals associated with the two inversions.

5.7 Conclusions

By combining seismic and geodetic data, we are able to estimate aperture changes that may indicate magma emplacement within a major fracture zone, the ERZ associated with the Kilauea volcano. Such magma is the source of heat that is used to generate energy at the nearby geothermal field. The aperture changes will help us to understand the additional heat source that has been added to the field and the changes in the stress field that will influence processes such as drilling and fluid flow. While we had to rely on two satellite systems in order to image those aperture changes, it is possible to combine InSAR, tilt, and GPS data in order to improve the temporal sampling. The multidimensional small baseline subset technique should allow for combining still more satellite observations, such as from the ALOS system or the TerraSAR-X and Cosmos-SkyMed SAR satellites.

6 Ocean-Island Geothermal Conceptual Model Development

To date, the general components of a conceptual model have been developed from prior workers focused on Kilauea volcanology, seismicity, and geothermal resources. We have only just been allowed access to proprietary PGV data and the knowledge and experience of Bill Teplow, and that effort is still in progress as of June 3, 2022. These PGV data will substantially contribute to updates to the geological and conceptual models thus far developed. Additionally, the models are expected to evolve with additional work should the project advance to Phase 2.

6.1 Hawaiian Play Fairway Analysis

The Hawai‘i PFA project identified prospective geothermal resource areas based on data that constrain occurrence of geothermal resource components heat, fluid, and permeability (Figure 100). The organization of the PFA is guided by and helps inform a conceptual model of geothermal resources associated with Hawaiian volcanos and rifts, including the 38 MW PGV in the LERZ of Kilauea volcano on Hawai‘i.

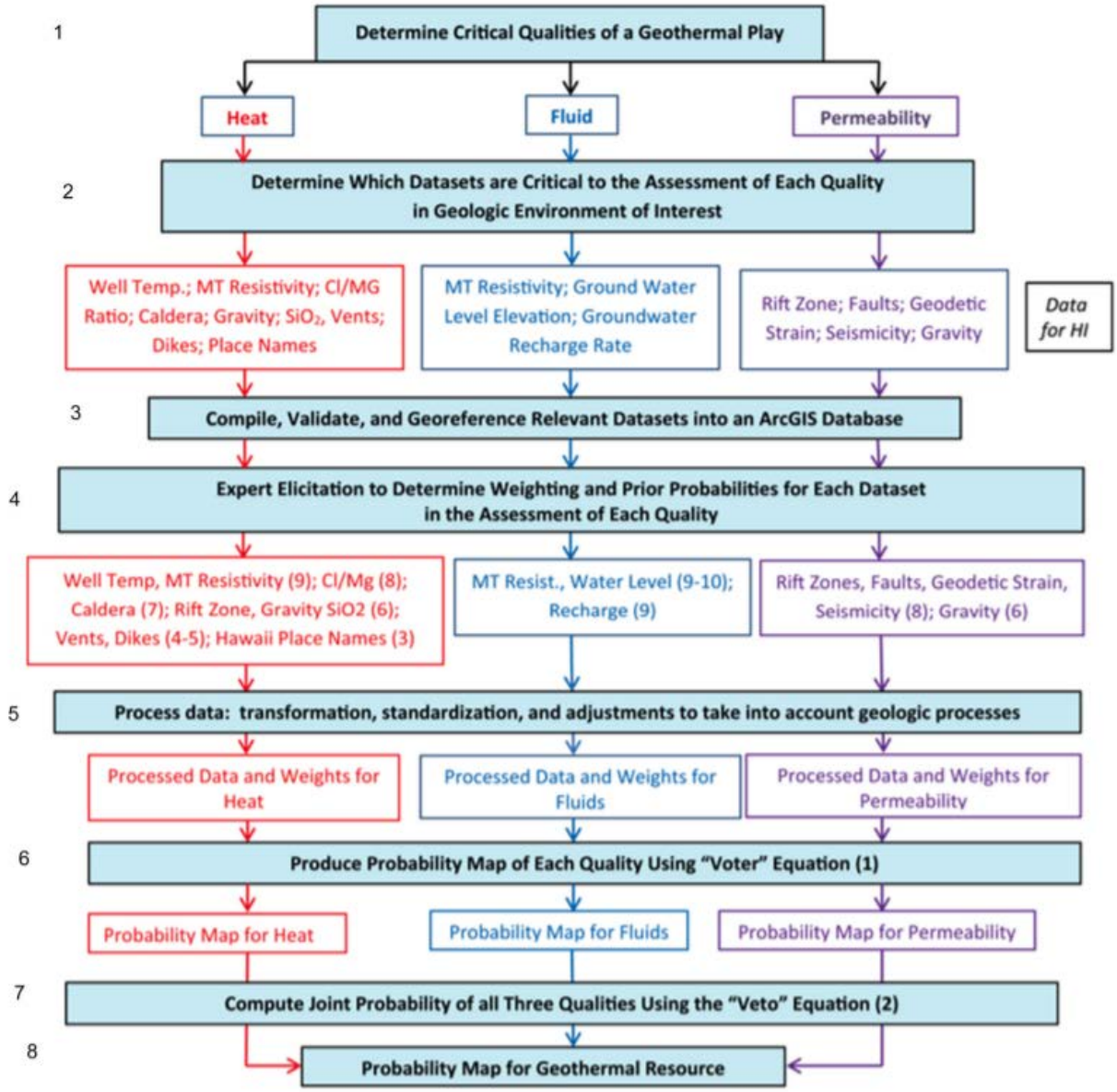

Figure 100. Process and data sets for the Hawaiian PFA project.

The same heat, fluid, and permeability components are captured in the preliminary conceptual model, to which is added a seal component (also addressed in PFA with fluid and permeability components). The PFA project also developed conceptual models to guide the resource favorability assessment and contribute to a more comprehensive conceptual model of ocean island geothermal resources (see Figure 101).

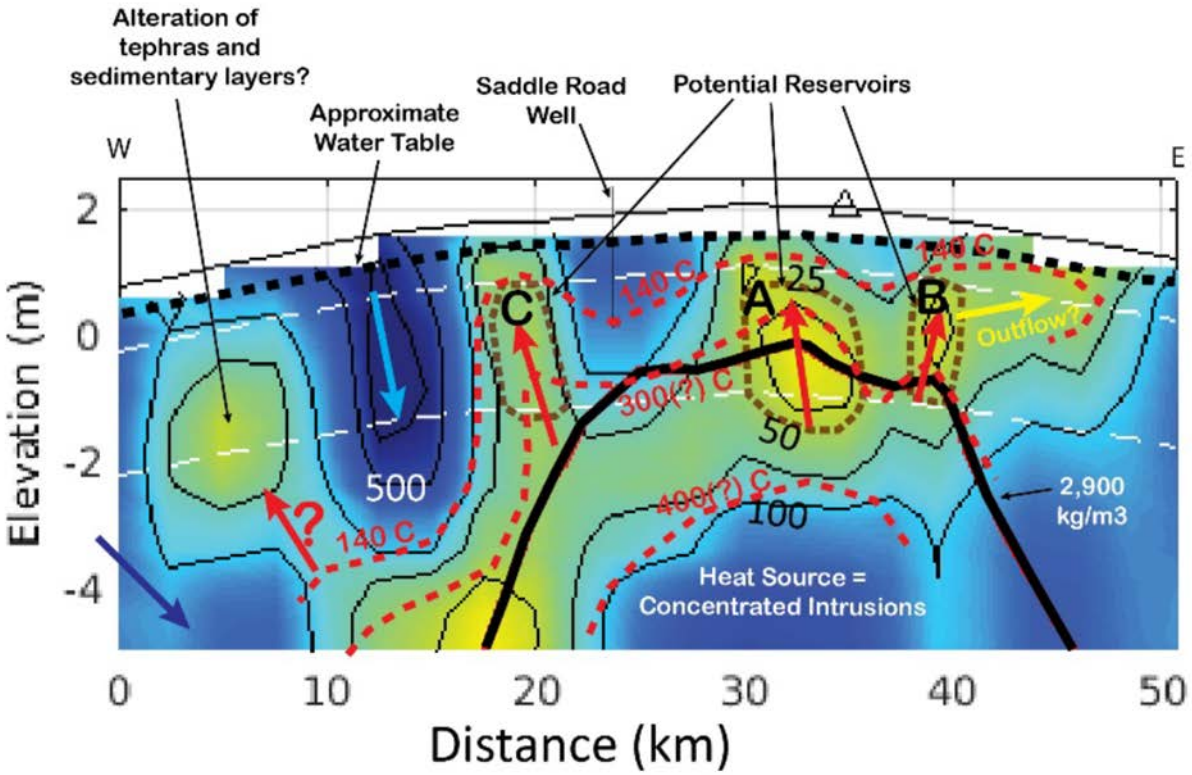

Figure 101. Conceptual model of the Mauna Kea/Saddle Road area identified with high geothermal potential by the Hawai‘i PFA project. Potential upflow zones and geothermal resources are indicated by low resistivity (inverted magnetotellurics) with heat produced by shallow, young intrusions indicated by the black line delineating high density (inverted gravity).

In addition to knowledge gained through the Hawaiian PFA project, published PGV resource area provide information about Hawai‘i’s only commercial geothermal development. Additionally, the active volcano and rifts at Kilauea have been studied in detail for decades, and Kilauea is continually monitored by the HVO, so abundant information is available about the geological setting of the PGV resource. Though geothermal resource favorability is most notable at Kilauea/LERZ, historic and extinct rift zones on Hawai‘i and other islands also have potential (Ito et al. 2017; Lautze et al. 2017; also see Figure 102). Our evolving conceptual model will consider how exploration of these rifts might differ from exploration in an active rift.

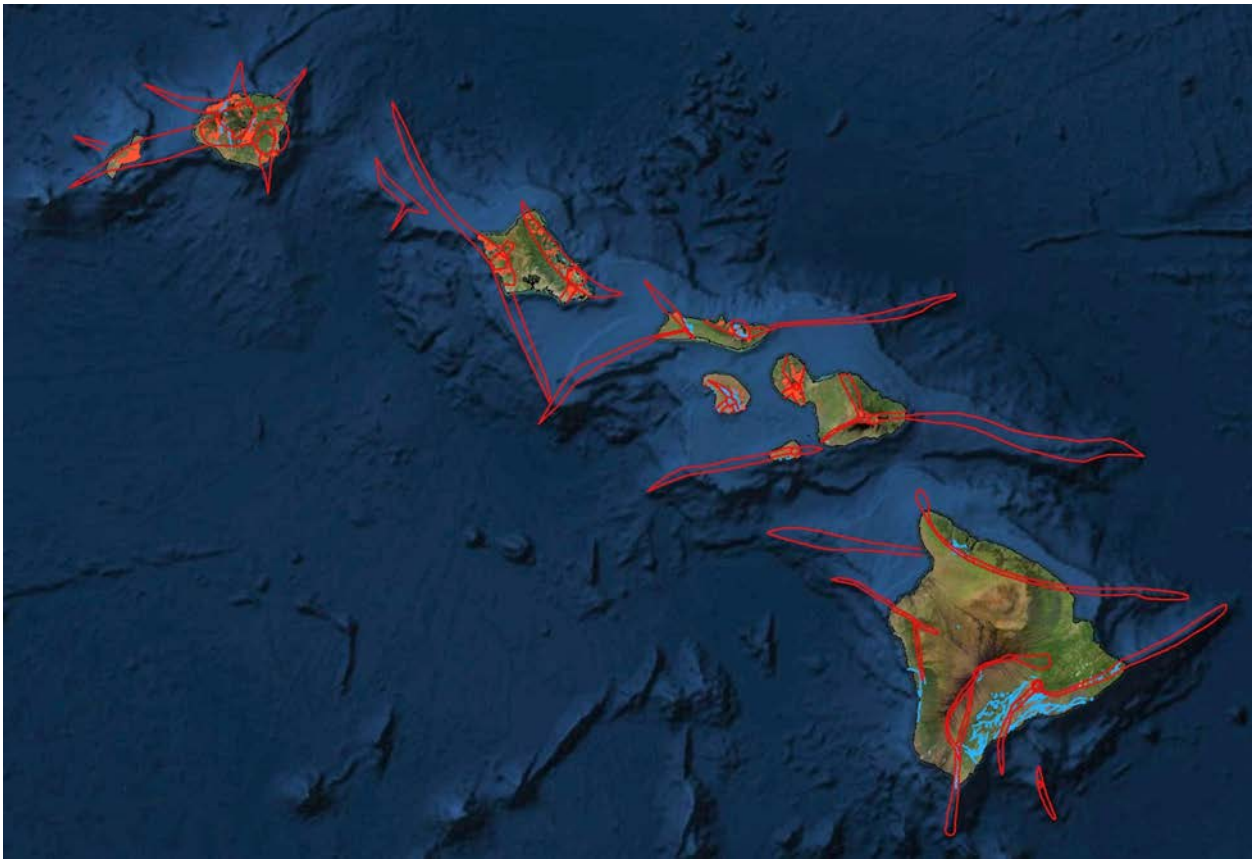

Figure 102. Hawaiian rifts (red polygons), young faults (blue lines), and dikes (red lines).

Kilauea and the LERZ are continually monitored by HVO, in addition to being the focus of other researchers' studies. Abundant recent data and analyses were published related to the 2018 eruption of Kilauea that significantly affected the LERZ, inundating a large area with lava flows that continually erupted from May to September of 2018 along a linear array of fissures adjacent to PGV. In combination with earlier studies, conceptual models of the Kilauea plumbing system provide crucial details of the heat and permeability that make the geothermal resource at PGV possible. Figure 103, Figure 104, and Figure 105 show schematic representations of Kilauea and its rifts that extend to the southwest and to the east from the summit caldera, a configuration that is typical and unique to Hawaiian shield volcanos (Figure 102; Fiske and Jackson 1972; Nakamura 1980). A primary feeder provides magma to Kilauea's summit crater and magmatic and gravitational processes contribute to rift extension, allowing distribution of magma downrift in both intermediate magma chambers and within dike complexes that feed effusive fissure eruptions like that in the LERZ in 2018. On other islands, exposed geology and volcanic features indicate similar processes took place with the possibility of relict heat making geothermal resources possible at a range of depths from a few kilometers to ~12 kilometers, the estimated depth to the Moho away from active volcanism.

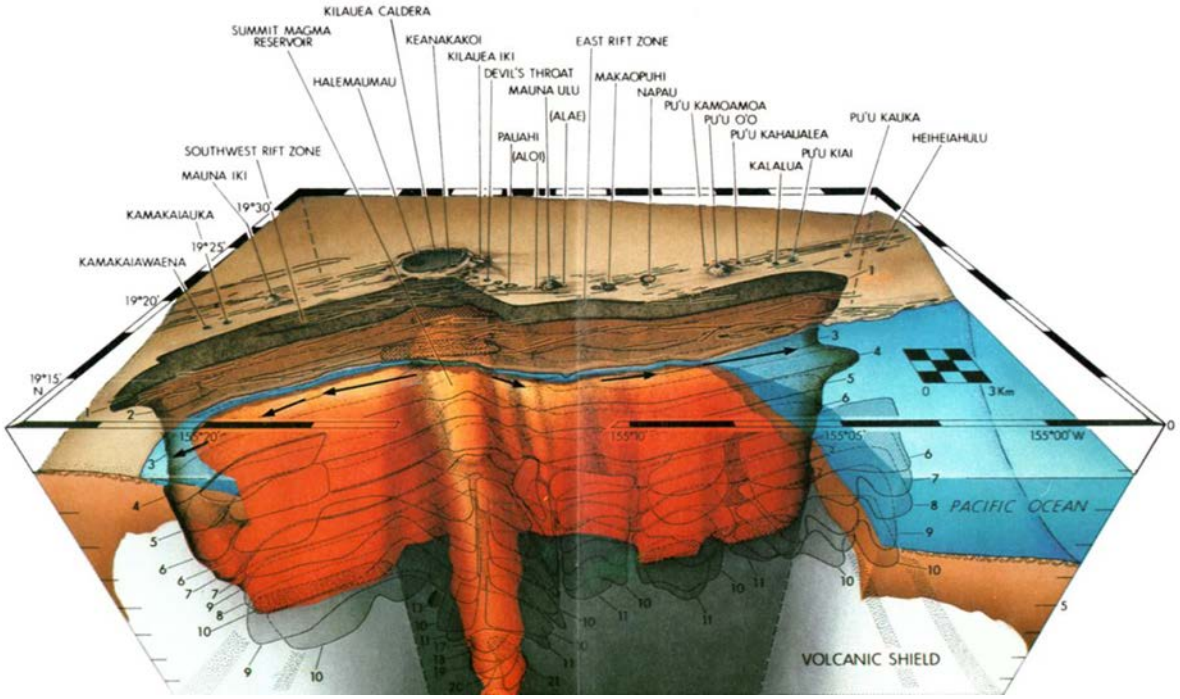

Figure 103. Schematic representation of Kilauea volcano looking north showing deep magmatic feeder to the summit caldera and transport of magma downrift via dike complexes (Ryan 1988). PGV is located further east and downrift from the edge of the figure.

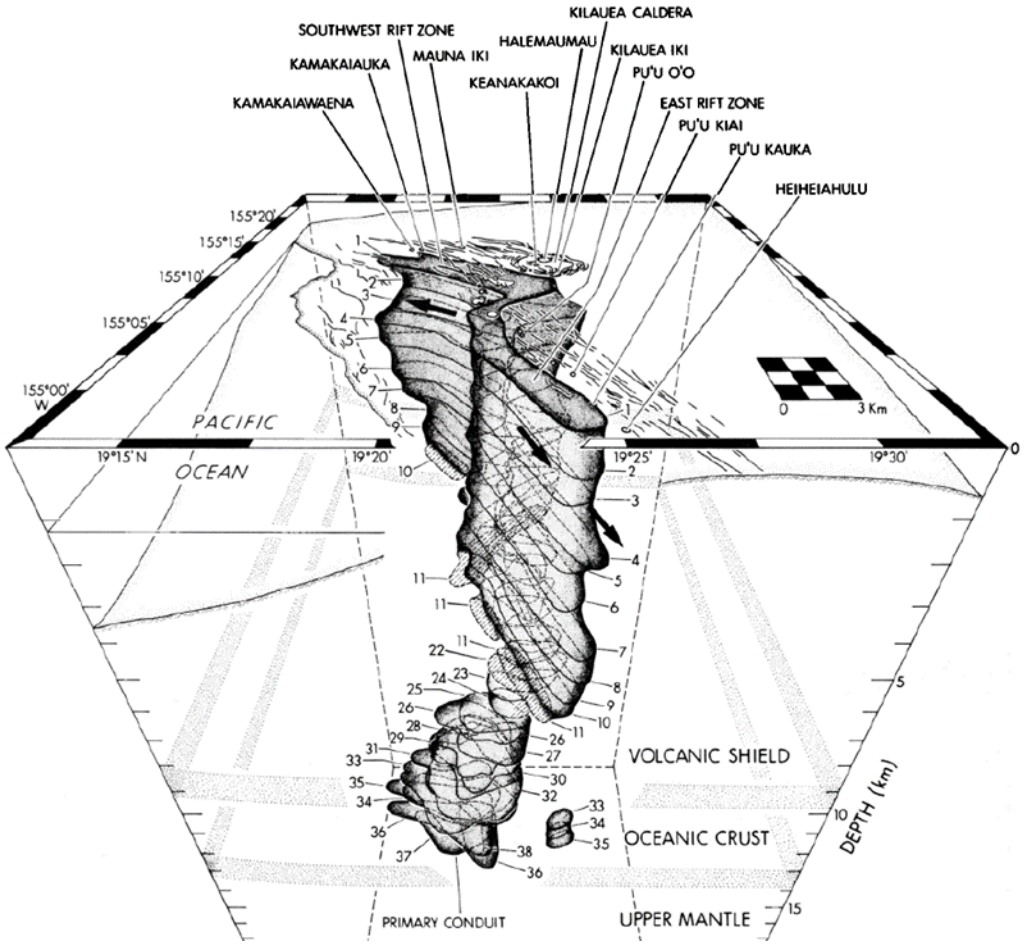

Figure 104. Schematic representation of Kilauea's magmatic plumbing system looking to the west, uprift from the LERZ (Ryan 1988). PGV is located ~10km downrift from the eastern/lower margin of the figure.

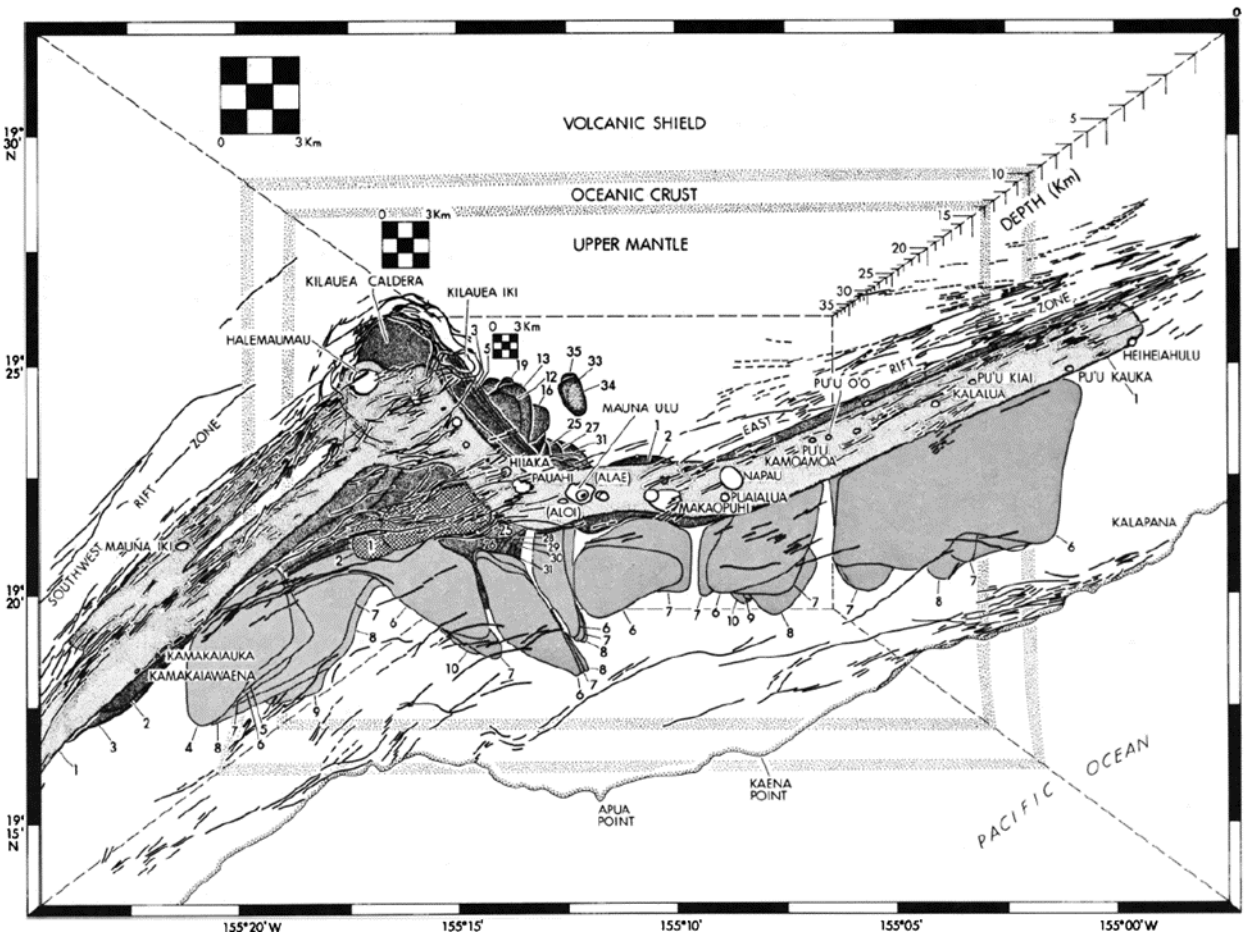

Figure 105. Schematic of Kilauea's magmatic plumbing and associated rift zones (Ryan 1988).

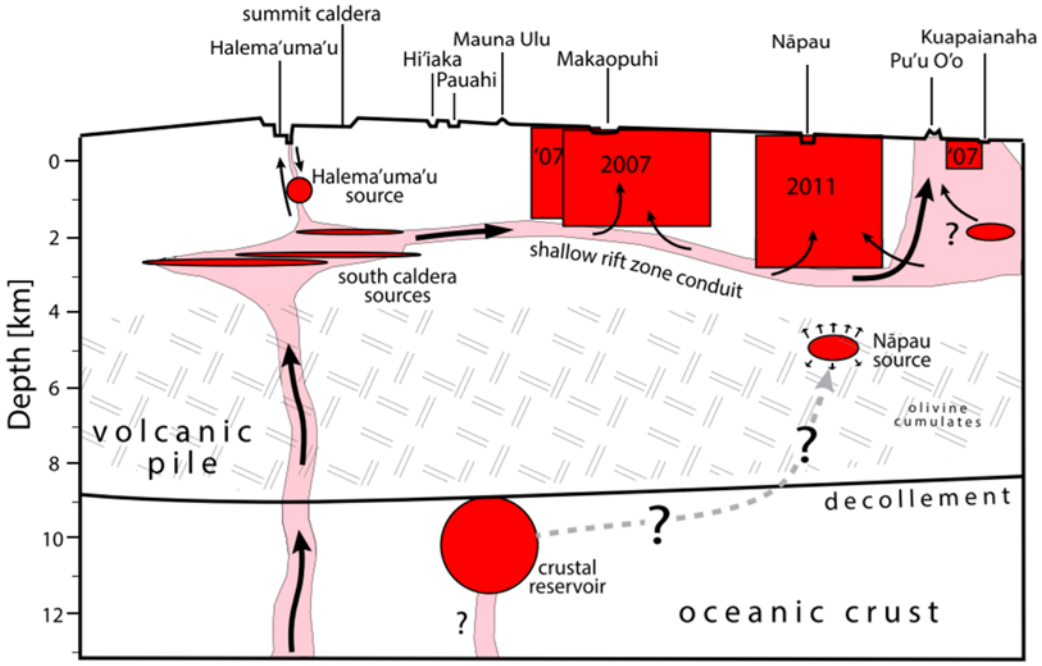

Figure 106. Schematic representation of Kilauea and the ERZ showing primary magmatic feeder, intermediate magma chambers, and shallow dike feeders. Red boxes and dates denote historic dike intrusion and eruptions (Baker and Amelung 2015). The 2018 eruption affected the system from Kilauea's summit to downrift beyond the PGV, past the eastern/right margin of the figure.

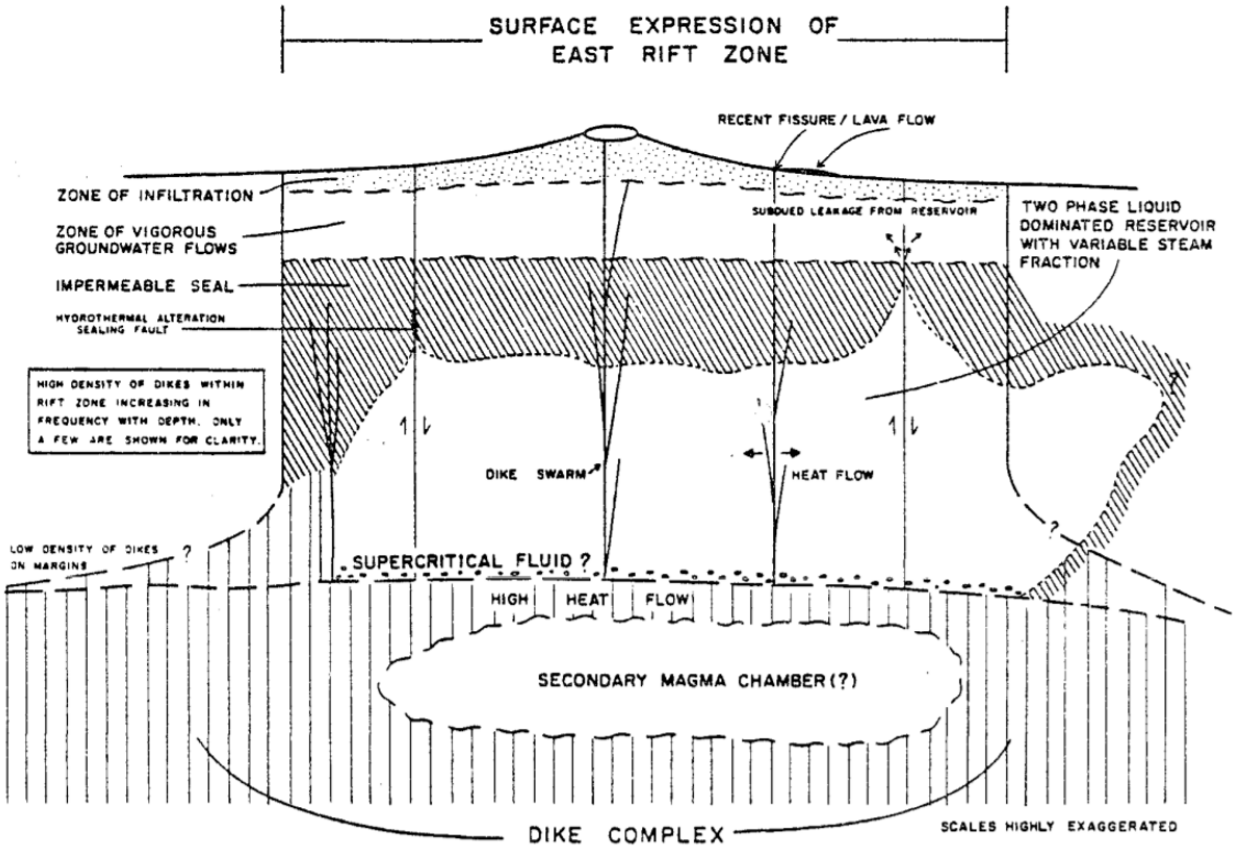

Figure 107. Conceptual model of the PGV geothermal resource.

Source: Iovenitti and D'Olier (1985)

Iovenitti and D'Olier (1985) presented a conceptual model of the Puna geothermal resource based on wells drilled and flow tested in the early 1980s (Figure 107). The presence of a geothermal system is masked by meteoric +/- seawater in permeable subaerial and shallow subaqueous basalts down to ~800 m, as reflected in near isothermal cool zones. Below 800 m, conductive gradients indicate substantial heat flow anomalies with local measured temperatures near the boiling point for depth of hydrostatic water at <2000 m depths. The high temperature gradients are developed in highly clay-altered hyaloclastites that form an effective seal to the underlying fracture permeability within the dike complex. Some wells on the south side of the rift show temperature reversals over the depth range ~1,500–1,750 m that suggest outflow to the south (Thomas 1987). Complex permeability and hydrology characterize the southern margin of the LERZ with dramatic temperature variation over short distances and variable incursion of seawater below sea level. Anhydrite alteration is common and reflects incursion of seawater and retrograde solubility. HGP-A showed evidence for multiple reservoirs, intermediate at ~1,250–1,500 m and 260°–280°C and dry steam from near total depth (1,976 m); temperatures are higher and more consistent interior to the rift versus at the southern margin (demonstrated in the rift-orthogonal PGV cross section shown in Figure 108). LERZ dikes are relatively less permeable compared to shield basalts except along dike margins and where dikes host rift-parallel fractures. The low permeability orthogonal to the rift impedes incursion of seawater from the south, while heating seawater will deposit anhydrite that also reduces permeability. Gravitational instability due to rapid loading of the unsupported seaward flank of the volcanic edifice, along with

pressure from intrusive episodes, enables dramatic dilation of rift fractures. This single factor may be the most important underlying cause for the meters-wide open fractures encountered at PGV that constitute the production zones. Another factor which should not be ignored is the existence of a "live" dacite magma chamber at drillable depth. One could conjecture that this magma is too viscous to flow into the active fracture system and therefore represents a long-lived, local, and intense heat source. This contrasts with the rapidly flowing basalt dikes which have low volume and are emplaced in active fissures with apertures of a few meters at most that are cooled rapidly by the overlying seawater-saturated basalt flows. The dacite magma chamber at a temperature of +/-1,050°C is just a few hundred meters below PGV production zones. (Teplow, personal communication, 2021).

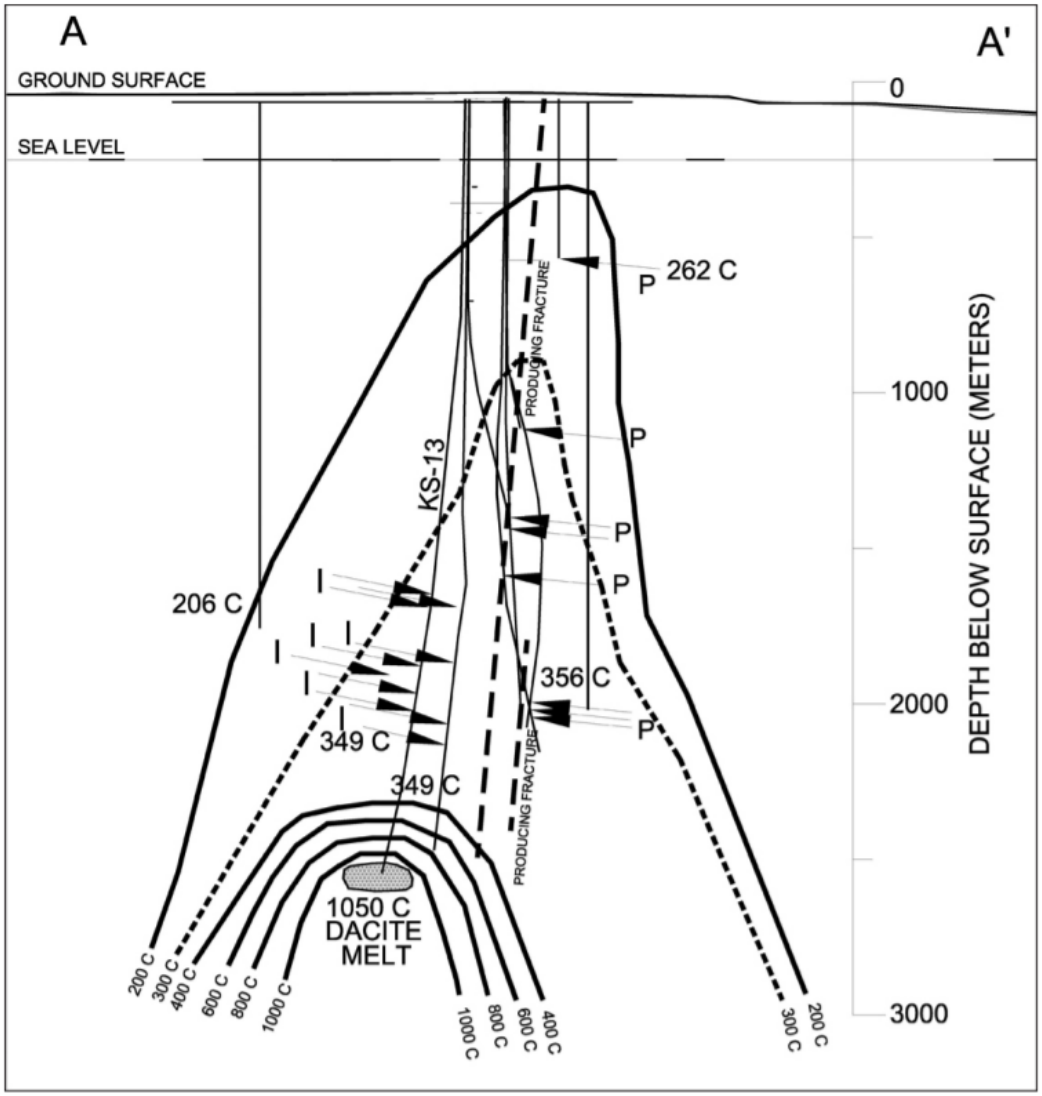

Figure 108. Cross section through the PGV wellfield showing dacitic magma intersected during the drilling of KS-13. The cross section is orthogonal to the rift and demonstrates the primary control on heat and permeability driven by rift-parallel, steeply dipping fractures with high heat flow associated with shallow intrusions and relict evolved melts. P indicates production zones, and I indicates injection zones.

Source: Teplow et al. (2009)

6.2 Proposed Geothermal Resource Conceptual Model

The following components are deemed the minimum necessary for development of a geothermal system. The analyses completed in Phase 1 aim to optimize prediction of these components in the subsurface in order to de-risk geothermal exploration in Hawai‘i.

- Permeability: dikes, dike margins, intersection of rift-parallel and rift-oblique structure. Explore with maps of volcanic and structural features using LiDAR, potential fields, electromagnetics, magnetotellurics, earthquake catalogues, and stress and strain analyses.
- Heat: shallow magma emplacement controls temperature, depth to Moho/base of seismogenic crust dictates geothermal gradient on non-active islands, relict and/or evolved magma/rock. Explore with aqueous chemistry, earthquake catalogues, geology, petrology, and resistivity-temperature relationships (where other constraints on temperature exist).
- Fluid: dense, relatively low-permeability dike rocks with fracture-controlled vertical and rift-parallel permeability (1) can limit seawater incursion and (2) encourage downward percolating meteoric water to form hydrothermal systems within the rift. Explore with aqueous chemistry, geology, hydrothermal alteration, magnetotellurics, electromagnetics, and spontaneous potential.
- Seal: relatively low intrinsic permeability of rift dikes, especially orthogonal to rifts, limits seawater incursion with further limitation due to retrograde solubility and deposition of anhydrite. Basalt-seawater interaction at high temperature produces low-permeability clay which prevents downward incursion of cool meteoric water +/- seawater. Explore with geology, hydrothermal alteration, and magnetotellurics.

The example of PGV shows how these components overlap in time and space to enable development of a geothermal reservoir. Basalt flows overlying the PGV production are highly permeable to a depth of +/- 800 m, with both seawater and overlying freshwater masking all signs of underlying heat, and reflected by the near-isothermal cool zone from surface to ~800 m. The static temperature gradient increases sharply in the hyaloclastite zone present below 800 m, with highly clay-altered hyaloclastites forming an efficient seal of the underlying fracture permeability within the dike complex. The hyaloclastite seal extends down to ~1,500 m and nearly all the temperature runup of +/- 250°C takes place in this zone, representing a static temperature gradient of ~290–365 C/km. Large aperture fractures are encouraged by gravity loading driving the seaward displacement of Kilauea’s southern flank, effectively a continual opening of the rift.

The team will continue to evaluate the implications of geothermal resource exploration in active versus inactive/extinct rift zones. Initial areas of focus include constraint on depth of targets where temperature gradients are modest, i.e., away from active volcanism, and behavior of gravitationally driven rifts where not accompanied by active dike complex development.

7 ISLAND HEAT Phase 2 Data Collection Plan

As we shift focus from the well-studied LERZ of Kilauea to the Saddle Region between Mauna Kea and Mauna Loa, where drilling identified ~100°C groundwater near sea level, we propose that the following data be collected during ISLAND HEAT Phase 2. Data collection will depend on two main factors: access and funding. The UH team is familiar with the terrain in the area, and access can be quite difficult, potentially impacting the ability to perform all the proposed data collection. We do not currently have permits in place to collect the desired data and will begin that process immediately upon a go-ahead decision from GTO. We have worked in this area before and expect that landowners will cooperate with our research and grant access to collect data. We will prioritize the collection of additional MT and gravity data, methods known to work well in the Saddle and Mauna Kea region. Our second priority will be acquisition of ambient noise seismic and self-potential data. The results of our effort will fill gaps in existing MT and gravity data and bring in new information in the form of seismic velocities and self-potential. Combined with existing data, the proposed collection will enhance our understanding of the subsurface and help refine the characteristics and occurrence of producible geothermal resources.

7.1 Magnetotellurics

Proposed MT data collection points are shown as orange circles and polygons in Figure 109. Mauna Kea summit measurements will be useful to help constrain the 3D inversion that is planned for the beginning of Phase 2. However, we can proceed with the planned inversion and then incorporate these data into joint inversion using the planned 3D resistivity model as a reference. Several of the sites on the East flank of Mauna Kea (Mana Road) are repeated to confirm the presence of a strong conductor reported in the south-to-north 2D profile that does not have a corresponding gravity high. Depending on access, it will take approximately four weeks to collect data at the proposed MT sites.

7.2 Gravity

Where we collect new MT data, we will collect gravity measurements as well. This will help constrain what we know about density around Mauna Kea and in the Saddle Region. We may also choose to tighten the gravity station spacings and repeat gravity measurements, filling gaps and repeating data of questionable quality in the existing gravity data set. A gravity survey along the same lines as the planned self-potential is estimated to take one team of two personnel approximately three weeks to collect. MT and gravity are our first priorities.

7.3 Seismic Data

For seismic data collection and survey design, UH will work with Roland Gritto (Array Information Technology). We will need approximately 30 days' duration of node deployment to collect ambient noise tomography data. It would take a much longer duration to collect P- and S-wave tomography data, which is what was performed in the LERZ. Though the planned data collection and outcomes are considered experimental, the UH team believes there is potential value in doing so, as the expected cost of deployment and instrument pickup is a small portion of the data collection budget, with deployment likely concurrent with MT data collection. Based on our comparisons of data sets along LERZ and Lanai, there is a strong correlation between

resistivity, velocity, self-potential, and density with each data type providing different and complementary pieces of information.

7.4 Self-Potential

As access, budget, and time allow, we will perform self-potential surveys at locations around the Saddle Region. We will first have to determine if contact resistances are within a range where self-potential is feasible. Our experience with MT data collection is that contact resistance around Mauna Kea can be quite high. If it is possible to collect useful self-potential data, we will focus on the proposed areas designated by white boxes in Figure 109. This, along with seismic data collection, has not been performed previously, so will be a new data set. Depending on access, we would prioritize starting near PTA as we have borehole logs and core available that indicated a geothermal resource is present in the Saddle Region (evidenced by ~100°C water near sea level within the PTA2 borehole and a projected equilibrated bottom hole temperature of 140°C). The next priority is the Parker Ranch property above Waimea, and time allowing, Mana Road, on Mauna Kea's east flank. Total collection will be approximately 500 data points at a 20 m spacing. More will be completed if time allows. The expected duration of self-potential data collection is approximately one week. Sampling self-potential in the Saddle Region will help us determine if data collection is balanced with information returned.

7.5 Additional Locations Under Consideration

Additional areas to be considered for data collection are Mauna Loa's southwest rift and Hualalai. As stated earlier, the ability to collect data will depend on access and the final data collection budget. For Phase 2, the primary focus will be on MT and gravity collection in the Saddle/Mauna Kea region.

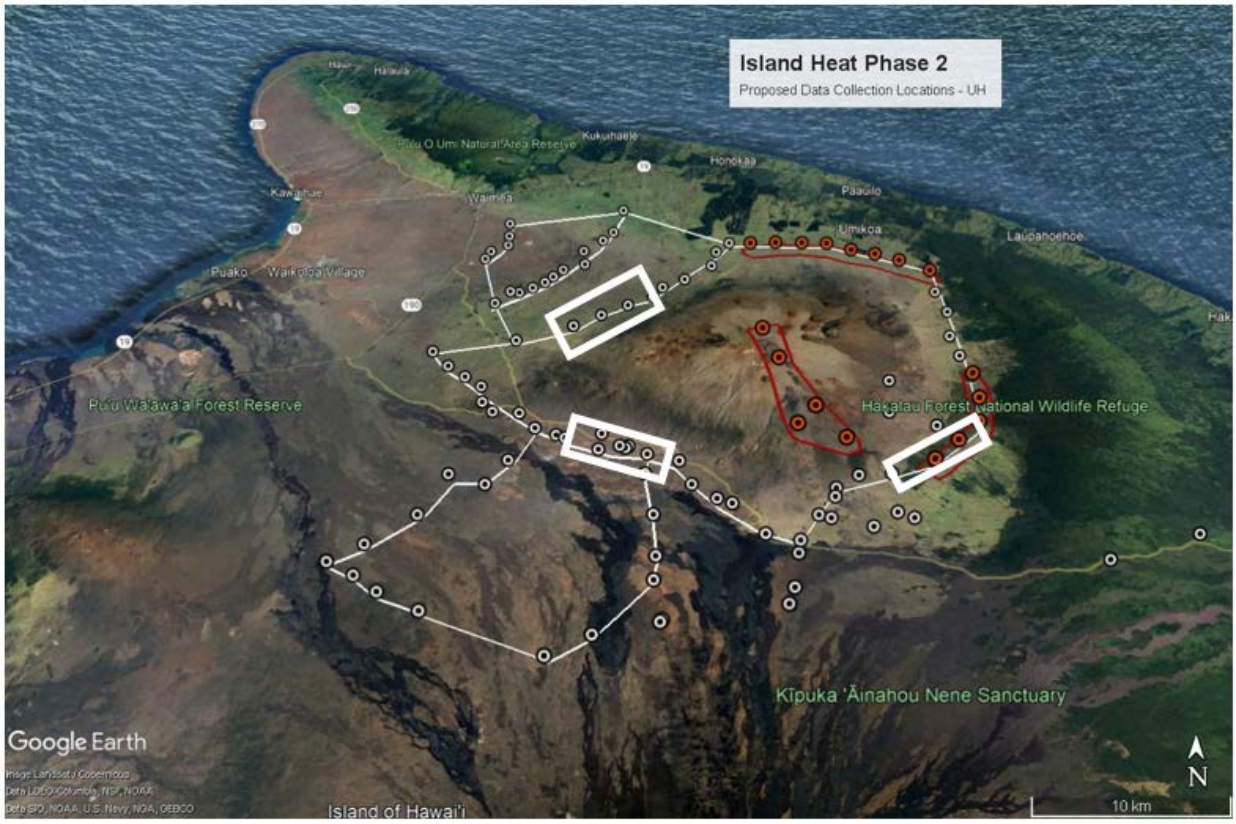

Figure 109. UH proposed data collection locations. Orange dots indicate new MT stations. White boxes are proposed self-potential survey locations and thin white lines are proposed gravity survey locations. White dots are existing MT data points.

8 Summary

Diverse data sets compiled and processed in Phase 1 were used to predict geologic characteristics and geophysical signatures of ocean-island hydrothermal systems, while an evolving conceptual model provides the context for understanding the components of hydrothermal systems occurring in active, historic, and extinct Hawaiian volcanic rifts.

Phase 1 focused on updating data from the Hawai‘i PFA project, specifically at Kilauea’s LERZ and at the Mauna Kea Saddle Region. Historic data from the PGV provide details of the power-generating resource and its geological and geophysical signatures. Existing gravity and MT data were inverted for density and resistivity, respectively, which will be used to constrain joint inversions in Phase 2. Seismic data from before, during, and after the 2018 Kilauea eruption were processed to yield V_P, V_S, and V_P/V_S volumes after relocation and refinement of data from available earthquake catalogues. GPS and InSAR data were used to understand deformation associated with the 2018 Kilauea eruption and to model fracture formation and its relationship to permeability at PGV. These data together are being used to inform MML algorithms in order to identify and predict the numerical and categorical features associated with geothermal systems that are blind to surface.

The MML methodology and framework will be advanced with new data collections in Phase 2 and with further refinement of data analyzed in Phase 1 to extract additional information about the subsurface and potential for hydrothermal reservoirs.

References

Anderson, K. R., Johanson I. A., Patrick, M. R., Gu, M., Segall, P., Poland, M. P., Motgomery-Brown, E. K., Miklius A., 2019. Magma reservoir failure and the onset of caldera collapse at Kilauea Volcano in 2018. *Science*, **366**, eaaz1822.

Bai, Y., Ye, L., Yamazaki, Y., Lay, T., and Cheung, K.F., 2018, The 4 May 2018 Mw 6.9 Hawai'i Island Earthquake and Implications for Tsunami Hazards: Geophysical Research Letters, 45, 11,040-11,049, doi:10.1029/2018GL079742.

Baker, S. and Amelung, F., 2015, Pressurized magma reservoir within the east rift zone of Kilauea Volcano, Hawai'i: Evidence for relaxed stress changes from the 1975 Kalapana earthquake: Geophysical Research Letters, 42, 8 p.

Barber, J.R., 2002, Elasticity: Dordrecht, The Netherlands, Kluwer Academic Publishers, 410 p.

Berardino, P., Fornaro, G., Lanari, R., 2002. A new algorithm for surface deformation monitoring based on small baseline differential SAR interferograms. *IEEE transactions on Geoscience and Remote Sensing,* **40** (11), 2375-2383.

Beyreuther, M., Barsch, R., Krischer, L., Megies, T., Behr, Y., and Wassermann, J. (2010), ObsPy: A Python Toolbox for Seismology, Seis. Res. Lett., **81**, pp. 530-533, http://www.seismosoc.org/publications/SRL/SRL_81/srl_81-3_es.

Blakely, R., 1995, Potential Theory in Gravity and Magnetic Applications. Cambridge: Cambridge University Press. doi:10.1017/CBO9780511549816.

Brooks, S., Gelman, A., Jones, G., & Meng, X. L. (Eds.). (2011). Handbook of Markov Chain Monte Carlo. CRC press.

Buscema, M., Breda, M., Lodwick, W., 2013. Training with input selection and testing (TWIST) algorithm: a significant advance in pattern recognition performance of machine learning. J. Intell. Learn. Syst. 5, 29–38.

Campbell, A.R., and Gardner, M.C., 1981, Geology and drilling history of the Lanipuna #1 geothermal test, Tokyu lands prospect, Hawaii, Geothermex for Banwell Industries, Honolulu, Hawaii.128 p.

Chen, J., Hoversten, G. M., Key, K., Nordquist, G., and Cumming, W. (2012). Stochastic inversion of magnetotelluric data using a sharp boundary parameterization and application to a geothermal site. Geophysics, 77(4), E265-E279.

Cheng, Kan Bun, Gedeon Dagan, Warren Barrash, Michael Cardiff, and Avinoam Rabinovich. 2022. "Statistical Analysis of Aquifer Hydraulic Properties by a Continuous Pumping Tomography Test: Application to the Boise Hydrogeophysical Research Site." *Water Resources Research.* Volume 58, Issue 12. https://doi.org/10.1029/2022WR032464.

Cohen, J., 1960. A coefficient of agreement for nominal scales. Educ. Psychol. Meas. 20, 37–46.

Constable, S. C., R. L. Parker, and C. G. Constable, 1987, Occam's inversion — A practical algorithm for generating smooth models from electromagnetic sounding data, Geophysics, 52 (03), 289–300.

Dahm, T. and T. Fischer (2013), Velocity ratio variations in the source region of earthquake swarms in NW Bohemia obtained from arrival time double-differences, *Geophys J. Int*., **196**, pp. 957–970, doi: 10.1093/gji/ggt410.

Davies, D.L., Bouldin, D.W., 1979, A cluster separation measure. IEEE Trans Patt Anal Mach Intel PAMI-1:224–227.

Davis, T., 2021, An analytical and numerical analysis of fluid-filled crack propagation in three dimensions: University of Potsdam, 187 p., https://publishup.uni-potsdam.de/opus4-ubp/frontdoor/deliver/index/docId/50960/file/davis_diss.pdf.

Denlinger, Roger P.; Morgan, Julia K. (2014). "Chapter 4: Instability of Hawaiian Volcanoes" (PDF). In Poland, Michael P.; Takahashi, Taeko Jane; Landowski, Claire M. (eds.). Characteristics of Hawaiian volcanoes. U.S. Geological Survey Professional Papers. Professional Paper 1801. U.S. Geological Survey. doi:10.3133/pp18014. ISSN 2330-7102.

Denlinger, Roger and Ashton Flinders. 2021. Personal Communication. Research Geophysicists, U.S. Geological Survey.

Dieterich, J. 1994. A constitutive law for rate of earthquake production and its application to earthquake clustering, *Journal of Geophysical Research*, **99**, 2601-2618.

Dieterich, J., Cayol, V., and Okubo, P. 2000. The use of earthquake rate changes as a stress meter at Kilauea volcano, *Nature*, **408,** 457-460.

Duffield, W.A., 1975, Structure and origin, Koae fault system, Kilauea Volcano, Hawaii: U.S. Geological Survey Professional Paper 856, 12 p.

Egbert, G.D., 1997, Robust multiple-station magnetotelluric data processing, *Geophys. J. Int., 130,* 475-496.

Ferretti, A. 2014. *Satellite InSAR Data – Reservoir Monitoring from Space*. EAGE Publications.

Finn, Carol. 2022. Personal Communication. Research Geophysicist, U.S. Geological Survey.

Fiske, R.S. and Jackson, E.D., 1972, Orientation and growth of Hawaiian volcanic rifts: the effect of regional structure and gravitational stresses: Proc. R. Soc. Lon., Ser. A, 329, pp. 299-326.

Flinders, F., Ito, G., Garcia, M.O., Sinton, J.M., Kauahikaua, J., and Taylor, B., 2013, Intrusive dike complexes, cumulate cores and the extrusive growth of Hawaiian volcanoes. Geophysical Research Letters, VOL. 40, 3367-3373, doi:10.1002/grl.5063. Additional resources including geochemistry, Play Fairway Phases.

Flinders, A.F., Caudron, C., Johanson, I.A., Taira, T., Shiro, B., and Haney, M., 2020, Seismic velocity variations associated with the 2018 lower East Rift Zone eruption of Kīlauea, Hawai‘i: Bulletin of Volcanology, 82, doi:10.1007/s00445-020-01380-w.

Freeze, R.A., and Cherry, J.A., 1979, Groundwater: Englewood Cliffs: New Jersey, 604 p.

Friedel, M.J., 2016, Estimation and scaling of hydrostratigraphic units: application of unsupervised machine learning and multivariate statistical techniques to hydrogeophysical data, Hydrogeology Journal, 24, 2103-2122.

Friedel, M.J. and Daughney, C., 2016, Statistical robustness of machine-learning estimates for characterizing a groundwater-surface water system, Southland, New Zealand, Achieving deep learning by systemizing machine learning with big data engines I, Poster IN11B-1619, Earth and Space Science Informatics, American Geophysical Union, San Francisco, CA, 2016.

Friedel, M.J., Wilson, S.R., Close, M.E., Buscema, M., Abraham, P., 2020 Comparison of four learning-based methods for predicting groundwater redox status, Journal of Hydrology, 580, 124200 [IF: 5.72] *

Friedel, Michael J., Nicole Lautze, Erin Wallin, and Aaron Rothfolk, 2022, “Multimodal Machine Learning for 3D Characterization of Hidden Groundwater and Geothermal Resources: Case Study, Lāna'i Hawaii.” Presented at the 47th Workshop on Geothermal Reservoir Engineering Stanford University, Stanford, California, February 7-9, 2022. SGP-TR-223. https://pangea.stanford.edu/ERE/db/GeoConf/papers/SGW/2022/Lautze2.pdf

Godson, R. H., Zablocki, C.J., Pierce, H.A., Frayser, J.B., Mitchell, C.M., and Sneddon, R.A., 1981, Aeromagnetic map of the Island of Hawaii, scale 1:250,000, U.S. Geol. Surv. Geophys. Invest. Map, GP-946, 1 p.

Gritto, R. and S.P. Jarpe (2014), Temporal variations of V_p/V_s-ratio at The Geysers geothermal field, USA, *Geothermics*, **52**, 112-119, doi: 10.1016/j.geothermics.2014.01.012.

Gritto R., A.E. Romero, T.M. Daley (2004), Results of a VSP experiment at the Resurgent Dome, Long Valley caldera, California, *Geophys. Res. Lett*., **31**, doi:10.1029/2004GL019451.

Gritto, R., S.H. Yoo, and S.P. Jarpe (2013), 3D Seismic Tomography at The Geysers Geothermal Field, CA, USA, *Proceedings of Thirty-Eighth Workshop on Geothermal Reservoir Engineering*, Stanford University, Stanford California, 11-13 February, 2013, SGP-TR-198, pp.1-12.

He, Q.Z, Barajas-Solano, D., Tartakovsky, G., Neural networks for multiphysics data assimilation with application to subsurface transport, Advances in Water Resources, 141, 2020, 103610, ISSN 0309-1708.

Hildenbrand, T.G., J. G. Rosenbaum, and J.P. Kauahikaua, 1993, Aeromagnetic study of the Island of Hawai‘i. Journal of Geophysical Research, Vol. 98, NO. B3, p.4099-4119.

Hinze, W.J., Von Frese, R.R.B. and Saad, A.H. 2013. Gravity and Magnetic Exploration Principles, Practices, and Applications. Cambridge University Press, New York, 515 p. https://doi.org/10.1017/CBO9780511843129

Hooper, A., H. Zebker, P. Segall, and B. Kampes 2004, A new method for measuring deformation on volcanoes and other natural terrains using InSAR persistent scatterers, *Geophys. Res. Lett.*, ***31***, doi:10.1029/2004GL021737.

Hooper, A. 2008. A multi-temporal InSAR method incorporating both persistent scatterer and small baseline approaches, *Geophys. Res. Lett.*, *35*(L16302), doi:10.1029/2008GL03465.

Hutchings, L., S. Jarpe, K. Boyle, H. Philson, and E. Majer (2011), Inexpensive, Automated Micro-Earthquake Data Collection and Processing System for Rapid, High-Resolution Reservoir Analysis, *Proceedings, Geothermal Resources Council*, August, 2011, pp. 16.

Incorporated Research Institutions for Seismology, 2022. IRIS. https://ds.iris.edu/ds/ last visited 4/5/2022.

Iovenitti, J.L. and D'Olier, W.L., 1985, Preliminary results of drilling and testing in the Puna geothermal system, Hawaii: PROCEEDINGS 10th Workshop on Geothermal Reservoir Engineering, Stanford University, Stanford, CA, January 22-24, 1985, pp. 65-71.

Ito, G., Frazer, N., Lautze, N., Thomas, D., Hinz, N., Waller, D., Whittier, R., and Wallin, E., 2017, Play fairway analysis of geothermal resources across the state of Hawaii: 2. Resource probability mapping: Geothermics 70, pp. 393-405.

Jacoby, W., & Smilde, P. L. (2009). Gravity interpretation: Fundamentals and application of gravity inversion and geological interpretation. Springer Science & Business Media.

Jaeger, J.C., Cook, N.G.W., and Zimmerman, R., 2007, Fundamentals of rock mechanics: Oxford, Wiley-Blackwell, 488 p.

Jerran, D.A., Millett, J.M., Kuck, Jochem, Thomas, Planke, S., Haskins, E., Lautze, N., and Peerdominici, S., 2019, Understanding volcanic facies in the subsurface: a combined core, wireline logging and image log data set from the PTA2 and KMZ2 boreholes, Big Island, Hawai'i, Sci. Dril., 25, 15-33. https://sd.copernicus.org/articles/25/15/2019/

Kalteh, A.M., Hjorth, P., Berndtsson, R., 2008, Review of the self-organizing map (SOM) approach in water resources: analysis, modeling and application. Environ Model Softw 23(7):835–845.

Kauahikaua, J.P., 2017, Gravity Data for Island of Hawai`i: U.S. Geological Survey data release, https://doi.org/10.5066/F7V1230Q.

Kauahikaua, J.P, 2000, Deep magmatic structures of Hawaiian volcanoes, imaged by three-dimensional gravity models. *Geology*; October 2000, v. 28; no. 10; p.883-886.

Kingston Reynolds Thom & Allardice Ltd., 1976, Hawai'i geothermal project well completion report HGP-A, Prepared for University of Hawai'i Research Corporation, and U.S. Energy Research & Development Administration, 34 p.

Kundu, B., Yadav, R. K., Burgmann, R., Wang, K., Panda, D., and Gahalaut, V. K. 2020. Triggering relationships between magmatic and faulting processes in the May 2018 eruptive sequence at Kilauea volcano, Hawaii, Geophysical Journal International, 222, 461-473, doi:10.1093/gji/ggaa178.

Kaven, J.O., and Martel, S.J., 2007, Growth of surface-breaching normal faults as a three-dimensional fracturing process: Journal of Structural Geology, 29, 1463–1476.

Key, K., 2009, 1D inversion of multicomponent, multifrequency marine CSEM data: Methodology and synthetic studies for resolving thin resistive layers. Geophysics V. 74, No. 2. P.F9-F20.

Kihara, D., Chen, B., Yuen, P., and Takahasi, P., 1977, Summary results of HGP-A well testing, in Proceedings of the Workshop Geothermal Reservoir Engineering, 138-144, Dec. 14-15, 1977.

Kirkby, A.L., Zhang, F., Peacock, J., Hassan, R., Duan, J., 2019, The MTPy software package for magnetotelluric data analysis and visualisation. Journal of Open Source Software, 4(37), 1358. https://doi.org/10.21105/joss.01358

Klein, F. W., 1981. A linear gradient crustal model for south Hawaii, *Bulletin of Seismological Society of America*, 71, 1503–1510.

Klein, F. W. 2016. Lithospheric flexure under the Hawaiian volcanic load: Internal stresses and a broken plate revealed by earthquakes, *J. Geophys. Res. Solid Earth*, 121, 2400–2428, doi:10.1002/2015JB012746.

Kohonen, T. 2001. Self-Organizing Maps. Springer-Verlag, New York, Berlin, Heidelberg. https://doi.org/10.1007/978-3-642-56927-2

Krieger, L., and Peacock, J., 2014, MTpy: A Python toolbox for magnetotellurics. Computers and Geosciences, 72, p. 167-175. https://doi.org/10.1016/j.cageo.2014.07.013

Lanari, R., Mora, O., Manunta, M., Mallorqui, J. J., Berardino, P, and Sansosti, E. 2004. A small baseline approach for investigating deformations on full-resolution differential SAR interferograms, *IEEE Transactions on Geoscience and Remote Sensing*, **42**, 1377-1386.

Lautze, N.C., Thomas, D., Hinz, N., Apuzen-Ito, G., Frazer, N., Waller, D., 2017, Play fairway analysis of geothermal resources across the State of Hawaii: 1. Geological, geophysical, and geochemical datasets. Geothermics 70 (2017): 376-392.

Lautze, N.C., Ito, G., Thomas, D.M., Frazer, N., Martel, S., Hinz, N., Tachera, D.K., Hill, G., Pierce, H.A., Wannamaker, P.E., Martin, T., 2020. Play Fairway Analysis of geothermal resources across the State of Hawai'i: 4. Updates with new groundwater chemistry, subsurface stress analysis, and focused geophysical surveys. Geothermics 86, https://doi.org/10.1016/j.geothermics.2019.101798.

Leahy, G.M., Collins, J.A., Wolfe, C.J., Laske, G., Solomon, S.C., 2010, Underplating of the Hawaiian Swell - evidence from teleseismic receiver function, Geophys. J. Int., 183, 213-329.

Lin, G. and P. M. Shearer (2007), Estimating Local Vp/Vs Ratios within Similar Earthquake Clusters, *Bull. Seis. Soc. Am.*, **97**, No. 2, pp. 379–388, doi: 10.1785/0120060115.

Lin, G. and P. M. Shearer (2009), Evidence for water-filled cracks in earthquake source regions, *Geophys. Res. Lett*., **36**, L17315, doi:10.1029/2009GL039098

Lin, G., & Shearer, P. M. (2021). Spatiotemporal variations of focal mechanism and in situ Vp/Vs ratio during the 2018 Kīlauea eruption, *Geophysical Research Letters*, 48, e2021GL094636. https://doi.org/10.1029/2021GL094636

Lin, G., P. M. Shearer, R. S. Matoza,P. G. Okubo, and F. Amelung, 2014. Three-dimensional seismic velocity structure of Mauna Loa and Kilauea volcanoes in Hawai'i from local seismic tomography, *J. Geophys. Res. Solid Earth*,119, 4377–4392, doi:10.1002/2013JB010820

Lin, G., & Okubo, P. G. (2020). Seismic evidence for a shallow detachment beneath Kīlauea's south flank during the 2018 activity. *Geophysical Research Letters,* 47, e2020GL088003. https://doi.org/10.1029/2020GL088003

Lipman, P.W., Rhodes, J.M., and Dalrymple, G.B., 1990, The Ninole Basalt-Implications for the structural evolution of Mauna Loa Volcano, Hawaii: Bulletin of Volcanology, v. 53, no. 1, p. 1-19.

Malahoff, A., Woollard, G.P., 1966, Magnetic surveys over the Hawaiian Islands and their geologic implications, Pac Sci 20(3): 265-311.

Martel, S.J., 2000, Modeling elastic stresses in long ridges with the displacement discontinuity method: Pure and Applied Geophysics, 157, 1039–1057, doi:10.1007/s000240050016.

Martel, S.J., 2004, Mechanics of landslide initiation as a shear fracture phenomenon: Marine Geology, 203, 319–339, doi:10.1016/S0025-3227(03)00313-X.

Martel, S.J., 2016. Effects of small-amplitude periodic topography on combined stresses due to gravity and tectonics. *Int. J. Rock Mech. Min. Sci*., 89 (2016), pp. 1-13, 10.1016/j.ijrmms.2016.07.026

Martel, S.J., and Boger, W., 1998, Geometry and mechanics of secondary fracturing around small three-dimensional faults in granitic rock: Journal of Geophysical Research, 103, p. 21299, doi:10.1029/98JB01393.

Martel, S.J., and Langley, J.S., 2006, Propagation of normal faults to the surface in basalt, Koae fault system, Hawaii: Journal of Structural Geology, 28, 2123–2143, doi:10.1016/j.jsg.2005.12.004.

Martel, S.J., Stock, G.M., and Ito, G., 2014, Mechanics of relative and absolute displacements across normal faults, and implications for uplift and subsidence along the eastern escarpment of the Sierra Nevada, California: Geosphere, 10, 243–263, doi:10.1130/GES00968.1.

Matoza, R. S., Shearer, P. M., Lin, G., Wolfe, C. J., and Okubo, P. G., 2013. Systematic relocation of seismicity on Hawai'i Island from 1992 to 2009 using waveform cross correlation and cluster analysis, *Journal of Geophysical Research*, 118, 2275– 2288, doi:10.1002/jgrb.50189.

Matoza, R. S., Okubo, P. G., and Shearer, P. M., 2020. Comprehensive high-precision relocation of seismicity on the Island of Hawai'i 1986–2018. *Journal of Geophysical Research*, 7, e2020EA001253. https://doi.org/10.1029/2020EA001253

Mccubbine, J., Caratori Tontini, F., O'Brien, G., Smith, E., and Stagpoole, V., 2018, Gsolve, a Python computer program with a graphical user interface to transform relative gravity survey measurements to absolute gravity values and gravity anomalies. SoftwareX. 7. 129-137, doi: 10.1016/j.softx.2018.04.003.

Miller, J.A., Whitehead, R.L., Oki, D.S., Gingerich, S.B., and Olcott, P.G., 1997, Ground water atlas of the United States: Segment 13, Alaska, Hawaii, Puerto Rico, and the U.S. Virgin Islands:, doi:10.3133/ha730N.

Moon, S., Perron, J.T., Martel, S.J., Holbrook, W.S., and St. Clair, J., 2017, A model of three-dimensional topographic stresses with implications for bedrock fractures, surface processes, and landscape evolution: Journal of Geophysical Research: Earth Surface, 122, 823–846, doi:10.1002/2016JF004155.

Montgomery-Brown, E. K., Sinnett, D. K., Poland, M. Segall, P., Orr, T., Zebker, H. and Miklius, A. 2010. Geodetic evidence for en echelon dike emplacement and concurrent slow slip during the June 2007 intrusion and eruption at Kilauea volcano, Hawaii, *Journal of Geophysical Research*, **115**, B07405, doi:10.1029/2009JB006658.

Montgomery-Brown, E. K., Poland, M. P. and Miklius, A. 2015. Delicate balance of magmatic-tectonic interaction at Kilauea Volcano, Hawaii, revealed from slow slip events, *Geophysical Monographs*, **13**, 208, doi:10.1002/9781118872079.ch13.

Moore, J.G., Norark, W.R., and Holcomb, R.T., 1994, Giant Hawaiian Landslides, Annual Review of Earth and Planetary Sciences 1994 22:1, 119-144.

Nakamura, K., 1980, Why do long rift zones develop in Hawaiian volcanoes – a possible role of thick oceanic sediments: Bull. Volcanol. Soc. of Japan, 25, pp. 255-269.

National Research Council, 1996, Rock fractures and fluid flow: contemporary understanding and applications: Washington, D.C., National Academy Press, 551 p., http://www.nap.edu/catalog/2309/rock-fractures-and-fluid-flow-contemporary-understanding-and-applications.

Neal, C.A. and Lockwood, J.P., 2003, Geologic Map of the Summit Region of Kilauea Volcano, Hawaii: U.S. Geological Survey Miscellaneous Investigations Series Map I-2759, 15 p., 1 sheet, scale 1:24,000, doi:10.3133/i2759.

Neal, C. A., S.R. Brantley, L. Antolik, J.L. Babb, M. Burgess, K. Calles, M. Cappos, J.C. Chang, S. Conway, L. Desmither, P. Dotray, T. Elias, P. Fukunga, S. Fuke, I.A. Johanson, K. Kamibayashi, J. Kauahikau, R.L. Lee, S. Pekalib, A. Miklius, W…. 2019. The 2018 rift eruption and summit collapse of Kilauea Volcano, *Science*, **363**, 367-374, doi: 10.1126/science.aav7046.

Newman, G. A., and D. L. Alumbaugh, 2000, Three-dimensional magnetotelluric inversion using non-linear conjugate gradients: Geophysical Journal International, 140, 410–424, doi: 10.1046/j.1365-246x.2000.00007.x.

Nugraha, H.D., Darma, I.W.D., Darmawan, F.H., 2016, Ngimbang Clastics Play in The East Java Basin: New Insight and Concepts for North Madura Platform, 40th IPA Annual Convention Proceedings.

Okada, Y., 1992. Internal deformation due to shear and tensile faults in a half-space, *Bulletin of the Seismological Society of America*, **82**, 1018-1040.

Okubo, P. G., Nakata, J. S., and Koyanagi, R. Y. 2014. The evolution of seismic monitoring systems at the Hawaiian Volanco Observatory. In M. P. Poland and C. M. Landowski (Eds.), *Characteristics of Hawaiian Volcanoes* (p. 67-94). Washington, D. C.

Paige, C. C., and Saunders, M. A. 1982. LSQR: An algorithm for sparse linear equations and sparse linear systems, *ACM Transactions Math. Software*, **8,** 195-209.

Park, J., Morgan, J.K., Zelt, C.A., Okubo, P.G., Peters, L., Benesh, N., 2007, Comparative velocity structure of active Hawaiian volcanoes from 3-D onshore-offshore seismic tomography, Earth and Planetary Science Letters 259, 500-516.

Pedersen, R., Sigmundsson, F., and Einarsson, P. 2007. Controlling factors on earthquake swarms associated with magmatic intrusions; constraints from Iceland, *Journal of Volcanology and Geothermal Research,* **162**, 73-80.

Peterson, D. 2021. Personal Communication. Geophysicist, U.S. Geological Survey.

Pierce, Herbert. 2021. Personal Communication. Geophysicist, Retired.

Podvin, P., and I. Lecomte (1991), Finite difference computation of travel times in very contrasted velocity models: A massively parallel approach and its associated tools, *Geophys. J. Int*., **105**, 271–284.

Poland, M.P., Miklius, A., and Montgomery-Brown, E.K., 2014, Magma supply, storage, and transport at shield-stage Hawaiian volcanoes: Chapter 5 in Characteristics of Hawaiian volcanoes, *in* Characteristics of Hawaiian volcanoes, doi:10.3133/pp18015.

Pollard, D.D., and Segall, P., 1987, Theoretical displacements and stresses near fractures in rock: with applications to faults, joints, veins, dikes, and solution surfaces, *in* Atkinson, B.K. ed., Fracture Mechanics of Rock, London, Academic Press, 277–349, doi:10.1016/B978-0-12-066266-1.50013-2.

Pratt, R. G., C. Shin, and G. J. Hicks, 1998, Gauss-Newton and full Newton methods in frequency-space seismic waveform inversion: Geophysical Journal International, 133, 341–362, doi: 10.1046/j.1365-246X.1998 .00498.x.

Puna Geothermal Venture, 1991, Hydrogeologic model of the Puna Geothermal Venture Geothermal resource update (update October 22, 1991), 91151.011, 26 p.

Putrika, K., 1997, Magma transport at Hawaii: Inferences based on igneous thermobarometry, Geology, 25 (1), 69-72.

Ryan, M.P., 1988, The Mechanics and Three-Dimensional Internal Structure of Active Magmatic Systems: Kilauea Volcano, Hawaii: Journal of Geophysical Research, 93, B5, pp. 4213-4248.

Qin, Z., Jiang, A., Faulder, D., Cladouhos, T.T., and Jafarpour, B., 2022, A physics-guided deep learning model for prediction of geothermal reservoir performance, Proceedings, 47th Stanford Geothermal Workshop, Stanford University, Stanford, California.

Riese, F.M., 2019, SuSi: SUpervised Self-organIzing maps in Python, 10.5281/zenodo.2609130.

Rodi, W. and Mackie, R.L., 2001, Nonlinear conjugate gradients algorithm for 2-D magnetotelluric inversion, Geophysics, v. 66, p. 174-187.

Rosid, M.S. and A.C Aprilia, 2020, Tilt angle analysis of gravity data to identify geothermal heat source in Mt. Lawu field. AIP Conference Proceedings 2296, 020036.

Roy, I. G., 2002, A robust descent type algorithm for geophysical inversion through adaptive regularization: Applied Mathematical Modeling, 26, 619–634, doi: 10.1016/S0307-904X(01)00072-5.

Rubin, A.M., and Pollard, D.D., 1987, Origins of blade-like dikes in volcanic rift zones, chap. 53 *of* Decker, R.W., Wright, T.L., and Stauffer, P.H., eds., Volcanism in Hawaii: U.S. Geological Survey Professional Paper 1350, 1449–1470, http://pubs.usgs.gov/ pp/1987/1350/.

Rucci, A., Vasco, D. W. and Novali, F. 2013. Monitoring the geologic storage of carbon dioxide using multicomponent SAR interferometry. *Geophysical Journal International*, **193**(1), 197-208.

Samsonov, S. and d'Oreye, N. 2012. Multidimensional time series analysis of ground deformation from multiple InSAR data sets applied to Virunga Volcanic Province. *Geophysical Journal International*, **191**, 1095-1108, http://dx.doi.org/10.1111/j.1365-246X.2012.05669.x.

Samsonov S., van der Koij M. and Tiampo, K., 2011. A simultaneous inversion for deformation rates and topographic errors of DInSAR data utilizing linear least square inversion technique, *Computers & Geosciences*, 37 (8), 1083-1091

Savage, W.Z., Swolfs, H.S., and Powers, P.S., 1985, Gravitational stresses in long symmetric ridges and valleys: International Journal of Rock Mechanics and Geomechanics Abstracts, 22, 291–302, doi:10.1016/0148-9062(85)92061-3.

Schoenball, M. and W. L. Ellsworth, 2017. Waveform-Relocated Earthquake Catalog for Oklahoma and Southern Kansas Illuminates the Regional Fault Network. *Seismological Research Letters* 88 (5): 1252–1258. doi: https://doi.org/10.1785/0220170083

Schutt, D.L., Lowry, A.R., Buehler, J.S., 2018, Moho temperature and mobility of the lower crust in western United States. Geology 46(3), 219-222.

Segall, P., Anderson, K.R., Johanson, I., and Miklius, A., 2019, Mechanics of Inflationary Deformation During Caldera Collapse: Evidence From the 2018 Kīlauea Eruption: Geophysical Research Letters, v. 46, p. 11782–11789, doi:10.1029/2019GL084689.

Shelly, D. R., & Thelen, W. A. (2019). Anatomy of a caldera collapse: Kīlauea 2018 summit seismicity sequence in high resolution. *Geophysical Research Letters*, 46, 14395– 14403. https://doi.org/10.1029/2019GL085636

Simpson, F., and Bahr, K., 2005, Practical magnetotellurics: Cambridge University Press, 254 p.

Snow, D.T., 1965, A Parallel Plate Model of Fractured Permeable Media: University of California, Berkeley, 331 p.

Sorey, M.L., and Colvard, E.M., 1994, Potential effects of the Hawai'i geothermal project on ground-water resources on the island of Hawaii, U.S. Geological Survey Water Resources Investigations Report 94-4028, 33 p.

Spies, B. R., & Frischknecht, F. C. (1991). Electromagnetic sounding. Electromagnetic methods in applied geophysics, 2(Part A), 285-426.

State of Hawai'i – USA, 1990, The Kilauea East Rift Zone: geothermal evaluation of the existing data. Annex B: Agreement for advisory services for the geothermal cable project, contract no. 27272.

Stearns, H.T., 1940, Geology and ground-water resources of the islands of Lāna'i and Kahoolawe, Hawaii: Hawai'i (Terr.) Division of Hydrography Bulletin 6, p. 177 p. (pt. 1, Geology and ground-water resources of Lāna'i, p. 1-115; pt. 2, Geology and ground-water resources of Kahoolawe, p. 117-173); 1 folded map in pocket (scale 1:62,500).

Stearns, H.T., and MacDonald, G.A., 1946, Geology and groundwater-resources of the Island of Hawai'i Division of hydrography, Bulletin 9, 363 p.

Stolper, E.M, DePaolo, D.J., and Thomans, D.M., 2009, Deep drilling into a mantle plume volcano: The Hawai'i scientific drilling project (HSDP), Sci. Dril., 7, 4–14. https://doi.org/10.2204/iodp.sd.7.02.2009.

Teplow, W., Marsh, B., Hulen, J., Spielman, P., Kaleikini, M., Fitch, D., and Rickard, W., 2009, Dacite Melt at the Puna Geothermal Venture Wellfield, Big Island of Hawaii: GRC Transactions 33, pp. 989-994.

Teplow, William. 2021. Personal Communication. Senior Geological Advisor, U.S. Geothermal Inc.

Thomas, D.M., 1987, A geochemical model of the Kilauea East Rift Zone: USGS Professional Paper 1350, Chapter 56, pp. 1507-1525.

Thomas, D.M., Lienert, B.R., and Wallin, E.L., 2015, Three-dimensional Magnetotelluric Modeling of the Pohukuloa Training Area, Hawai'i Island. Abstract GP13A-1281 presented at Fall Meeting, American Geophysical Union, San Francisco, Calif., 14-18 Dec.

Thomas, A.L., 1993, POLY3D: a three-dimensional, polygonal element, displacement discontinuity boundary element computer program will applications to fractures, faults, and cavities in the Earth's crust: Stanford University, 221 p., https://searchworks.stanford.edu/view/2830996.

Trusdell, F.A., Wolfe, E.W., and Morris, J., 2006, Digital database of the geologic map of the island of Hawai'i: USGS Data Series 144 supplement.

UBC. 2013. "GRAV3D: A Program Library for Forward Modelling and Inversion of Gravity Data over 3D Structures. Version 5.0." University of British Columbia. https://gif.eos.ubc.ca/sites/default/files/grav3dManual.pdf

U.S. Geological Survey, 2020. "libcomcat software release." Accessed June 27, 2023. https://github.com/usgs/libcomcat/.

Vasco, D. W., Johnson, L. R., & Goldstein, N. E., 1988. Using surface displacement and strain observations to determine deformation at depth, with an application to Long Valley, caldera, California, J. Geophys. Res., 93, 3232-3242.

Vasco, D. W., and Mali, G. 2021. On the use of adjoints in the inversion of observed quasi-static deformation, *Geophysical Journal International,* 224, 896-908.

Vasco, D. W., Rucci, A., Ferretti, A., Novali, F., Bissell, R. C., Ringrose, P. S., Mathieson, A. S., and Wright, I. W., 2010. Satellite-based measurements of surface deformation reveal fluid flow associated with the geological storage of carbon dioxide, *Geophysical Research Letters*, **37**, L03303, 1-5, doi:10.1029/2009GL041544.

Vasco, D. W., Harness, P., Pride, S., and Hoversten, M. 2017. Estimating fluid-induced stress change from observed deformation, *Geophysical Journal International*, **208**, 1623-1642.

Vasco, D. W., Farr, T. G., Jeanne, P., Doughty, C., and Nico, P., 2019. Satellite-based monitoring of groundwater depletion in California's Central Valley, *Nature Scientific Reports*, **9**, 16043, doi.org/10.1038/s41598-019-52371-7.

Vasco, D. W., Smith, J. T., and Hoversten, G. M. 2020. Seismicity and stress associated with a fluid-driven fracture: Estimating the evolving geometry, *Journal of Geophysical Research*, **125**, 1-27, https://doi.org/10.1029/2020JB020190.

Vesanto J., 1999, SOM-based data visualization methods. Intell Data Anal. 3:111–126.

Vesanto, J., Alhoniemi, F., 2000, Clustering of the self-organizing map, IEEE Trans Neural Netw 11:586–600.

Vesselinov, V.V., Mudunuru M.K., Ahmmed, B., Karra, S., and Middleton, R.S., 2020, Discovering signatures of hidden geothermal resources based on unsupervised learning, Proceedings, 45th Stanford Geothermal Workshop, Stanford University, Stanford, California.

Waldhauser, F., 2001. hypoDD—A Program to Compute Double-Difference Hypocenter Locations, *U.S. Geological Survey Open-File Report* 01-113. https://pubs.usgs.gov/of/2001/0113/.

Waldhauser F. and W.L. Ellsworth, 2001. A double-difference earthquake location algorithm: Method and application to the northern Hayward fault, *Bulletin of Seismological Society of America*, 90, 1353-1368.

Wang, S., 2003, Application of self-organising maps for data mining with incomplete data sets. Neural Comput Applic 12:42–48

Wang, R., Martin, F., and Roth, F., 2003. Computation of deformation induced by earthquakes in a multi-layered elastic crust-Fortran programs EDGRN/EDCMP, *Computers and Geosciences*., 29, 195-207.

Warpinski, N.R., 1991, Hydraulic Fracturing in Tight, Fissured Media: Journal of Petroleum Technology, v. 43, 146–209.

Whitehead, R.L., 1994, Ground Water Atlas of the United States: Segment 7, Idaho, Oregon, Washington, doi:10.3133/ha730H.

Witherspoon, P.A., Wang, J.S.Y., Iwai, K., and Gale, J.E., 1980, Validity of Cubic Law for fluid flow in a deformable rock fracture: Water Resources Research, 16, 1016–1024.

Wolfe, E.W., and Morris, J., 1996, Geologic map of the island of Hawaii: U.S. Geological Survey Miscellaneous Investigations Series Map I-2524-A, 18 p., 3 sheets, scale 1:100,000.

Yoffe, E.H., 1960, The angular dislocation: Philosophical magazine A, Physics of condensed matter, defects and mechanical properties, v. 50, p. 161–175.

Yu, L, and Liu, H. Feature selection for high-dimensional data: A fast correlation-based filter solution, Proceedings of the Twentieth International Conference on Machine Learning (ICML-2003), Washington DC, 2003.

Zhdanov, M., I. M. Varentsov, J. Weaver, N. Golubev, and V. Krylov, 1997, Methods for modelling electromagnetic fields results from COMMEMI – the international project on the comparison of modelling methods for electromagnetic induction: Journal of Applied Geophysics, 37, 133–271.

Zhang, H. and C.H. Thurber (2003), Double-Difference Tomography: The Method and Its Application to the Hayward Fault, California, *Bul. Seism. Soc. Am.*, **93**, 1875–1889.

Zhong, S., and Watts, A. B., 2013, Lithospheric deformation induced by loading of the Hawaiian Islands and its implications for mantle rheology. Journal of Geophysical Research, 118 (11), 6025-6048.

Zhu, W., and G.C. Berosa, 2019, PhaseNet: a deep-neural-network-based seismic arrival-time picking method, *Geophys. J. Int.*, 216, 261–273.

Zonge, K. L., & Hughes, L. J. (1991). Controlled source audio-frequency magnetotellurics. In Electromagnetic Methods in Applied Geophysics: Volume 2, Application, Parts A and B (pp. 713-810). Society of Exploration Geophysicists.

Bibliography

Bachura M. and T.Fischer (2016), Detailed velocity ratio mapping during the aftershock sequence as a tool to monitor the fluid activity within the fault plane, *Earth Plan. Sc. Lett.*, **453**, pp. 215–222.

Bodini, Nicola, Dino Zardi, and Julie K. Lundquist. 2017. "Three-Dimensional Structure of Wind Turbine Wakes as Measured by Scanning Lidar." Atmospheric Measurement Techniques 10: 2881–2896. https://doi.org/10.5194/amt-10-2881-2017.

Caldwell, T.G., Bibby, H.M., and Brown, C., 2004, The magnetotelluric phase tensor. *Geophys. J.* 467 *Int.* **158**, 457–469.

Chave, A.D., and Jones, A.G. (eds), 2012, *The Magnetotelluric Method: Theory and Practice*, Cambridge University Press, 552 pp.

Connor, C.B., 2021, Magnetic anomaly over an inclined igneous dike. http://www.cas.usf.edu/~cconnor/magnetic_dike.html Last checked 12/5/2021

Denlinger, R. P., and Flinders, A., 2022, Density structure of the island of Hawai'i and the implications for gravity-driven motion of the south flank of Kilauea Volcano. Geophys. J. Int. (2021), 1-10. Advance Access publication 2021 October 04, *GJI Gravity, Geodesy and Tides*.

Dobrin, M.D., and C.H. Savit, 1988, Introduction to geophysical prospecting, New York, McGraw-Hill. 864 pp.

Finn, C., and Williams, D.L., 1982, Gravity evidence for a shallow intrusion under Medicine Lake volcano, California, *Geology*; October 1982, v. 10; p. 503-507.

Gunasekera, R.C., G.R. Foulger, and B.R. Julian (2003), Reservoir depletion at The Geysers geothermal area, California, shown by four-dimensional seismic tomography, *J. Geophys. Res*., **108**, 2134, doi:2110.1029/ 2001JB000638.

Hill, G., Wannamaker, P.E., Maris, V., Stodt, J.A., Kordy, M., Unsworth, M.J., Bedrosian, P.A., Wallin, E.L., Uhlmann, D.F., Ogawa, Y., and Kyle, P., accepted for publication, 2022 Trans-crustal structural control of CO_2-rich extensional magmatic systems revealed at Mount Erebus Antarctica. Nature Communications.

Hu, X., Steinsland, I., Simpson, D., Martino, S., & Rue, H., 2013. Spatial modelling of temperature and humidity using systems of stochastic partial differential equations arXiv, 1307.1402 v1.

Husen S., R. B. Smith, G. P. Waite (2004), Evidence for gas and magmatic sources beneath the Yellowstone volcanic field from seismic tomographic imaging, *J. Vol. and Geoth. Res*., **131**, pp. 397-410.

Ichiki, M., Kaida, T., Nakayama, T. *et al.* Magma reservoir beneath Azumayama Volcano, NE Japan, as inferred from a three-dimensional electrical resistivity model explored by means of magnetotelluric method. *Earth Planets Space* **73,** 150 (2021). https://doi.org/10.1186/s40623-021-01451-y

Jerram, D., Millett, J.M., Kuck, J., Thomas, D.M., Planke, S. Haskins, E., Lautze, N.C. and Pierdominici, S., 2019, Understanding volcanic facies in the subsurface: A combined core, wireline logging and image log data-set from the PTA2 and KMA1 boreholes, Big Island, Hawai'i, Scientific Drilling, v. 25, p. 15-33, doi: 10.5194/sd-25-15-2019.

Julian B.R., A. Ross, G.R. Foulger, and J.R. Evans (1996), Three-dimensional seismic image of a geothermal reservoir: The Geysers, California, *Geoph.l Res. Lett.*, **23**, doi:10.1029/96GL03321.

Kukarina, E., Michael West, Laura Hutchinson Keyson, Ivan Koulakov, Leonid Tsibizov, Sergey Smirnov; Focused magmatism beneath Uturuncu volcano, Bolivia: Insights from seismic tomography and deformation modeling. *Geosphere* 2017; 13 (6): 1855–1866. doi: https://doi.org/10.1130/GES01403.1

Lin, G. (2013), Seismic investigation of magmatic unrest beneath Mammoth Mountain, California, USA, *Geology*, **41**, 8, p. 847–850, doi:10.1130/G34062.1

Lin, G., and B. Wu (2018), Seismic velocity structure and characteristics of induced seismicity at the Geysers Geothermal Field, eastern California, *Geothermics*, **71**, pp. 225–233.

Lindgren, F. Rue, H., 2011. An explicit link between Gaussian fields and Gaussian Markov random fields: the stochastic partial differential equation approach, J. R. Statist. Soc. B (2011)73, Part 4, 423–498.

Pierce, H., and Thomas, D.M., 2009, Magnetotelluric and audiomagnetotelluric groundwater survey along the Humu'ula portion of Saddle Road near and around the Pohakuloa Training Area, Hawaii: U.S. Geological Survey Open-File Report 2009–1135, 160 p., https://pubs.usgs.gov/of/2009/1135.

Revil, A., Le Breton, M., Niu, Q., Wallin, E.L., Haskins, E., and Thomas, D.M., 2017, Induced polarization of volcanic rocks – 1. Surface versus quadrature conductivity, Geophysical Journal International, v. 208, n. 2, p. 826–844, doi: 10.1093/gji/ggw444.

Revil, A., Le Breton, M., Niu, Q., Wallin, E.L., Haskins, E., and Thomas, D.M., 2017, Induced polarization of volcanic rocks. 2. Influence of pore size and permeability, Geophysical Journal International, v. 208, n. 2, p. 814–825, doi: 10.1093/gji/ggw382.

Smith, C.M., Nwosu, C., Aljubran, J., Ochie, K., Guidmundsdottir, H., and Okorafor, E.R., 2022, Recent trends in artificial intelligence for geothermal energy, Proceedings, 47th Stanford Geothermal Workshop, Stanford University, Stanford, California.

USGS, 2022, Quaternary Fault and Fold Database of the United States. Online (03/29/2022) https://www.sciencebase.gov/catalog/item/589097b1e4b072a7ac0cae23

Vozoff, K., 1991, The magnetotelluric method, in Nabighian, M.N., Electromagnetic methods in applied geophyiscs: Tulsa, Okla., Society of Exploration Geophysicists, v.2. pt. B, p. 641-711.

Zhang, Q., and G. Lin (2014), Three-dimensional Vp and Vp/Vs models in the Coso geothermal area, California: Seismic characterization of the magmatic system, *J. Geophys. Res. Solid Earth*, **119**, doi:10.1002/ 2014JB010992.

Appendix A. MT3D Inversion (pGEMINI) Code Development

A.1 Capability

- 3D Parallel Geophysical Electromagnetic Modeling and Inversion of Natural and Induced sources
- Massively parallel code: tested scalability for thousands for supercomputing cores (Jaysaval et al., 2021)
- Can perform forward modeling and inversion for almost all geophysical EM data, e.g., controlled-source EM, airborne EM, borehole EM, magnetotelluric, etc.
- Uses unstructured tetrahedral meshes

A.2 Challenges

- Model building/meshing can be involving due to unstructured tetrahedral mesh
- Needs data to be reformatted to be compatible with pGEMINI
- Needs proper 3-D coverage and preferably prior information for solid results
- Needs to test topography models for accuracy

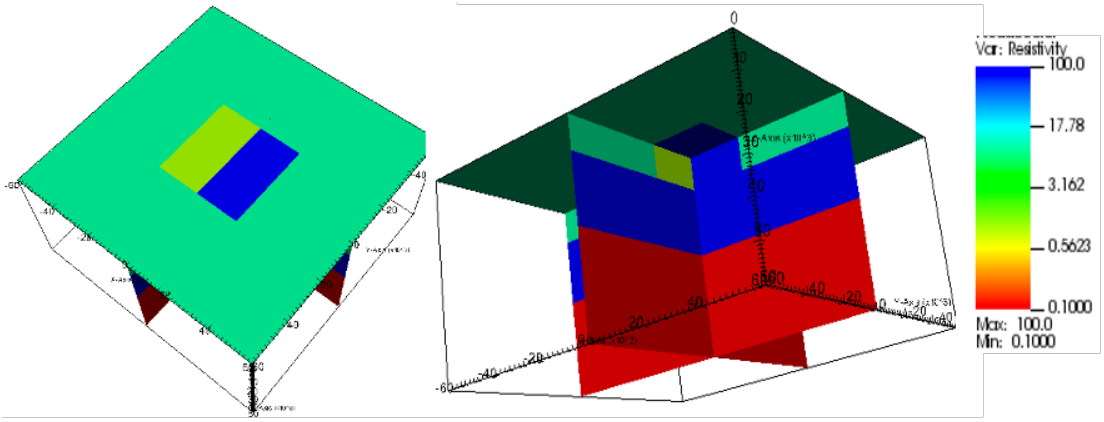

COMMEMI 3D-2 Resistivity Model

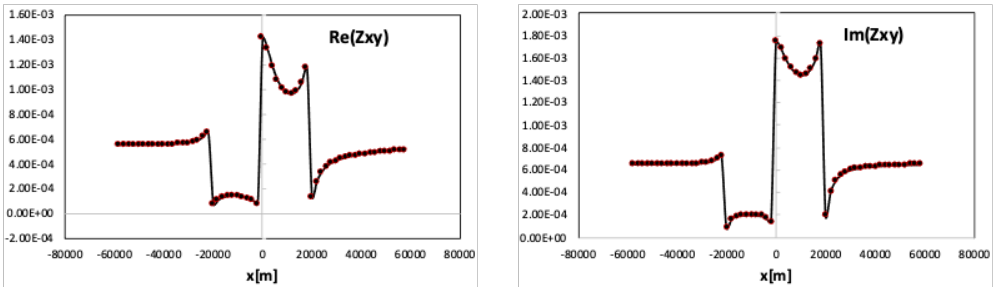

Figure 110. *xy*-component of MT tensor for COMMEMI 3D-2 (Zhdanov et al. 1997) benchmarked against published results.